ABSTRACT

Title of Document:	SYNTHESES, STRUCTURES AND PROPERTIES OF NANOPOROUS METAL-ORGANIC FRAMEWORK MATERIALS
	Ping-Yen Hsieh, Doctor of Philosophy, 2011
Directed By:	Professor Robert M. Briber Professor Mark A. Green Department of Materials Science and Engineering

This dissertation describes the synthesis and characterization of a number of extended framework materials. Firstly, a series of transition metal and lanthanide metal-organic framework materials (MOFs) possessing both two and three-dimensional (2-D/ 3-D) structures as a result of linkage with different rigid carboxylate ligands have been synthesized. The crystal structures have been determined by single crystal X-ray diffraction, and their thermal/ structural stability evaluated by thermogravimetric analysis, powder neutron diffraction, *in-situ* and combined synchrotron powder X-ray and Raman spectroscopy. The structural stability strongly relates to the dimensionality and chemical bonding within the frameworks. In this dissertation, a geometric strategy has been proposed to elucidate these complex structures. A nanoporous structure stable up to $500^{o}C$ can be obtained by dehydrating holmium MOF with 1, 3, 5-Benzene tricarboxylic

acid (H_3BTC) ligand. Its porosity is shown to be $879.1 m^2/g$ specific surface area by gas isotherm experiments and absorbing 1.46wt% excess of hydrogen at 77K. High resolution neutron powder diffraction has been performed on the dehydrated Ho-MOF-BTC system with *$P4_122$* chiral space group under different deuterium gas pressures and a new mechanism for gas adsorption in framework materials. A unique "helical" deuterium adsorption phenomenon results from direct interaction between the guest molecules and the non-centrosymmetric (chiral) framework architecture. Reconstruction of the nuclear scattering density using the charge flipping method has been utilized as a novel strategy for the qualitative analysis of the adsorbed molecules, in combination with maximum entropy method (MEM) density maps that provide quantitative information of the exact distribution of the diffusion pathways. In addition, the structure, magnetic and photo-luminescent properties of three lanthanide- and transition metal MOFs with shorter formate ligand are investigated by single crystal X-ray and neutron diffraction as well as solid-state fluorescence spectroscopy techniques, demonstrating unusual magnetic behaviors of Co-formate systems and strongly characteristic emission spectra from europium (Eu(III)) and terbium (Tb(III)) compounds.

SYNTHESES, STRUCTURES AND PROPERTIES OF NANOPOROUS METAL-ORGANIC FRAMEWORK MATERIALS

By

Ping-Yen Hsieh

Dissertation submitted to the Faculty of the Graduate School of the
University of Maryland, College Park, in partial fulfillment
of the requirements for the degree of
Doctor of Philosophy
2011

Advisory Committee:
Professor Robert M. Briber, Chair/Advisor
Professor Mark A. Green, Advisor
Professor Manfred Wuttig
Professor Chunsheng Wang
Professor Gregory S. Jackson

Dedication

To my beloved family.

Acknowledgements

First of all, I would like to express my sincere thanks to my two advisors, Dr. Robert M. Briber and Dr. Mark A. Green. They gave me the opportunity to join their research groups, and show their valuable advice, patience, inspiration and freedom of research. They teach me not only on the research techniques but also the attitude to explore the truth. A lot of appreciation also goes to the committee members: Dr. Wuttig, Dr. Wang and Dr. Jackson for their advice in this dissertation; Dr. Yun Liu and Dr. Craig M. Brown in NIST Center for Neutron Research (NCNR) for their generous guidance on gas loading experiments; Dr. Peter Y. Zavalij at X-ray Crystallographic Center in UMD for single crystal measurements and identifications; and Dr. Pawel Zajdel and Dr. Van Beek Wouter for their help on synchrotron X-ray measurements in ESRF. Especial thanks go to Dr. Efrain Rodriguez, who has given me very useful suggestions and shared his research experience to me. My thanks also go to all the friends, Sang Hak Shin, Gimmy Liao, T. C. Lin, Dale Huang and Tommy Tsai. We share our American lives together and it's really my pleasure to meet all of you.

Most importantly, I would like to show my incomparable appreciation to all my family, my parents and grandmother for their full support, my brother for his encouragement, my son, David, for his joyful smiles and especially my wife, Hui-Wen. You lead me to accomplish this Ph.D. degree. Thank you for walking in my life and staying with me.

Finally, I always know you are watching me, supporting me, and encouraging me. I can't finish all of these things without you. These achievements owe to you:

Grandfather

in Heaven

Table of Contents

List of Tables

List of Figures

Chapter 1: Introduction

1.1 Metal-Organic Frameworks as Functional Materials

Metal-organic framework materials (MOFs), a novel class of inorganic-organic hybrid materials, have attracted significant attention over the past decade. As indicted by the name, MOFs are constructed from inorganic nodes coupled with organic linkers. The inorganic nodes can be transition metal clusters or isolated lanthanide metal ions, which offer potentially interesting magnetic and optical properties, making MOFs excellent candidates in such applications as molecule-based magnets and photo-luminescent phosphors[1,2]. The majority of organic linkages so far are focused on carboxylates and their derivatives[3-6]. Dehydrated MOFs can be very porous with low density and extremely high specific surface area (S.S.A.), which can achieve over 6000m^2/g[7]. The pore size and geometry are adjustable depending on the lengths of the ligands and molecular designs that make MOFs suitable for use as molecular sieves, nano-catalysts and gas storage materials[8-30]. All of these properties are strongly related to the fundamental crystal structure of each particular MOF. Therefore, the structure identification is a focus of this dissertation and will form each of the discussion in chapter 4-8. This chapter contains a brief overview of the progress made so far to these materials.

1.2 Structures and Properties: Syntheses and Design
1.2.1 Syntheses of MOF Materials

Generally, the most common and traditional strategy for the synthesis of MOF materials is solvent evaporation or precipitation from an oversaturated solution, although many synthetic methods have been used to synthesize MOFs, such as diffusion, hydro-/

solvothermal synthesis, microwave reaction and ultrasonic methods. This will be discussed below[31].

(i) Solvent evaporation. This synthetic procedure follows by the sequence: (a) The metal salts or oxides should be dissolved in the solvent, (b) Elevated temperatures may be applied to increase the solubility and create a uniform reaction environment and (c) Crystals are then precipitated during the cooling step or from an oversaturated solution.

(ii) Diffusion method. The major principle of this technique is the slow mixing of reagents that are separated by a buffer region. For example, in solvent liquid diffusion, multilayers (generally three) containing liquid of different densities are employed. These consist of one good solvent for the final crystal, one precipitant solvent (bad solvent), and one neutral solvent as a layer for a diffusion buffer. The precipitant solvent will slowly diffuse into the separate layer and crystals grow at the interface. The key challenge to utilize this method lies with the selection of solvents and the control the diffusion rate (e. g. reaction rate) by adjusting the thickness of the layers. Similarly, in this dissertation, another approach for slow diffusion of the volatile solvents across some physical barriers, such as two vials of different sizes, has been used. In some specific case, gels are also used as diffusion and crystallization media to reduce the reaction rate and to avoid a precipitation of polycrystalline material. However, in some situations, the reproducibility and productivity of samples from this method is poor and whole process can be very time-consuming.

(iii) Hydro-/ solvothermal synthesis[32-36]. This method was originally explored for the synthesis of zeolites, but has been adapted to the synthesis of MOFs. The synthesis mechanism is the self-assembly of crystals from soluble precursors. The operation temperature range can be between 80 to 260$^{\rm o}$C and the reaction is carried out inside a

Teflon-lined autoclave under autogenous pressures as shown in Figure 1.1 (a)[37]. The important parameters for this synthesis are the annealing temperature, the concentration ratios between metal salts and ligands, the solubility of the reagents in the solvent, the pH value of the solution and the cooling rates. Although experience can help direct the best process for growing crystalline MOFs, experimentation and trial-and-error methods are still always necessary. It should be emphasized that the filled rate of solution in an autoclave should be less than 30% for the temperature range since high pressure will be generated during the thermal treatment and chemical reaction as shown as Figure 1.1 (b).

(iv) Microwave reaction and ultrasonic method are novel techniques to prepare MOFs with relatively high synthesis speed and well controlled size and the shape of the resulting crystals, which depend on the concentration of precursors. However these two strategies are still not widely applied so far.

(a)

(b)
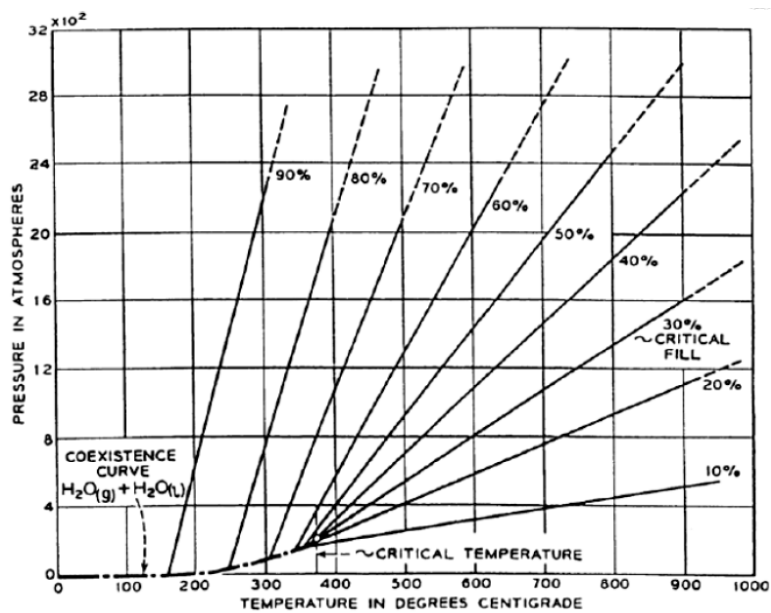
Figure 1.1 (a) Illustrations of a Teflon-lined autoclave and (b) Temperature dependence of autogenous pressure.

1.2.2 Structure and Design of MOF Materials

As mentioned previously, MOFs are hybrid materials composed of inorganic and organic components. The inorganic parts are composed of transition-metal clusters and isolated lanthanide metal ions as nodes and act as good electron acceptors, whereas the organic components consist of multidentate- and multifunctional organic ligands[5,18,38] containing O- or N- electron donors such as carboxylate or amine. The neutralization of charges induces the combination of metal ions and linkers to form strong chemical bonds making an extended framework. In the MOF skeleton, the inorganic parts exhibit rigid behavior, and the organic moieties provide flexibility. However, interactions in these hybrid materials can also be relatively weak, such as hydrogen bonding, van der Waals force or π-π interactions. A comprehensive identification of MOF materials (also called porous coordination polymers, PCPs) has been proposed and classified in 1st, 2nd and 3rd generation by Kitagawa and his co-workers[39-41], as shown in Figure 1.2. For the 1st generation PCP materials, the microporous frameworks are sustained only with the existence of guest molecules. An irreversible framework collapse will be observed on removal of the guest molecules. For 2nd generation PCP materials, stable and robust porous frameworks can be obtained with a permanent porosity after the departure of guest molecules. 3rd generation PCP materials exhibit flexible and dynamic frameworks, which can adapt to external stimuli, such as light, electric field, guest molecules and exhibit reversible structural transitions. The reversible structural transitions can be from crystalline to amorphous, amorphous to crystalline and crystalline to crystalline phase transitions. Recently, an interesting "large breathing effect" in transition metal MOFs have been observed and proposed by Férey et al.[12,42-44]. Although no chemical bonds break between the metal cations and organic ligands during the departure of guest water

molecules, the framework structure shows a significant anisotropic change of the pores and a reversible crystalline-crystalline phase transition. This phenomenon can be caused by (i) The creation of strong hydrogen bonds between the water molecules and the hydrophilic parts of the pore, (ii) The onset of π-π interaction from benzyl group on ligands, (iii) The bridged oxygens with different bonding types between transition metals and linkers (ionocovalent vs. covalent), and (iv) The local symmetry of inorganic secondary building units (SBUs) with mirror plane[12]. However, for some lanthanide MOF materials with a 1-D inorganic subnetwork system show irreversible crystal changes between low and high temperature conditions, which is caused by a change in the connection mode of carboxylic acid and a decrease in the coordination number on the lanthanide cations[45]. In the last decade, there are at least 11,000 MOF materials which have been synthesized since 2003. Of these about 3000 compounds are three-dimensional (3-D) and about 6000 are two-dimensional (2-D) frameworks[46]. To date, it is still very difficult to design successful and universal synthetic strategies for the preparation of MOFs that have predictable structures and desired performance. Although numerous papers often mention such terms as "design", "combinatorial", "logic synthesis", "molecular design", or "modular chemistry" the self-assembly of the framework is significant affected by factors such as geometry of the ligands, coordination environment of the metal ions, the solvent system, the template, the pH value of the solution, steric requirement of the counter ions, reaction temperature and the ratio of metal to ligand etc. Recently, the organic solvent molecules (including organic ammonium cations) have drawn much attention and played three different, but important roles in the formation of various types of MOF structures: (i) As a solvent for organic ligand (to deprotonate O-donor ligands); (2) As a structure-directing agent; (3) Balance the charges by

coordinating to the metal ion[47,48]. More detailed discussion for the dimensionality and structural stability will be involved in chapter 5.
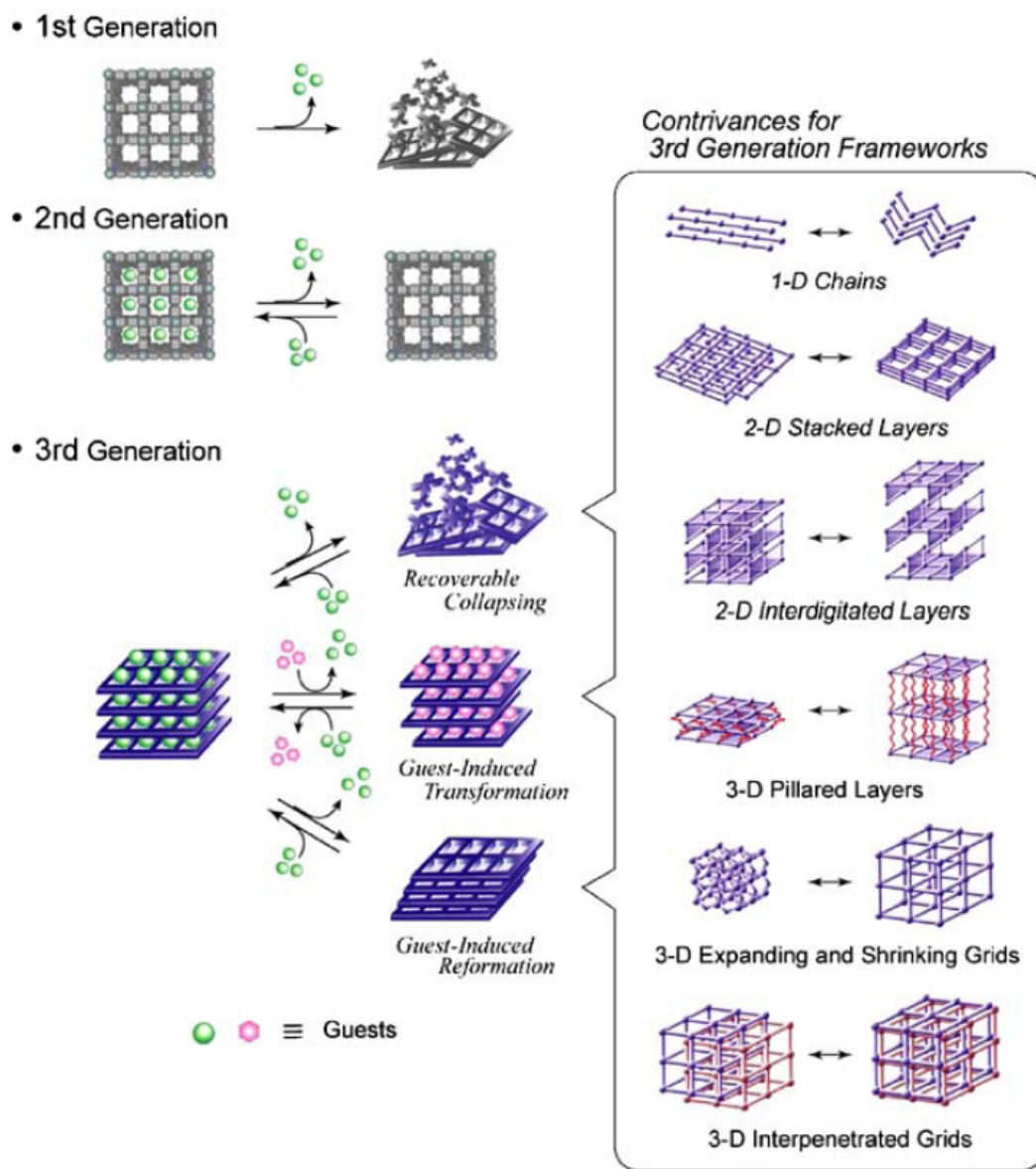
Figure 1.2 Illustration for three generation porous coordination polymers.
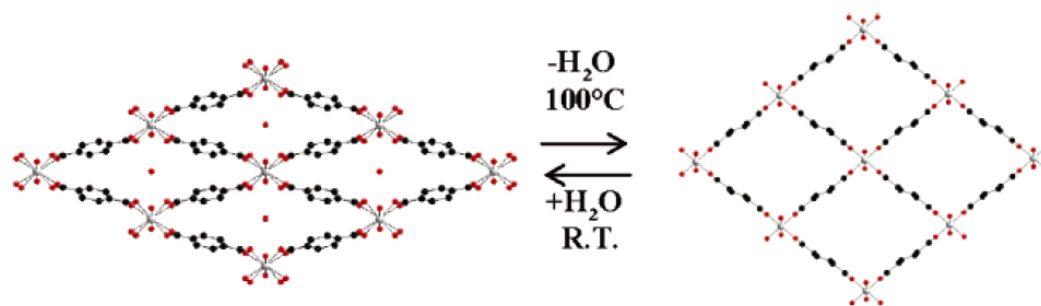
Figure 1.3 "Large breathing effect" in a transition metal MOF structure.

1.2.2.1 Metallic Nodes

Extensive investigations into the design of MOFs has been proposed and led to numerous practical and conceptual developments in this field[3-5,11,12,19,29,38,39,42,44,46,49-52]. Yaghi et al. have pointed out a main issue on the prediction of MOF structures: the transition metal cations exhibit little directional information, which results in geometrical distribution around the cations depending on the ligands and a resultant diversity of possible structures. Therefore, Yaghi and co-workers introduced the "reticular synthesis"[38,46,53] using the functional carboxylates to chelate the metal cations and lock them into a rigid and directional metal-oxygen-carbon cluster, with the points of extension defining geometries and dimensionalities refereed to as secondary building units (SBUs)[38,46,51,52,54-56]. Depending on the strategy, the structural integrity and rigidity of the building blocks are maintained during the assembly process of the entire lattice. Therefore, the MOF structures can be more controllable and predictable by appropriate selection of SBUs combined with selection of specific ligands. In addition, reticular synthesis is also essentially different from supramolecular self-assembly because the framework structure has been constructed by strong covalent bonds. The substantial

attraction for supramolecular self-assembly is similar to the definition of PCPs with weaker and non-covalent interactions. Examples of SBUs in carboxylate MOFs are given in Figure 1.4. This approach clearly determines the steric structure of the resulting framework with the points of lattice extension and can be applied to numerous inorganic SBUs and organic linkers resulting in versatile geometries. Although reticular synthesis concepts can help understand the structural diversity for transition metal MOF materials, there is still no ability to predict rare earth MOF materials. In addition, the lanthanide ions are relatively difficult to coordinate with the N-donor linkers since coordination ability of O-donor ligands are stronger than N-donor ligands.
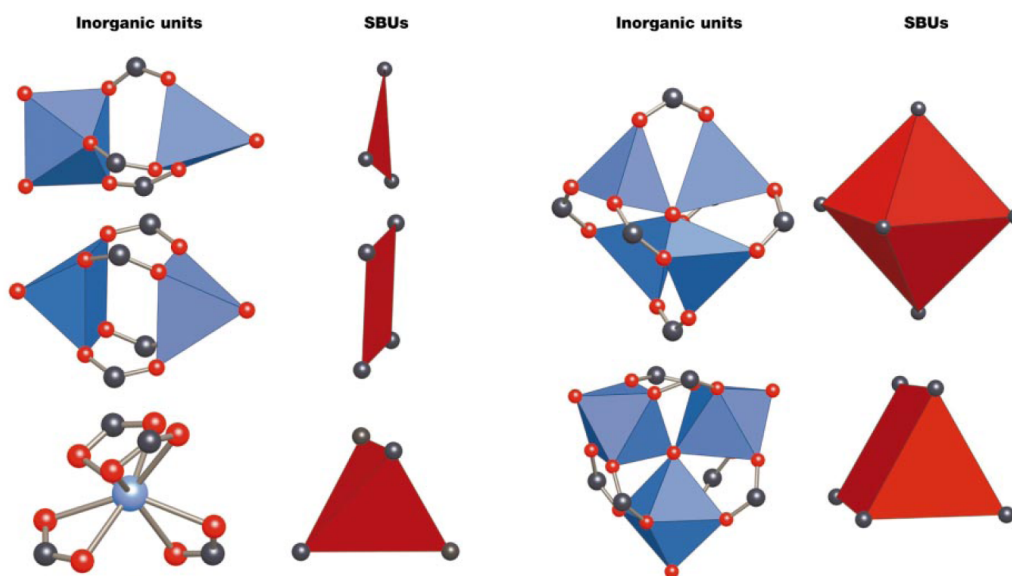
Figure 1.4 Illustration for the metal ion clusters and their geometric definitions as secondary building units (SBUs).

1.2.2.2 Organic Linkers

There are three major selections of organic linkers: (i) Neutral organic ligands. Generally, ligands in this case possess azaheterocyclic rings that have lone-pair electrons on nitrogen atoms which can coordinate with metal ions (N-donor ligands), (ii) Anionic organic ligands. Carboxylate linkers are classified in this type of ligand (O-donor ligands), and (iii) Cationic organic ligands[57]. As shown in Figure 1.5, hundreds of O- and N-donor type organic ligands have been used to synthesize MOF materials[46]. In particular, the multi-carboxyl linkers with aromatic rings offer a range of rigidity to construct the framework structures. Although the selection of the carbon-based linkage is important, it is not the only factor that influences the dimensionality of MOFs. The ligand motifs can be classified as: (i) 1-D or linear ligands and derivatives such as 1, 4-Benzenedicarboxylic acid (BDC) and 4, 4'-bipyridine (4, 4'-BPY), (ii) 2-D or planer ligands and derivatives such as 1, 3, 5-Benzene tricarboxylic acid (BTC) and 1,3,5-Tris(4-carboxyphenyl) benzene (BTB), and (iii) 3-D and steric (tetrahedron) ligands and derivatives such as methanetetrabenzoate (MTB) and adamantanetetrabenzoate (ATB). Simple diagrams summarizing the main structural motif of the organic linker can be constructed, examples are shown in Figure 1.6. Interestingly, a 3-D organic linkage has been synthesized and provides an opportunity to form 3-D MOF structures that are sometimes difficult to obtain from 1-D and 2-D ligands.
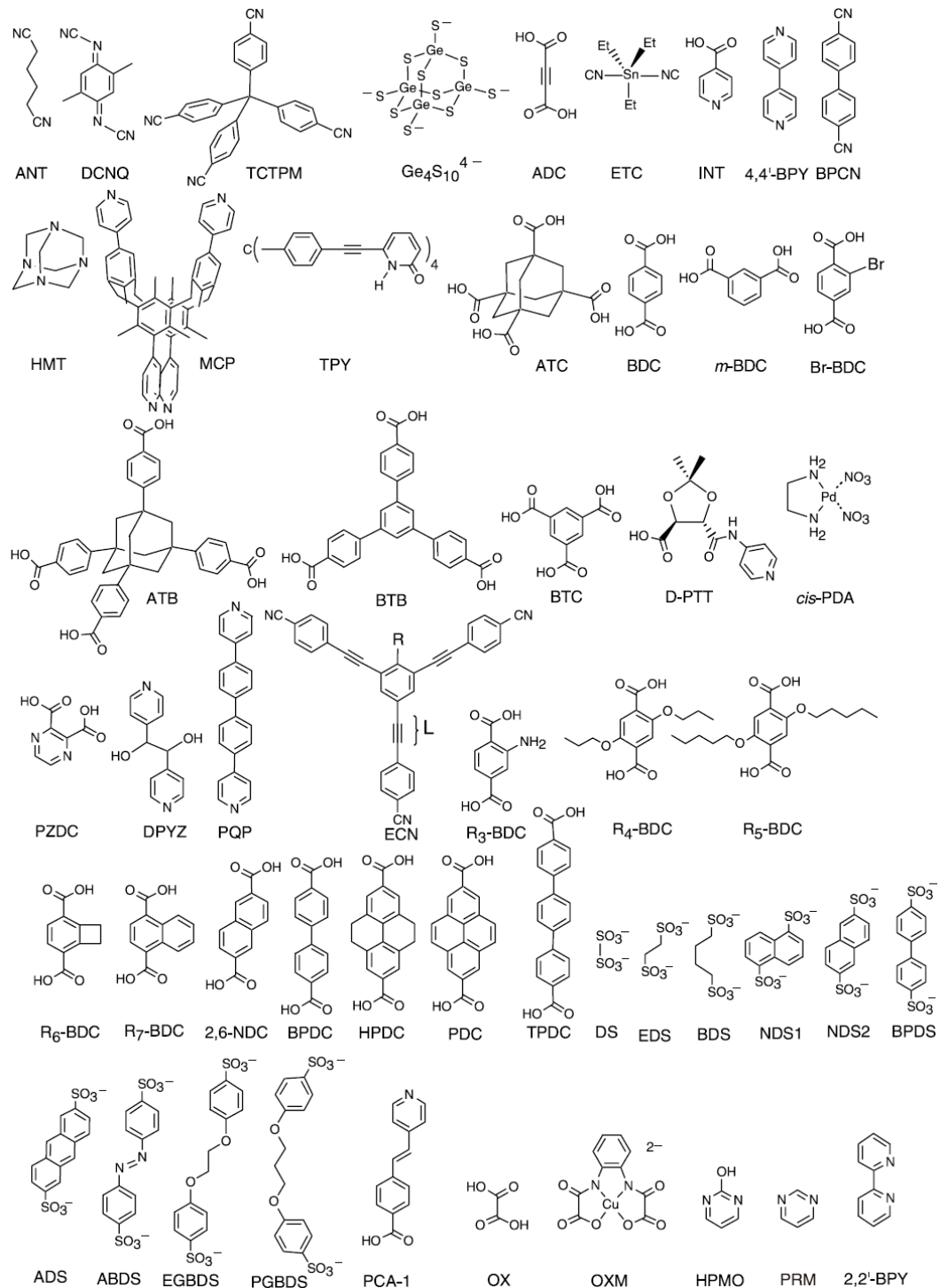
Figure 1.5 Examples for organic linkers with 1-D, 2-D and 3-D molecular motifs.
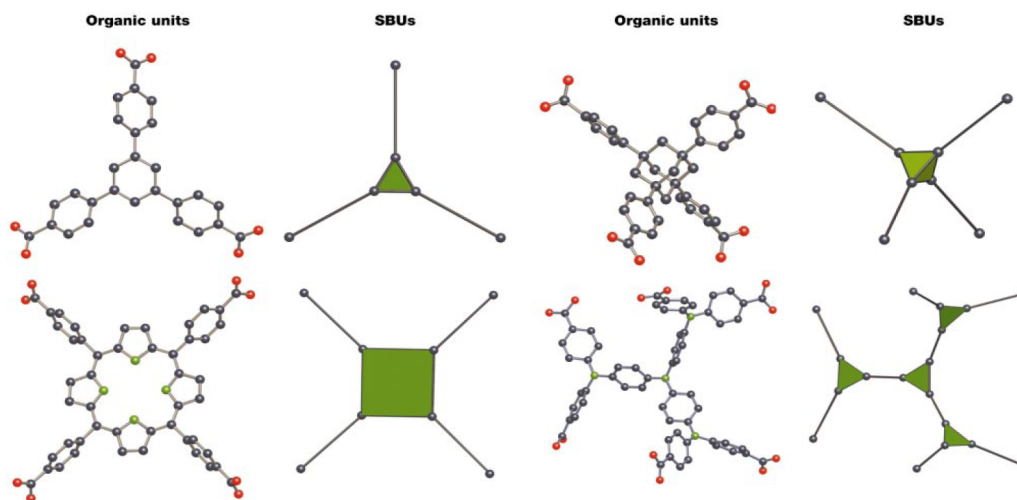
Figure 1.6 Illustration for the organic ligands and geometric definitions as secondary building units (SBUs).

1.2.3 Structures of Lanthanide MOF Materials

Recently, lanthanide MOF materials possessing unique optical and magnetic properties arising from unpaired electronic transitions in the $4f$ orbits have been synthesized. Unlike d-block metal cations, lanthanide cations have high coordination numbers, a property that can be employed partially as linkers to construct networks; furthermore, the geometry of these linkers is more widely variable than that of transition metals, yielding a result as new and unusual network topologies, such as five-connected nodes sustained by bridging ligands[58]. In addition, the high affinity of lanthanide cations as electron-acceptor atoms makes carboxylates excellent candidates as organic linkers and form stable architectures[59-63]. Previously, tricarboxylic acid (H_3BTC) has been used as a ligand due to three branching sites to form a versatile geometry and dimensionality. A series of lanthanide MOF systems synthesized from 1, 2, 4-benzenetricarboxylate (1, 2,

12

4-H$_3$BTC)[45,64] and 1, 3, 5-benzenetricarboxylate (1, 3, 5-H$_3$BTC) have been proposed[65-68]. The complete study of lanthanide elements with 1, 2, 4-H$_3$BTC systems show that the larger rare-earth cations (Ce, Pr, …, Gd) adopt different crystal structures from that when the smaller lanthanide cations (Tb, Dy, Er) are used, revealing a prominent rare-earth cation size effect[45]. Furthermore, in this 1-D inorganic subnetwork system, distinguishable crystal changes between low and high temperature conditions have been observed, implying that a flexible framework can be obtained. However, these lanthanide MOFs demonstrate an irreversible phase transition that is caused by a change in the connection mode of carboxylic acid and a decrease in the coordination number on the lanthanide cations[45]. In comparison, a family of thermally and structurally stable lanthanide MOFs formed with the 1, 3, 5-H$_3$BTC ligands have 1-D channels along c axis[65-68]. Interestingly, the in-situ PXRD results performed in vacuum confirm a reversible phase transition during dehydration[61]. Some studies utilized longer carboxylic acid ligands to tailor the lanthanide-based MOFs to improve the specific surface area have been published[69,70]. Generally, the phase transition behaviors can be identified by a combination with thermogravimetric analysis (TGA) and *in-situ* synchrotron powder X-ray (PXRD). However, more important details such as bonding configuration on the metal cations in MOF structure are sometimes missing. Some MOF frameworks maintain crystallinity after the dehydration, and bonding configuration can be obtained by the full-matrix Rietveld refinement method. Particularly, in more cases for rare-earth MOFs, the frameworks collapse at elevated temperature range[71-74] and result in a total or partial amorphous phase, implying that it is more difficult to analyze the bonding configuration via diffraction technique. *In-situ* Raman spectroscopy can be a powerful tool to evidence the detailed bonding condition even in non-crystal phase.

1.3 Metal-Organic Frameworks as Hydrogen Storage Materials

Hydrogen gas (H_2) is of great interest as a potential clean energy carrier. The reaction of hydrogen and oxygen converts the chemical energy into electrical energy and only exhausts water and energy. From the energy density aspect, the gravimetric energy density of hydrogen is 141.9kJ/g which is almost 3.5 times higher than traditional fossil fuels of 45.5kJ/g[75]. However, the volumetric density of hydrogen gas is extremely low (0.08988g/L). The condensation of hydrogen gas into highly dense environments is necessary for an efficient storage and delivery system. Two conventional strategies have been used which are (i) Compress hydrogen gas in high pressure tanks, and (ii) Cool down the hydrogen in cryogenic containers[76]. However, compression of hydrogen gas is difficult and open up several safety concerns. On the other hand, liquefaction of hydrogen via a cryostat system is inefficient in energy as the melting point and boiling point of hydrogen are very low at 14.01K and 20.28K, respectively, and therefore requires a complicated and bulky system that would use more than 30% of the energy content of hydrogen[77] to operate. Therefore, new hydrogen storage materials are required that would offer high density and be cheap and safe to operate. The United States Department of Energy (DOE) set short-term goal for hydrogen storage systems are 6.0wt% or 45g/ L by the year 2010, and 9.0wt% or 81g/ L by the 2015[78]. Two principal storage mechanisms have been explored: (i) Chemisorption (or chemical adsorption) of hydrogen atoms in metal hydrides and (ii) Physisorption (or physical adsorption) of hydrogen gas molecules in porous materials. Chemisorption and physisorption possess their own advantages and disadvantages. For example, the chemical adsorption has much stronger chemical bonding (typically 50–200kJ/ mole) between hydrogen atoms and host materials, whereas

physical adsorption depends on the weak attraction such as van der Waals force (typically 4–10 kJ/ mole). This results in operation temperature for chemisorption system at greater than 400°C, whereas liquid nitrogen temperatures would be required for physisorption. From the same reason, chemical adsorption has higher hydrogen adsorption density than physisorption at room temperature, but pyhsisorption offers faster desorption kinetics which are unobtainable in chemisorption. Although room temperature hydrogen storage technologies are desirable for all applications, cryogenic devices working at 77K offer more manageable systems than those of liquid hydrogen temperature 20.28K. Research on hydrogen adsorption in porous materials, particularly the metal-organic framework (MOF) materials, has become an important topic because of their high porosity and large specific surface areas[9,16-18,79-90]. It is important to note that currently available MOFs adsorb very little hydrogen (< 1wt%) at room temperature. Several strategies have been proposed to improve hydrogen storage capacity, including (i) Control of the pore size of the framework, (ii) Change the pore geometry of the framework to enhance the open space for exposed metal ion sites, (iii) Utilization of different metal ions, and (iv) Modification of the carbon-based ligands by doping with metal ions such as Li^+, Na^+ and K^+ to improve the attraction of hydrogen gas[91,92]. Much discussion has been centered on the optimal pore size for hydrogen adsorption which in MOFs is twice that of the hydrogen kinetic diameter $(2.89Å)$[93]. The fact that hydrogen uptake is appreciably enhanced at the optimal pore size is best utilized by two or more interpenetrating frameworks, termed catenation which are used to construct MOFs with tailored pore sizes[94-97]. The ideal pores for effective hydrogen adsorption in MOFs should consist of a large total pore volume coupled with optimal pore size at the molecular diameter for the adsorbing gas. This feature favors hydrogen interaction with the aromatic rings of the

organic linkers and improves the binding energy of hydrogen[98-100]. As shown in Figure 1.7, the isotherm gas experiment demonstrates the different hydrogen storage performances. The high slope in the linear region in low pressure range is highly desirable, indicating that the adsorption capacity can reach saturation with faster kinetics. Additionally, a large free pore volume leads to a large excess of gas uptake in the high pressure range. Unfortunately, these two characteristics typically compete against each other and are not realized in the same framework. More research on crystal engineering is required to explore the best MOF crystal structure.

Although macroscopic observation of gas storage behavior is evidenced by adsorption-desorption isotherm experiments[16,88,90,101], atomic level understanding of these functional structures is a key to understand the details of their storage capacity, and to show how improvement and optimization can be achieved in the future. Yaghi and his coworkers[81] determined the hydrogen adsorption sites in Zn_4O(1,4-benzenedicarboxylate) system by using single crystal neutron diffraction. On the other hand, Yildirim[80] and Brown[86,88] established a strategy to identify the gas adsorption positions in MOF systems via high resolution powder neutron diffraction (PND). These results demonstrated a strong relationship between the adsorption sites and details of crystal structures[88,101-105]. In general, the types of unsaturated metal ions and the architecture of the open space play dominant roles to determine the adsorption positions in the dehydrated MOF frameworks. Zhou and Wu[102-105] proposed that the enhancement of H_2 and methane adsorption in isostructural MOFs with open metal sites is strongly dependent on the binding strength on different metal ions. However, other point towards the importance of the pore size formed from the carbon-based organic ligand for the H_2 adsorption[106-108]. The optimal pore dimension about twice the kinetic diameter of the hydrogen molecule (i.e., around

5.8Å in diameter) enhances the interaction and adsorption heat between the H_2 molecules and organic walls. A comprehensive discussion on the gas adsorption behavior, positions and the correlation with size of the framework is included in chapter 6.
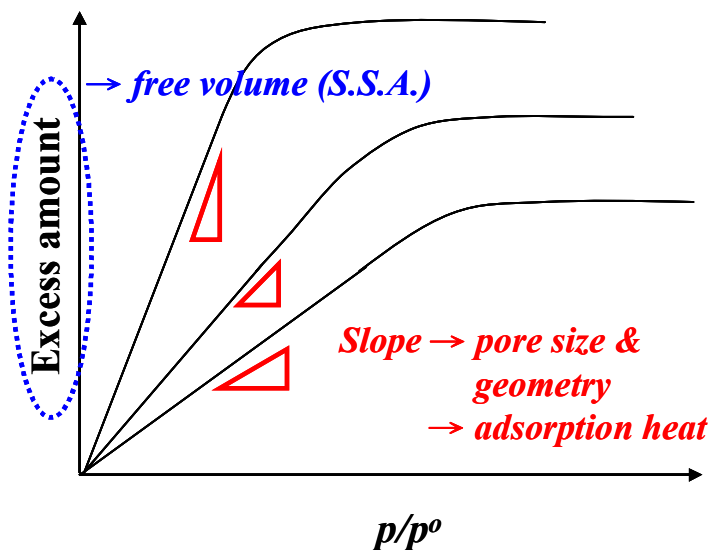
Figure 1.7 Illustration of different possible gas adsorption performances.

1.4 Optical Properties of Ln^{3+} ions

1.4.1 Introduction

Lanthanide MOFs with 4f orbits exhibit remarkable optical properties such as sharp (atomic-like) and full-wavelength range emission spectra that are strongly related to the nature of orbits. A number of Lanthanide MOFs have been synthesized and their photo-luminescent properties investigated[1,109]. In this section, some fundamental theories and terminologies corresponding to these measurements are introduced and explained. The detailed results will be presented and discussed in chapter 8.

1.4.2 Energy Levels for Ln^{3+} Ions

The spectroscopic properties of the lanthanides can be explained using the Russell-Saunders coupling scheme, which states that the energy level for an atom or an ion is influenced by three different coupling behaviors and interaction from electrons: (i) spin coupling, (ii) orbital (total angular momentum) coupling, and (iii) spin-orbital coupling[110]. The spin coupling, s, can be described by the spin quantum number, m_s, with values of $+\frac{1}{2}$ for spin up and $-\frac{1}{2}$ for spin down. The orbital angular momentum (with magnetic quantum number m_l), l is used to the total orbital angular momentum quantum number, L and the spin-orbital coupling with quantum number J, can be described as values of $(L+S)$, $(L+S)$-1,….. ,$|L-S|$. Therefore, energy level symbols of an ion can be expressed as $^{2S+1}L_J$. The ground state for a free ion should obey Hund's rules: (i) Maximum spin for electrons in a given shell, (ii) Maximum angular momentum possible for the given spin orientation, (iii) For a shell with less half-filled electrons, J will be taken as the lowest value for the ground state, and (iv) For a shell with half-filled or more electrons, J will be taken as the highest value for the ground state. Different state symbols of L are tabulated in Table 1.1. However, in this table, it should be emphasized that the state S here is symbolized for L quantum number, but not equal to the total spin momentum S.

L	0	1	2	3	4	5	6
State Symbols	S	P	D	F	G	H	I

Table 1.1 Different state symbols of quantum number L.

Terbium (Tb) can be used as an example. The electron configuration of Tb is [Xe]$4f^96s^2$. Therefore, the electron configuration of Tb^{3+} ion can be written as [Xe]$4f^8$. There are seven sub-shells in the f orbit indicating $l = 3$ and the values of m_l can be expressed as m_l = 3, 2, 1, 0,-1,-2,-3. An electron has $s = \pm\frac{1}{2}$ and m_s is $+\frac{1}{2}$ for spin up and $-\frac{1}{2}$ for spin down. According to Hund's rules the electron configuration in $4f$ orbit of Tb^{3+} can be displayed in Table 1.2. This arrangement allows to determine values of S, L, and J as well as the term symbol ($^{2S+1}L_J$) exhibiting the ground and excited states.

$4f$ orbit with 7 sub-shells for Tb^{3+}							
m_s status	↑↓	↑	↑	↑	↑	↑	↑
m_l values	+3	+2	+1	0	-1	-2	-3

Table 1.2 The electron configuration in $4f$ orbit of Tb^{3+} ion.

For $S = \sum m_s = 7\cdot(+\frac{1}{2})+1\cdot(-\frac{1}{2})=3$ corresponds to multiplicity $2S+1 = 7$

For $L = \sum m_l =2\cdot(+3)+1\cdot(+2)+1\cdot(+1)+1\cdot(0)+1\cdot(-1)+1\cdot(-2)+1\cdot(-3)=3$ corresponds to the label F.

For $J = L+S$, $L+S$-1,…..$|L - S|$= 6, 5, 4,…..0.

Therefore, the spin-orbital coupling (Russell-Saunders Coupling) levels are defined as $^7F_6$, $^7F_5$, $^7F_4$, $^7F_3$, $^7F_2$, $7F_1$, $7F_0$. Depending on the Hund's law, the electron number in the outer $4f$ sub-shells is 8, in this Tb^{3+} case, larger than the number of half-filled orbits (7

electrons) indicating the maximum J value introduces the lowest energy. The ground state can be identified as $^7F_6$. An energy level diagram called "Dieke diagram" for all the lanthanide ions has been established in Figure 1.8, which is an important tool in understanding, predicting and interpreting the luminescence spectra of lanthanide elements[111,112]. This diagram plays the same role like "Tanabe-Sugabo" diagram of energy levels in d-block transition metals. However, an important difference is that the contribution of the spin-orbit coupling is more prominent than in the crystal field effect for the lanthanide metal systems, but totally inverse situations is present in transition metals. This phenomenon reflects the true nature of the f orbits which are shielded by outer fulfilled 5s and 5p orbits that show no significant effect from the ligands.

Figure 1.8 The Dieke energy level diagram for lanthanide elements[101].

1.4.3 Luminescent properties of the Ln^{3+} Ions

Luminescence is the term for radiation or light from a system arising from absorbed energy from external stimuli, such as electromagnetic (X-ray, UV/Vis or IR photons), electron beams, heat, electricity, mechanical energy, or biochemical energy[113]. The excited state can release energy directly in the form of heat or radiation, or transfer energy or charge to another excited state via intersystem crossing. The whole energy transition diagram known as Jablonski energy diagram is shown in Figure 1.9. Some terminology should be defined for the explanation of luminescence. (i) Fluorescence (FL). FL is the emission of light from a singlet excited state to the ground state with a lifetime in the range of nanoseconds (10^{-9} s), (ii) Phosphorescence (PL). PL is the emission of light from a triplet excited state to the ground state with much longer lifetime in the range of milliseconds (ms) to seconds (s), (iii) Lifetime (τ). τ indicates the time period from the start of excitation to the final of emission (return to the ground state) which also is the inverse of the radiative constant from the fluorescent or phosphorescent transitions, (iv) Energy transfer (ET). ET is a process where an excited sample transfers excitation energy to an acceptor molecule such as lanthanide metal ions, (v) Quenching. Quenching is either a static or dynamic phenomenon which exhibits partial or total luminescent lose due to the interaction between the luminescent phosphor and internal/ external environments, (vi) Quantum yield (Φ). Φ is the ratio of the number of luminescence emitted photons to the number of absorbed photons. (vii) Singlet state (S): Most molecules have a ground state (spin quantum number m_s: $+\frac{1}{2}$ or $-\frac{1}{2}$) with all electron spin antiparallel paired and most excited states also have electron spin antiparallel paired, even though there may be one electron each lying in a different orbit. Such states have

zero total spin ($\Delta S = +\dfrac{1}{2} + \left(-\dfrac{1}{2}\right) = 0$) and spin multiplicities of 1 ($2 \cdot \Delta S + 1 = 2 \cdot 0 + 1 = 1$), and (viii) Triplet state (T): For some excited states, there are states with a pair of electrons having their spins parallel in two orbits, leading to total spin of 1 ($\Delta S = +\dfrac{1}{2} + \left(+\dfrac{1}{2}\right) = 1$) and multiplicities of 3 ($2 \cdot \Delta S + 1 = 2 \cdot 1 + 1 = 3$). Under the influence of external field, there are three values (i.e. 3 energy states) of +1, 0, -1 times the angular momentum. According to IUPAC definition, emission process without spin change will be described as "fluorescence" while "phosphorescence" behavior involves a spin change[114]. Many lanthanides ions exhibit luminescent properties with sharp (atomic-like) emission lines because of the *f-f* transition in Ln^{3+} ions.
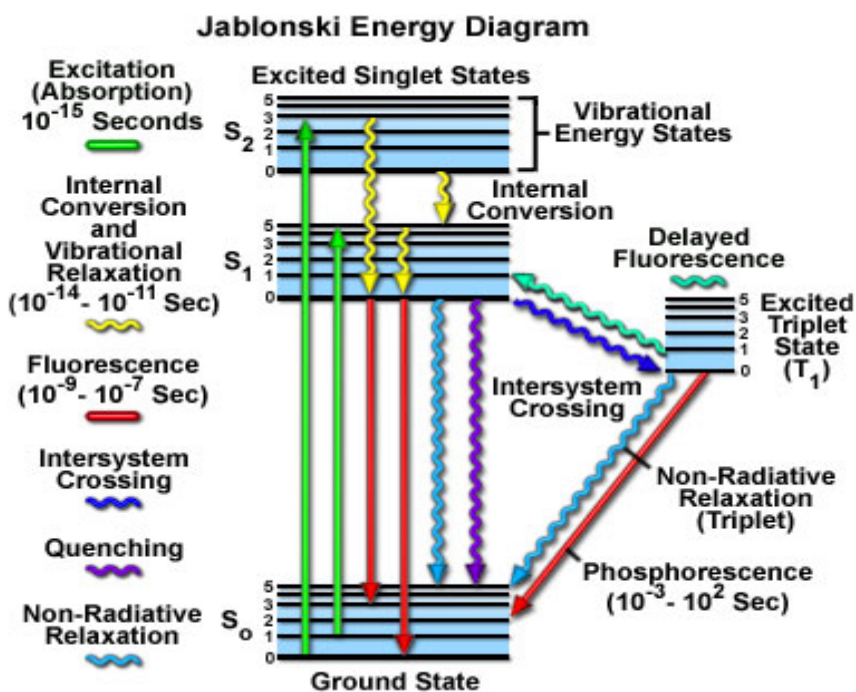
Figure 1.9 Energy transition diagram (Jablonski) for luminescent phenomenon.

However, Lanthanide ions possess low absorption coefficient of energy due to the screened $4f$ orbits, resulting in a huge difficulty for direct excitation. Three possible solutions shown in Figure 1.10 have been proposed to overcome this issue[106]. Solution (a) uses a matrix excitation followed by energy transfer to the lanthanide ion. The process occurs by exciting an inorganic matrix such as TiO_2, ZrO_2, Al_2O_3 included with lanthanide ions[115]. Solution (b) is a ligand-to-metal "charge transfer" (LMCT) which leads to a dramatic charge increase in the lanthanide excited states followed by the luminescence from these lanthanide centers. Solution (c) occurs major energy absorption from organic ligands followed by an "energy transfer" to the lanthanide ion. In this process, the luminescence can be enhanced by applying a suitable organic ligand with appropriately energy level to the lanthanide ions. The key concept for all three ideas mentioned above is the enhancement of luminescence from the ambient media, which is also known as the antenna effect. Figure 1.11 presents more detailed information for the luminescent emission in lanthanide complexes containing with a suitable organic ligand. In this case, the principal challenge has been addressed in the selection of the ligand with suitable energy level of excited triplet which can match the excited energy level of lanthanide ions. Otherwise, the energy or charge transfer will not happen.

(a)   (b)   (c)

ET   ET

Ln Emission   Ln Emission   Ln Emission

Matrix Excitation   LC

LMCT

Ln^{3+} Ln^{3+} Ln^{3+}

Matrix Materials   Ligand   Ligand
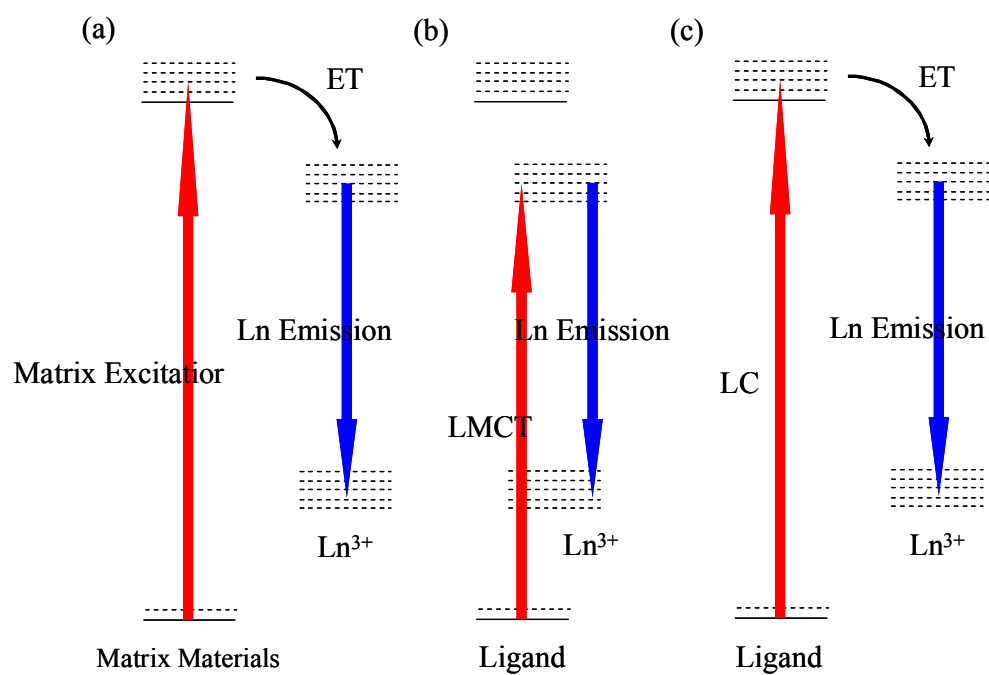
Figure 1.10 Three possible solutions to enhance of Ln^{3+} adsorption efficiency[115].

Excited singlet

Excited triplet

Ln^{3+} excited states

Ligand fluorescence

Lanthanide luminescence

Ligand phosphorescence

Radiative absorption

Radiative emission

Nonradiative emission

Ground state singlet
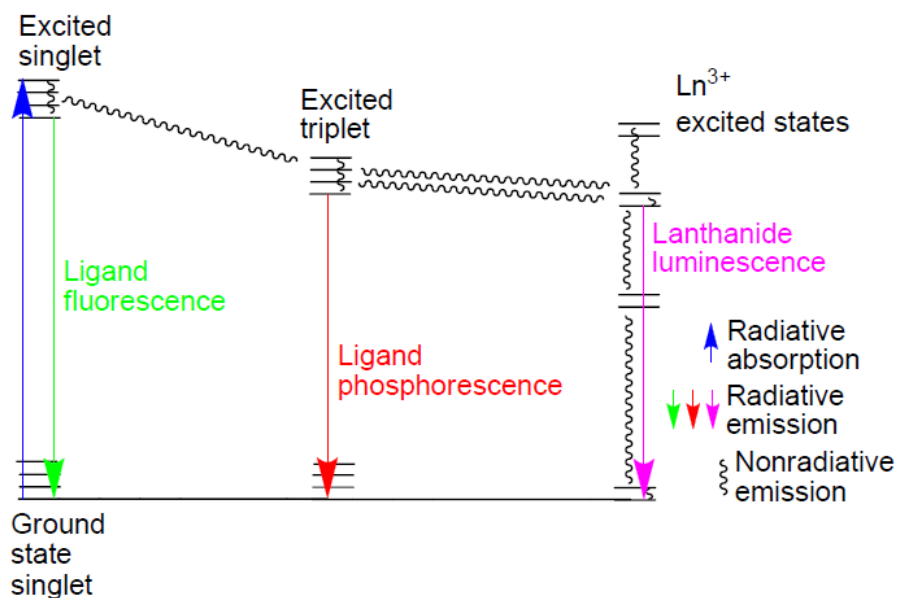
Figure 1.11 Detailed information for the luminescent emission in lanthanide complexes via antenna effect[110].

1.5 Dissertation Objectives

Metal-organic framework materials possessing large specific surface area offer new opportunities in the quest for high density storage materials for sustainable energy applications. In this dissertation, progress is made on two fronts. Firstly, new materials are synthesized and their applicability for new storage materials tested. Secondly, progress is made on advanced neutron diffraction techniques to gain a better understanding of the mechanism involved with gas storage. Several types of metal-organic frameworks have been synthesized, and their structures, gas adsorption and optical properties investigated. The relationship between gas adsorption positions within structures is crucial to progress gas storage research. Optimizations of metal-organic architectures by molecular designs can dramatically enhance the storage capacity. This dissertation focuses on systematic studies comparing various metal-organic framework structures, as well as the correlation between gas adsorption sites, storage capacity and framework architectures by single crystal X-ray diffraction, *in-situ* and combined powder synchrotron X-ray (PXRD) and Raman spectroscopy, thermogravimetric analysis (TGA) and powder neutron diffraction (PND). Furthermore, two new methods of analyzing diffraction data, charge flipping and maximum entropy method, are implemented for the first time in combination to gain a better understanding of the gas adsorption behaviors in porous materials.

1.6 References

(1) Allendorf, M. D.; Bauer, C. A.; Bhakta, R. K. and Houk, R. J. T. *Chem. Soc. Rev.* **2009**, *38*, 1330.

(2) Kurmoo, M. *Chem. Soc. Rev.* **2009**, *38*, 1353.

(3) O'Keeffe, M. *Chem. Soc. Rev.* **2009**, *38*, 1215.

(4) Perry IV, J. J.; Perman, J. A. and Zaworotko, M. J. *Chem. Soc. Rev.* **2009**, *38*, 1400.

(5) Tranchemontagne, D. J.; Mendoza-Cortes, J. L.; O'Keeffe, M. and Yaghi, O. M. *Chem. Soc. Rev.* **2009**, *38*, 1257.

(6) Wang, Z. and Cohen, S. M. *Chem. Soc. Rev.* **2009**, *38*, 1315.

(7) Furukawa, H.; Ko, N.; Go, Y. B.; Aratani, N.; Choi, S. B.; Choi, E.; Yazaydin, A. Ö.; Snurr, R. Q.; O'keeffe, M.; Kim, J. and Yaghi, O. M. *Science* **2010**, 1.

(8) Alaerts, L.; Seguin, E.; Poelman, H.; Thibault-Starzyk, F.; Jacobs, P. A. and De Vos, D. E. *Chem. Eur. J.* **2006**, *12*, 7353.

(9) Czaja, A. U.; Trukhan, N. and Müller, U. *Chem. Soc. Rev.* **2009**, *38*, 1284.

(10) Dincă, M.; Dailly, A.; Liu, Y.; Brown, C. M.; Neumann, D. A. and Long, J. R. *J. Am. Chem. Soc.* **2006**, *128*, 16876.

(11) Düren, T.; Bae, Y.-S. and Snurr, R. Q. *Chem. Soc. Rev.* **2009**, *38*, 1237.

(12) Férey, G. and Serre, C. *Chem. Soc. Rev.* **2009**, *38*, 1380.

(13) Gandara, F.; Gornez-Lor, B.; Gutierrez-Puebla, E.; Iglesias, M.; Monge, M. A.; Proserpio, D. M.andSnejko, N. *Chem. Mater.* **2008**, *20*, 72.

(14) Horike, S.; Dincă, M.; Tamaki, K. and Long, J. R. *J. Am. Chem. Soc.* **2008**, *130*, 5854.

(15) Lee, J.; Farha, O. K.; Roberts, J.; Scheidt, K. A.; Nguyen, S. T. and Hupp, J. T. *Chem. Soc. Rev.* **2009**, *38*, 1450.

(16) Li, J.-R.; Kuppler, R. J. and Zhou, H.-C. *Chem. Soc. Rev.* **2009**, *38*, 1477.

(17) Ma, L.; Abney, C. and Lin, W. *Chem. Soc. Rev.* **2009**, *38*, 1248.

(18) Murray, L. J.; Dincă, M. and Long, J. R. *Chem. Soc. Rev.* **2009**, *38*, 1294.

(19) Spokoyny, A. M.; Kim, D.; Sumrein, A. and Mirkin, C. A. *Chem. Soc. Rev.* **2009**, *38*, 1218.

(20) Zacher, D.; Shekhah, O.; Woll, C. and Fischer, R. A. *Chem. Soc. Rev.* **2009**, *38*, 1418.

(21) Kaye, S. S.; Dailly, A.; Yaghi, O. M.andLong, J. R. *J. Am. Chem. Soc.* **2007**, *129*, 14176.

(22) Ma, S. Q.; Sun, D. F.; Wang, X. S. and Zhou, H. C.; *Angew. Chem. Int. Ed.* **2007**, *46*, 2458.

(23) Muller, M.; Hermes, S.; Kaehler, K.; van den Berg, M. W. E.; Muhler, M. and Fischer, R. A. *Chem. Mater.* **2008**, *20*, 4576.

(24) Rowsell, J. L. C.; Spencer, E. C.; Eckert, J.; Howard, J. A. K. and Yaghi, O. M. *Science* **2005**, *309*, 1350.

(25) Sabo, M.; Henschel, A.; Froede, H.; Klemm, E. and Kaskel, S. *J. Mater. Chem.* **2007**, *17*, 3827.

(26) Serre, C.; Millange, F.; Surblé, S. and Férey, G. *Angew. Chem. Int. Ed.* **2004**, *43*, 6286.

(27) Won, J. G.; Seo, J. S.; Kim, J. H.; Kim, H. S.; Kang, Y. S.; Kim, S. J.; Kim, Y. M. and Jegal, J. G. *Adv. Mater.* **2005**, *17*, 80.

(28) Xamena, F.; Abad, A.; Corma, A. and Garcia, H. *J. Catal.* **2007**, *250*, 294.

(29) Yoon, J. W.; Jhung, S. H.; Hwang, Y. K.; Humphrey, S. M.; Wood, P. T. and Chang, J. S. *Adv. Mater.* **2007**, *19*, 1830.

(30) Zhang, J. J.; Zhao, Y.; Gamboa, S. A.; Munoz, M. and Lachgar, A. *Eur. J. Inorg. Chem.* **2008**, 2982.

(31) Qiu, S. and Zhu, G. *Coord. Chem. Rev.* **2009**, *253*, 2891.

(32) Barrer, R. M. *Hydrothermal chemistry of zeolites,* Academic Press, London, **1982**.

(33) Byrappa, K. and Yoshimura, M. *Handbook of hydrothermal technology*, William andrew publishing, Norwich, New York, **2001**.

(34) Rabenau, A. *Angew. Chem. Int. Ed.* **1985**, *24*, 1026.

(35) Walton, R. I. *Chem. Soc. Rev.* **2002**, *31*, 230.

(36) Demazeau, G. *J. Mater. Chem.* **1999**, *9*, 15.

(37) Parr Instrument Company, Moline, IL 61265, USA.

(38) Tranchemontagne, D. J. L.; Ni, Z.; O'Keeffe, M. and Yaghi, O. M. *Angew. Chem. Int. Ed.* **2008**, *47*, 5136.

(39) Kitagawa, S. and Kondo, M. *Bull. Chem. Soc. Jpn.* **1998**, *71*, 1739.

(40) Uemura, K.; Matsuda, R. and Kitagawa, S. *J. Solid State Chem.* **2005**, *178*, 2420.

(41) Uemura, T.; Yanai, N. and Kitagawa, S. *Chem. Soc. Rev.* **2009**, *38*, 1228.

(42) Barthelet, K.; Marrot, J.; Riou, D. and Férey G. *Angew. Chem. Int. Ed.* **2002**, *41*, 281.

(43) Millange, F.; Serre, C. and Férey, G. *Chem. Commun.* **2002**, 822.

(44) Serre, C.; Millange, F.; Thouvenot, C.; Nogues, M.; Marsolier, G.; Louer, D. and Férey, G. *J. Am. Chem. Soc.* **2002**, *124*, 13519.

(45) Surblé, S.; Serre, C.; Millange, F.; Pelle, F. and Férey, G. *Solid State Sci.* **2005**, *7*, 1074.

(46) Yaghi, O. M.; O'Keeffe, M.; Ockwig, N. W.; Chae, H. K.; Eddaoudi, M. and Kim J. *Nature* **2003**, *423*, 705.

(47) Fang, Q. R.; Zhu, G. S.; Xue, M.; Sun, J. Y.; Tian, G.; Wu, G. and Qiu, S. L. *Dalton Trans* **2004**, 2202.

(48) Morris, R. E. *Chem. Comm.* **2009**, 2990.

(49) Férey, G. *J. Solid State Chem.* **2000**, *152*, 337.

(50) Shimizu, G. K. H.; Vaidhyanathan, R. and Taylor, J. M. *Chem. Soc. Rev.* **2009**, *38*, 1430.

(51) Yaghi, O. M.; Li, H.; Davis, C.; Richardson, D. and Groy, T. L. *Acc. Chem. Res* **1998**, *31*, 474.

(52) Yaghi, O. M.; O' Keeffe, M. and Kanatzidis, M. G. *J. Solid State Chem.* **2000**, *152*, 1.

(53) Rosi, N. L.; Eddaoudi, M.; Kim, J.; O'Keeffee, M. and Yaghi, O. M. *Cryst. Eng. Comm.* **2002**, *68*, 401.

(54) Kim, J.; Chen, B.; Reineke, T.M.; Li, H.; Eddaoudi, M.; Moler, D. B.; O'Keeffe, M. and Yaghi, O. M. *J. Am. Chem. Soc.* **2001**, *123*, 8239.

(55) O'Keeffe, M.; Eddaoudi, M. ; Li, H.; Reineke, T.; and Yaghi, O. M. *J. Solid State Chem.* **2000**, *152*, 3.

(56) Rowsell, J. L. C. and Yaghi, O. M. *Microporous Mesoporous Mater.* **2004**, *73*, 3.

(57) Kitagawa, S.; Kitaura, R. and Noro, S.-i. *Angew. Chem. Int. Ed.* **2004**, *43*, 2334.

(58) Long, D.-L.; Blake, A. J.; Champness, N. R.; Wilson, C. and Schröder, M. *J. Am. Chem. Soc.* **2001,** *123,* 3401.

(59) Chen, B.; Yang, Y.; Zapata, F.; Lin, G.; Qian, G. and Lobkovsky, E. B. *Adv. Mater.* **2007**, 1693.

(60) Harbuzaru, B. V.; Corma, A.; Rey, F.; Atienzar, P.; Jorda, J. L.; Garcia, H.; Ananias, D.; Carlos, L. D. and Rocha, J. *Angew. Chem. Int. Ed.* **2008**, *47*, 1080.

(61) Reineke, T. M.; Eddaoudi, M.; Keeffe, M. O. and Yaghi, O. M. *Angew. Chem. Int. Ed.* **1999**, *38*, 2590.

(62) Reineke, T. M.; Eddaoudi, M.; Fehr, M.; Kelley, D. and Yaghi, O. M. *J. Am. Chem. Soc.* **1999**, *121*, 1651.

(63) Serre, C.; Millange, F.; Thouvenot, C.; Gardant, N.; Pellé, F.; and Férey, G. *J. Mater. Chem.* **2004**, *14*, 1540.

(64) Surblé, S.; Serre, C.; Millange, F. and Férey, G. *Solid State Sci.* **2006**, *8*, 413.

(65) Guo, X.; Zhu, G.; Li, Z.; Sun, F.; Yang, Z. and Qiu, S. *Chem. Commun.* **2006**, 3172.

(66) Gustafsson, M.; Bartoszewicz, A.; Martín-Matute, B.; Sun, J.; Grins, J.; Zhao, T.; Li, Z.; Zhu, G. and Zou X. *Chem. Mater.* **2010**, *22*, 3316.

(67) Luo, J.; Xu, H.; Liu, Y.; Zhao, Y.; Daemen, L. L.; Brown, C.; Timofeeva, T. V. ; Ma, S. and Zhou, H.-C. *J. Am. Chem. Soc.* **2008**, *130*, 9626.

(68) Rosi, N. L.; Kim, J.; Eddaoudi, M.; Chen, B.; O'Keeffe, M. and Yaghi, O. M. *J. Am.*

Chem. Soc. **2005**, *127*, 1504.

(69) Choi, J. R.; Tachikawa, T.; Fujitsuka, M. and Majima, T. *Langmuir* **2010**, *26*, 10437.

(70) Devic, T.; Serre, C.; Audebrand, N.; Marrot, J. and Férey, G. *J. Am. Chem. Soc.* **2005**, *127*, 12788.

(71) Chui, S. S.-Y.; Siu, A.; Feng, X.; Zhang, Z. Y.; Mak, T. C. W. and Williams, I. D. *Inorg. Chem. Commun.* **2001**, *4*, 467.

(72) de Lill, D. T.; Gunning, N. S. and Cahill, C. L. *Inorg. Chem.* **2005**, *44*, 258.

(73) Serre, C.; Pelle, F.; Gardant, N. and Férey, G. *Chem. Mater.* **2004**, *16*, 1177.

(74) Zhang, Z.-H.; Shen, Z.-L.; Okamura, T.; Zhu, H.-F.; Sun, W.-Y. and Ueyama, N. *Cryst. Growth Des.* **2005**, *5*, 1191.

(75) http://www.all-creatures.org/hope/gw/02_fossil_fuels_general.htm.

(76) Schlapbach, L. and Züttel, A. *Nature* **2001**, *414*, 353.

(77) Züttel, A. *Naturwissenschaften* **2004**.

(78) DOE Office of Energy Efficiency and Renewable Energy Hydrogen, Fuel Cells & Infrastructure Technologies Program Multi-Year Research, Development and Demonstration Plan, available at: http://www.eere.energy.gov/ hydrogenandfuelcells/mypp.

(79) Rosi, N. L.; Eckert, J.;   Eddaoudi, M.; Vodak, D.T.; Kim, J.; O'Keeffe, M. and Yaghi, O. M. *Science* **2003**, *300*, 1127.

(80) Yildirim, T. and Hartman, M. R. *Phys. Rev. Lett.* **2005**, *95*.

(81) Spencer, E. C.; Howard, J. A. K.; McIntyre, G. J.; Rowsell, J. L. C. and Yaghi, O. M. *Chem. Comm.* **2006**, *3*, 278.

(82) Collins, D. J. and Zhou, H.C. *J. Mater. Chem.* **2007**, *17*, 3154.

(83) Hirscher, M. and Panella, B. *Scr. Mater.* **2007**, *56*, 809.

(84) Isaeva, V. I. and Kustov, L. M.   *Russ. J. Gen. Chem.* **2007**, *77*, 721.

(85) Lin, X.; Jia, J. H.; Hubberstey, P.; Schröder, M. and Champness, N. R. *Cryst. Eng. Comm.* **2007**, *9*, 438.

(86) Brown, C. M.; Liu, Y. and Neumann, D. A. *Pramana-Journal of Physics* **2008**, *71*, 755.

(87) Dincă, M. and Long, J. R. *Angew. Chem. Int. Ed.* **2008**, *47*, 6766.

(88) Liu, Y.; Kabbour, H.; Brown, C. M.; Neumann, D. A. And Ahn, C. C. *Langmuir* **2008**, *24*, 4772.

(89) Han, S. S.; Mendoza-Cortes, J. L. and Goddard Iii, W. A. *Chem. Soc. Rev.* **2009**, *38*, 1460.

(90) Moellmer, J.; Celer, E. B.; Luebke, R.; Cairns, A. J.; Staudt, R.; Eddaoudi, M. and Thommes, M. *Microporous Mesoporous Mater.* **2010**, *129*, 345.

(91) Mulfort, K. L. and Hupp, J. T. *Inorg. Chem.* **2008**, *47*, 7936.

(92) Yang, S.; Lin, X.; Blake, A. J.; Thomas, K. M.; Hubberstey, P.; Champness, N. R. and Schröder, M. *Chem. Commun.* **2008**, 6108.

(93) Wang, Q. and Johnson, J. K. *J. Chem. Phys.* **1999**, *110* 577.

(94) Dincă, M.; Dailly, A.; Tsay, C. and Long, J. R.   *Inorg. Chem.* **2008**, *47*, 11.

(95) Jung, D. H.; Kim, D.; Lee, T. B.; Choi, S. B.; Yoon, J. H.; Kim, J.; Choi, K. and Choi, S. H. *J. Phys. Chem. B* **2006**, *110*, 22987.

(96) Ma, S. Q.; Sun, D. F.; Ambrogio, M.; Fillinger, J. A.; Parkin, S. and Zhou, H. C. *J. Am. Chem. Soc.* **2007**, *129*, 1858.

(97) Rowsell, J. L. C. and   Yaghi, O. M. *Angew. Chem. Int. Ed.* **2005**, *44*, 4670.

(98) Chun, H.; Dubtsev, D. N.; Kim, H. and Kim, K. *Chem. Eur. J.* **2005**, *11*, 3521.

(99) Kesanli, B.; Cui, Y.; Smith, M. R.; Bittner, E. W.; Bockrath, B. C. and Lin, W. *Angew. Chem. Int. Ed.* **2005**, *44*, 72.

(100) Rzepka, M. and Lamp, P. and de la Casa-Lillo, M. A. *J. Phys. Chem. B* **1998**, *102*, 10894.

(101) Kuppler, R. J.; Timmons, D. J.; Fang, Q. R.; Li, J. R.; Makal, T. A.; Young, M. D.; Yuan, D. Q.; Zhao, D.; Zhuang, W. J. and Zhou, H. C. *Coord. Chem. Rev.* **2009**, *253*, 3042.

(102) Wu, H.; Zhou, W.andYildirim, T. *J. Phys. Chem. C* **2009**, *113*, 3029.

(103) Wu, H.; Zhou, W. and Yildirim, T. *J. Am. Chem. Soc.* **2009**, *131*, 4995.

(104) Zhou, W.; Wu, H.; Hartman, M. R. and Yildirim, T. *J. Phys. Chem. C* **2007**, *111*, 16131.

(105) Zhou, W.; Wu, H. and Yildirim, T. *J. Am. Chem. Soc.* **2008**, *130*, 15268.

(106) Gogotsi, Y.; Dash, R. K.; Yushin, G.; Yildirim, T.; Laudisio, G. and Fischer, J. E. *J. Am. Chem. Soc.* **2005**, *127*, 16006.

(107) Yang, Z. X.; Xia, Y. D. and Mokaya, R. *J. Am. Chem. Soc.* **2007**, *129*, 1673.

(108) Yushin, G.; Dash, R.; Jagiello, J.; Fischer, J. E. and Gogotsi, Y. *Adv. Funct. Mater.* **2006**, *16*, 2288.

(109) Binnemans, K. *Chem. Rev.* **2009**, *109*, 4283.

(110) Cotton, S. *Lanthanide and actinide chemistry* 2 Rev ed, John Wiley and Sons, Inc., England, **2006**.

(111) Carnall, W. T.; Fields, P. R. and Rajnak, K. *J. Chem. Phys.* **1968**, *49*, 4424.

(112) Stein, G. and Wurzberg, E. *J. Chem. Phys.* **1975**, *62*, 208.

(113) Bunzli, J. C. G. and Choppin, G. R. *Lanthanide Probes in Life, Chemical and Earth Sciences: Theory and Practice*, Elsevier Science, Netherlands, **1989**.

(114) Bunzli, J.-C. G. and Piguet, C. *Chem. Soc. Rev.* **2005**, *34*, 1048.

(115) Maas, H.; Currao, A. and Calzaferri, G. *Angew. Chem. Int. Ed.* **2002**, *41*, 2495.

Chapter 2: Fundamentals

2.1 Crystal Structures

2.1.1 The Lattice Points and Unit Cell

A crystal is defined as a homogenous solid formed by the infinite three-dimensional (3-D) repetition of a basis consisting of a unit cell and its motifs (i.e. atomic contents of the cell). This coordinate system is generally constructed by three basis vectors *a, b, c* with different lengths (a, b, c) and angles α, β, γ, which are defined as the included angle between the vectors *b* and *c, c* and *a, a* and *b*. (Figure 2.1, the four possibilities for the orthorhombic lattice).
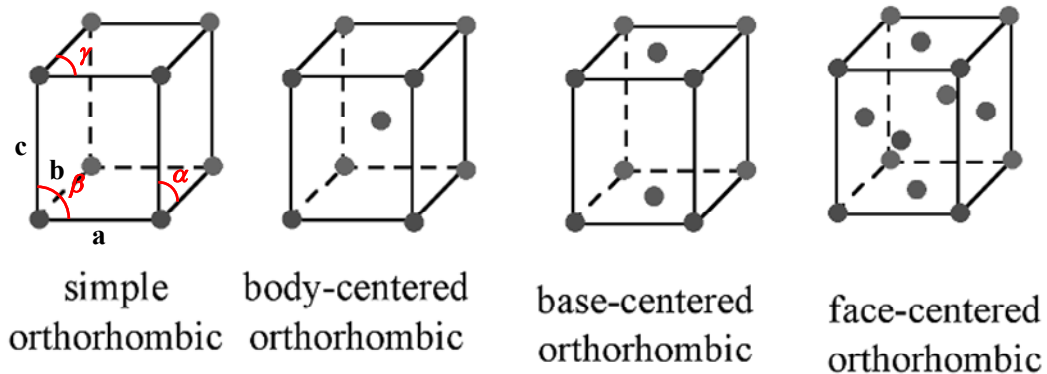
Figure 2.1 The four possibilities for the orthorhombic lattice.

There are seven 3-D lattice systems that are used to classify crystals: cubic, hexagonal, trigonal, tetragonal, orthorhombic, monoclinic and triclinic. These systems are identified upon the internal symmetry of the system: a combination of translation (shift and slide), rotations about an axis (1, 2, 3, 4 and 6 fold) and reflections (mirror planes). The primitive unit cell considered as only one lattice point per unit cell is defined by Bravais,

33

who discovered that some cells are more complicated but still comply with the symmetry of one of these seven crystal systems. The non-primitive A, B, C, I and F lattice systems contain two or more lattice points per unit cell and can be viewed as a combination of a primitive lattice with one or more identical copies of itself that are offset. There are a total of 14 Bravais lattices[1] (as shown in Figure 2.2), seven of them being primitive lattices. The unit cell is chosen to possess the highest symmetry present. Therefore, there are sometimes other factors that can lead to different lattice designation. For example, a tetragonal F-centred cell can be equivalently described as a smaller tetragonal I-centred cell. The definition of the point group is different from the space group. A point group describes the symmetry at a specific point and ignores translational operations. There are 32 point groups distributed among the seven crystal systems, 11 of which are centrosymmetric (also called the *Laue symmetry*). A space group defines the symmetry of 3-D periodic structures including translational symmetry. Combining the 32 point groups with the 14 Bravais lattices and further includes symmetry axes by screw axes of the same order and mirror planes by glide planes, 230 crystallographic space groups can all be derived. The *International Tables for Crystallography*[2] contains all the space group information that is useful in solving crystal structures from diffraction data.
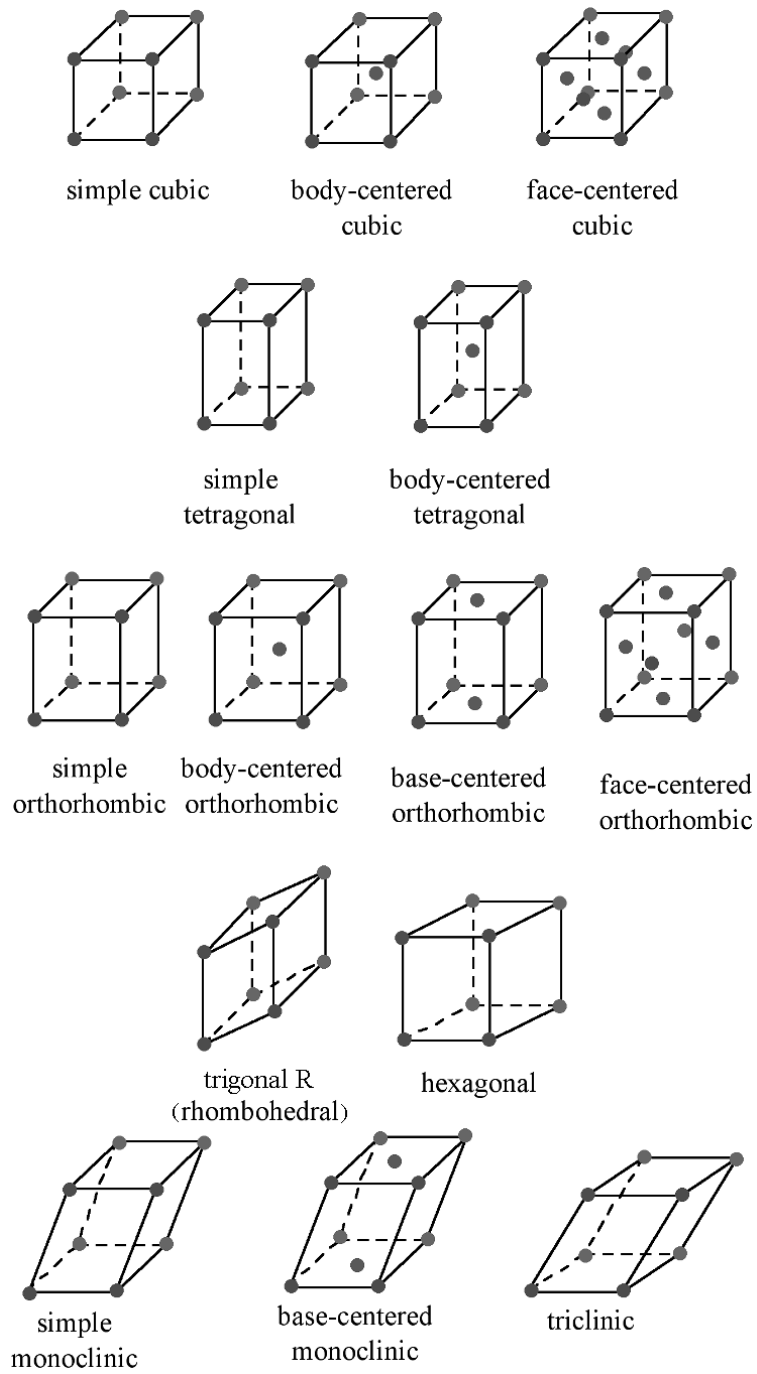
Figure 2.2 The 14 Bravais lattices.

2.1.2 Real Space and Reciprocal Lattice

In the section 2.1.2, 2.2, and 2.3 all the discussed information is collected from

reference [3-6][3-6].

2.1.2.1 Real Space and Miller index

Since crystals are the well-defined atomic or ionic arrangements, it is necessary to distinguish the different directions and distances. A general point position is characterized by the coordinates u, v, w or by the position vector $\vec{r}$:

$$\vec{r} = n_1\vec{a} + n_2\vec{b} + n_3\vec{c} \qquad (2.1)$$

Three non-collinear lattice points define a lattice plane, the equation of which $hu = n_1$, $vk = n_2$, $lw = n_3$ cuts the unit cell into h; k and l parts (or intercepts the axes at distances of $\vec{a}/h$; $\vec{b}/k$; $\vec{c}/l$). Here n_i can be any integer, negative, zero or positive. The Miller indices, (hkl) represent a family of planes extending from the origin throughout the crystal by the inverses of the intercepts on each axis as shown in Figure 2.3.

2.1.2.2 Reciprocal Lattice

The reciprocal lattice is a very important concept and necessary to understand diffraction and to solve crystal structures. Each real-space lattice has its corresponding reciprocal lattice in k space. Since it is sometimes a difficult to characterize materials via real-space techniques such as atomic-level TEM (Transmission Electron Microscopy), the reciprocal lattice offers an easy approach to gain the comprehensive information on the lattice arrangement via diffraction of radiation. The reciprocal lattice can be related to the real-space lattice by the following three primitive vectors:

$$\vec{a}^* = 2\pi \frac{\vec{b} \times \vec{c}}{\vec{a} \cdot (\vec{b} \times \vec{c})}, \quad \vec{b}^* = 2\pi \frac{\vec{c} \times \vec{a}}{\vec{a} \cdot (\vec{b} \times \vec{c})}, \quad \vec{c}^* = 2\pi \frac{\vec{a} \times \vec{b}}{\vec{a} \cdot (\vec{b} \times \vec{c})} \qquad (2.2)$$

Here the $\vec{a} \cdot (\vec{b} \times \vec{c})$ is also defined as V_c, the volume of the unit cell; then the reciprocal

lattice vectors can be described as

$$\vec{d}^{*} = h\vec{a}^{*} + k\vec{b}^{*} + l\vec{c}^{*} \qquad (2.3)$$

According to the equation (2.2), the reciprocal lattice vectors $\vec{d}^{*}$ are perpendicular to the real crystal planes, and vice versa. The magnitude of the vector $\vec{d}^{*}$ is the inverse of the shortest distance between real-space planes with Miller indices (*hkl*):

$$\left|\vec{d}^{*}\right| = \frac{1}{d_{hkl}} \qquad (2.4)$$
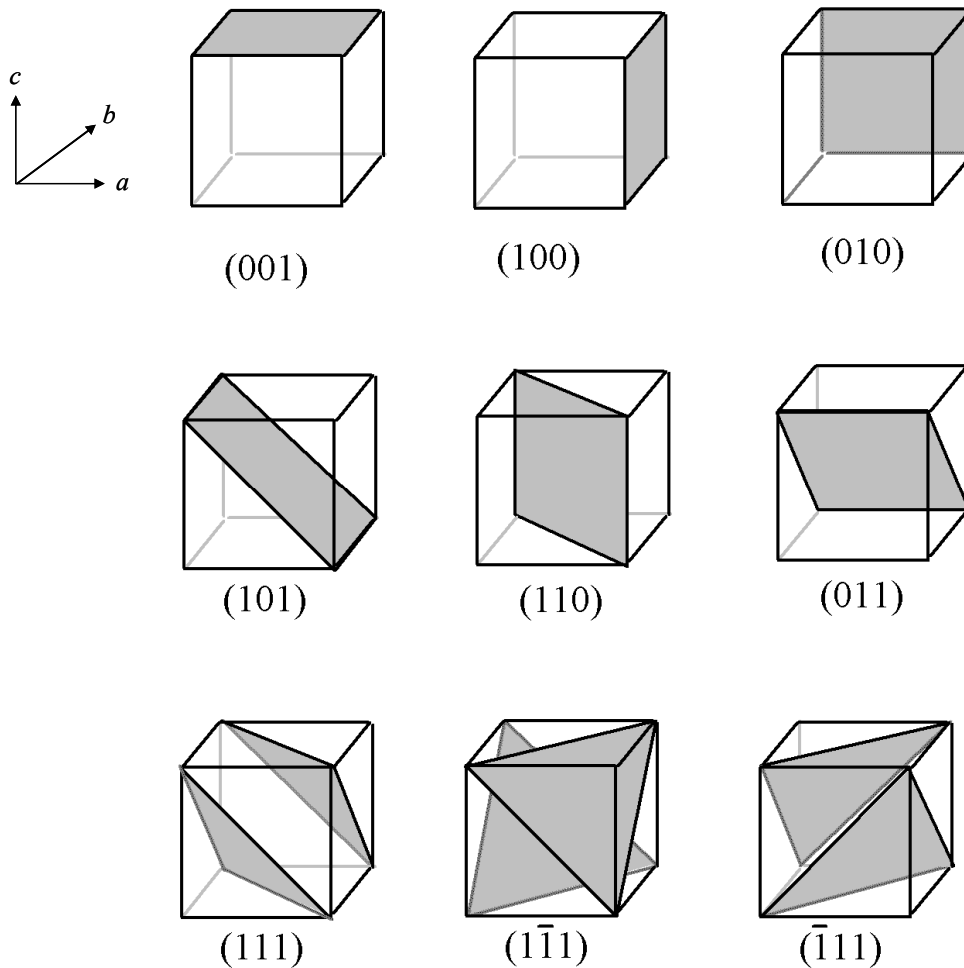
Figure 2.3 Some examples of major Miller indices.

37

2.2 Diffraction Theory

2.2.1 Bragg's Law

   Diffraction is a wave behavior of electromagnetic radiation that causes the radiation to deflect when it passes by an edge or through an aperture. Diffraction effects increase when the dimension of the aperture is close to the wavelength of the radiation. The resulting interference (constructive or destructive) effects are useful in determining structural information on solid materials, especially on the crystal structures. In general, the distances between atoms or ions in crystals are on the angstrom level. Therefore, diffraction techniques require radiation of the electromagnetic spectrum in the X-ray region, or beams of electrons or neutrons with a similar wavelength. Electrons and neutrons are generally recognized to have wave-particle duality, and the wavelength is inversely proportional to the kinetic energy of the particles as described by the de Broglie relation. The diffraction is considered under the condition for coherent elastic scattering and described qualitatively by Bragg's Law, which is shown in Figure 2.4.
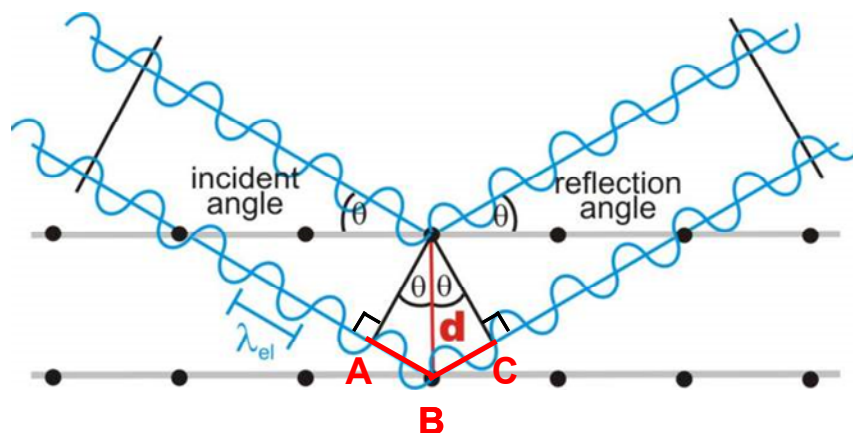
Figure 2.4 Bragg's law of diffraction by lattice planes.

In Figure 2.4, if there are two parallel and monochromatic incident beams which have been reflected by different crystal lattice points with same incident and reflection angle θ, the path difference for these two positions in crystal is equal to $\overline{AB} + \overline{BC}$. The space between these two crystal planes is given by d. For Bragg's law, constructive diffraction is required to obtain the strong scattering intensity, then $\overline{AB} + \overline{BC}$ must be an integer times, n of wavelength of the incident beam, λ. Bragg's law can be described as

$$\overline{AB} = \overline{BC} = d\sin\theta,$$

$$\overline{AB} + \overline{BC} = 2d\sin\theta, \text{ and}$$

$$\overline{AB} + \overline{BC} = n\lambda$$

Then

$$n\lambda = 2d\sin\theta \qquad\qquad (2.5)$$

Bragg's law and the conditions of coherent elastic scattering can be explained by combined with the illustration of reciprocal lattice in the Ewald construction (Figure 2.5).
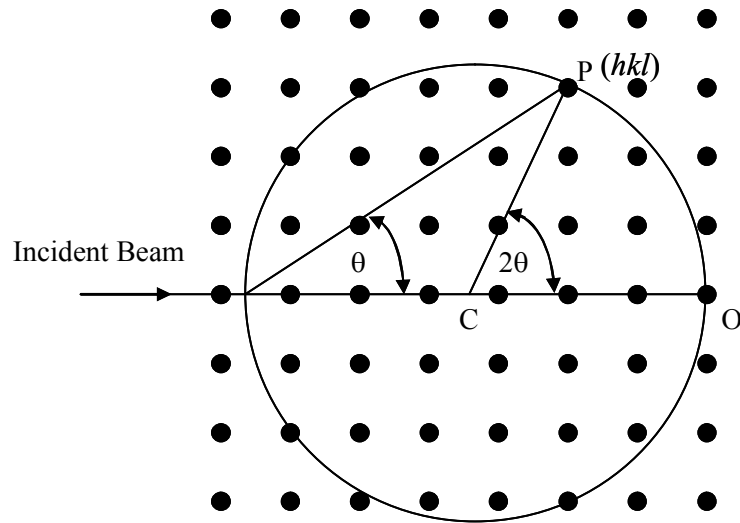
Figure 2.5 The Ewald construction for the diffracted condition of P in reciprocal space.

In Ewald construction, O is defined as the origin of reciprocal lattice and C as the center Ewald sphere. The incident beam with wave vector $k_o = 2\pi/\lambda$ means the radius of sphere is $1/\lambda$, and the Bragg diffraction condition is satisfied on reciprocal lattice point P, which lies on the surface of sphere with scattering angle 2θ. In the reciprocal space, the lattice points will form constructive Bragg scattering if intersected by the Ewald sphere.

2.2.2 Scattering Amplitude

As discussed in the previous section, the positions of diffraction (Bragg) peaks are determined by the unit cell lengths, each reflection can be identified by its Miller index (*hkl*). In this section, the relative intensities for each scattering peaks will be demonstrated to relate with the corresponding positions and the types of atoms (or ions) in the unit cell.

The electromagnetic wave scattered by atoms in solids interfere with each another, and total scattering power from a reflection (*hkl*) is defined by the structure factor F_{hkl}, which can be described as proportional to square of the amplitude of the intensity I_{hkl}:

$$I_{hkl} \propto \left| F_{hkl} \right|^2 \tag{2.6}$$

However, radiation from X-ray and neutron, will interact with atoms in different ways, resulting in differences between the relative diffraction intensities. The details will be discussed in the 2.3.1 and 2.3.2 sections. The structure factors for X-rays and neutrons are given in equation (2.7) and (2.8), respectively:

$$F_{hkl} = \sum_i f_i \exp\left[-2\pi i\left(hx_i + ky_i + lz_i\right)\right]\exp\left(-W_i\right) \qquad \text{(X-ray)} \tag{2.7}$$

$$F_{hkl} = \sum_i b_i \exp\left[-2\pi i\left(hx_i + ky_i + lz_i\right)\right]\exp\left(-W_i\right) \qquad \text{(Neutron)} \tag{2.8}$$

Here the f_i is the scattering amplitude for X-ray, and b_i the neutron scattering length for neutron diffraction. The x_i, y_i and z_i are the fractional coordinates of the ith atom in the unit cell, and W_i is the Debye-Waller isotropic thermal factor as shown in equation (2.9):

$$W_i = \frac{8\pi^2 \sin^2 \theta \langle u_i^2 \rangle}{\lambda^2} \tag{2.9}$$

where $\langle u_i^2 \rangle$ is the mean square thermal displacement of the ith atom from its regular site.

2.3 The Powder Diffraction Techniques

2.3.1 Introduction

X-ray diffraction has been extensively used to identify phases. For single crystal diffraction, good quality crystals are required. The crystal is detected and analyzed by rotating along three azimuthal angles θ, ω and φ, to make sure a sphere or hemisphere of data are collected. Since comprehensive crystal information can be collected in three dimensions, the data are easy to reduce and reconstruction of the crystal structure becomes more feasible. In many cases, sufficiently high quality crystals are not available and the powder diffraction technique provides a convenient method to understand the atomic arrangement when a single crystal is unobtainable. Diffraction also can be applied to monitor the structural transitions under external stimuli such as temperature, pressure and electrical/magnetic field. In this dissertation two major sources that have been utilized for diffraction which are X-ray and neutron, and will be discussed in detail.

2.3.2 X-ray Powder Diffraction

X-ray is a type of electromagnetic wave and interacts with the outer electron clouds

surrounding the atomic nuclei in the materials. The atomic scattering factor f_i, or scattering ability of X-ray, is proportional to the atomic number (Z) of elements, which means that the heavier elements with higher atomic numbers are associated with stronger X-ray scattering intensity. Conversely, X-ray diffraction is very insensitive and therefore difficult to use for the light elements, particularly hydrogen (H) in materials because there is only one peripheral electron. For the same reason, X-ray diffraction technique also has difficulty in distinguishing two elements with similar number of electrons.

For a laboratory-based X-ray diffractometer, X-rays are generated by the bombardment of a metal target (typically copper, cobalt or molybdenum) by a beam of electrons emitted from a heated tungsten filament as shown in Figure 2.6[7]. For example, a beam of electrons is accelerated towards to a copper target anode in a vacuum chamber by a potential voltage of 40kV, the electrons impact and ionize the copper metal atoms. The incident radiation transfers energy and the electrons from the inner (lower energy) shell are ejected (here called K shell), resulting in a vacancy or an excitation (unstable) electronic state. In order to reduce the system energy back to a stable ground state, electrons in outer shell (called L and M shells) drop into K shell to fill the vacancy and release Cu characteristic X-rays (Figure 2.7[8]). Two intense lines, Cu K_α and Cu K_β, are present in the emission spectrum with λ (wavelength) = 1.541Å and 1.392Å, respectively. The beam can be screened either by using a Ni filter or by diffracting the X-ray beam from a crystal monochromator. Beryllium (Be) windows are used to: (i) to seal and maintain the vacuum in the X-ray chamber and (ii) metal Be thin film is a stable material with low absorption and high penetrations for X-rays[9]. Although lab-scale X-ray machines are easy to operate, some subtle structure variations may not be detectable because of insufficient X-ray flux.

In this dissertation, in addition to laboratory facilities, powder X-ray diffraction data also has been collected at a synchrotron source. Synchrotron light starts from an electron gun by a high electric field, and the beam of free electrons are introduced and directed into a linear accelerator (LINAC) where they speed up to close the speed of light. The LINAC feeds into a booster ring which uses magnetic field to confine the electrons to travel in a circle. The beam is increased in energy (ex: 6GV for ESRF) to reach the X-ray range and then enters the storage ring. Synchrotron light is generated when bending magnets or additional insertion devices deflect the electron beam; each set of bending magnets is connected to a beamline or experimental station. The brightness of synchrotron light can be 10^4 times higher than an in-house X-ray device by precisely controlling the focus of the beam and adjusting the undulator magnets to enhance the interference effect as shown in Figure 2.8[10].
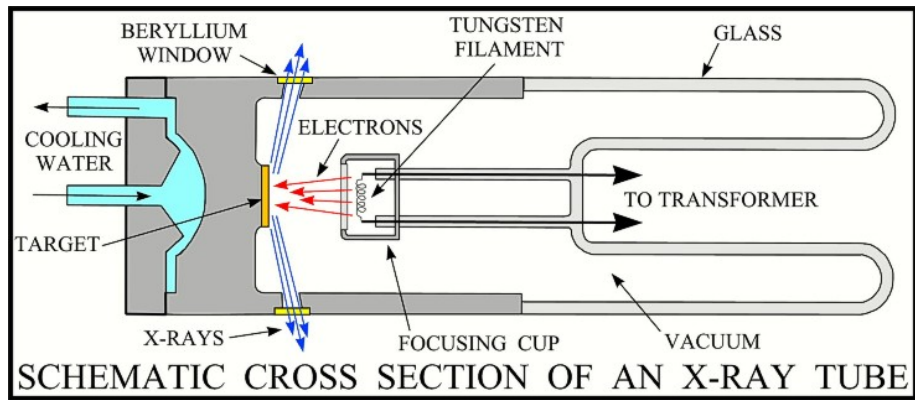
Figure 2.6 Schematic of a commercial X-ray tube[7].
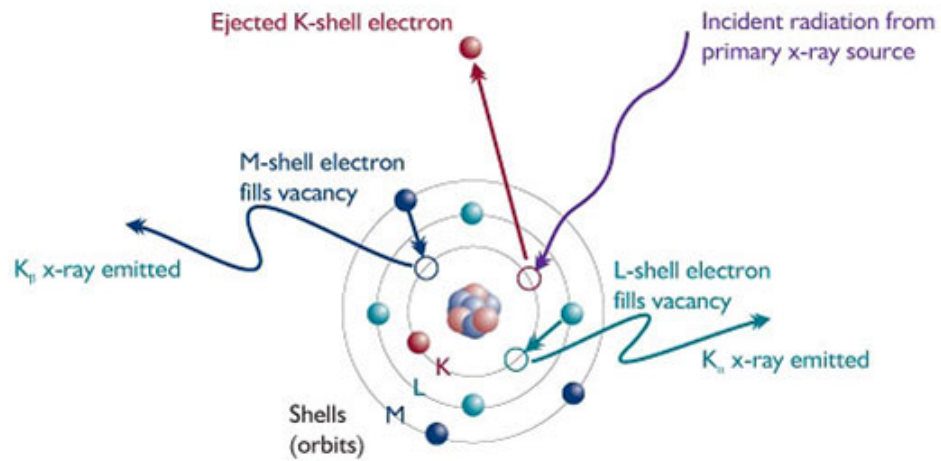
Figure 2.7 Schematic for the generation for characteristic X-ray of Cu K_α and K_β[8].
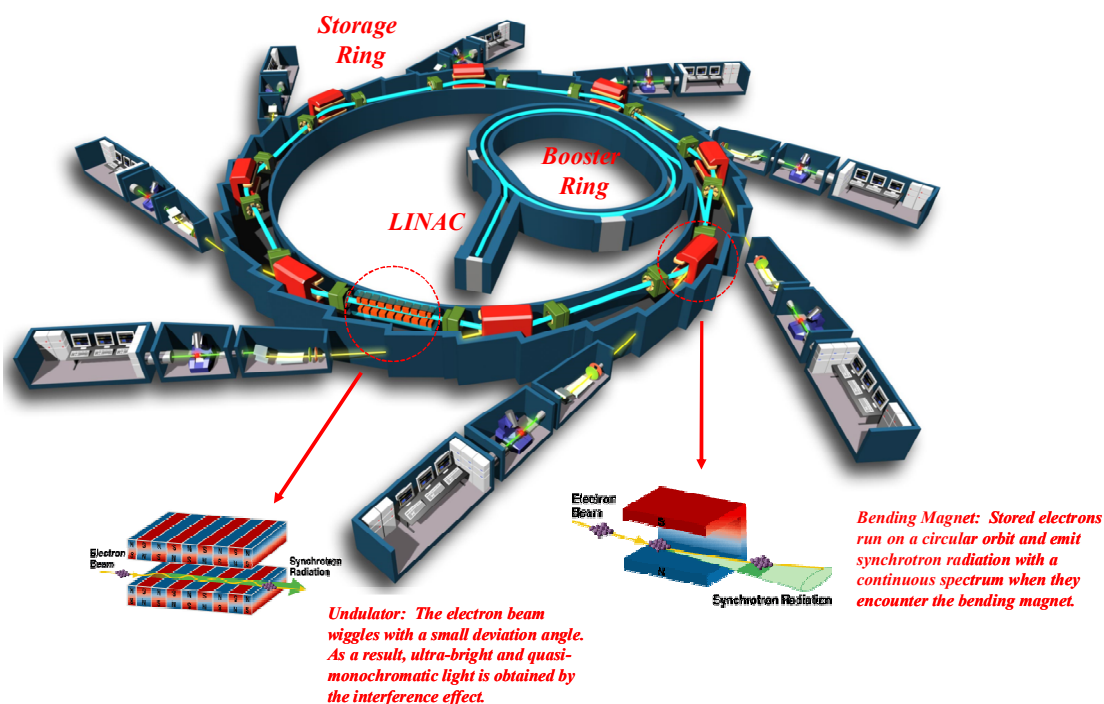
Figure 2.8 Schematic of Synchrotron devices and facility[10].

2.3.3 Neutron Powder Diffraction

In contrast to X-ray diffraction, neutron scattering occurs from the direct interaction of neutrons with the nuclei of atoms. The scattering factor b_i (or scattering length) of neutron is independent to the atomic numbers and can vary significantly between elements or even between isotopes of the same element, such as between hydrogen (H_2) and deuterium (D_2). Another unique property of the neutron diffraction results from the neutrons having a magnetic moment and scattering takes place from long ranged magnetic order within a material, and thus can be used to determine the magnetic structure.

For a paramagnetic material, if there is no external field applied, the random magnetic scattering causing a diffuse background around the Bragg peaks which decreases in

magnitude with increasing scattering angle, θ. In ferromagnetic materials, the magnetic spins aligned in parallel give rise to magnetic reflections which can add additional intensity to the nuclear scattering peaks or appear as new peaks. The magnetic contribution can be differentiated from the nuclear reflections by experiments as a function of temperature through the magnetic ordering temperature. In a simple 1-D antiferromagnet (as shown in Figure 2.9)[11], the magnetic moments on adjacent atoms are aligned antiparallel, resulting in the lattice parameters of the magnetic structure being twice that of the nuclear structure. This means the repeat distance of magnetic structure will be a half of crystal lattice in reciprocal space. Therefore, the magnetic scattering peaks will usually appear between crystal reflections at the 2θ positions.
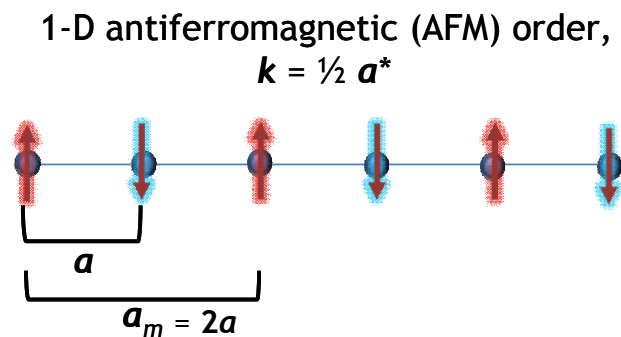
Figure 2.9 Schematic for 1-D antiferromagnetic order.

There are two major strategies to produce thermal neutrons: fusion reaction in a nuclear reactor or a spallation process. Reactor sources are more commonly used to perform constant wavelength neutron diffraction experiments. Typically, the beam of white thermal neutrons from a nuclear reactor is passed through a horizontal collimator to a single crystal monochromator where the desired wavelength (energy) of beam is filtered

out. The monochromatic beam is scattered by the sample into a detector. There are also other two collimators set-up between the monochromator to sample, and from sample position to detector which are applied to reduce the diverge angle of neutron beams (enhance the resolution) and minimize the inaccuracy of measurements. Furthermore, a set of multiple detectors equipped to cover full scattering angles range has been used to effectively increase scattering intensity. The data also can be obtained on different scattering angles 2θ at the same time and dramatically decrease the collected time. There are several factors to influence the shape of diffraction peaks in this type of experiment such as the imperfect collimation (geometry of the defining collimators), the mosaic structure of the monochromator and the crystallinity of the sample (preferred orientation, grain size effects, crystalline strain etc.)

Another useful neutron source is an accelerator-based source where pulsed neutron beams are produced. In this type of neutron facility, high energy protons (~800 MeV) are accelerated and impact on a heavy metal target, such as mercury, uranium or tantalum (as known as spallation reaction). A high flux of neutrons is generated with various wavelengths (called white neutrons). In general, these white neutrons have too high an energy to characterize materials, so they must be reduced in energy by moderator to the appropriate wavelength range which is comparable to the interatomic distance in crystalline materials for usage. Accelerator-based neutron sources are used as the time-of-flight (T. O. F.) neutron detection since the neutrons are produced by pulses of protons. From the layout of this facility, the total flight path, L, is defined by the distance for a neutron to travel from the moderator, pass through the sample and arrives at the detector. The total time of flight, t is also measured. If this is a totally elastic scattering and no any energy loss happened during the travel, then the equation can be used to

calculate the wavelength, λ of the neutron:

$$t_{hkl} = \frac{m_n L \lambda}{h} = \left(\frac{2 m_n L \sin \theta}{h} \right) d_{hkl} \tag{2.10}$$

where m_n is the mass of the neutron and h is Planck's constant.

It is not necessary to use the monochromators for the neutron beam and a high flux of neutrons can be used for diffraction experiments in the time of flight technique. Depending on Bragg's law, the wavelengths of the neutrons can be calculated from equation (2.10) and the d_{hkl} also can be obtained. Uniquely, a wide range of scattering vectors q (inverse proportional to d-spacing) can be measured at a single scattering angle by a single detector. The detectors are arranged in banks, each with its own d-spacing range, count rate and resolution.

2.3.4 Rietveld Refinement

One fundamental issue in powder diffraction that has to be addressed is the "phase problem". In the diffraction analysis of a randomly oriented crystal powder, the 3-D crystalline data are reduced to a 1-D pattern. Since the intensity is proportional to the square of structure factor (equation (2.6)), information on the scattering phase is lost. In addition, there are many crystal planes with the same or similar spacings and therefore superimposed on top of each other.

Hugo M. Rietveld[6,12] proposed a profile fitting method in 1969 for neutron powder diffraction to reasonably analyze the overlapping of peaks. This Rietveld refinement utilizes the least square method and allows for the optimization of structural parameters to obtain the best fit to the experimental data. Thus, method minimizes the residual:

$$S_y = \sum_i w_i |y_i - y_{ic}|^2 \tag{2.11}$$

where y_i is the observed intensity of ith position in diffraction pattern and y_{ic} is the calculated intensity of ith position from the model. w_i is a weighted value defined as $w_i = \dfrac{1}{y_i}$. However, for this strategy, an appropriate initial model is required as a starting point. The starting model can be selected by comparing the same or similar positions of Bragg peaks in a crystallographic database, or some isostructural materials with known structure. If there is no matched crystallographic information for a totally new structure, then the *ab-initio* or a directed method calculation maybe applied.

Typically, for the X-ray diffraction, the calculated intensity of a Bragg reflection (*hkl*) at ith position can be expressed as equation (2.12).

$$y_{ic} = s \sum_{hkl} m_{hkl} L_{hkl} |F_{hkl}|^2 A_i \phi(2\theta_i - 2\theta_{hkl}) P_{hkl} T + y_{ib} \tag{2.12}$$

where:

- s is the scale factor,

- L_{hkl} is the Lorentz-polarization factor for the reflection *(hkl)*,

- m_{hkl} is the multiplicity factor,

- F_{hkl} is the structure factor,

- A_i is the asymmetry parameter,

- $\phi\,(\theta)$ is the peak shape function,

- $2\theta_{hkl}$ is the calculated position of the Bragg peak, corrected for the zero-point shift,

- P_{hkl} is the preferred orientation function,

- T is the absorption correction,

- y_{ib} is the background contribution at the *i*th position.

49

The pseudo-Voigt approximation is the most common function for combining with Lorentzian and Gaussian function compositions. In this dissertation, both X-ray and neutron powder diffraction data have been refined using the general structure analysis suite, GSAS[13]. In GSAS, the background function is fitted by a Chebyshev function with a variable number of parameters used a modified Thompson-Cox-Hastings pseudo-Voigt (TCHZ) peak shape function given by:

$$TCHZ = \eta L = (1-\eta)G \tag{2.13}$$

Where L is the Lorentzian component given by:

$$\Gamma_L = \frac{X}{\cos\theta} + Y\tan\theta \tag{2.14}$$

G is the Gaussian contribution given by:

$$\Gamma_G^2 = U\tan^2\theta + V\tan\theta + W$$

and η is the mixing parameter given by:

$$\eta = 1.36603q - 0.47719q^2 + 0.1116q^3$$

where $q = \dfrac{\Gamma_L}{\Gamma}$ and $\Gamma = (\Gamma_G^5 + A\Gamma_G^4\Gamma_L + B\Gamma_G^3\Gamma_L^2 + C\Gamma_G^2\Gamma_L^3 + D\Gamma_G\Gamma_L^4 + \Gamma_L^5)^{0.2}$ (2.15)

where A=2.69269, B=2.42843, C=4.47163 and D=0.07842.

The cutting of the curved surface of the Debye-Scherrer cone by a finite detector slit height results in the asymmetric component A_i of the reflection profile, which is modified by a parameter P and shown as equation (2.16).

$$A_i = \frac{1 - P \pm (2\theta_i - 2\theta_k)}{\tan\theta_k} \tag{2.16}$$

where θ_k is the angle below where the asymmetry happened.

There are several fitting factors have been used to quantitatively evaluate the goodness-of-fit for the refinement. These factors in the Rietveld analysis are defined as fellow:

- The Bragg R-factor, R_B,

$$R_B = \frac{\sum |I_{hkl}(obs) - I_{hkl}(calc)|}{\sum I_{hkl}(obs)} \qquad (2.17)$$

- The profile R-factor, R_p,

$$R_p = \frac{\sum |y_i - y_{ic}|}{(\sum y_i)} \qquad (2.18)$$

- The weighted profile R-factor, wR_p,

$$wR_p = \sqrt{\left[\frac{\sum w_i(y_i - y_{ic})^2}{\sum w_i y_i^2}\right]} \qquad (2.19)$$

where w_i is the weighted value.

- The expected R-factor, R_{exp},

$$R_{exp} = \sqrt{\left[\frac{N - P + C}{\sum w_i y_i^2}\right]} \qquad (2.20)$$

where N, P and C are the number of profile points, refined parameters and constraints, respectively.

- The goodness-of-fit factor, ,

$$\chi^2 = \frac{R_{wp}}{R_{exp}} \qquad (2.21)$$

that is unity for perfect fit.

Even if good residual factors (R-factors) are obtained after a Rietveld refinement, they can not guarantee the accuracy for the structures. The bond lengths and angles from the

51

refined structure provide an essential check to evaluate the quality of refinement.

2.3.5 Charge Flipping (CF) Calculation

2.3.5.1 Introduction

In the past couple of decades, sophisticated calculations for the analysis of crystal structures via direct or *ab-initio* methods have been developed. These techniques are more convenient for solving a totally unknown structure, however, in general, it is still very time-consuming. In this dissertation, the charge flipping (CF) calculation[14-19] is used. There are several attractive characteristics for using the CF algorithm: (i) It is extremely simple and easy to implement, (ii) It is *ab-initio*. The nuclear or electron density of a grid (not necessary equal to the unit cell) is represented but the knowledge of atoms is absent from the solution. Therefore, atom types, chemical formula, or total charge of a unit cell are a necessary input for the running of a CF calculation. Even the information for symmetry of structure is not needed as it starts from the lowest space group *P*1 and the algorithm attempts to determine the space group. Once the nuclear or electron density has been constructed, then the chemical composition and space group symmetry can be identified. The CF algorithm is very different from the classical direct method or Monte Carlo techniques because it doesn't involve complex calculations for statistical phase relations.

2.3.5.2 The Charge Flipping (CF) Algorithm

A simple flow chart of the CF algorithm is shown in Figure 2.10 and can be divided

into several steps and one iteration cycle:

(1) The calculation is initialized by selecting a random phase set $\{\varphi(\boldsymbol{h})\}$ which satisfies Friedel's law (e.g. $|F_{hkl}| = |F_{\overline{hkl}}|$ or $\varphi_{hkl} = -\varphi_{\overline{hkl}}$). The starting set of structure factors can be generated as $F_0(\boldsymbol{h}) = F_{exp}(\boldsymbol{h})\exp[i\varphi(\boldsymbol{h})]$, where $F_{exp}(\boldsymbol{h})$ for all Bragg reflections $\boldsymbol{h}$ obtained from the measured X-ray or neutron diffraction data. The subscript n in Figure 2.10 refers to the repetition number for the CF calculation. The position $\boldsymbol{h}$ with no peak and $F_0(0)$ are set to zero. The starting electron density $\rho_1(\boldsymbol{r})$ is then calculated from the set of structure factors $F_0(\boldsymbol{h})$ by an inverse of fast Fourier transform (FFT).

(2) The electron or nucleus density $\rho_1(\boldsymbol{r})$ is subjected to the charge flipping step. The positive user-defined threshold parameter δ ($\delta \geq 0$) is applied to classify the generated "flipped" density $g_1(\boldsymbol{r})$ by reversing the sign of any density for which $\rho_1(\boldsymbol{r}) < \delta$ as described in equation (2.22).

$$\text{if } \rho_1(\boldsymbol{r}) \geq \delta \geq 0, \text{ then } g_1(\boldsymbol{r}) = \rho_1(\boldsymbol{r})$$

$$\text{if } \rho_1(\boldsymbol{r}) < \delta \geq 0, \text{ then } g_1(\boldsymbol{r}) = -\rho_1(\boldsymbol{r}) \tag{2.22}$$

Moreover, all the negative values of $\rho_1(\boldsymbol{r})$ must be flipped to become positive, whereas all small positive values of $\rho_1(\boldsymbol{r})$ within range $0 < \rho_1(\boldsymbol{r}) < \delta$ must be flipped to become negative.

(3) A set of intermediate structure factors $G_1(\boldsymbol{h})$ are transformed from FFT of $g_1(\boldsymbol{r})$ with a parallelepiped-shaped volume that includes both the resolution sphere of observed reflection and outer shape of unobserved reflections[14]. However, only the phases $\alpha_1(\boldsymbol{h})$ of these structure factors are selected to use for next step.

(4) The updated structure factors $F_1(\boldsymbol{h})$ are constructed by using the combination of

selected phases $\alpha_1(\boldsymbol{h})$ with experimental amplitudes of structure factors $|F_{exp}(\boldsymbol{h})|$. Here the $F_1(0) = G_1(0)$ is accepted for unchanged, but the residual part out of $F_1(\boldsymbol{h})$ resolution sphere (outside the phases $\alpha_1(\boldsymbol{h})$) are reset to zero as described in step (3). However, in the CF algorithm, the amplitude of intermediate structure factors $|G_n(\boldsymbol{h})|$ are only used to determine the R-factors, which is functionalized to watch the progress of the iterative cycle rather than actually used in the calculation.

(5) The structure factors, $F_1(\boldsymbol{h})$ are inverted by FFT to obtain the new electron or nucleus scattering density $\rho_2(\boldsymbol{r})$ and the iterative process is repeated until an acceptable R-factor is obtained and the electron density $\rho_n(\boldsymbol{r})$ reaches sufficient quality to start a structure refinement. However, one important aspect must be emphasized: the structure factors $F_n(0)$ which correspond to the total number of electrons in a unit cell is not necessary being fixed at $F_n(0) = 0$ during the CF calculation[20,21]. Nevertheless in this dissertation, this approach has been adopted.
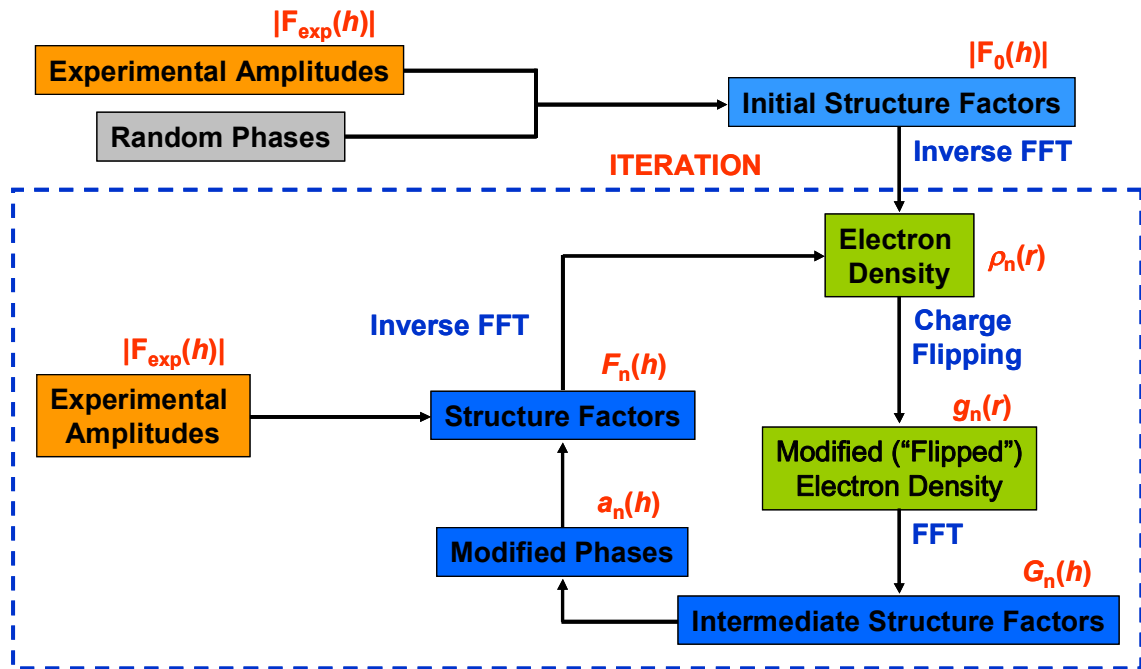
Figure 2.10 Schematic flow chart of the CF algorithm for X-ray diffraction data.

2.3.5.3 Selection of the Threshold Parameter, δ

Although remarkable advantages are possible through the application of the CF technique, there are still some aspects to be noted that limits its general use: (1) The basic CF algorithm requires a single parameter: the threshold δ, to specifically control the charge flipping step. The selection of an "optimal" value is delicate and a critical problem to successfully apply this technique because it determines (i) The size of the computation for a solution and (ii) The quality of final density map. There is currently no analytical approach for determining the optimal value of δ in advance for any specific problem[22] and the value of optimal δ is very case-dependent. Although several empirical attempts have been provided[15,22], the optimal selection of this parameter still determines the success of the CF calculation and remains a challenging issue. Furthermore, the rate of success for some complicated or difficult structures is low as a result of these limitation[15,21]. (2) In general, a successful implementation of the CF algorithm has three characteristics: (i) an initial transient, (ii) a long stagnation (corresponding to a high value of R-factor is not substantially changed during many iterations) period before convergence and (iii) the stable state after convergence. In fact, the period of stagnation where the high value of R-factor that stays roughly constant can be extremely long before it suddenly converges and a solution is obtained especially for complicated structures[21]. This behavior can misguide the selection of the parameter δ, and make the application of the CF calculation better suited to expert in the technique.

2.3.6 Maximum Entropy Method (MEM)

The requirement for introducing rigid bodies, constraints, restraints and an anisotropic displacement parameter for the disordered or diffusion parts in crystals makes Rietveld refinement hard to reach convergence for some systems. The maximum entropy method (MEM)[23-29] can offer a complementary strategy for deriving nuclear or electron density from limited information. The combination of the MEM and Rietveld methods was proposed by Takata et al. in 1995[27]. In this method, the structural model keeps refining via substituting the values of the observed structure factors (F_{obs}) obtained from MEM calculations for the corresponding values of the calculated structure factors (F_{calc}) from Rietveld refinement.

In the field of crystallography, the concept of entropy is related to the resolution of Fourier maps. The value of $(\sin\theta /\lambda)_{max}$ for a perfect Fourier map which is required for a complete structure has to be at least 5.0Å^{-1} [30]. The overlap of peaks in 1-D powder diffraction pattern limits the information necessary for a 3-D crystal structure. However, the MEM method can extract the most information from limited experimental data by defining the G constraints to deal with the overlapping reflections[28]. The entropy of any trial density can be defined by a prior density ρ^{prior} and is given by

$$S = -\sum_{i=1}^{N_{pix}} \rho_i \ln\left(\frac{\rho_i}{\rho_i^{prior}}\right) \qquad (2.23)$$

where the density is defined at the spaces of a $N_1 \times N_2 \times N_3 = N_{pix}$ grid over the unit cell. The prior density ρ^{prior} can either be a constant function called a flat or uniform prior, or represents any desirable distribution of the available scattering over the unit cell. A useful prior density ρ^{prior} is the pro-crystal density which is defined as the electron or nuclear

density corresponding to the independent atom model (IAM) obtained from the best refined model from the Rietveld or Le Bail method [31]. In equation (2.23), the maximum entropy S is obtained by varying different constraints. The maximum $Q = S - \lambda_N C_N - \lambda_F C_F - \lambda_G C_G$ using Lagrange multipliers λ and the constraints C, which are defined below. In order to get maximum values, the differential $(\partial Q / \partial \lambda) = 0$ when all the constraints $C_N = C_F = C_G = 0$. All constraints are functions of the electron or nuclear density. The constraint C_N is the normalization of the electron density for X-ray diffraction as shown in equation (2.24).

$$C_N = N_{el} - \frac{V}{N_{pix}} \sum_{i=1}^{N_{pix}} \rho_i = 0 \qquad (2.24)$$

where N_{el} is the electron numbers of the unit cell volume V. λ_N can be eliminate from the MEM iterative calculation. The normalized flat prior density $\rho_i = N_{el}/V$. The constraint C_F is constructed from the observed structure factors of phases F_{obs} and defined as

$$C_F = -1 + \frac{1}{N_F} \sum_{i=1}^{N_F} w_i \left(\frac{|F_{obs}(H_i) - F_{MEM}(H_i)|}{\sigma(H_i)} \right)^2 = 0 \qquad (2.25)$$

where

- N_F is the number of isolated phase with the observed structure factors $F_{obs}(H_i)$, which include the standard uncertainties $\sigma(H_i)$.

- $F_{MEM}(H_i)$ are the phased structure factors obtained by Fourier transform of the trial electron density ρ_i.

- w_i is the weighted parameter which is unity (one) if no weights are applied.

To reiterate, the overlapping Bragg peaks in powder diffraction are handled by the G

57

constraints in MEM method[28] and can be written as

$$C_G = -1 + \frac{1}{N_{all}} \sum_{i=1}^{N_F} w_i \left(\frac{\left| F_{obs}(H_i) - F_{MEM}(H_i) \right|}{\sigma(H_i)} \right)^2 + \frac{1}{N_{all}} \sum_{j=N_F+1}^{N_{all}} \left(\frac{G_{obs}^j - G_{MEM}^j}{\sigma(G_{obs}^j)} \right)^2 = 0$$

(2.26)

where N_G is the number of overlapping group and

$$G^j = \sum_{k=1}^{N_G(j)} \left(\frac{m_k}{\sum m_k} \left| F(H_k) \right|^2 \right)^{1/2}$$

(2.27)

where m_k is the multiplicity of reflection k and $N_G(j)$ is the number of reflections contributing to the jth overlapping group.

The error propagation law has been applied to calculate the standard uncertainty of the group reflection by

$$\sigma(G) = \frac{1}{G(j)} \left[\sum_i \left(F_j \left(\frac{m_j}{\sum m_k} \right) \sigma(F_j) \right)^2 \right]^{1/2}$$

(2.28)

The MEM calculation can only reach convergence when a sufficiently large fraction of the reflections are involved in the F constraint[28]. A single Lagrange multiplier which was utilized by the combination of F and G constraints are shown as

$$C_{FG} = C_G = -1 + \frac{1}{N_{all}} \sum_{i=1}^{N_F} w_i \left(\frac{\left| F_{obs}(H_i) - F_{MEM}(H_i) \right|}{\sigma(H_i)} \right) + \frac{1}{N_{all}} \sum_{j=N_F+1}^{N_{all}} \left(\frac{G_{obs}^j - G_{MEM}^j}{\sigma(G_{obs}^j)} \right) = 0$$

(2.29)

where $N_{all} = N_F + N_G$.

The initial electron density (prior density) ρ^{prior} can be introduced as a uniform prior for the description of the disordered parts or anharmonic temperature vibrations of atoms in a

crystal when the exact positions of atoms are important. Even structure factors extracted from a Le Bail fit, the unbiased structure model from MEM map is still considered since the amplitudes of phases and structure factors come directly from experimental data. Uncertainty factors or model inaccuracy on amplitudes can be eliminated using the combination the F and G constraints which is shown in the block of Figure 2.11 marked by red dashed line[32].

Synchrotron X-ray powder diffraction data & cell parameters & space group

without reference model

Charge Flipping (CF) & histogram matching (HM) to reconstruct the phases (ϕ^{CF}), starting by cell parameters, F_{leBail} and random phases

with reference model

Rigid body Rietveld refinement

Extraction of the structure factors (Le Bail method)

ϕ^{CF} , $F_{Le\ Bail}$

Inverse Fourier

ρ^{IFT} Fourier map of the results of CF

ϕ^{CF} , F_{obs}

MEM F-constraints

ρ^{MEM} (ϕ^{CF} , F_{obs}) Combination of MEM&CF & Rietveld

ϕ^{CF} , F_{obs}

MEM F+G-constraints

ρ^{MEM} (ϕ^{CF} , F_{obs}) Combination of MEM&CF & Rietveld (A)

ϕ^{CF} , $F_{Le\ Bail}$

MEM F+G-constraints

ρ^{MEM} (ϕ^{CF} , $F_{Le\ Bail}$) Combination of MEM & CF & Le Bail (B)

$\phi^{Rietveld}$, F_{calc}

IAM (Undependent Atomic Model) Analytical FFT

ρ^{pro} Strong biased by the model

x,y,z and ADPs

$\phi^{Rietveld}$, F_{calc}

MEM F- constraints

ρ^{MEM}_{calc} Completely biased

$\phi^{Rietveld}$, F_{obs}

MEM F- constraints

ρ^{MEM}_{obs} Partially biased

$\phi^{Rietveld}$, F_{obs}

MEM F+G-constraints

$\rho^{MEM}_{obs\ +G}$ Less biased

$\phi^{Rietveld}$, F_{leBail}

MEM F+G-constraints

$\rho^{MEM}_{Le\ Bail\ +G}$ Unbiased by the model

Figure 2.11 The Flow chart showing the procedure for extracting the different types of structure factors and phases used to reconstruct the different type of electron density maps from powder diffraction data. The procedure of the MEM method is marked by red dashed line.

2.4 Magnetism

All the discussed information for the magnetism section comes from the references [3,4, 33-35].[3,4,33-35]

2.4.1 Magnetic properties and Magnetization of materials

When an external magnetic field, H is applied, magnetic materials will be induced to possess a magnetization, M. There are usually two common magnetic unit systems being used: SI and CGS units. The basic difference between these two unit systems is due to the definition of flux density, B. In SI units, the relationship between H, M and B can be described as

$$B = \mu_0 \left(H + M \right) \qquad (2.22)$$

where H and B are in A/m and Tesla, respectively; and $\mu_0 = 4\pi \times 10^{-7}$ Tm/A is defined as the permittivity of free space. In CGS unit system, the relationship is shown

$$B = H + 4\pi M \qquad (2.23)$$

where the unit for H is Oersted and Gauss for B. In addition, The SI unit of magnetic moment, μ is given in J/T and in the CGS unit is given in erg/G, also defined as emu. The magnetization M in materials can be described as $M = N \langle \mu \rangle$ where N is the number of unit volume and $\langle \mu \rangle$ is average magnetic moment per unit volume. Magnetization can be easily defined by magnetic susceptibility in equation (2.24) since it is strongly related to the external applied field.

$$\chi = \frac{M}{H} \qquad (2.24)$$

2.4.2 Classifications of Magnetic Characteristics

The magnetic interactions within materials lead to different magnetic ground states,

five of which are discussed below.

2.4.2.1 Diamagnetism

Diamagnetism is the phenomenon in which the direction of magnetization is induced in the opposite direction of external magnetic field and generates a negative magnetization. Specifically, an external magnetic field changes the magnetic dipole moment by altering the orbital velocity of electrons around their nuclei, which is against the external field according to Lenz's law. This type of material is constructed by the atoms with filled electron shells in structures and has no permanent magnetic moment, depending on neither temperature nor proportional to the applied field. The susceptibility of a diamagnet is given by

$$\chi = -\frac{\mu_0 Z e^2 n \langle r^2 \rangle}{6 m_e} \qquad (2.25)$$

where n is the number of atoms per unit volume, Z is the number of electrons per atom, e is the electronic charge, m_e is the electronic mass and $\langle r^2 \rangle$ is the root mean square atomic radius. Typically, diamagnetism is much weaker than paramagnetic or ferromagnetic magnetization, and its magnitude is typically -10^{-5} erg/Oe^2mol. However, the superconductor is a specific case of large diamagnetism, in which the susceptibility comes from current vortexes which oppose the applied field, rather than the changes in orbital motion of the closely bound electrons.

2.4.2.2 Paramagnetism

Paramagnetism is a common magnetic behavior in materials where the atoms possess

odd electron number in the orbits and form the net magnetic moments from unpaired electrons. The order of paramagnetic susceptibility is about 10^{-3}-10^{-5} erg/Oe^{2}mol, which depends both on applied field and temperature. Although the value is positive, it is relatively small if compared with a ferromagnet. For paramagnets, the moments are randomly orientated and it is only the presence of an applied magnetic field that gives the materials an axis that dynamic moment would prefer alignment is related to the magnitude of the magnetic field. The molar susceptibility of paramagnetism is often described by the Curie Law:

$$\chi_m = \frac{C}{T} = \frac{N\mu_{eff}^2 \mu_B^2}{3kT} \qquad (2.26)$$

where T is the temperature in Kelvin, C is known as Curie constant, N is the number of magnetic sites per mole and the effective moment μ_{eff} will be defined below.

$$\mu_{eff} = g\sqrt{J(J+1)} \qquad (2.27)$$

The total angular momentum J, is sum of the orbit and spin momentums and g is the gyromagnetic ratio, usually approximated to 2. For paramagnets, the molar susceptibility is given by the Curie-Weiss law.

$$\chi_m = \frac{C}{T - \theta} \qquad (2.28)$$

The Weiss constant, which is a measure of the strength of the magnetic exchange, θ is defined as

if $\theta > 0$, then ferromagnetic interactions

if $\theta < 0$, then anitferromagnetic interactions

Since the susceptibility is inversely proportional to temperature according to the Curie-Weiss law, the values of C and θ can be able to extract from the curve fitting for a plot of susceptibility against temperature in Curie Weiss region The value C reflects the

number of unpaired electrons in the material.

2.4.2.3 Ferromagnetism

Compared with diamagnets and paramagnets, ferromagnetic materials with spontaneous magnetization (a net magnetic moment) in the absence of an external magnetic field possess large and positive magnetic susceptibility, typically in the range χ = 50-10,000 ergOe^{-2}mol^{-1} Ferromagnetism exists when there is a strong interaction between spins resulting in the parallel alignment of the moments in a long range magnetic ordering. They are characterized by displaying magnetic hysteresis, as shown in Figure 2.12. Initially, the loop starts from the origin point with zero applied field H. With increasing the external field, the magnetization M rises and finally reaches a saturation value, M_s, where all the spins orientate to the direction of magnetic field and M_s will be unaltered by large fields. Reduction of the magnetic field will have little effect on the magnetization until the field is pointed in an opposite direction and the moments begin to flip in that direction. This phenomenon can be explained using the concept of magnetic domains within the materials. Initially, these moments are aligned locally (microscopically) in magnetic domains that are randomly orientated with respect to each other and cancel each other out on a macroscopic level giving zero magnetization in zero field. As a ferromagnet has been driven to saturation, not only are the moments but also the magnetic domains aligned to the direction of applied field.
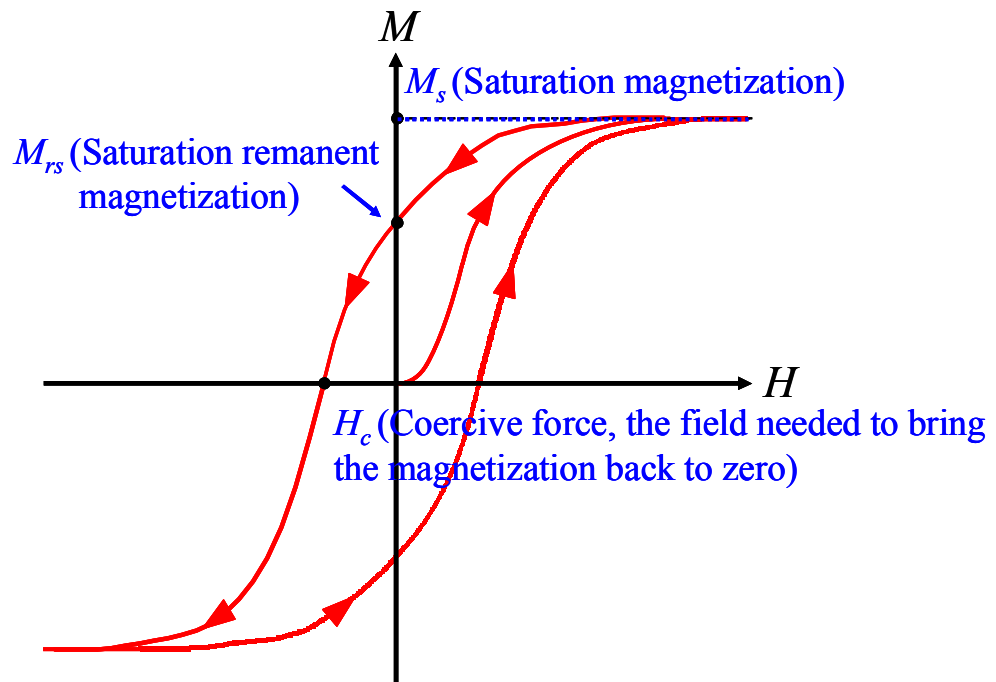
Figure 2.12 Hysteresis loop of a typical ferromagnetic material.

The magnetization at zero field following from it being taken to its saturation is defined as saturation remanent magnetization M_{rs}. Another important value related to a magnetic hysteresis loop is that of the coercive field H_c, which is the field required to bring the magnetization back to zero. These two characteristics make ferromagnets excellent recording devices.

2.4.2.4 Antiferromagnetism

An antiferromagnetic system is characterized by having the ordered moments aligning in such a way that there is no net magnetization. The magnetic susceptibility for an antiferromagnet is less temperature and field dependent than a ferromagnet. The

temperature below which a paramagnet orders into an antiferromagnetic arrangement is known as the Néel temperature, T_N.
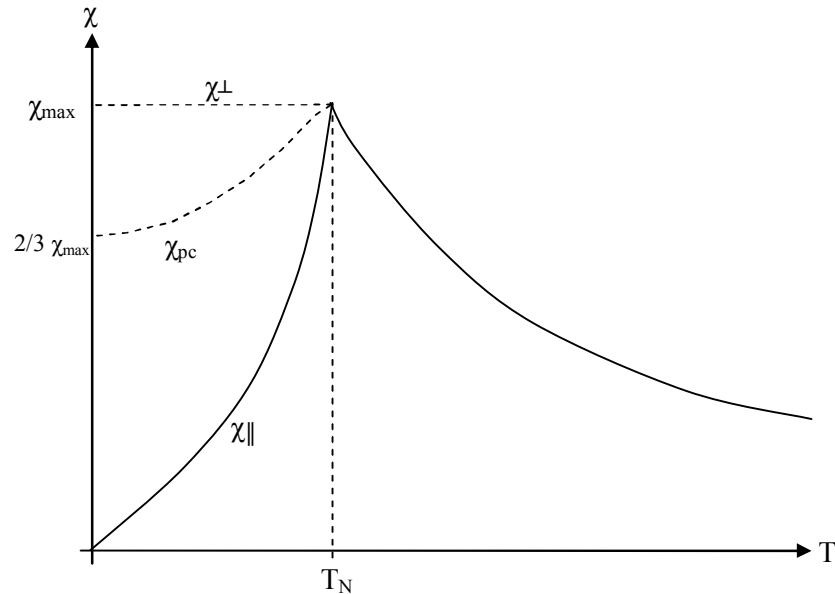
Figure 2.13 The plot of magnetic susceptibility as a function of temperature for an ideal antiferromagnet.

The typical behaviors of the susceptibility of an ideal antiferromagnet, for a single crystal and a powder are shown in Figure 2.13. There are three curves that are for single crystals aligned with the applied field perpendicular ($\chi_\perp$), parallel ($\chi_\parallel$) to the easy axis of the sublattices, as well as a polycrystalline sample (χ_{pc}). A field applied parallel to the easy axis will have no theoretical susceptibility at $T = 0$. When the temperature increases (still below T_N), thermal effects prevent the cancelation of moments to be complete and a finite susceptibility is observed. For a polycrystalline sample, the susceptibility, χ_{pc}, is equal to $2/3 \chi_\perp + 1/3 \chi_\parallel$ when temperature is below T_N. Above T_N, the susceptibility follows the Curie-Weiss Law for paramagnets.

2.4.2.5 Ferrimagnetism

Ferrimagnets have an antiparallel arrangement of spins, but differentiate themselves from antiferromagnets because they contain moments of different magnitude and therefore results in a net magnetization. All the magnetic properties such as the magnetization dependence of temperature are very similar to that of the ferromagnets. However, a situation can accidentally happen at some temperature points below T_c, as known as the magnetization compensation point, where the coupled sublattices possess same magnitude of moments and result in zero net magnetization. The ferrimagnetic properties can be very complex and strongly depending on the nature of the chemical compositions.

2.4.3 Models of Magnetic Exchange

2.4.3.1 The Heisenberg Model

The exchange interaction between two spins can be fundamentally described by the Heisenberg Hamiltonian in equation (2.27).

$$H = -J S_1 \cdot S_2 \qquad (2.29)$$

where J is the exchange constant.

$$\text{if } J > 0, \text{ then } \uparrow\uparrow \text{ or } \downarrow\downarrow \text{ (parallel alignment)}$$

$$\text{if } J < 0, \text{ then } \uparrow\downarrow \text{ or } \downarrow\uparrow \text{ (antiparallel alignment)}$$

Each ion in a solid-state material is always surrounded by several others and the sum of Heisenberg interaction can be written as

$$H = -\sum_{i,j} J_{ij} S_i \cdot S_j \qquad (2.30)$$

The spins, S_i in this model are allowed for an arbitrary direction in 3-D space and the

exchange J_{ij} is isotropic. The latter assumption limits this model which can only apply to cubic systems.

2.4.3.2 The Ising Model

In the Ising model, all the spins are assumed to lie on one specific (generally z axis) axis, and the exchange interaction occurs as a simple pair interaction between two spins. The Hamiltonian modified by the Ising model can be described as

$$H = \sum_{i,j} J_{ij} S_i^z S_j^z \tag{2.31}$$

where J_{ij} is the exchange integral and keeps the same for any pair of spins. The assumption of spin $S_{i \text{ or } j} = \dfrac{1}{2}$ reduces $(S^z)_{i \text{ or } j}$ into two possible values, $+\dfrac{1}{2}$ or $-\dfrac{1}{2}$. The Ising model is suitable to explain the behaviors in highly anisotropic magnets and particularly useful for 1-D magnetic ordering systems.

2.4.3.3 The XY Model

The XY model describes the spins within two (x and y) directions. The Hamiltonian equation modified by the XY model can be written as

$$H = -\sum_{i,j} J_{ij} \left[S_i^x S_j^x + S_i^y S_j^y \right] \tag{2.32}$$

The XY model can appropriately describe the magnetic behaviors of 2-D (planar) ordering structures.

2.4.4 Exchange Interactions

Many different types of exchange contribute to the total exchange constant, J of a system. The different types of exchange are discussed below.

2.4.4.1 Direct Exchange

Direct exchange is an interaction caused by direct overlap of electrons on adjacent magnetic sites. The direct exchange in magnetic systems is often weak as the interaction is very sensitive to distance.

2.4.4.2 Indirect Exchange

Indirect exchange occurs between two magnetic carriers through an intermediary. The main types of indirect exchange are discussed below.

2.4.4.2.1 Superexchange

Superexchange describes an exchange interaction between two individual magnetic carriers through a non-magnetic ion, typically oxygen. This type of interaction usually exhibits antiferromagnetic exchange or ferromagnetic exchange possibly as shown in Figure 2.14 (a) and (b). In Figure 2.14 (a), an antiferromagnetic superexchange is achieved by two d orbits (e_g) from metal cations and one p orbit (σ) from the bridged oxygen ion which develop a 180° M-O-M bond. In the ground state, the electrons have to occupy each empty lobe first to obey the Hund's rule. Moreover, the spin configuration must be antiparallel in the same orbit to comply Paul's exclusion principle. In this case, the electron configuration in antiparallel arrangement for oxygen p orbit leads the spins with opposite direction in two metal d orbits resulting in an antiferromagnetic configuration. In the Figure 2.14 (b), the ferromagnetic superexchange can be obtained by combining two t_{2g} orbits from metal cations and one π orbit from the intermediate oxygen. This phenomenon also strongly related to the deviation angle from the 180°

configuration as shown in Figure 2.14 (a). An important conclusion can be made that the antiferromagnetic interaction is usually induced for a superexchange phenomenon with 180° bonding angle in a material, whereas the angle is much smaller than 180°, the ferromagnetic can be observed. The crossover between these two states occurs at an angle of around 120°.

(a)

(b)
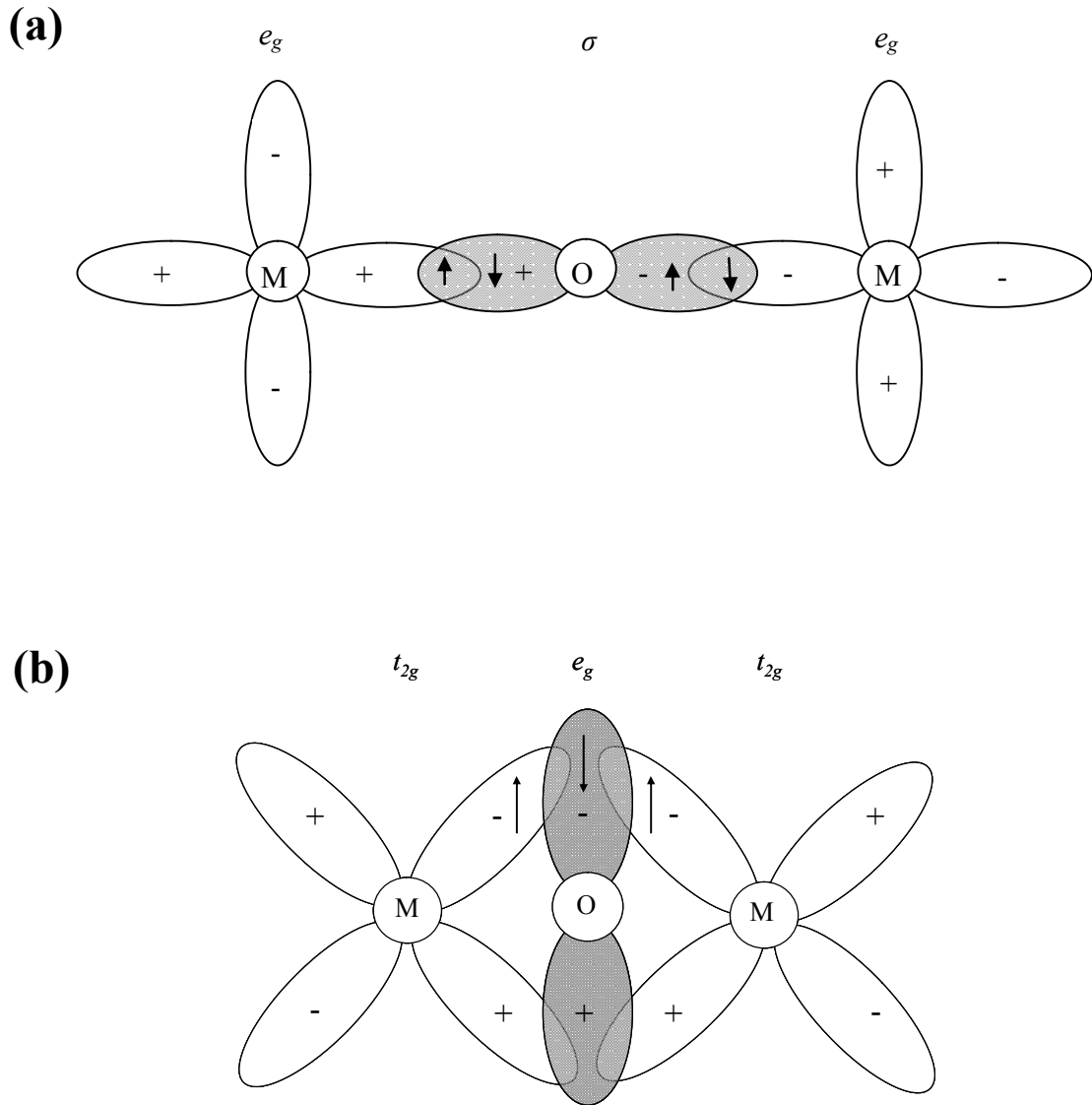
Figure 2.14 Antiferromagnetic (a) and ferromagnetic (b) superexchange interaction between two metal ions via a non-magnetic oxygen.

2.4.4.2.2 The RKKY Theory

The RKKY theory (named by Ruderman, Kittel, Kasuya and Yoshida) first developed to explain the indirect exchange coupling of nuclear magnetic moments through conduction electrons in metallic compounds such as rare earth metals. Essentially, a

magnetic ion self-polarizes its surrounding conduction electrons, which can transfer their polarization to the next distant magnetic ion with some distance, r. Therefore, a long-range coupling interaction can be achieved by this mechanism. The exchange integral, J_{RKKY}, is written as

$$J_{RKKY}(r) = 6\pi Z J^2 N(E_F) \left[\frac{\sin(2k_F r)}{(2k_F r)^4} - \frac{\cos(2k_F r)}{(2k_F r^3)} \right] \tag{2.33}$$

where Z is the number of conduction electrons per atom, J the exchange constant, $N(E_F)$ the density of states at Fermi level, k_F the Fermi momentum and r the distance between two impurities. The interaction can have alternative signs depending on the distance between the magnetic ions (ferromagnetic or antiferromagnetic) since this equation is constructed by a sine and cosine function.

2.5 Principles of Raman Spectroscopy

Raman scattering (named after C. V. Raman)[36-40] occurs as an electromagnetic wave encounters a molecule or material. Although the vast majority of photons (>99.99%) are scattered elastically (as known as Rayleigh scattering), a very small proportion (<0.001%) will be subjected to inelastic scattering (Raman scattering) and undergo a shift of energy. The Raman scattering is a complementary spectroscopic technique to infrared (IR) spectroscopy. Both these two techniques are able to detect the rotational or roto-vibrational transitions of molecules, but the fundamental selection rules are regarded for the interactions with different types of molecular motions resulting in distinct information can be obtained from each spectrum. On the other hand, Raman spectroscopy is measured by the interactions between the incident photons and differently rotational or roto-vibrational modes with distinguishable levels of distortion on electron clouds, as

shown in Figure 2.15.
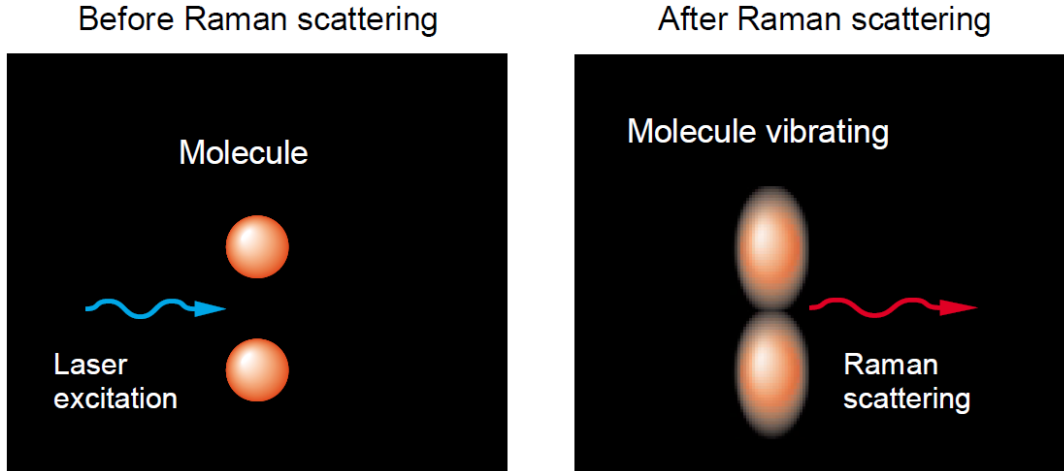
Figure 2.15 Schematic diagrams for Raman effect.

Basically, there are three major steps for the energy transfer in the Raman effect. (i) The incident light excites the electrons of molecules to a higher-energy "virtual" state, (ii) The electrons exchange energy (lose or obtain) with molecules. (iii) The electrons go back to ground state and release the radiation. As illustrated in Figure 2.16, if this process is totally without energy-exchanged, it is known as Rayleigh scattering. If there is an energy loss ($\Delta E = h(\omega_i - \omega_0)$) during the process, which is called as Stokes scattering shift. If the energy is obtained ($\Delta E = h(\omega_i + \omega_0)$) then named anti-stokes scattering shift.

According to the theory of classical electromagnetism, an incident wave and atomic vibration can be described as

$$\vec{E}(t) = \vec{E}_0 \cos \omega_i t = \vec{E}_0 \, e^{-iw_i t} + \vec{E}_0^* \, e^{iw_i t} \quad \text{(incident wave)} \qquad (2.34)$$

$$\mu(t) = \mu_0 + \cos \Phi t \quad \text{(atomic vibration)} \qquad (2.35)$$

and an induced oscillating polarization $\vec{P}(t)$ is shown by

$$\vec{P}(t) = \alpha(t)\,\vec{E}(t)$$

where $\alpha(t)$ is Tensor of polarization as a function of vibration types of atoms or molecules and effected by electric field E. If there is a normal mode Φ with frequency ω_0, $\alpha(t)$ can be described as

$$\alpha(t) = \alpha_0 + \left(\frac{\partial \alpha}{\partial \mu}\right)_0 \cdot \frac{\mu}{1!} + \left(\frac{\partial^2 \alpha}{\partial \mu^2}\right)_0 \cdot \frac{\mu^2}{2!} + ... = \alpha_0 + \alpha_1 \mu + ...$$

Apply first order approximation

$$\alpha(t) = \alpha_0 + \Delta\alpha \cdot \cos\Phi t = \alpha_0 + \alpha_1 e^{-i\omega_0 t} + \alpha_1^* e^{i\omega_0 t} \tag{2.36}$$

Then the induced oscillating polarization $\vec{P}(t)$ can be re-written as

$$\begin{aligned}
\vec{P}(t) &= \alpha(t)\,\vec{E}(t) = (\alpha_0 + \Delta\alpha \cdot \cos\Phi t)\cdot(\vec{E}_0 \cos\omega_i t) = \alpha_0\,\vec{E}_0 \cos\omega_i t \\
&+ \frac{1}{2}\Delta\alpha\,\vec{E}_0 \left[\cos(\omega_i + \Phi)t + \cos(\omega_i - \Phi)t\right] \\
&= (\alpha_0\,\vec{E}_0\,e^{-iw_i t} + \alpha_0\,\vec{E}_0^*\,e^{iw_i t}) + (\alpha_1\,\vec{E}_0^*\,e^{i(\omega_i+\omega_0)t} + \alpha_1^*\,\vec{E}_0^*\,e^{i(\omega_i+\omega_0)t}) \\
&+ (\alpha_1\,\vec{E}_0^*\,e^{i(\omega_i-\omega_0)t} + \alpha_1^*\,\vec{E}_0^*\,e^{i(\omega_i-\omega_0)t})
\end{aligned} \tag{2.37}$$

$$\tag{2.38}$$

The physical meaning for the first item in the polynomials (2.37 and 2.38) is coherent Rayleigh scattering ($\omega_s = \omega_i$). The second item means anti-Stokes Raman scattering ($\omega_s = \omega_i + \omega_0$), and the last part is described by Stokes Raman shift lines ($\omega_s = \omega_i - \omega_0$).

The Poynting vector of a radiation from an electric dipole moment can be defined as

$$\left|\vec{S}_{scattered}\right| = \frac{\omega_s^4 n_s}{(4\pi)^2 \varepsilon_0 R^2 c^3}\left|\varepsilon_s \cdot P_s(t)\right|^2 = \frac{\omega_s^4 n_s}{(4\pi)^2 \varepsilon_0 R^2 c^3}\left|\varepsilon_s \cdot \alpha(t)\cdot \vec{E}(t)\right|^2 \tag{2.39}$$

Generally, the measured scattering intensities of Raman spectra are proportional to the

scattering cross-section and can be written by

$$\left[\frac{d\sigma}{d\Omega}\right]_{energy} = \frac{R^2 \left|\vec{S}_{scattered}\right|}{\left|\vec{S}_{incident}\right|} = \frac{\omega_s^4 n_s \left|\varepsilon_s \, \vec{P}(t)\right|^2}{(4\pi)^2 \varepsilon_0 c^3 \cdot c\varepsilon_0 n_i \left|\vec{E}_0\right|^2} = \frac{\omega_s^4}{(4\pi\varepsilon_0)^2 c^4}\left(\frac{n_s}{n_i}\right)\left|\varepsilon_s \alpha(t)\varepsilon_i\right|^2$$

(2.40)

and

$$\left[\frac{d\sigma}{d\Omega}\right]_{photon} = \left[\frac{d\sigma}{d\Omega}\right]_{energy}\left(\frac{\omega_i}{\omega_s}\right)$$
(2.41)

where ε_i is the direction of polarization for incident wave and ε_s is the direction of polarization for a scattered wave. An important part $\left|\varepsilon_s \alpha(t)\varepsilon_i\right|$ from scattering cross-section equation, called Raman response or selection rule, has been applied to verify the symmetric types of vibration modes and distinguish from infrared (IR) spectroscopy.
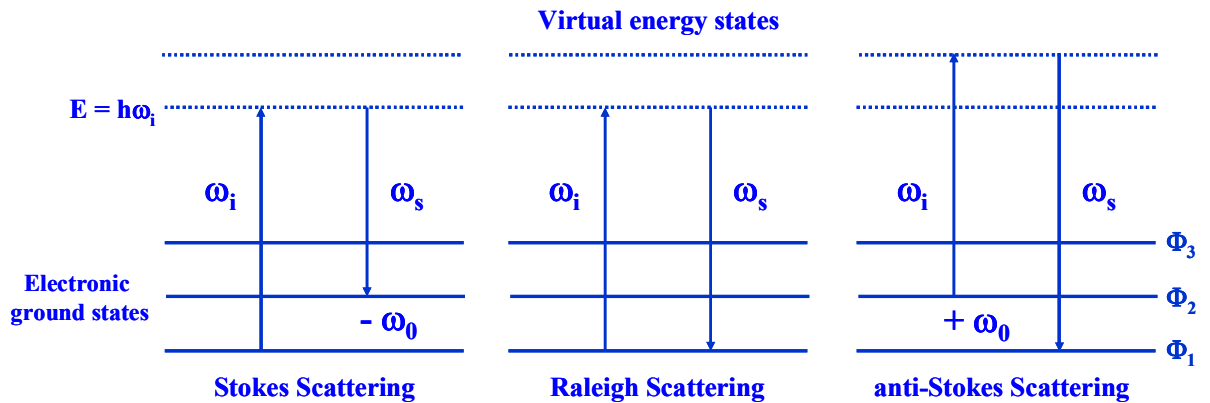
Figure 2.16 The schematic of energy transition for Rayleigh Scattering (middle), Stokes scattering (left) and anti-Stokes scattering (right).

2.6 Physical Adsorption (Physisorption)

2.6.1 Principles of Physisorption and Adsorption Isotherms

Physical adsorption of a gas on a solid can be described as an enrichment of molecules at the interface between the solid surface and the gas phase due to a combination of van der Waals attractions and short range repulsion between the adsorbent and the adsorbing molecules. The minimum on the potential energy curve occurs at approximately one molecular radius from the solid surface. The attractive interaction originates from the fluctuations of the charge distribution in the gas molecules and the atoms on the surface, resulting in weak bonding of hydrogen to the solid surface through either dipole/ induced-dipole or induced-dipole/ induced-dipole interactions as shown in Figure 2.17.
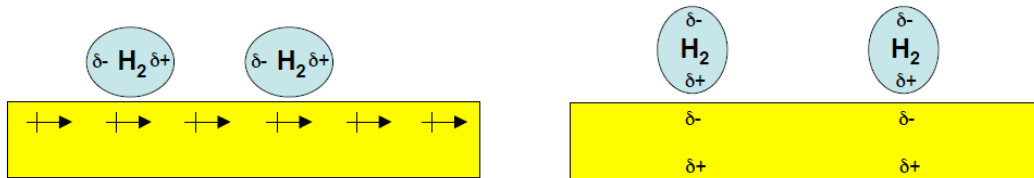
Figure 2.17 Illustration of the induced attraction between gas molecules and a solid surface.

With decreasing the distance between the gas molecules and the solid surface results in repulsion rapidly increasing due to the overlap of the electron clouds from the adsorbent atoms with the adsorbate molecules. The potential curve for this physisorption phenomenon is the well described by the Lennard-Jones potential[41], as shown in Figure 2.18. Although the magnitude of this physical interaction is related to the nature of the gas molecule and adsorbent material, for the hydrogen it is typically in the range of

4-10kJ/ mole. Figure 2.18 presents the potential energy curves of a hydrogen molecule as a function of the distance from the adsorbent surface for chemisorption with dissociative ion status, and physisorption for molecular status. There is no activated energy barrier for physisorption to hinder the molecules from approaching the surface which is present in the case chemisorption.
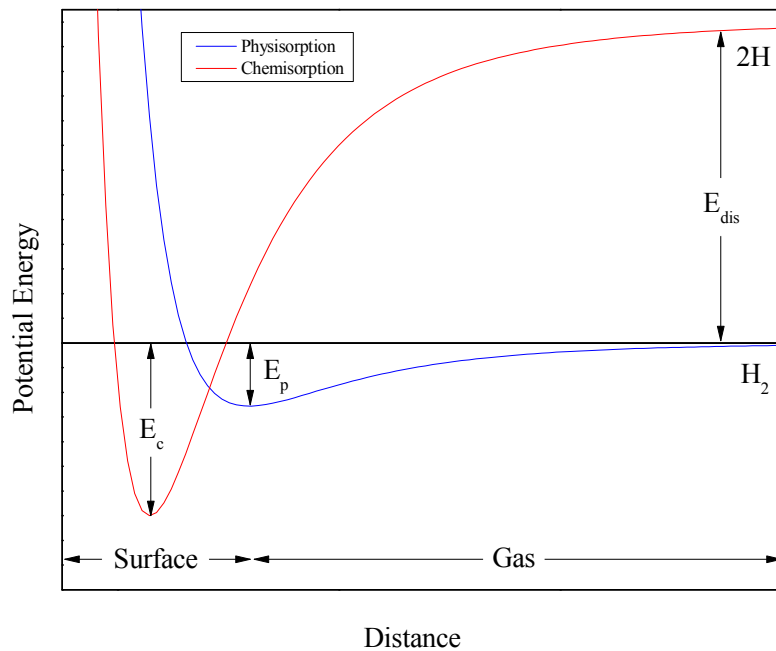
Figure 2.18 The potential energy curve for a hydrogen molecule as a function of distance from the adsorbent surface.

Figure 2.19 shows six different classes of isotherm curves for physical adsorption presented by the IUPAC (International Union of Pure and Applied Chemistry) in 1985[42]. Microporous materials possess type I adsorption isotherm behavior, which follows an initial linear increase, corresponding to progressive filling of the micropore volume, then

reaches the saturated plateau at higher pressures, corresponding to a monolayer coverage of the surface. This is evidence that high specific surface area is preferred to obtain a high hydrogen storage capacity, but not essential for physisorption at some pressure ranges.
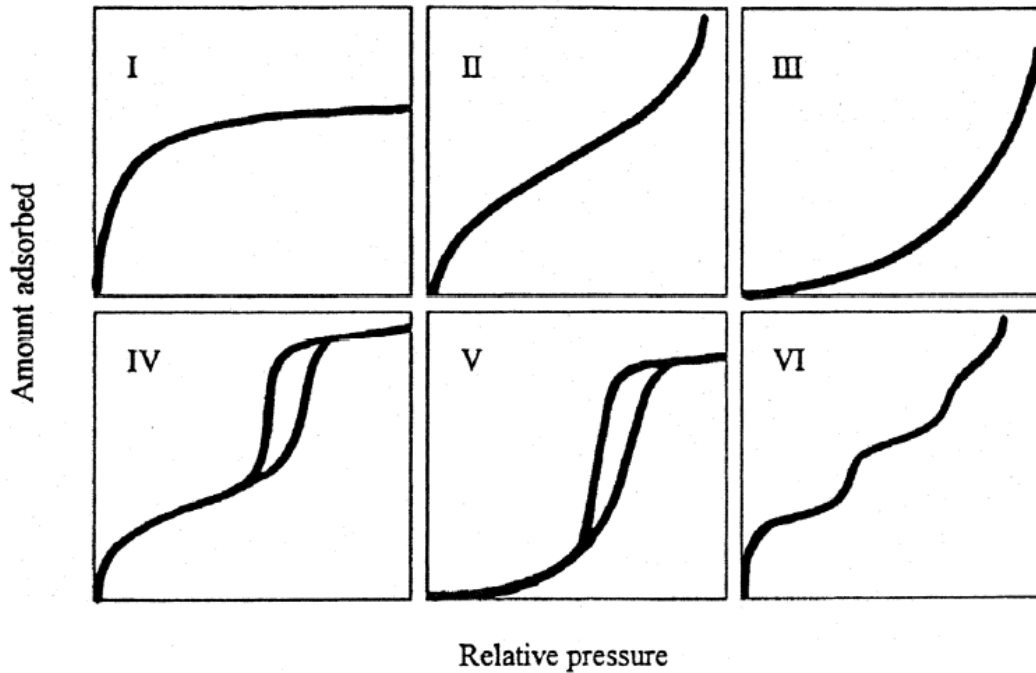
Figure 2.19 Six different classes of isotherm curves for physical adsorption as classified by IUPAC.

2.6.2 The Brief Theory Review for Physisorption

The Langmuir model has been applied to describe the type I isotherm behaviors which assumes that the adsorption enthalpy is independent of the coverage of the surface[43]. This model yields the Langmuir equation (2.42) relating to the coverage, θ, and the applied gas pressure P:

$$\theta = \frac{a \cdot \dfrac{P}{P^0}}{1 + a \cdot \dfrac{P}{P^0}}$$

(2.42)

where P^0 is the standard pressure when the temperature is above the critical temperature of the adsorbate. Otherwise, P^0 will be the saturation pressure in this equation. The surface coverage, θ, can be recognized as the ratio between the adsorbed gas at pressure P and the maximum adsorption amount at full monolayer coverage. The adsorption coefficient, a, is a function of the heat of adsorption, Ea and the temperature, T, and can be expressed as

$$a = K \cdot \exp\left(\frac{E_a}{RT}\right)$$

(2.43)

The initial linear slope in the type I isotherm curve demonstrates the strong interaction (adsorption heat) between the gas and host material at low pressure. The curve approaches a saturation plateau at high pressures where the hydrogen storage capacity is constant and independent of the interaction energy, indicating complete monolayer coverage of the adsorbent surface. The fraction of coverage in Langmuir equation can also be described by equation (2.44).

$$\theta = \frac{1}{1 + \left(\dfrac{\varepsilon - \mu}{RT}\right)}$$

(2.44)

Then equation can be rewritten as

$$\varepsilon = RT \ln\left(\frac{1}{\theta} - 1\right) + \mu$$

(2.45)

where μ is the chemical potential of the gas and ε is the adsorption potential.

For an ideal gas, the chemical potential can be written as an expression of the standard chemical potential, μ^0, at the measured temperature and pressure as shown in equation

(2.46).

$$\mu = \mu^0 + RT \ln\left(\frac{P}{P^0}\right) \tag{2.46}$$

where P^0 corresponds to the standard pressure. The chemical potential as a function of $\ln(P/P^0)$ can be calculated from the enthalpy and the entropy of the gas. An expression for the adsorption potential can be obtained by a combination of equation (2.42), (2.45) and (2.46).

$$\varepsilon = \mu^0 - RT \ln a \tag{2.47}$$

This equation demonstrates that the adsorption energy is independent of the surface coverage in the Langmuir model because it assumes no lateral interaction between each adsorbed molecule. The adsorption enthalpy is also independent of the number of gas molecules adsorbed on the surface. These adsorbed molecules behave like a 2-D ideal gas at low pressures, and can be described by Henry's law as

$$\theta = k' \cdot \left(\frac{P}{P^0}\right) \tag{2.48}$$

where k' is a function of the potential energy of adsorption ϕ and is given by

$$k' = \frac{v_p}{RT}\left[\exp\left(-\frac{\phi}{kT}\right) - 1\right] \tag{2.49}$$

where v_p is the pore volume, T the temperature and k the Boltzmann constant.

Another common isotherm behavior observed in physical adsorption is the type II isotherm, which is typically present for multi-layers of adsorbed molecules at high pressure. As shown in Figure 2.19, the inflection point B indicates the completion of the first monolayer. The Brunauer-Emmett-Teller (BET) theory was modified from the Langmuir model for multilayer adsorption to explain the type II isotherm[44]. BET theory assumes that the adsorption energy of the second and higher layers is equal to the liquefaction energy of the adsorbed molecules. The BET equation is often expressed as:

$$\frac{P}{n \cdot (P^0 - P)} = \frac{1}{n_m C} + \frac{C-1}{n_m C} \cdot \frac{P}{P^0} \qquad (2.50)$$

where n is the number of adsorbed molecules, n_m the monolayer capacity, P^0 is the pressure at saturation and the constant C is related to the difference between adsorption energy of the first layer and the liquefaction energy of the adsorbate. The BET model does not precisely describe the behavior of a physisorption system[45], but the model is still widely used to determine the specific surface area (S.S.A.) for porous materials by nitrogen adsorption isotherms at 77 K.

2.6.3 Hydrogen Storage Capacity

The adsorption amount of gas, n_{ads}, in a porous material is defined as the gas quantity in a unit volume of sample, n_i, minus the portion of free molecules in the gas phase.

$$n_{ads} = n_i - V_g \rho_g \qquad (2.51)$$

where V_g is the volume occupied by the gas, including the pore volume of the sample, and ρ_g is its density. Since the real volume of gas phase is unknown, experimental adsorption isotherms typically report the excess uptake, n_{ex}, which is defined in equation (2.51).

$$n_{ex} = n_i - V_0 \rho_g \qquad (2.52)$$

where V_0 is the void volume including the pore volume of the sample which generally can be measured by He gas expansion[46]. Therefore, the relation between excess uptake and absolute uptake is described as

$$n_{ex} = n_{ads} + \rho_g (V_g - V_0) \qquad (2.53)$$

The difference $(V_g - V_0)$, corresponds to the volume occupied by the adsorbed phase with

density ρ_a, in the cavities of the adsorbent and leads to the following expression for the excess uptake

$$n_{ex} = \left(1 - \frac{\rho_g}{\rho_a}\right) \cdot n_{ads} \qquad (2.54)$$

The definition and difference between the absolute and excess uptake via gas physisorption has been exhibited in Figure 2.20.
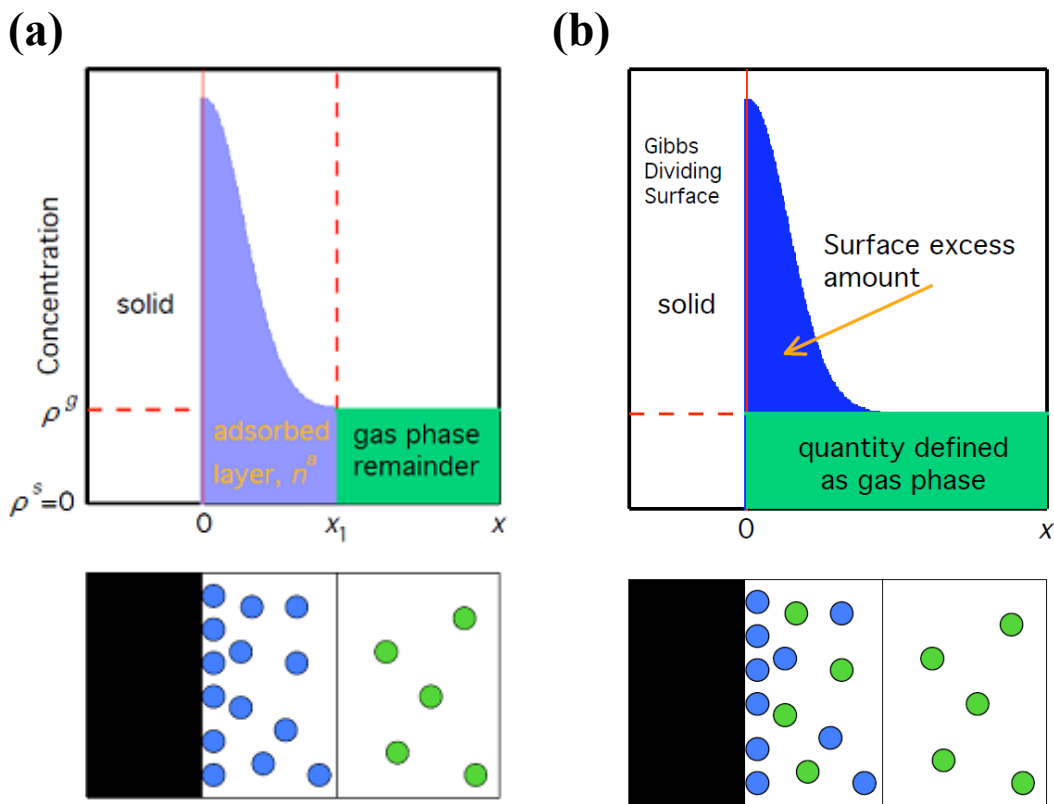
Figure 2.20 Illustrations of the definition and difference between the (a) absolute and (b) excess uptake via gas physisorption.

However, if observed the adsorption behavior from macroscopic aspect by type I isotherm curves from Figure 2.21, the absolute adsorption capacity, n_{ads} exhibits a

constant value of saturation at high pressure range. Comparatively, the excess adsorption

isotherm reaches a maximum then decreases at high gas density region. Typically, the

inflection of the excess adsorption isotherm is observed only at very high pressures.
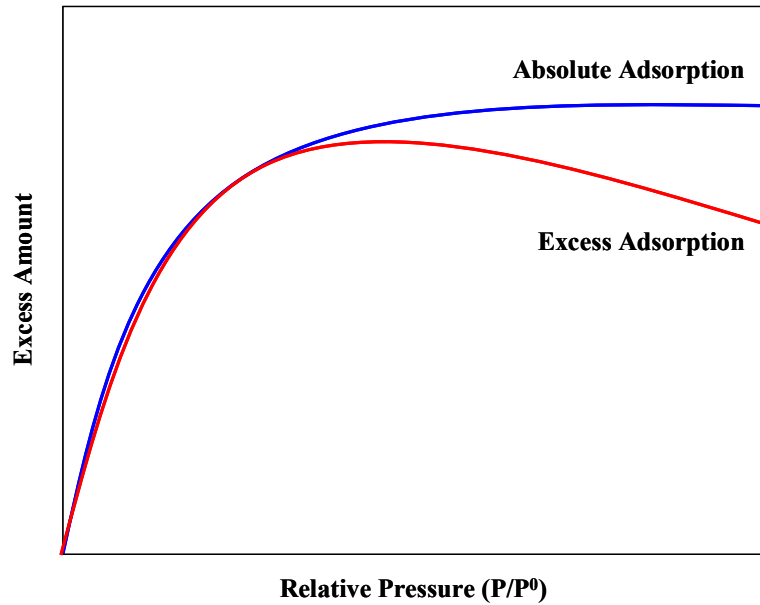
Figure 2.21 Illustration of the definition and difference between the absolute and excess

adsorptions via gas isotherm curves.

The common methods to evaluate the hydrogen storage capacity are the weight percent

(wt%) storage and the volumetric storage (vol). The weight percent storage is defined as

$$wt\% = \frac{m_{H_2}}{m_{H_2} + m_s} \times 100\% \tag{2.55}$$

where m_{H_2} is the mass of adsorbed hydrogen and m_s is the mass of the adsorbent.

The volumetric uptake is defined as

$$vol = \frac{m_{H_2}}{V_s} = \frac{m_{H_2}}{m_s}\rho_s \qquad\qquad (2.56)$$

where ρ_s is the packing density determined by the mass of the sample and its occupied volume when mechanical compression is present. In some cases the packing density of the material has been applied to calculate the volumetric uptake.

2.7 References

(1) Bravais, A. M. A. *Journal de l'Ecole polytechnique, Paris* **1850**.

(2) Reidel, D. *International tables for crystallography, Vol. A, Space group symmetry* **1983**

(3) Blakemore, J. S. *Solid State Physics* 2 ed., Cambridge: Cambridge University Press, **1969**.

(4) Rudden, M. N. and Wilson, J. *Elements of Solid State Physics* John Wiley and Sons Inc., **1993**.

(5) Suryanayana, C. and M. Grant *Norton X-ray Diffraction Plenum Press,* **1998**.

(6) Young, R. A. *The Rietveld Method. IUCr Monographs on Crystallography Oxford* 1 ed, vol. 5, 298, Oxford Science Publications, **1993**.

(7) *http://pubs.usgs.gov/of/2001/of01-041/htmldocs/xrpd.htm*.

(8)*http://www.nmai.si.edu/subpage.cfm?subpage=collections&second=conserv&third=pest_id*.

(9) West, A. R. *Basic Solid State Chemistry. 1997, Chichester: J. Wiley and Sons.*

(10) *http://www.esrf.eu/AboutUs/GuidedTour*.

(11) *Figure courtesy of Dr. Efrain Rodriguez at the NIST*.

(12) H. M. Rietveld *J. Appl. Cryst.* **1969**, 65.

(13) Larson, A. C. and Von Dreele, R. B. *GSAS, 1990, Los Alamos National Laboratory: Los Alamos, California.*

(14) Oszlányi, G. and Sütő, A. *Acta Cryst.* **2008**, *A*, 123.

(15) Oszlányi, G. and Sütő, A. *Acta Cryst.* **2005**, *A*, 147.

(16) Oszlányi, G. and Sütő, A. *Acta Cryst.* **2004**, *A*, 134.

(17) Dumas, C. and van der Lee, A. *Acta Cryst.* **2008**, *D*, 864.

(18) Wu, J. S.; Leinenweber, K.; Spence J. C. H. and O'keeffe, M. *Nat. Mater.* **2006**, *5*, 647.

(19) Zhou, Z. and Harris, K. D. M. *J. Phys. Chem. A* **2008**, *112*, 4863.

(20) Palatinus, L. *Acta Cryst.* **2004**, *A*, 604.

(21) Coelho, A. A. *Acta Cryst.* **2007**, *A*, 400.

(22) Palatinus, L. and Chapuis, G. *J. Appl. Crystallogr.* **2007**, 786.

(23) Yashima, M. and Tsunekawa, S. *Acta Cryst.* **2006**, *B*, 161.

(24) Yamamoto, K.; Takahashi, Y.; Ohshima, K.; Okamura, F. P. and Yukino, K. *Acta Cryst.* **1996**, *A*, 606.

(25) Takata, M. and Sakata, M. *Acta Cryst.* **1996**, *A*, 287.

(26) Takata, M. *Acta Cryst.* **2008**, *A*, 232.

(27) Takata, M.; Umeda, B.; Nishibori, E.; Sakata, M.; Saito, Y.; Ohno, M. and Shinohara, H. *Nature* **1995**, 46.

(28) Sakata, M.; Mori, R.; Kumazawza, S.; Takata, M. and Toraya, H. *J. Appl. Cryst.* **1990**, 526.

(29) Dinnebier, R. E.; Vensky, S.; Jansen, M. and Hanson, J. C. *Chem. Eur. J.* **2005**, 1119.

(30) de Vries, R. Y.; Briels, W. J. and Feil, D. *Phys. Rev. Lett.* **1996**, 1719.

(31) Le Bail, A.; Duroy, H. and Fourquet, J. L. *Mater. Res. Bull.* **1988**, *23*, 447.

(32) Samy, A.; Dinnebier, R. E.; van Smaalenb, S. and Jansen, M. *Acta Cryst.* **2010**, *B*, 184.

(33) Blundell, S. J. *Magnetism in condensed matter. Oxford master series in condensed matter physics.* Oxford University Press, **2001**.

(34) Cox, P. A. *The Electronic Structure and Chemistry of Solids* 1 ed., 259, Oxford Science Publications, Oxford University Press, **1993**.

(35) Harrison, W. A. *Electronic structure and the properties of solids* 1 ed., 586, New York, Dover Publications Inc., **1989**.

(36) Raman, C. V. and Krishan, K. S. *Nature* **1928**, *121*, 501.

(37) Turrell, G. and Corset, J. *Raman Microscopy: Developments and Applications*, eds., Elsevier Academic Press, **1996**.

(38) Ferraro, J. R.; Nakamoto, K. and Brown, C. W. *Introductory Raman Spectroscopy*, Academic Press, **2003**.

(39) McCreery, R. L. *Raman Spectroscopy for Chemical Analysis,* Wiley Interscience, **2000**.

(40) Lewis, I. R. and Edwards, H. G. M. *Handbook of Raman Spectroscopy*, eds. Marcel Dekker, **2001**.

(41) Rouquerol, F.; Rouquerol, J. and Sing, K. *Adsorption by Powders and Porous Solids*, Academic Press, San Diego, London, Boston, New York, Sidney, Tokyo, Toronto,**1999**.

(42) Reccommendations, IUPAC *Pure Appl. Chem.* **1985**, *57*, 603.

(43) Langmuir, I. *J. Am. Chem. Soc.* **1916**, *22*, 2221.

(44) Brunauer, S.; Emmett, P. H. and Teller, E. *J. Am. Chem. Soc.* **1938**, *60*, 309.

(45) González, M. T.; Sepúlveda-Escribano, A.; Molina-Sabio, M. and Rodríguez-Reinoso, F. *Langmuir* **1995**, *11*, 2151.

(46) Myers, A. L. and Monson, P. A. *Langmuir* **2002**, *18*, 10261.

Chapter 3: Experimental Section

3.1 Thermogravimetric Analysis (TGA)

TGA experiments were performed under N_2 atmosphere at 1atm with a heating rate of 2-10°C/min on a TA Instruments Q500 TGA.

3.2 Single Crystal X-ray Crystallographic Analysis

Suitable single crystals of appropriate size for X-ray structural analysis were cut and identified using optical microscopy. The X-ray intensity data can be measured at different temperatures from liquid nitrogen temperature (77K) to 400K on a three-circle diffractometer system equipped with Bruker Smart Apex II CCD area detector using a graphite monochromator and a MoK$_\alpha$ fine-focus sealed tube (λ= 0.71073Å). The detector position is adjustable at a distance range of 4-15cm from the crystal. The specimen is detected and analyzed by rotating along three azimuthal angles θ, ω and φ, and a sphere or hemisphere of data are obtained by using an incremental scan method. In general, frames are collected in 0.1° to 0.3° increments. For highly symmetric materials, collection can be constrained symmetrically to reduce the collection time. Data is typically collected between 2° and 60° 2θ for molybdenum radiation. A complete data collection may require time between 6-24 hours, depending on the sample quality and the operating condition of diffractometer. Exposure times of 10-30 seconds per frame for a hemisphere of data will require total run times about 6-30 hours. The structures were solved and refined using the SHELXS-97 (Sheldrick, 1990) and SHELXL-97 (Sheldrick, 1997) software. All hydrogen atoms were fixed at calculated positions and refined by using riding mode.

3.3 Low Pressure H_2, N_2, and CO_2 Adsorption Isotherm Measurements

Low pressure gas adsorption isotherm experiments from 0 to 1atm were performed by using Quantachrome Instruments Autosorb-1-C surface area and pore size analyzer. The dehydrated sample was ground using an agate mortar and pestle; then loaded in a quartz tubes which were covered by a well-sealed lid within a helium-filled glovebox equipped with water and oxygen monitors. The sample (at least 100mg for the better accuracy of measurement), gas-lines and regulators were automatically flushed and pumped to 10^{-3}torr about 10 times by Autosorb-1-C machine before measurement. A 1-minute leakage check was carried out to certify the connection between the quartz tube (with sample) and instrument. Ultra high purity gases (UHP level) were used for each experiment. The temperature was maintained at 77K by liquid nitrogen bath for H_2 and N_2 measurement and at 273.15K by ice-water bath for CO_2 measurement.

3.4 Powder X-ray Diffraction and Raman Spectroscopy at European Synchrotron and Radiation Facility (ESRF), Grenoble, France

A series of *in-situ* synchrotron powder diffraction (PXRD) experiments were carried out on station BM1A of Swiss-Norwegian beamline (SNBL) at ESRF. The beamline is installed on a bending magnet source (dipole BM 1) and monochromatized by Si (111) double crystals. An Rh-coated collimating mirror is placed before the monochromator crystals, and the reflection of incident beam from this mirror is highly parallel, enabling both high brightness and narrow energy resolution to be achieved. Another mirror after the monochromator provides vertical focusing at the sample (Figure 3.1). The size of the collimated beam is nominally 0.5×0.5mm^2 FWHM and available spectral range between

6 to 22(30)keV. A multi-purpose diffractometer (KUMA KM6-CH) system is installed for single-crystal and polycrystal samples, with an adjustable image-plate area detector (MAR345) that is available for macromolecular crystallography work. A He cryostat (4-350K) or furnace (room temperature-1000°C) are available for use.
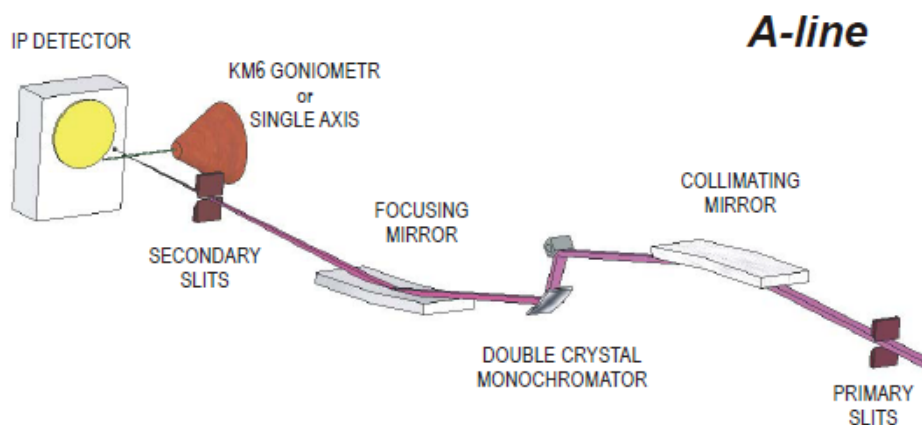
Figure 3.1 Schematic layout of the SNBL BM1A optics[1].

In order to realize the dynamic behaviors (ex. rotations or vibrations) of atoms in solid-state materials, especially for the simultaneous measurements, the combination of synchrotron and Raman spectrometer which has been equipped on station BM1A becomes a powerful tool to offer valuable information in different length scales. The BM1A station supports high pressure gas loading experiments during the real-time measurements. MOF powders of around 10mg were fine ground and loaded in glass or quartz capillaries with 0.3, 0.5 and 0.7mm diameters; then mounted on the goniometer head. The sample can be aligned and centered in the synchrotron beam path by viewing the position under an attached video camera and adjusting the X, Y and Z directions. The

measurements were performed over the angular range about $1.4^o \leq 2\theta \leq 41^o$ with a step size of ca. 0.031^o. A combination of in-situ synchrotron powder X-ray and Raman spectroscopy has been applied to analyze MOF materials. The devices are shown in Figure 3.2.
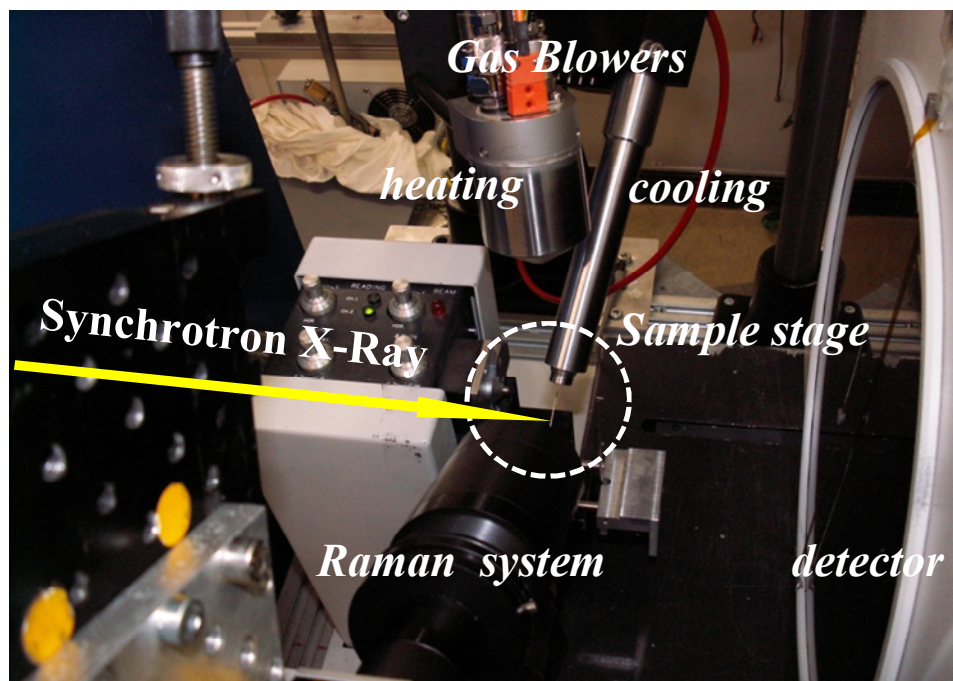
Figure 3.2 Illustration for the device set-up at the SNBL BM1A station.

3.5 X-ray Powder Diffraction Experiments

The laboratory-based diffractometer: Rigaku Ultima III has been used and operated in Bragg-Bretano geometry with Cu $K_{\alpha1}$ radiation (λ =1.54059Å). The fine-ground powder samples were either uniformly spread on a glass holder with a recess or loaded in quartz or glass capillaries with different diameters (0.3, 0.5, 0.7 and 1.0mm). A capillary spinner can be used to avoid preferred orientation of materials if necessary. Measurements were

performed for two major purposes: (1) quick scans to evaluate the purity of sample, and (2) longer scans to ascertain the structural variation of materials before and after re-adsorption. The shorter measurements were taken over the angular range $5^{o} \leq 2\theta \leq 60^{o}$ with a 2θ step size of 0.5^{o} and a counting time of 1 or 2 seconds. Longer scans were measured in the same angular range with a 2θ step size of 0.25^{o} and a counting time of between 5 and 10 seconds. The diffractometer was controlled by use of the Rigaku D/MAX2200 Right System software package.

3.6 Neutron Powder Diffraction Experiments

Neutron powder diffraction data were obtained from the High Resolution Neutron Powder Diffractometer BT-1 in NIST Center for Neutron Research (NCNR). The reactor operates using uranium as fuel elements producing a continuous $4 \times 10^{14} cm^{-2} s^{-1}$ thermal neutron flux at a rated power of 20 MW. There are three different monochromators: Ge(311), Cu(311) or Ge(733), with either 15' or 7' collimation that can be selected. The take off angles are 120°, 90° and 75°, respectively. The maximum beam size is around 15mm width × 50mm height. There are 32 sets of He-3 detectors at 5° intervals with 13° scan range covering 2θ from 0° to 167° (Figure 3.3). The properties of the different monochromators are organized in Table 3.1, and the relative resolution (full-width at half-maximum (FWHM), measured in degrees) is plotted in Figure 3.4.
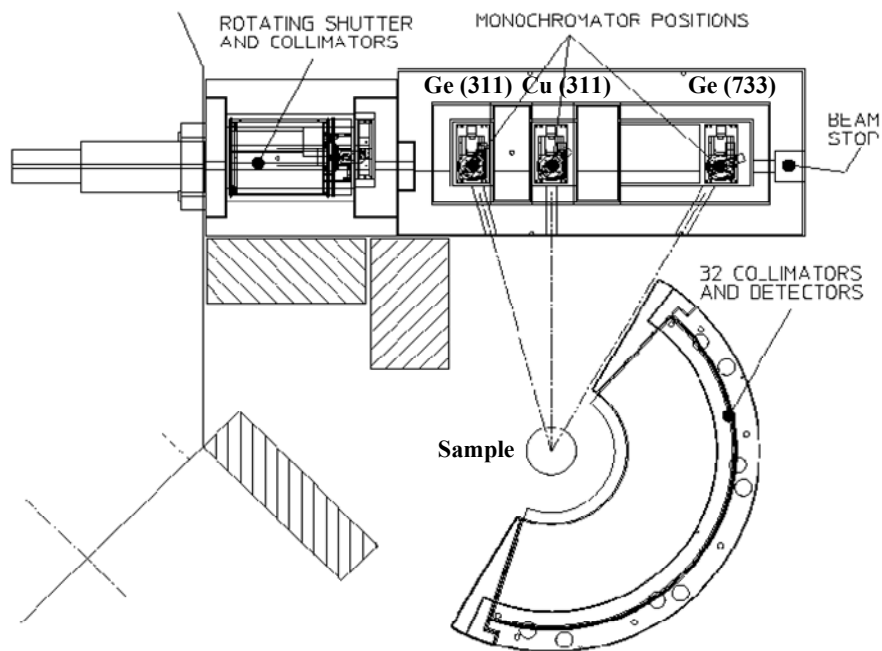
Figure 3.3 Schematic of the BT1 diffractometer, NIST Center for Neutron Research (NCNR)[2].

Monochromator	in-pile Collimation (arcmin)	Monochr. 2 Theta	Relative Bragg Intensities	Flux $(n\ s^{-1}cm^{-2})$	Wavelength (Å)
Ge(311)	15'	75°	2.69	400,000	2.079
Ge(311)	7'	75°	1.50	200,000	2.079
Cu(311)	15'	90°	1.00	400,000	1.540
Cu(311)	7'	90°	0.59	200,000	1.540
Ge(733)	15'	120°	0.24	200,000	1.197
Ge(733)	7'	120°	0.16	100,000	1.197

Table 3.1 The information for different monochromators of BT1 diffractometer[3].
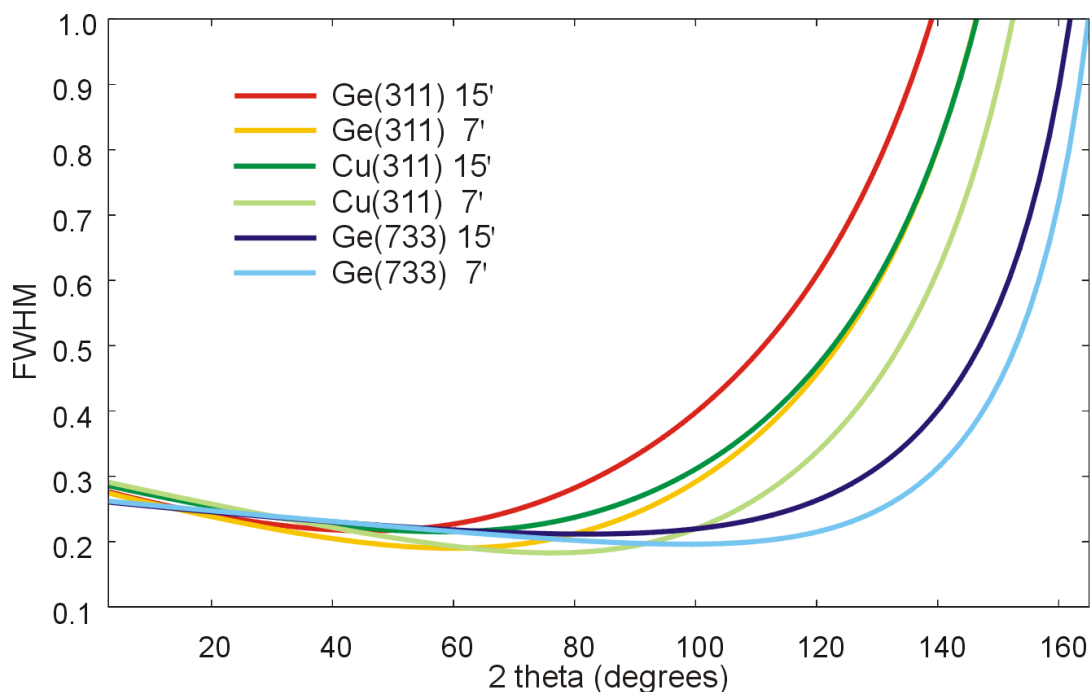
Figure 3.4 Resolution as FWHM (^{o}) as a function of 2θ (^{o}), for BT-1 using each of the three monochromators and either 7' or 15' collimation. All monochromators gives data covering the full range of the instrument, 1.3-165° in $2\theta^4$.

3.6.1 Neutron Diffraction for Deuterium (D$_2$) Loading Experiments

The dehydrated MOF materials (ca. 1g) were prepared under high vacuum for neutron diffraction of D$_2$ loading experiments. The degassed powders were placed in vanadium A-type can (6.0mm inner diameter and 1.5c.c. volume) and in the golvebox, then connected with a capillary gas-line and a packless valve and sealed with an indium O-ring. The sample can was fixed on the sample stick equipped with a stainless gas-line and an extra needle valve for the top-loading closed cycle refrigerator (TLCCR) as shown in Figure 3.5. Before starting the experiment, the sample was cooled down to 4K in advance and kept pumping overnight until high vacuum (10^{-6} to 10^{-7}torr) was obtained.

During this experiment, a known amount of D_2 was loaded into sample depending on the molar fraction between gas molecules and lanthanide ion (e.g. holmium Ho^{3+} in this thesis) such as bare sample, 1 : 1, 2 : 1, 3 : 1 and 4 : 1. These ratio numbers can be verified after the Rietveld Refinement for each case. The loading gas temperature was set at 65K, 55K, 45K and 35K respectively for each ratio and held 1 to 2 minutes until no pressure drop was observed. The slack time before the beginning of each experiment was 50 minutes to reach and stabilize the temperature at 4K. All the experiments were measured at 4K for 2 hours. A set of experiments with different molar ratios would take 8 to 10 hours based on 4 or 5 cycle runs. The neutron scattering pattern of a bare sample without any D_2 loading was first measured and analyzed by Rietveld refinement with the GSAS program. This was the basic model used for the refinement of subsequently collected data. Deuterium molecules are recognized as point scatters with double occupancy since they are expected to be spherically averaged at ground state. The parameters such as coordinates for all atoms, thermal factor (Debye-Waller factor) were available to adjust during the refinement of each deuterium loading experiment. The difference Fourier map for ordinal patterns was calculated and clearly indicated the deuterium adsorption positions. Each Fourier difference map for previous gas loading pattern served as the basis for each successive one and introduced new deuterium adsorption sites from the Rietveld calculation.

3.6.2 Neutron Diffraction for Deuterated Methane (CD_4) Loading Experiments

The process of neutron diffraction measurement for deuterated methane (CD_4) is similar to that for deuterium. A known amount of CD_4 was loaded into sample depending on the desired molar fraction between gas molecules and holmium ion (Ho^{3+}) such as

bare sample, 0.8 : 1 and 1.6 : 1. The loading gas temperature was set at 140K and 120K respectively for each ratio. All the experiments were measured at 4K for 2 hours to collect each cycle data.
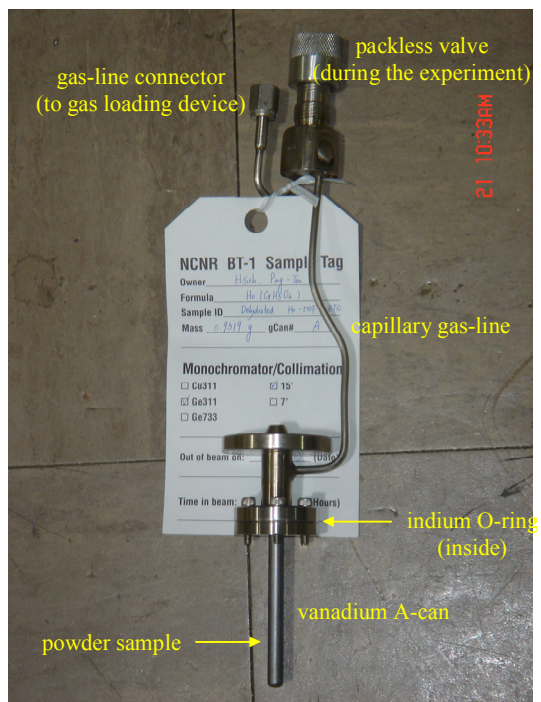
Figure 3.5 Illustration of the sample holder for gas loading experiments via neutron diffraction.

3.7 Magnetic Experiments

In this dissertation, all the magnetic data were performed on a Quantum Design MPMS SQUID (Superconducting Quantum Interference Device). The DC magnetic susceptibility measurements were typically performed in the temperature range of 4-300K, with a step size of 2K below 20K, 10K to 100K then a step size of 25K to 300K. Furthermore, the Zero Field Cooled (ZFC), and Field Cooled (FC) magnetic

susceptibility at 100Oe were investigated over the temperature range of 4-30K, and the susceptibility hysteresis experiments were done at 4K by measuring the variation of magnetization with different applied magnetic field from -50000Oe to 50000Oe with a step size of 100Oe. Details of measurement conditions for each data set recorded will be described individually. For all of these magnetic experiments, approximately 10mg of sample crystals were prepared in a glovebox and loaded into a gelatine capsule, then sealed with another capsule lid to prevent the sample moving and to provide an averaged environment. The capsule was fixed on the holder stick on which the position has been precisely measured and marked. The magnetic data were then converted into the molar susceptibility χ_M (emu/ mol) using the Origin program.

3.8 Solid-State Fluorescence (FL) Experiments

All of the solid-state fluorescence measurements of materials have been performed using a Hitachi F-4500 Solid-State Fluorescence Spectrometer (Figure 3.6). UV/Vis spectroscopy was done in advance to assess the maximum UV absorption which is the maximum excitation wavelength in FL measurements. Two different types of experiments were done (i) Qualitative investigation: approximately 10mg of sample powder was weighed and examined for the full-range characteristic emission spectra of 350(400)-700nm, and (ii) Quantitative study: 3mg sample powders was weighed and immersed in different solvents (solvent exchange) for days to determine the change in properties. Details of measurement conditions for each data set recorded will be described individually.
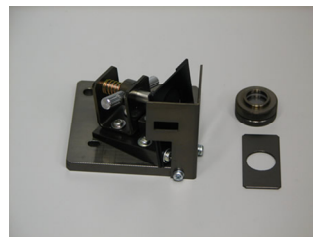
Solid State sample holder

Light track
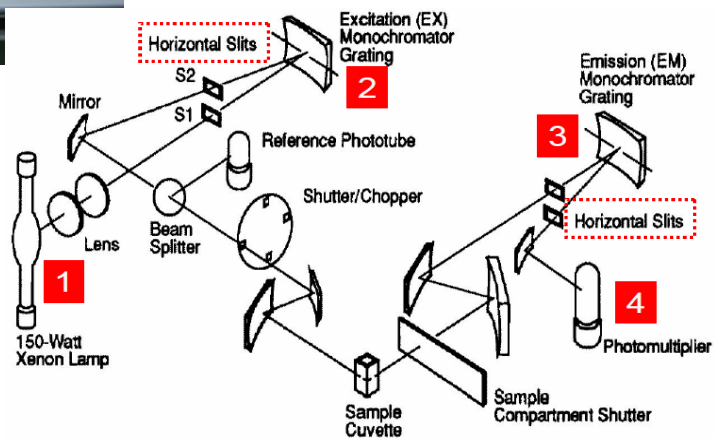
Figure 3.6 Illustration of Solid-State Fluorescence Spectrometer.

3.9 References

(1) http://www.esrf.eu/UsersAndScience/Experiments/CRG/BM01/bm01-a.

(2) http://www.ncnr.nist.gov/instruments/bt1/bt1_plan.html.

(3) Http://www.ncnr.nist.gov/instruments/bt1/bt1_spec.html.

(4) http://www.ncnr.nist.gov/instruments/bt1/bt1_for_xtal.html.

Chapter 4: Synthesis and Structural Determinations of some Metal-Organic Framework Materials

4.1 Introduction

In this dissertation, 22 metal-organic framework materials (MOFs) have been synthesized, and the crystal structures identified by single crystal X-ray diffractions. These 22 MOFs can be classified by the various ligands (carbon-based linkers) which are shown in Figure 4.1. The MOFs with shorter ligands (e.g. formic acid) will be discussed in chapter 8. The basic methodology to select ligands is dependent on their molecular geometry and functional groups such as carboxylic acid. Moreover, the rigid linkers were chosen to have aromatic rings to construct stable framework structures. Specifically, 1, 4-Benzenedicarboxylic acid (H_2BDC) is a one-dimensional (linear) ligand with two carboxylic groups which has been utilized as model system to design MOF materials. Other ligands are chosen to modify or improve the properties of the BDC MOFs. For example, 1, 3, 5-Benzene tricarboxylic acid (H_3BTC) has a two-dimensional (planer) molecular geometry with three divergent carboxylic acids which is designed to build a highly dimensional frameworks; 1, 3, 5-Tris(4-carboxyphenyl) benzene (H_3BTB) ligand offers a long molecular length to create a large scaffold; 3, 5-Pyridinedicarboxylic acid (H_2PDC) provides one different azaheterocyclic group which may affect the geometry of frameworks and 2, 6-Naphthalenedicarboxylic acid (H_2NDC) possesses more aromatic rings on the carbon-based linkage to modify and enhance the optical and adsorption properties of MOF samples.
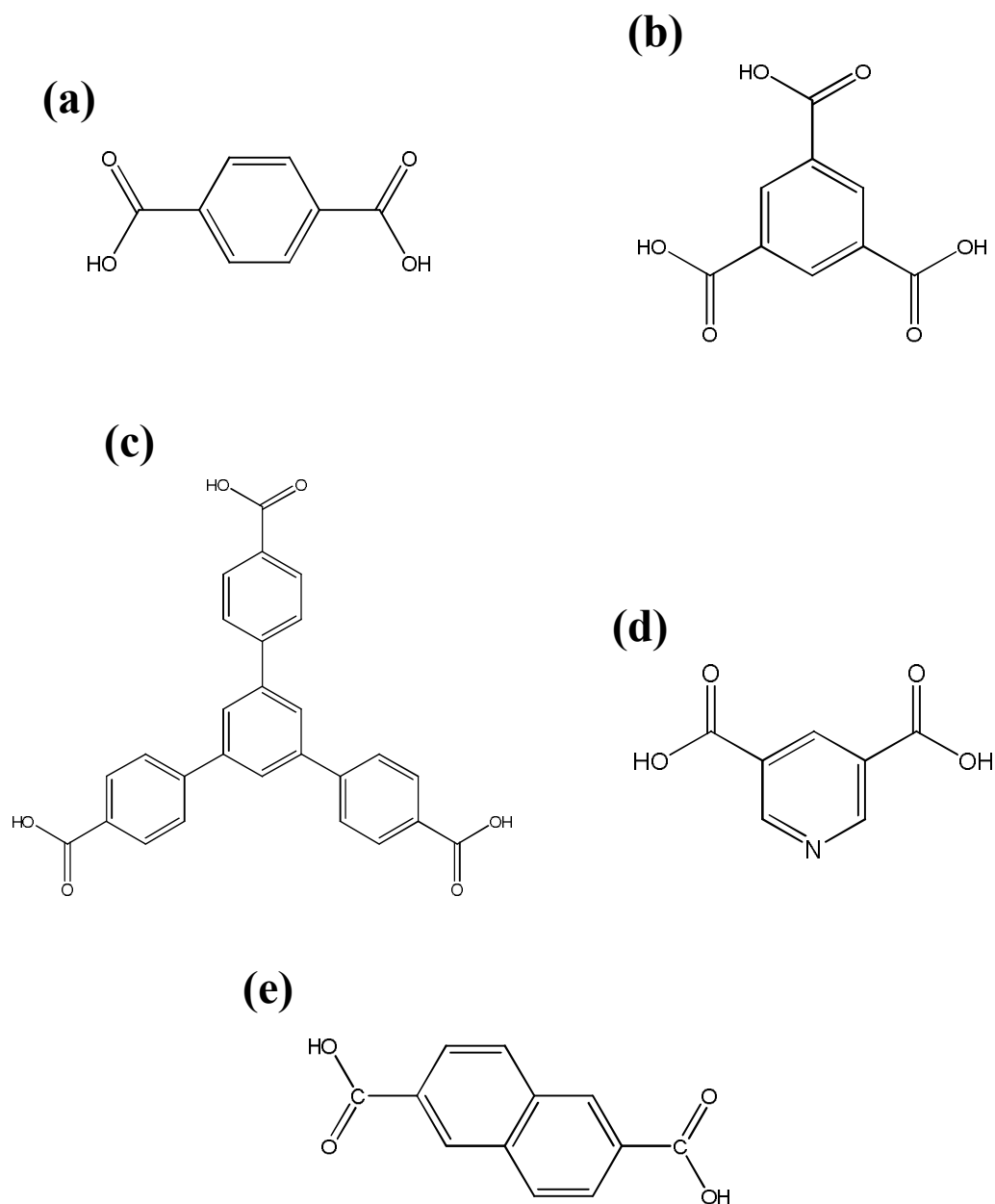
Figure 4.1 The ligands used in the MOF materials. (a) 1, 4-Benzenedicarboxylic acid (H$_2$BDC), (b) 1, 3, 5-Benzene tricarboxylic acid (H$_3$BTC) (c) 1, 3, 5-Tris(4-carboxyphenyl) benzene (H$_3$BTB), (d) 3, 5-Pyridinedicarboxylic acid (H$_2$PDC), (e) 2, 6-Naphthalenedicarboxylic acid (H$_2$NDC).

4.2 1, 4-Benzenedicarboxylic acid (H$_2$BDC) Ligand

All chemicals purchased from Aldrich were of reagent grade or better and were used without further purification.

4.2.1 Synthesis of Ln(C$_8$H$_4$O$_4$)·(C$_3$H$_7$NO)$_2$·NO$_3$ (Ln-MOF-BDC) System

A series of lanthanide complexes **(Ln: Y(1), Gd(2), Dy(3) and Ho(4))** have been synthesized by solvothermal reactions. Lanthanide nitrate (Ln(NO$_3$)$_3$·xH$_2$O) was mixed with 1, 4-Benzenedicarboxylic acid (H$_2$BDC) powder by 2 : 1 molar fraction, dissolved in 15 ml *N,N*-dimethylformamide (DMF), then placed in a 20ml Teflon-lined steel autoclave under autogenous pressure at 90°C for 3 days and then naturally cooled to room temperature. The crystals were washed with ethanol (~10ml) for three times and dried at room temperature (**1, 3**: colorless prism; **2**: colorless plate; **4**: pink prism).

4.2.2 Synthesis of (C$_{30}$H$_{28}$N$_2$O$_{15}$Ln$_2$)$_x$·C$_3$H$_7$NO (Ln-MOF-BDC) System

Two lanthanide complexes **(Ln: Ce(5), x=3 and Pr(6), x=1)** can be obtained by the same synthetic process which was described in section 3.1.1.1 showing different structures and chemical compositions (**5**: colorless prism; **6**: green prism).

4.2.3 Discussion of Structures with 1, 4-Benzene dicarboxylic acid (H$_2$BDC) Ligand

A series of lanthanide MOFs have been synthesized by solvothermal synthesis. Although identical synthesis parameters have been applied, the MOFs still exhibit different chemical formulas and can be classified into two major chemical types: **(1) Ln(C$_8$H$_4$O$_4$)·(C$_3$H$_7$NO)$_2$·NO$_3$**, where Ln = yttrium (Y), gadolinium (Gd), dysprosium (Dy), and holmium (Ho), and **(2) (C$_{30}$H$_{28}$N$_2$O$_{15}$Ln$_2$)$_x$·C$_3$H$_7$NO**, where Ln = cerium (Ce),

x = 3 and praseodymium (Pr), *x* = 1. The details of the measured parameters, structural information and refinement results are tabulated in Table 4.1. Specifically, for this Ln-MOF-BDC system, the framework is constructed of related 3-D networks with 1-D rhombic channels along the *c* axis in Y-MOF-BDC, Gd-MOF-BDC, Dy-MOF-BDC and Ho-MOF-BDC crystals, and along the *b* axis in Ce-MOF-BDC and Pr-MOF-BDC samples. Furthermore, high structural symmetry is present in family **(1)** (***C2/c*** and ***P1 21/c 1***) in contrast to the low symmetry of family **(2)** (***P1̄*** symmetry). The details of the 3-D configurations (Y-MOF-BDC against Pr-MOF-BDC for example) are plotted in Figure 4.2 for comparisons. These diagrams exhibit an obvious difference in the arrangement of DMF molecules that coordinate with the lanthanide metal ions. In the Y-MOF-BDC case, the chemically bonded DMF molecules on nearest yttrium atoms along the *b* axis are organized "head to head", whereas in the case of Pr-MOF-BDC system, they are aligned "shoulder to shoulder" and alternating along the *a* axis. This difference results in distinct channel sizes from ca. 6.6 × 2.6Å in Pr-MOF-BDC to ca. 6.4 × 3.3Å in Y-MOF-BDC (taking into account the van der Waals radii of the atoms). The eight coordinated oxygen molecules on the Pr ions contain (i) Six carboxyl groups from different benzoic-acid ligands, one terminal water and one DMF molecule, or (ii) Five carboxyl groups from the monodentated benzoic-acid ligands, one carboxyl group of bidentated ligand and one connected DMF molecule. The complicated bonding on the Pr ions and the distortion of BDC ligands within the framework results in a reduction of symmetry within family **(2)** to ***P1̄***, but also increases the volume of the unit cell which is almost three times larger than family **(1)**. In this dissertation, all the detailed information of the bonding angles and lengths for each crystal structure will be organized and presented in the appendix. Moreover, a comprehensive study on the framework structure

and properties for family **(1)** (Ho-MOF-BDC as an example) will be discussed in chapter 7.

(a)
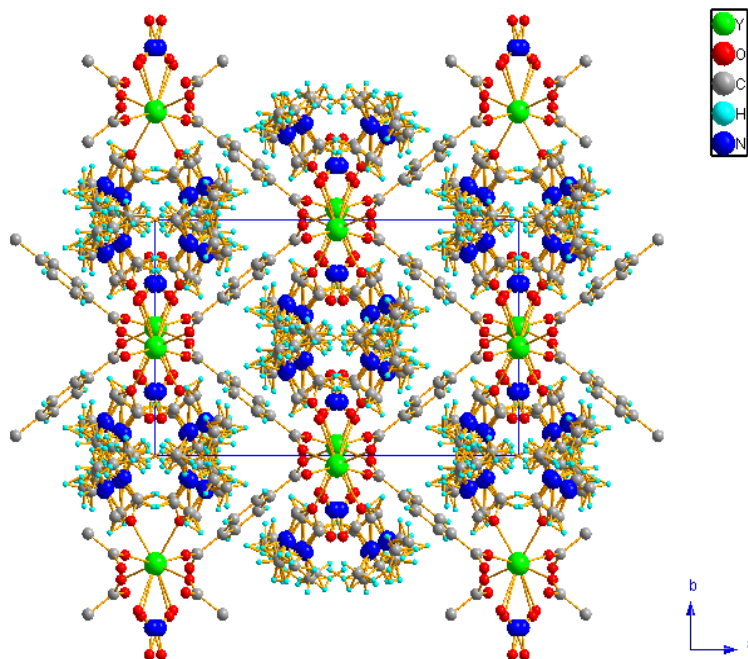
(b)
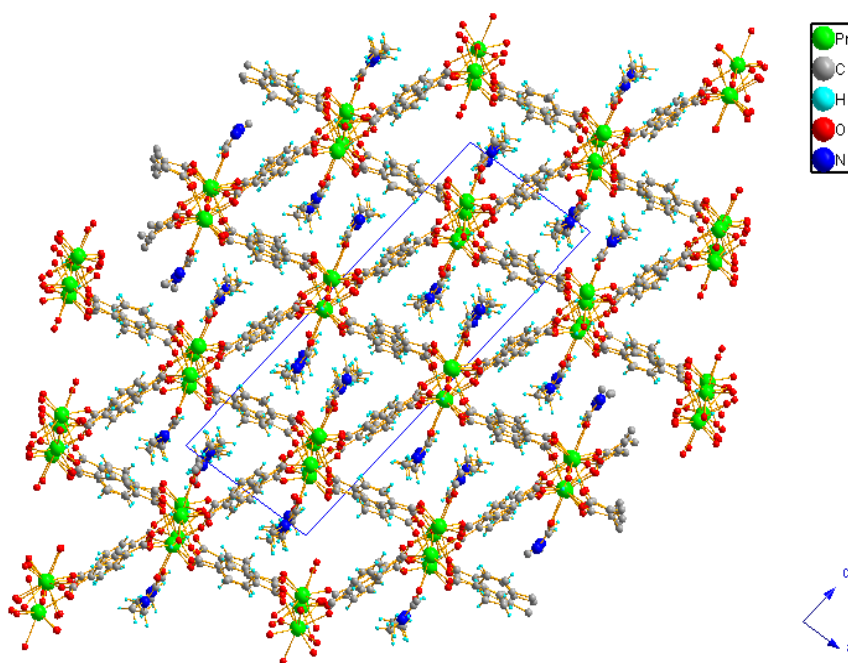
Figure 4.2 The 3-D structures for the (a) Y-MOF-BDC and (b) Pr-MOF-BDC systems.

Systems	Y-MOF-BDC	Ce-MOF-BDC
Empirical formula	$Y(C_8H_4O_4)\cdot(C_3H_7NO)_2\cdot NO_3$	$(C_{30}H_{28}N_2O_{15}Ce_2)_3\cdot C_3H_7NO$
Formula weight	461.22 g/mole	3029.64 g/mole
Temperature	298(2) K	240(2) K
Wavelength	0.71073 Å	0.71073 Å
Crystal size	$0.32 \times 0.225 \times 0.18$ mm^3	$0.30 \times 0.27 \times 0.18$ mm^3
Crystal habit	colorless prism	colorless prism
Crystal system	Monoclinic	Triclinic
Space group	C2/c	P$\bar{1}$
Unit cell dimensions	a = 17.0309(16) Å, α = 90°	a = 11.1044(7) Å, α = 86.5030(10)°
	b = 10.6792(10) Å, β = 96.070(2)°	b = 17.7726(12) Å, β = 79.3750(10)°
	c = 10.5721(10) Å, γ = 90°	c = 29.1664(19) Å, γ = 72.9620(10)°
Volume	1912.0(3) Å^3	5409.0(6) Å^3
Z	4	2
Density, ρ_{calc}	1.602 g/cm^3	1.860 g/cm^3
Absorption coefficient, μ	3.101 mm^{-1}	2.571 mm^{-1}
θ range for data collection	2.25 to 27.50°	1.85 to 27.50°
Index ranges	$-22 \leq h \leq 22$, $0 \leq k \leq 13$, $0 \leq l \leq 13$	$-14 \leq h \leq 14$, $-23 \leq k \leq 23$, $-37 \leq l \leq 37$
Reflections collected	31641	61526
Independent reflections	2190	24535
Observed reflection, I>2σ(I)	1949	20362
Data / restraints / parameters	3005 / 207 / 232	24535 / 0 / 1477
Goodness-of-fit on F^2	1.004	1.001
Δ/σ$_{max}$	0.001	0.002
Final R indices:	R$_1$, I > 2σ(I) = 0.0223	R$_1$, I > 2σ(I) = 0.0344
	wR$_2$, all data = 0.0544	wR$_2$, all data = 0.0782
	R$_{int}$ = 0.0414	R$_{int}$ = 0.0295
	R$_{sig}$ = 0.0217	R$_{sig}$ = 0.0356
$R_1 = \Sigma||F_o|-|F_c||/\Sigma|F_o|$, $\quad wR_2 = [\Sigma w(F_o^2 - F_c^2)^2/\Sigma w(F_o^2)^2]^{1/2}$		

Table 4.1 The details of measured parameters, structural information and refinement results obtained from single crystal analyses of the Ln-MOF-BDC systems.

Systems	Pr-MOF-BDC	Gd-MOF-BDC
Empirical formula	$(C_{30}H_{28}N_2O_{15}Pr_2)\cdot C_3H_7NO$	$Gd(C_8H_4O_4)\cdot(C_3H_7NO)_2\cdot NO_3$
Formula weight	1011.46 g/mole	529.56 g/mole
Temperature	250(2) K	220(2) K
Wavelength	0.71073 Å	0.71073 Å
Crystal size	$0.31 \times 0.20 \times 0.11$ mm^3	$0.38 \times 0.37 \times 0.085$ mm^3
Crystal habit	green prism	colorless plate
Crystal system	Triclinic	Monoclinic
Space group	P$\bar{1}$	C2/c
Unit cell dimensions	a = 11.0971(9) Å, α =86.507(2)°	a = 17.2632(17) Å, α = 90°
	b = 17.7485(15) Å, β =79.6940(10)°	b = 10.6097(10) Å, β = 95.936(2)°
	c = 29.119(3) Å, γ = 72.8360(10)°	c = 10.6296(10) Å, γ = 90°
Volume	5391.1(8) Å^3	1936.5(3) Å^3
Z	6	4
Density, ρ_{calc}	1.869 g/cm^3	1.816 g/cm^3
Absorption coefficient, μ	2.758 mm^{-1}	3.475 mm^{-1}
θ range for data collection	2.40 to 25.00°	2.37 to 30.00°
Index ranges	$-13 \leq h \leq 13, -20 \leq k \leq 21, -34 \leq l \leq 34$	$-24 \leq h \leq 24, -14 \leq k \leq 14, -12 \leq l \leq 14$
Reflections collected	110196	16834
Independent reflections	18424	2825
Observed reflection, I>2σ(I)	15773	2735
Data / restraints / parameters	18424 / 150 / 1495	2825 / 213 / 231
Goodness-of-fit on F^2	1.000	1.043
Δ/σ_{max}	0.002	0.001
Final R indices:	R$_1$, I > 2σ(I) = 0.0396	R$_1$, I > 2σ(I) = 0.0156
	wR$_2$, all data = 0.0850	wR$_2$, all data = 0.0356
	R$_{int}$ = 0.0292	R$_{int}$ = 0.0235
	R$_{sig}$ = 0.0387	R$_{sig}$ = 0.0146
$R_1 = \Sigma||F_o|-|F_c||/\Sigma|F_o|, \quad wR_2 = [\Sigma w(F_o^2 - F_c^2)^2/\Sigma w(F_o^2)^2]^{1/2}$		

Table 4.1 The details of measured parameters, structural information and refinement results obtained from single crystal analyses of the Ln-MOF-BDC systems (continued).

Systems	Dy-MOF-BDC	Ho-MOF-BDC
Empirical formula	$Dy(C_8H_4O_4)\cdot(C_3H_7NO)_2\cdot NO_3$	$Ho(C_8H_4O_4)\cdot(C_3H_7NO)_2\cdot NO_3$
Formula weight	534.81 g/mole	537.24 g/mole
Temperature	288(2) K	298(2) K
Wavelength	0.71073 Å	0.71073 Å
Crystal size	N/A	$0.29 \times 0.23 \times 0.20$ mm^3
Crystal habit	colorless prism	pink prism
Crystal system	Monoclinic	Monoclinic
Space group	P1 21/c 1	C2/c
Unit cell dimensions	a = 51.218(10) Å, α = 90°	a = 17.0583(14) Å, α =90°
	b = 10.650(2) Å, β = 95.945(3)°	b = 10.6730(9) Å, β = 96.116(2)°
	c = 10.588(2) Å, γ = 90°	c = 10.5721(9) Å, γ = 90°
Volume	5744(2) Å^3	1913.8(3) Å^3
Z	12	4
Density, ρ_{calc}	1.855 g/cm^3	1.865 g/cm^3
Absorption coefficient, μ	3.953 mm^{-1}	4.185 mm^{-1}
θ range for data collection	1.60 to 28.28°	2.25 to 27.50°
Index ranges	$-68 \le h \le 67$, $-14 \le k \le 13$, $-13 \le l \le 14$	$-22 \le h \le 22$, $-13 \le k \le 13$, $-12 \le l \le 13$
Reflections collected	50351	12749
Independent reflections	13632	2198
Observed reflection, I>2σ(I)	5253	2154
Data / restraints / parameters	13632 / 105 / 728	2198 / 213 / 232
Goodness-of-fit on F^2	1.197	1.000
Δ/σ_{max}	3.182	0.001
Final R indices:	R$_1$, I > 2σ(I) = 0.0479	R$_1$, I > 2σ(I) = 0.0121
	wR$_2$, all data = 0.1143	wR$_2$, all data = 0.0288
	R$_{int}$ = 0.0619	R$_{int}$ = 0.0210
	R$_{sig}$ = 0.0645	R$_{sig}$ = 0.0122
$R_1 = \Sigma||F_o|-|F_c||/\Sigma|F_o|$, $\quad wR_2 = [\Sigma w(F_o^2 - F_c^2)^2/\Sigma w(F_o^2)^2]^{1/2}$		

Table 4.1 The details of measured parameters, structural information and refinement results obtained from single crystal analyses of the Ln-MOF-BDC systems (continued).

4.3 1, 3, 5-Benzene tricarboxylic acid (H$_3$BTC) Ligand

4.3.1 Synthesis of (C$_9$H$_3$O$_6$)Ce(OH)·C$_3$H$_7$NO·H$_2$O (Ce-MOF-BTC) System

A cerium complex crystal was synthesized by solvothermal reaction. Cerium nitrate (Ce(NO$_3$)$_3$·6H$_2$O) was mixed with 1, 3, 5-Benzene tricarboxylic acid (H$_3$BTC) powder at 2 : 1 molar fraction, dissolved in 15 ml DMF, then placed in a 20ml Teflon-lined steel autoclave under autogenous pressure at 90°C for 3 days and then naturally cooled to room temperature. Colorless needle-like crystals were washed with ethanol (~10ml) three times and dried at room temperature.

4.3.2 Synthesis of 2[(C$_9$H$_3$O$_6$) Ho(H$_2$O)]·C$_3$H$_7$NO·0.5H$_2$O (Ho-MOF-BTC) System

A holmium complex crystal was synthesized by mixed-solution reaction. Holmium nitrate (Ho(NO$_3$)$_3$·xH$_2$O) was mixed with 1, 3, 5-Benzene tricarboxylic acid (H$_3$BTC) powder at 1 : 1 molar fraction, dissolved in mixed solvent of 3ml DMF, 3ml ethanol and 2ml H$_2$O, then placed in a 20ml Teflon-lined steel autoclave under autogenous pressure at 80°C for 24 hours and then naturally cooled to room temperature. Light yellow needle-like crystals were obtained in ca. 76.27wt% yield (based on Ho), washed by ethanol (~10ml) three times and dried at room temperature.

4.3.3 Discussion of Structures with 1, 3, 5-Benzene tricarboxylic acid (H$_3$BTC) Ligand

Two different lanthanide (Ce and Ho) MOFs with the BTC ligand have been synthesized. The crystal structure and properties of Ho-MOF-BTC system (as shown as Figure 4.3 (b)) will be discussed in chapter 5 and 6, and all of detailed information for both cases is shown in Table 4.2. The Ce-MOF-BTC crystallizes in the tetragonal crystal

system, with space group $P4_32_12$, and lattice parameters $a = 15.019(1)$Å, $b = 15.019(1)$Å, $c = 13.936(3)$Å. Each structural unit is constructed with one eight-coordinated cerium ion, one BTC ligand and one terminal water molecule. As shown in Figure 4.3 (a), 1-D square channels oriented along the c axis are filled with free water and DMF solvent. The eight oxygen atoms coordinated on each cerium ion consist of five carboxyl groups from different monodentated benzoic-acid ligands, one bidentated carboxylic group and one terminal water molecule. The bond distances between Ce-O_{BTC} are in the range of 2.426(5)-2.955(4)Å and the Ce-O_{water} bond distance is 2.489(5)Å. The thermal stabilities of both samples are examined by thermogravimetric analysis (TGA) and shown in Figure 4.4 (a) and (b), respectively. The experimental TGA results demonstrate that the Ce-MOF-BTC compound loses weight and structural decomposition occurs at ca. 350°C. There is no obvious plateau at elevated temperatures implying no phase with high thermal stability is present in this system. In contrast, the Ho-MOF-BTC sample shows two stable phases and the decomposition temperature of structure is above 500°C (details given in chapter 5). The structural and chemical bonding configurations along [110] and [1$\bar{1}$0] directions in the Ce-MOF-BTC and [100] and [010] direction (a and b axes) in the Ho-MOF-BTC system are complex and to simplify the structures we have substituted the ligand with a geometric form. For example, a co-planer tripod is used to replace the BTC ligand. The same methodology will be applied for the comparison of structures in later chapters. The original and simplified structure of the Ce-MOF-BTC crystal along the [110] direction (as same as viewed along [1$\bar{1}$0] direction because of the symmetry) are plotted in Figures 4.5. Interestingly, the diagrams exhibit similar geometry and arrangement of the rigid ligands in both cases (the diagrams for Ho-MOF-BTC case are shown in chapter 5). It implies that more attention should be paid to the configuration of

chemical bonding between oxygen molecules and metal ions. A slight difference between these two structures has been addressed on one μ_2 (shared) oxygen which is coordinated with two adjacent cerium ions and one hard-bridged ligand as marked by red dashed circles in Figure 4.5. The bonding configuration of oxygen is absent in Ho-MOF-BTC system and results in much longer metal-oxygen distances (in range of 2.426(5)-2.955(4)Å) for Ce-MOF-BTC structure than that (2.284(3)-2.297(3)Å) for Ho-MOF-BTC system. This phenomenon also implies that the chemical bonding between Ce-O_{BTC} should be easier to break and lose structural integrity at high temperature.
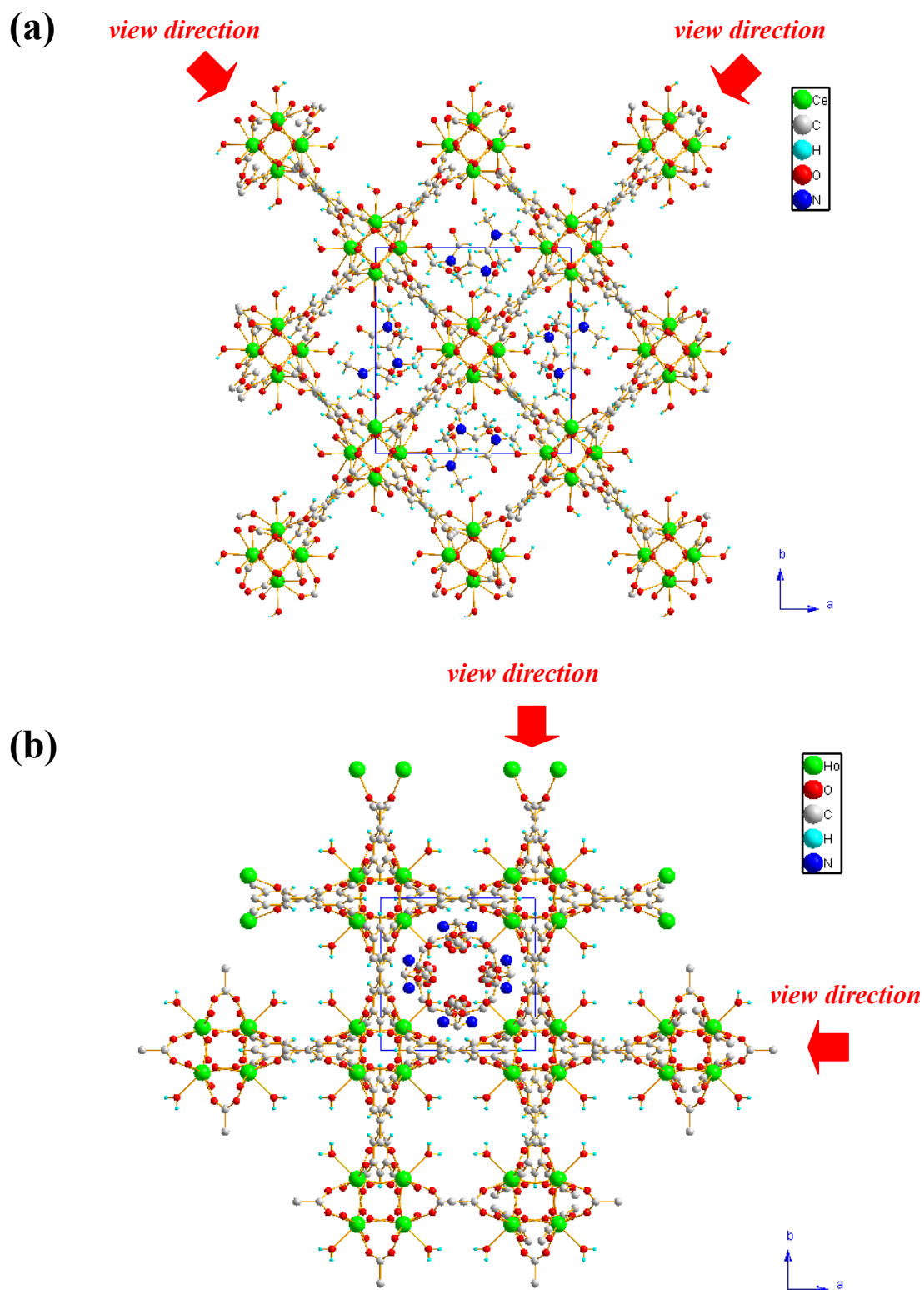
Figure 4.3 The 3-D molecular structures for the (a) Ce-MOF-BTC and (b) Ho-MOF-BTC

systems viewed along the *c* axis.
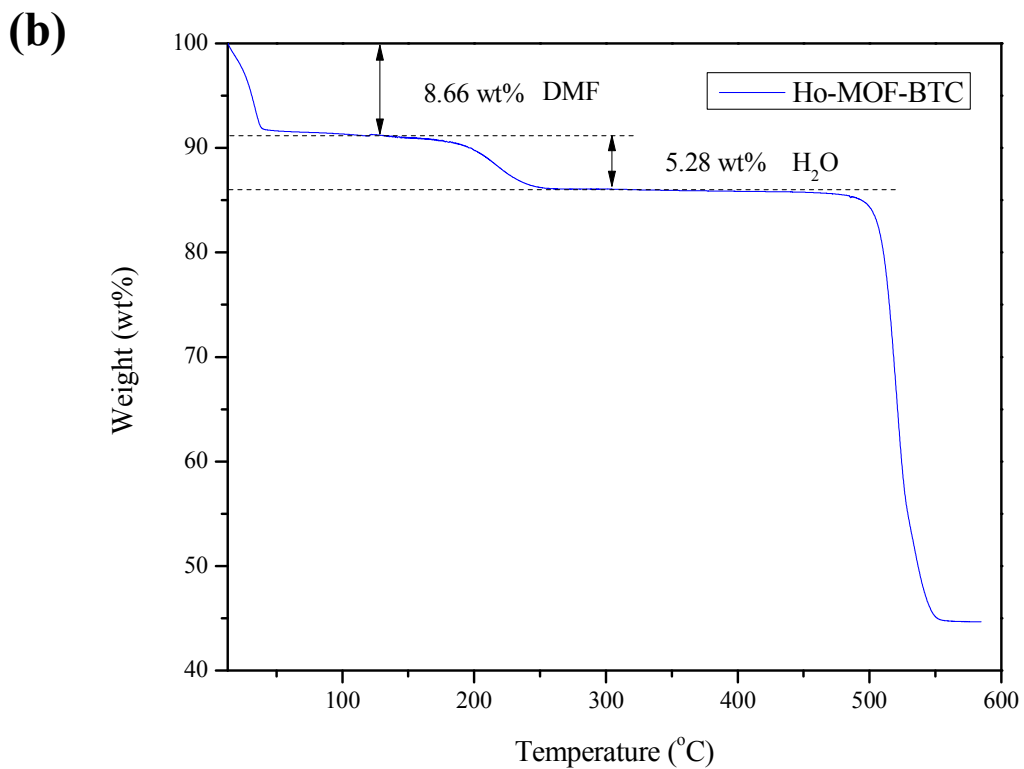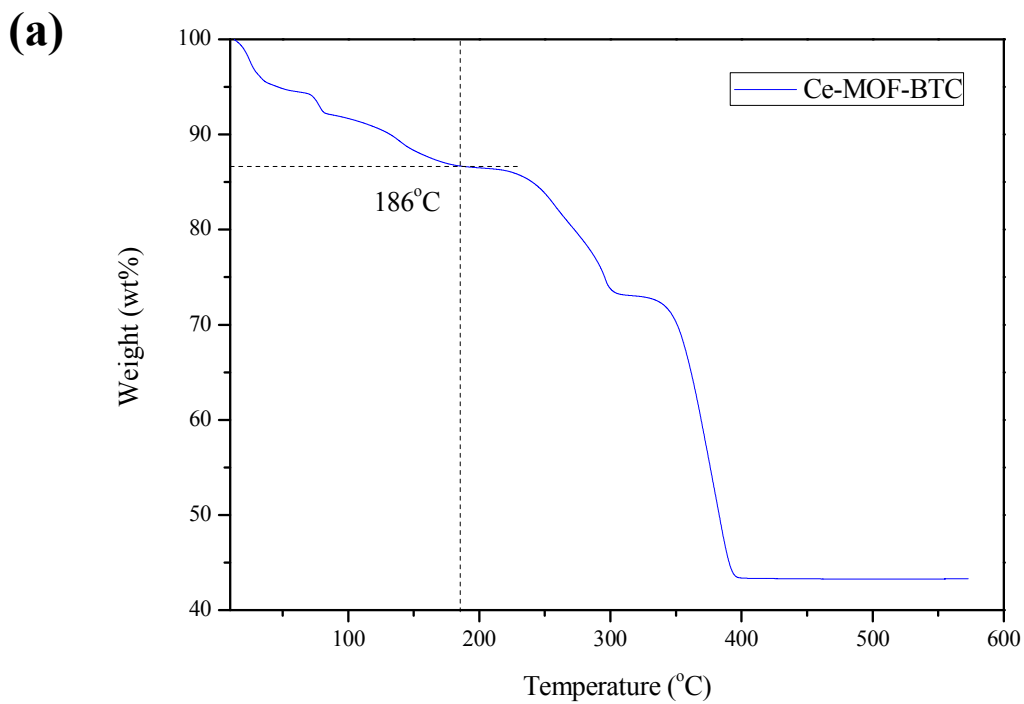
Figure 4.4 Thermogravimetric analyses (TGA) for (a) Ce-MOF-BTC and (b) Ho-MOF-BTC systems.
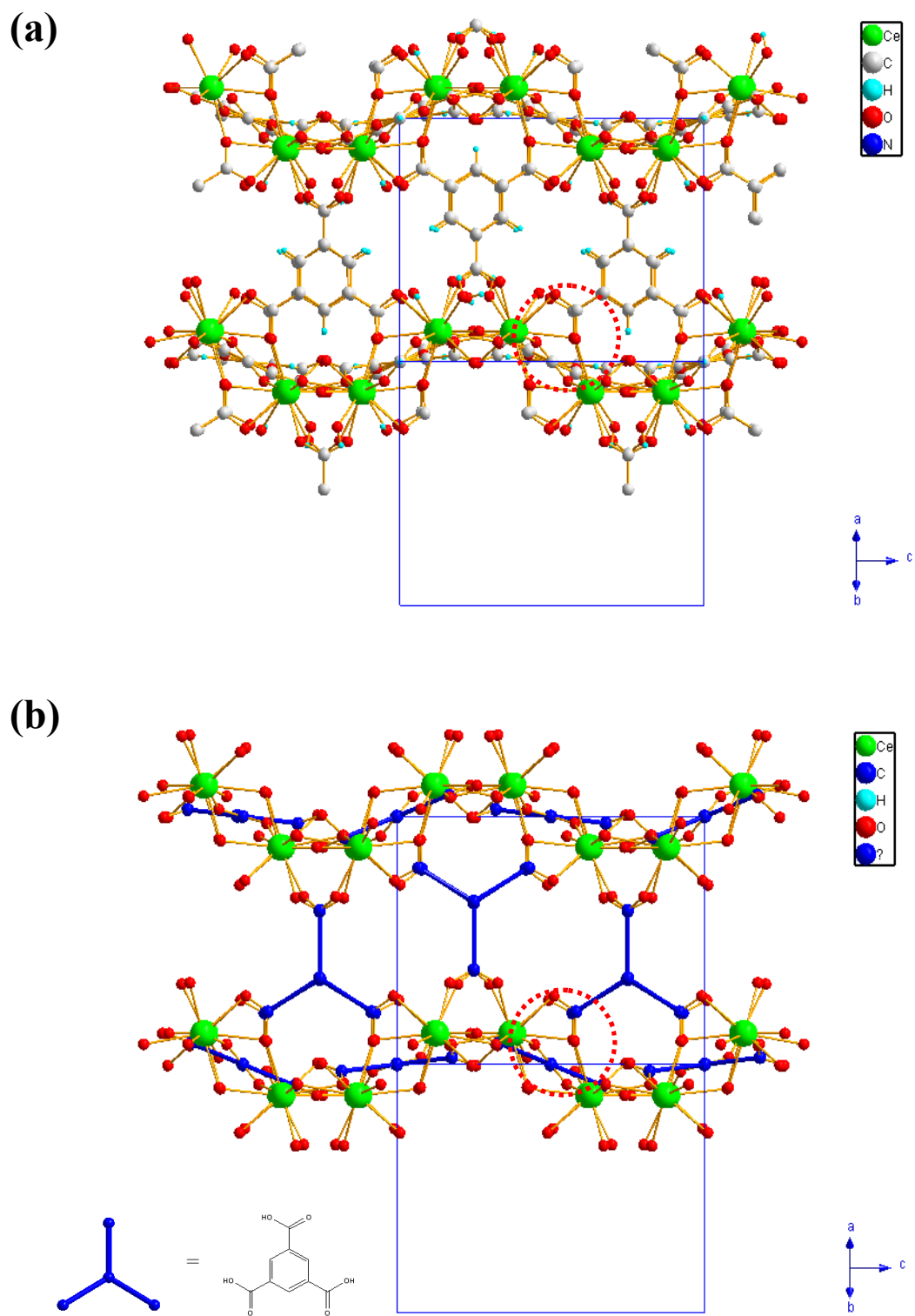
Figure 4.5 Illustration of (a) original and (b) simplified structural framework for the Ce-MOF-BTC crystal viewed along the [110] direction.

Systems	Ce-MOF-BTC	Ho-MOF-BTC
Empirical formula	$(C_9H_3O_6)Ce(OH) \cdot C_3H_7NO \cdot H_2O$	$2[(C_9H_3O_6)\,Ho(H_2O)] \cdot C_3H_7NO \cdot 0.5H_2O$
Formula weight	455.35 g/mole	862.23 g/mole
Temperature	150(2) K	250(2) K
Wavelength	0.71073 Å	0.71073 Å
Crystal size	$0.11 \times 0.04 \times 0.04$ mm^3	$0.51 \times 0.030 \times 0.025$ mm^3
Crystal habit	colorless needle	light-yellow needle
Crystal system	Tetragonal	Tetragonal
Space group	$P4_32_12$	$P4_122$
Unit cell dimensions	a = 15.0194(14) Å, $\alpha = 90°$	a = 10.2749(3) Å, $\alpha = 90°$
	b = 15.0194(14) Å, $\beta = 90°$	b = 10.2749(3) Å, $\beta = 90°$
	c = 13.936(3) Å, $\gamma = 90°$	c = 14.4832(10) Å, $\gamma = 90°$
Volume	3143.7(7) Å^3	1529.04(12) Å^3
Z	8	2
Density, ρ_{calc}	1.924 Å^3	1.892 g/cm^3
Absorption coefficient, μ	2.941 mm^{-1}	5.205 mm^{-1}
θ range for data collection	1.92 to 27.49°	2.43 to 29.99°
Index ranges	$-19 \leq h \leq 19$, $-16 \leq k \leq 19$, $-12 \leq l \leq 18$	$-12 \leq h \leq 12$, $-2 \leq k \leq 14$, $-20 \leq l \leq 19$
Reflections collected	18592	5759
Independent reflections	3612	2172
Observed reflection, I>2σ(I)	2339	2060
Data / restraints / parameters	3612 / 61 / 223	2172 / 83 / 160
Goodness-of-fit on F^2	0.995	0.986
Δ/σ$_{max}$	0.000	0.000
Final R indices:	R_1, I > 2σ(I) = 0.0344	R_1, I > 2σ(I) = 0.0197
	wR$_2$, all data = 0.0794	wR$_2$, all data = 0.0533
	R$_{int}$ = 0.0557	R$_{int}$ = 0.0443
	R$_{sig}$ = 0.0423	R$_{sig}$ = 0.0364
$R_1 = \Sigma||F_o|-|F_c||/\Sigma|F_o|$, $wR_2 = [\Sigma w(F_o^2 - F_c^2)^2/\Sigma\, w(F_o^2)^2]^{1/2}$		

Table 4.2 The details of measured parameters, structural information and refinement results obtained from single crystal analyses of the Ln-MOF-BTC systems.

4.4 3, 5-Pyridinedicarboxylic acid (H$_2$PDC) Ligand

4.4.1 Synthesis of (C$_{27}$H$_{23}$N$_5$O$_{14}$Ho$_2$)·~C$_3$H$_7$NO (Ho-MOF-PDC) System

A Ho-MOF-PDC crystal was obtained by solvothermal synthesis. The mixed holmium

nitrate (Ho(NO$_3$)$_3$·xH$_2$O) and 3, 5-Pyridinedicarboxylic acid (H$_2$PDC) powders (at 1 : 3

molar fraction) were dissolved in 10ml DMF solution, loaded in a 20ml Teflon-lined steel

autoclave under autogenous pressure at 120°C for 24 hours and then naturally cooled to

room temperature. Yellow needle-like crystals were obtained and washed with ethanol

(~10ml) for three times then dried at room temperature.

4.4.2 Discussion of Structure with 3, 5-Pyridinedicarboxylic acid (H$_2$PDC) Ligand

The Ho-MOF-PDC structure crystallizes in the orthorhombic crystal system, with

space group ***Pnma***, and lattice parameters a = 8.506(2)Å, b = 28.063(8)Å, c =

15.966(4)Å. Each structural unit is composed of one eight-coordinated holmium ion, two

PDC ligands and one coordinated DMF molecules. The eight oxygen atoms coordinated

on each holmium ion consist of five carboxyl groups from different monodentated

benzoic-acid ligands, one bidentated carboxylic group and one connected DMF molecule.

The bond distances between Ho-O$_{PDC}$ are in the range of 2.292(3)-2.852(3)Å and

Ho-O$_{DMF}$ bond distance is 2.379(3)Å. This 3-D framework has large, one-dimensional

hexagonal channels along the a axis. The coordinated DMF molecules on the holmium

ion disordered in two orientations in about 1:1 ratio, and the solvent DMF molecules are

highly disordered in a 460Å^3 cavity and derived using the "SQUEEZE"[1,2] procedure

yielding 14-160 electrons per unit cell, which corresponds approximately to four DMF

solvents per unit cell. For this reason, the *Crystallographic Information File* (CIF) file

from the single crystal analysis does not involve all the free solvent molecules, resulting

in a clear mismatch of the intensity from the Rietveld refinement from as-synthesized Ho-MOF-PDC system shown in Figure 4.6. However, qualitatively, the lattice parameters of the crystal are consistent with the experimental PXRD result. Thermogravimetric analysis (TGA) was used to evaluate the thermal stability for this MOF. A broad plateau at elevated temperatures between ca. $170^{\circ}C$ to $450^{\circ}C$ implying a phase with high thermal stability was observed (Figure 4.7). A dehydrated Ho-MOF-PDC sample was prepared at $250^{\circ}C$ for 12 hours under high vacuum (10^{-6}torr), then measured within a sealed quartz capillary by X-ray diffraction. As shown in Figure 4.8, although the resolution for this powder X-ray diffraction pattern (PXRD) is not high enough to do full-matrix refinement, our results still show a good qualitative fit. The lower number of Bragg peaks result from the higher symmetry and multiplicity for this crystal. Finally, a 3-D molecular model can be constructed from the Rietveld refinement for dehydrated Ho-MOF-PDC, which shows this system is a porous framework and a potential candidate for gas storage applications.
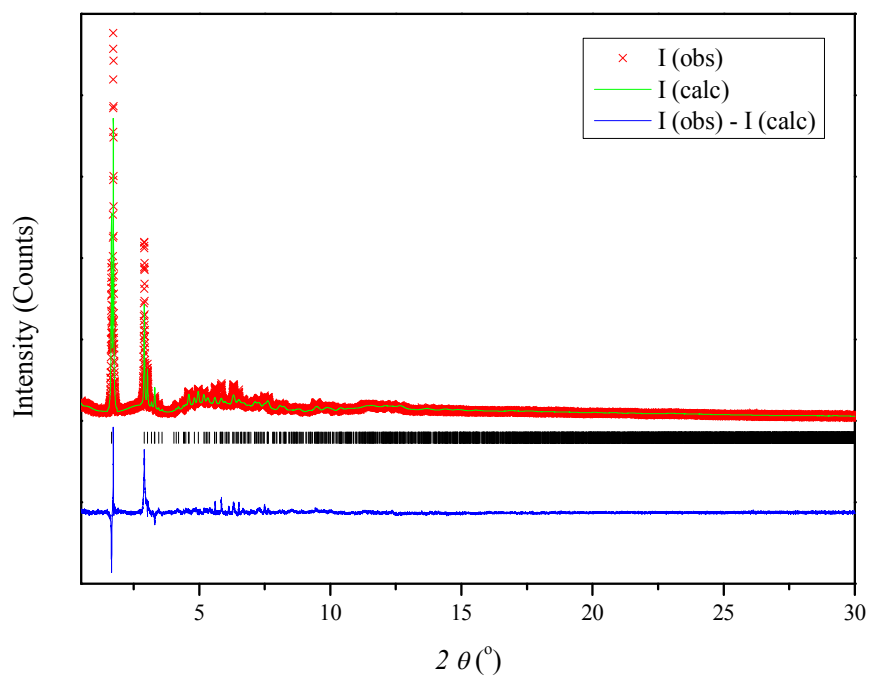
Figure 4.6 The Rietveld refinement of PXRD for as-synthesized Ho-MOF-PDC system.
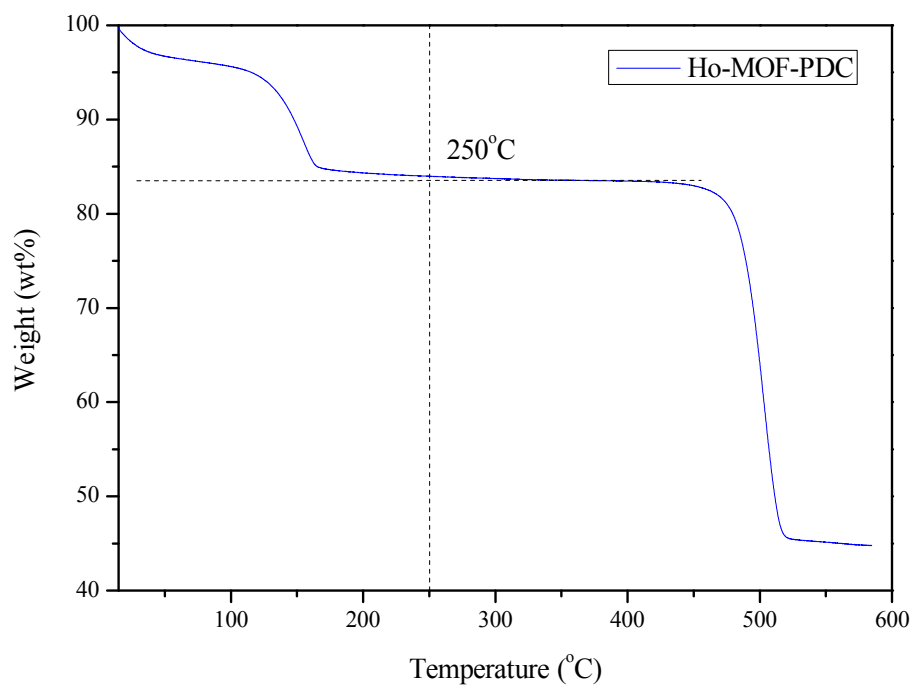
Figure 4.7 Thermogravimetric analysis (TGA) for Ho-MOF-PDC system.
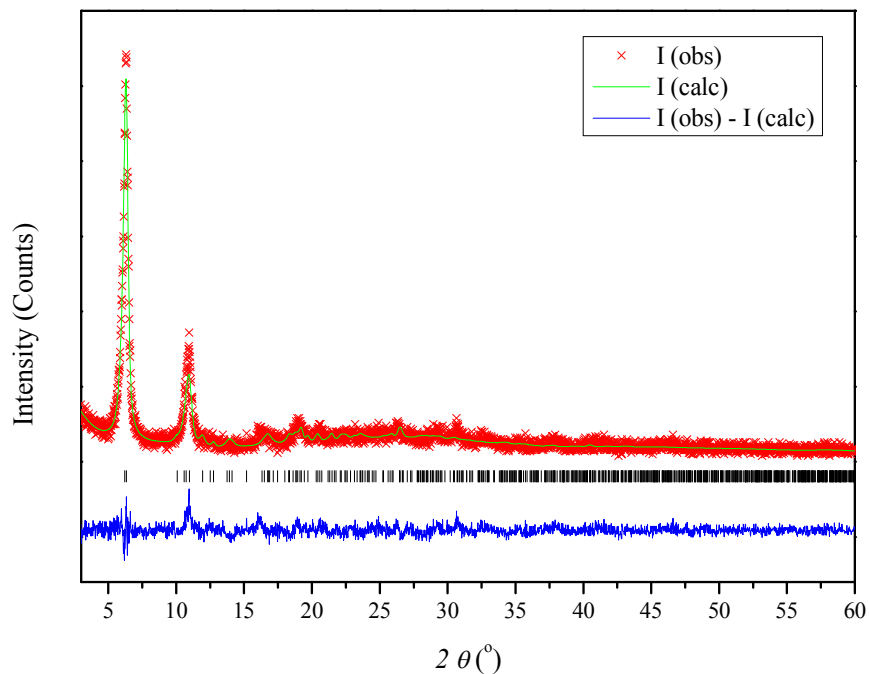
Figure 4.8 The Rietveld Refinement of PXRD for dehydrated Ho-MOF-PDC system.
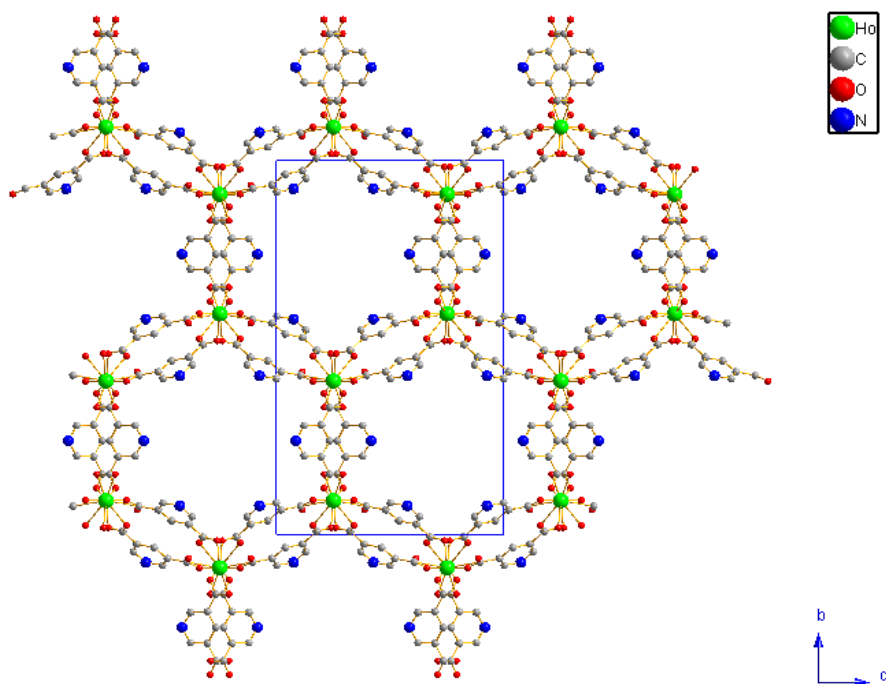
Figure 4.9 The 3-D structure for the dehydrated Ho-MOF-PDC system from Rietveld refinement (hydrogen atoms are removed for clarity).

Systems	Ho-MOF-PDC
Empirical formula	$(C_{27}H_{23}N_5O_{14}Ho_2)\cdot\sim C_3H_7NO$
Formula weight	1045.47 g/mole
Temperature	250(2) K
Wavelength	0.71073 Å
Crystal size	$0.315 \times 0.16 \times 0.025$ mm^3
Crystal habit	yellow needle
Crystal system	Orthorhombic
Space group	Pnma
Unit cell dimensions	a = 8.506(2) Å, $\qquad$ α = 90°
	b = 28.063(8) Å, $\qquad$ β = 90°
	c = 15.966(4) Å, $\qquad$ γ = 90°
Volume	3811.4(18) Å^3
Z	4
Density, ρ_{calc}	1.822 g/cm^3
Absorption coefficient, μ	4.195 mm^{-1}
θ range for data collection	2.52 to 27.50°
Index ranges	$-11 \le h \le 9, -36 \le k \le 35, -20 \le l \le 20$
Reflections collected	29635
Independent reflections	4458
Observed reflection, I>2σ(I)	4012
Data / restraints / parameters	4458 / 9 / 224
Goodness-of-fit on F^2	0.999
Δ/σ_{max}	0.001
Final R indices:	R_1, I > 2σ (I) = 0.0294
	wR_2, all data = 0.0646
	R_{int} = 0.0321
	R_{sig} = 0.0206
$R_1 = \Sigma||F_o|-|F_c||/\Sigma|F_o|, \quad wR_2 = [\Sigma w(F_o^2 - F_c^2)^2/\Sigma w(F_o^2)^2]^{1/2}$	

Table 4.3 The details of measured parameters, structural information and refinement results obtained from single crystal analysis of the Ho-MOF-PDC system.

4.5 2, 6-Naphthalenedicarboxylic acid (H$_2$NDC) Ligand

4.5.1 Synthesis of (C$_{18}$H$_9$O$_6$Ho)·C$_3$H$_7$NO (Ho-MOF-NDC-1) System

To synthesize this MOF a mixture of holmium nitrate (Ho(NO$_3$)$_3$·xH$_2$O) and 2, 6-Naphthalenedicarboxylic acid (H$_2$NDC) at 1 : 1 molar fraction was dissolved in the mixed solution system which consisted of 3ml DMF, 3ml ethanol and 2ml H$_2$O. All of these reagents were loaded in a 20ml Teflon-lined steel autoclave under autogenous pressure at 90°C for 24 hours and then naturally cooled to room temperature. Colorless needle-like crystals were obtained and washed with ethanol (~10ml) three times then dried at room temperature.

4.5.2 Synthesis of [Ho$_2$(C$_{12}$H$_4$O$_4$)$_3$·(2+x)H$_2$O·(1-x)EtOH]·3C$_3$H$_7$NO, x=0.6 (Ho-MOF-NDC-2) System

This Ho-MOF-NDC-2 crystal can be obtained by the same synthetic parameters which were described in section 3.1.5.1. This is a co-existing system for Ho-MOF-NDC-1 and Ho-MOF-NDC-2 during the synthesis reaction.

4.5.3 Synthesis of Ho$_2$(C$_{12}$H$_4$O$_4$)$_3$·C$_3$H$_7$NO (Ho-MOF-NDC-3) System

To obtain this MOF a mixture of holmium nitrate (Ho(NO$_3$)$_3$·xH$_2$O) and 2, 6-Naphthalenedicarboxylic acid (H$_2$NDC) at 1 : 2 molar fraction was dissolved in a mixed solvent system which consisted of 3 ml ethanol and 7 ml H$_2$O. Four drops of 0.1M acetic acid have been added giving a PH value for solution close to 5. All of these reagents were loaded in a 20ml Teflon-lined steel autoclave under autogenous pressure at 200°C for 16 hours and then cooled to room temperature at 60°C/hr cooling rate. Colorless needle-like crystals were obtained and washed with ethanol (~10ml) three times

119

then dried at room temperature.

4.5.4 Discussion of Structures with 2, 6-Naphthalenedicarboxylic acid (H₂NDC) Ligand

A series of holmium MOF materials with 2, 6-Naphthalenedicarboxylic acid (NDC) ligand have been successfully synthesized and are composed of three different structures. The detailed information is organized and tabulated in Table 4.4. The Ho-MOF-NDC-1, as shown as Figure 4.10 (1), exhibits a non-merohedral, twin crystal with 180° rotation around (001) axis, near 1 : 1 domain ratio during the single crystal analysis, and crystallizes in the monoclinic crystal system, with space group *P21/c*, and lattice parameters of a = 22.803(2)Å, b = 9.082(0)Å, c = 18.962(2)Å, β = 101.008(2)^o. Each structural unit consists of two holmium ions, three NDC ligands and two bonded DMF solvent molecules on each metal atom. The seven oxygen atoms coordinated on each holmium ion include six carboxyl groups from different monodentated benzoic-acid ligands, and one terminal DMF molecule. The bond distances between Ho-O$_{NDC}$ are in the range of 2.260(3)-2.328(3)Å and Ho-O$_{DMF}$ bond distances are in range of 2.308(3)-2.371(4)Å. This crystal is comprised of a 3-D network with 1-D rhombic channels along the c axis and very similar to family **(1)** crystals in the Ln-MOF-BDC system. The Ho-MOF-NDC-2 crystal (Figure 4.10 (b)) shows not only a non-merohedral twin crystal, 180° rotation around (011) reciprocal axis with 3 : 2 domains ratio, but also disorder which consists of (i) Alternative orientation for one of three ligands, (ii) Alternating H₂O and EtOH coordinated to Ho ions, and (iii) Two DMF solvent molecules disordered between three positions. It is suggested that this structure crystallizes in the triclinic crystal system, with space group *PĪ*, and lattice parameters of a = 9.533(1)Å, b =

12.382(2)Å, c = 12.449(2)Å, α = 107.970(3)°, β = 99.337(3)° and γ = 109.759(2)°. This framework is constructed of a 3-D scaffold with 1-D triangular channels along the a axis. The Ho-MOF-NDC-3 system in Figure 4.10 (c) crystallizes in the monoclinic crystal system, with space group **C2/c**, and lattice parameters of a = 23.366(5)Å, b = 8.498(2)Å, c = 17.820(4)Å, β = 99.033(3)°. The coordinated DMF solvent molecules occupy the 1-D rhombic channels along the c axis and shows disorder in two alternative orientations around a two fold axis. Each structural unit is constructed from two holmium ions, three NDC ligands and one DMF molecule alternatively bonded on these two metal atoms. The bonding configurations (six or seven coordination number) on the holmium ion either include six carboxyl groups from different monodentated benzoic-acid ligands, and one terminal DMF molecule or six carboxyl groups from different monodentated benzoic-acid ligands but without the terminal DMF molecule. The bond distances between Ho-O_{NDC} are in the range of 2.216(3)-2.269(3)Å and the Ho-O_{DMF} bond distance is 2.323(9)Å. Although the structural configurations of Ho-MOF-NDC-1 and Ho-MOF-NDC-3 crystals are very similar, the major difference is on the arrangement of the coordinated DMF solvent molecules in channels. There are two coordinated DMF molecules for Ho-MOF-NDC-1 but only one has been observed for the Ho-MOF-NDC-3 system. The channel pore sizes vary from ca. 8.8 × 2.1Å to ca. 9.3 × 1.8Å (taking into account the van der Waals radii of the atoms).

(a)

(b)
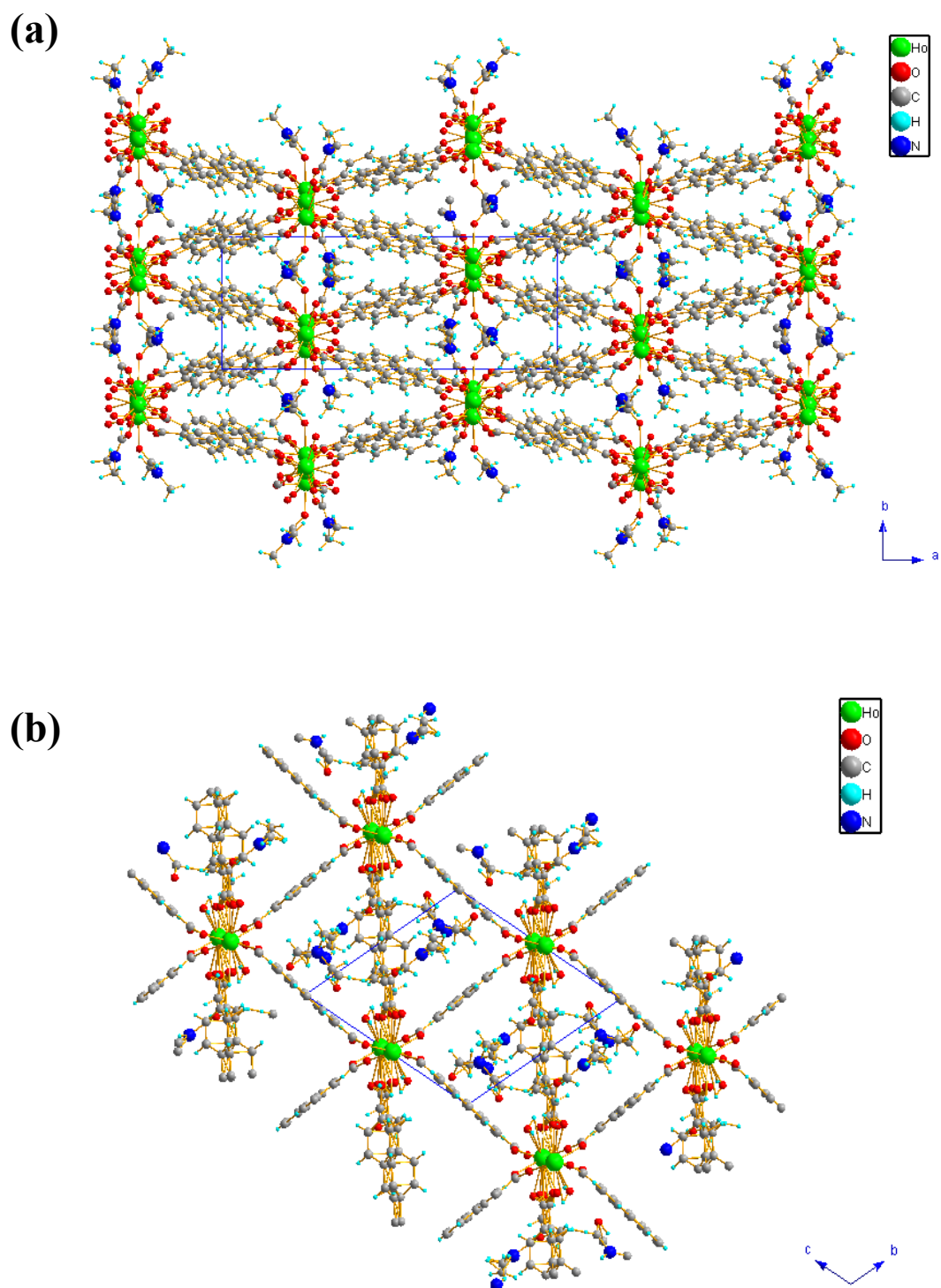
Figure 4.10 The 3-D frameworks for (a) Ho-MOF-NDC-1 viewed along *c* axis, (b) Ho-MOF-NDC-2 viewed along *a* axis, and (c) Ho-MOF-NDC-3 viewed in *c* axis.

(c)
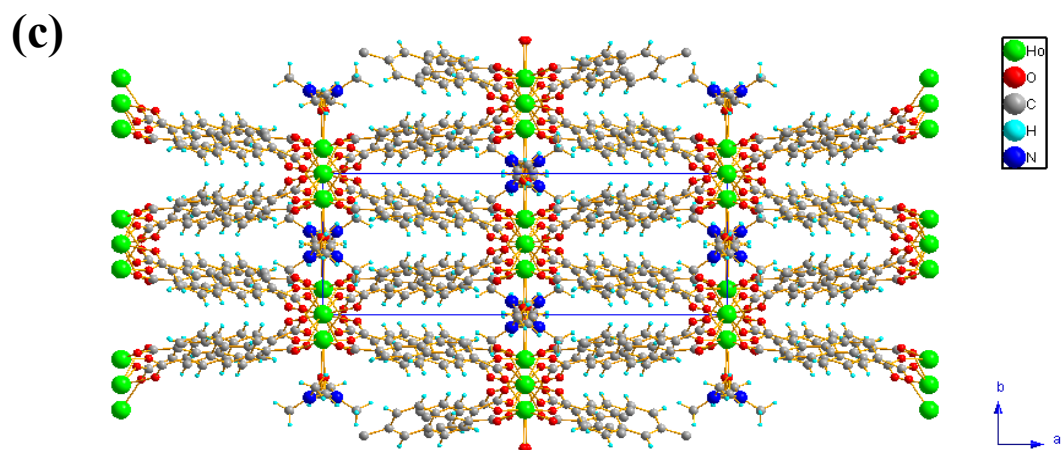
Figure 4.10 The 3-D frameworks for (a) Ho-MOF-NDC-1 viewed along the *c* axis, (b) Ho-MOF-NDC-2 viewed along the *a* axis, and (c) Ho-MOF-NDC-3 viewed along the *c* axis (continued).

Systems	Ho-MOF-NDC-1	Ho-MOF-NDC-2
Empirical formula	$(C_{18}H_9O_6Ho) \cdot C_3H_7NO$	$[Ho_2(C_{12}H_4O_4)_3 \cdot (2+x)H_2O \cdot (1-x)EtOH] \cdot 3$ DMF, x=0.6
Formula weight	559.28 g/mole	1287.00 g/mole
Temperature	250(2) K	250(2) K
Wavelength	0.71073 Å	0.71073 Å
Crystal size	$0.48 \times 0.055 \times 0.045$ mm^3	$0.14 \times 0.075 \times 0.04$ mm^3
Crystal habit	colorless needle	colorless plate
Crystal system	Monoclinic	Triclinic
Space group	$P2_1/c$	$P\bar{1}$
Unit cell dimensions	a = 22.803(2) Å, α = 90°	a = 9.5327(14) Å, α = 107.970(3)°
	b = 9.0816(8) Å, β = 101.0077(15)°	b = 12.382(2) Å, β = 99.337(3)°
	c = 18.9621(16) Å, γ = 90°	c = 12.4489(19) Å, γ = 109.759(2)°
Volume	3854.5(6) Å^3	1255.8(4) Å^3
Z	8	1
Density, ρ_{calc}	1.928 g/cm^3	1.702 g/cm^3
Absorption coefficient, μ	4.151 mm^{-1}	3.205 mm^{-1}
θ range for data collection	1.82 to 27.50°	1.80 to 27.50°
Index ranges	$0 \le h \le 29$, $-11 \le k \le 0$, $-24 \le l \le 24$	$-11 \le h \le 12$, $-11 \le k \le 16$, $-16 \le l \le 14$
Reflections collected	63242	16876
Independent reflections	8846	5750
Observed reflection, I>2σ(I)	7513	5487
Data / restraints / parameters	16754 / 0 / 546	5750 / 215 / 456
Goodness-of-fit on F^2	1.000	0.990
Δ/σ_{max}	0.001	0.001
Final R indices:	R_1, I > 2σ(I) = 0.0296	R_1, I > 2σ(I) = 0.0271
	wR$_2$, all data = 0.0772	wR$_2$, all data = 0.0689
	R_{int} = 0.0324	R_{int} = 0.0288
	R_{sig} = 0.0302	R_{sig} = 0.0297
$R_1 = \Sigma||F_o|-|F_c||/\Sigma|F_o|$, wR$_2 = [\Sigma w(F_o^2 - F_c^2)^2/\Sigma\ w(F_o^2)^2]^{1/2}$		

Table 4.4 The details of measured parameters, structural information and refinement results obtained from single crystal analyses on Ho-MOF-NDC systems.

Systems	Ho-MOF-NDC-3
Empirical formula	$Ho_2(C_{12}H_4O_4)_3 \cdot C_3H_7NO$
Formula weight	1045.46 g/mole
Temperature	250(2) K
Wavelength	0.71073 Å
Crystal size	$0.375 \times 0.075 \times 0.02$ mm^3
Crystal habit	colorless needle
Crystal system	Monoclinic
Space group	C2/c
Unit cell dimensions	a = 23.366(5) Å, α = 90°
	b = 8.4975(19) Å, β = 99.033(3)°
	c = 17.820(4) Å, γ = 90°
Volume	3494.4(13) Å^3
Z	4
Density, ρ_{calc}	1.987 g/cm^3
Absorption coefficient, μ	4.568 mm^{-1}
θ range for data collection	1.76 to 27.49°
Index ranges	$-30 \leq h \leq 30$, $-11 \leq k \leq 11$, $-23 \leq l \leq 23$
Reflections collected	17518
Independent reflections	4012
Observed reflection, I>2σ(I)	3407
Data / restraints / parameters	4012 / 45 / 268
Goodness-of-fit on F^2	1.026
Δ/σ_{max}	0.001
Final R indices:	R_1, I > 2σ(I) = 0.0286
	wR$_2$, all data = 0.0700
	R_{int} = 0.0326
	R_{sig} = 0.0267
$R_1 = \Sigma||F_o|-|F_c||/\Sigma|F_o|, \quad wR_2 = [\Sigma w(F_o^2 - F_c^2)^2/\Sigma w(F_o^2)^2]^{1/2}$	

Table 4.4 The details of measured parameters, structural information and refinement results obtained from single crystal analyses on Ho-MOF-NDC systems (continued).

4.6 1, 3, 5-Tris(4-carboxyphenyl) benzene (H₃BTB) Ligand

4.6.1 Synthesis of [(C$_{27}$H$_{17}$O$_6$)Ho(H$_2$O)$_2$]·3C$_3$H$_7$NO·2H$_2$O (Ho-MOF-BTB) System

To synthesize this MOF a mixture of holmium nitrate (Ho(NO$_3$)$_3$·xH$_2$O) and 1, 3, 5-Tris(4-carboxyphenyl) benzene (H$_3$BTB) was dissolved in 10 ml DMF and 25ml H$_2$O in a small vessel. This small vessel was sealed in a bigger beaker containing ether (10 ml), which evaporated and diffused into the DMF/H$_2$O mixed solution. After the ether totally dissolved in the solution, the small vessel was covered with Parafilm® which had small holes, and stored in a static, dark and cool place at room temperature for several weeks. The complex would participate as the mixed solvent evaporated.

4.6.2 Synthesis of [Co$_3$(BTB)$_2$(H2O)$_{3.75}$(DMF)$_{1.5}$]·~9 C$_3$H$_7$NO (Co-MOF-BTB-cube) System

The millimeter-sized crystals (~3mm) of Co-MOF-BTB-cube were synthesized via mixing Co(II) nitrate (Co(NO$_3$)$_2$·6H$_2$O) with 1, 3, 5-Tris(4-carboxyphenyl) benzene (H$_3$BTB) ligand at 7 : 1 molar fraction, dissolved in mixed solution of 2ml H$_2$O and 8ml DMF in a 20ml Teflon-lined steel autoclave under autogenous pressure at 85°C for 2 days and then naturally cooled to room temperature. The brown cubic crystals could not be washed because of the extremely large pore size.

4.6.3 Synthesis of (C$_{54}$H$_{36}$O$_{15}$Co$_3$)·3C$_3$H$_7$NO·16.5H$_2$O (Co-MOF-BTB-plate) System

This Co-MOF-BTB-plate material can be gained by the similar synthetic parameters which were described in section 3.1.3.2. The annealing temperature is the only difference changing from 85°C to 100°C. The purple plate crystals also could not be washed for the same reason on Co-MOF-BTB-cube system.

4.6.4 Synthesis of [Eu(C$_{27}$H$_{15}$O$_6$)·H$_2$O]·~1.7C$_3$H$_7$NO (Eu-MOF-BTB) System

This Eu-MOF complex can be synthesized by mixing europium nitrate (Eu(NO$_3$)$_3$·5H$_2$O) with 1, 3, 5-Tris(4-carboxyphenyl) benzene (H$_3$BTB) ligand at 7 : 1 molar fraction, dissolved in a mixed of 2ml H$_2$O and 8ml DMF in a 20ml Teflon-lined steel autoclave under autogenous pressure at 85$^{\text{o}}$C for 3 days and then naturally cooled to room temperature. Colorless needle-like crystals were washed with ethanol (~10ml) three times and dried at room temperature.

4.6.5 Discussion of Structures with 1, 3, 5-Tris(4-carboxyphenyl) benzene (H$_3$BTB) Ligand

Two different types of Co-MOF-BTB crystals can be obtained under distinct synthetic conditions and the corresponding 3-D frameworks are shown in Figure 4.11. Moreover, the detailed characterization information have been organized and tabulated in Table 4.5. Co-MOF-BTB-plate crystal (Figure 4.11 (a)) is in the monoclinic crystal system, with space group ***P21/n***, and lattice parameters of a = 17.833(2)Å, b = 17.666(2)Å, c = 27.405(3)Å, β = 91.017(2)$^{\text{o}}$. Substantial disorder of the DMF and water solvents has been removed using SQUEEZE procedure due to the large cavities inside and two of six wings of the ligands are disordered in two alternative orientations. The structural unit in this case consists of one triple cobalt ion cluster (e. g. three cobalt ions), and two BTB ligands. There are six coordinated oxygen atoms on each cobalt ion, which are formed by (i) Four monodentated carboxylic acids from different BTB ligands, one terminal oxygen from a disordered solvent molecule and one μ_3 (connected with three cobalt ions) oxygen atom, and (ii) Two monodentated carboxylic acids from different BTB ligands, one bidentated

carboxylic acid from a BTB ligand, one μ_2 oxygen and one μ_3 oxygen.

The brown cubic crystal with millimeter size of Co-MOF-BTB-cube system has been successfully synthesized and is shown in Figure 4.11 (b). However, the single crystal refinement for this crystal is really challenging because (i) Figure 4.12 (a) and (b) show the order and disordered cobalt core where only two of the four central cobalt atoms are occupied in each particular cluster giving four-cobalt chain (only COO- groups are shown for clarity); (ii) The four-cobalt core is coordinated by eight BTB ligands bridging Co1 (terminal) and Co2 (internal) atoms; (iii) Two oxygen atoms (O_3 and O_4) in the core have H atoms located and refined and seem to belong to water; however, two other oxygen atoms (O_1 and O_2) can not be clearly defined. O_1 could be an oxygen from a DMF or NO_3 groups that could not be identified clearly due to disorder, while O_2 could be water which coordinates with two cobalt atoms and makes perfect hydrogen bonds with non-coordinated COO- groups of BTB ligands. These hydrogen bonds are shown as dotted lines in Figure 4.12 (a); (iv) Also delocalized electron density in the cavities were accounted for using SQUEEZE procedure which yielded about 3465 electrons per unit cell. This corresponds to 72 DMF molecules. (v) Considering the third (Co2) and forth (Co2 A) cobalt atoms the composition is $[Co_3(BTB)_2(H_2O)_{3.75}(DMF)_{1.5}]$ ~9·DMF; (vi) This structure should be considered only at framework level (excluding all solvent molecules) of quality probably due to the following: (a) The structure contains a large amount of disordered solvent which could water and/ or DMF which could be partially gone before or during the measurement; (b) Diffraction observed only up to $2\theta = 40^o$ and therefore limits the confidence; (c) Decomposition of the crystal was observed during the experiment. This also could be a phase transition to an ordered/ disordered phase; (d) It also could be that the true symmetry is lower and what we observed is superposition in a

pseudo-cubic arrangement; (vii) The refinement of this crystal was performed with a I23 group with 222 symmetry of the core, however, the structure could be also refined as centrosymmetric $Im\bar{3}$ with mmm symmetry of the core. Although measured at 150K, the doubled reflections are still weak which creates ambiguity in the space group determination; (viii) The structure consists of two three-dimensional interpenetrating frameworks not touching each other. The frameworks are transformed into each other by a body-centered (1/2, 1/2, 1/2) translation vector. Two lanthanide MOF systems with BTB ligands, Eu-MOF-BTB and Ho-MOF-BTB, have been synthesized and detailed information of the measurements and characterization are in Table 4.6. However, the detailed discussion for Ho-MOF-BTB system will be included in chapter 5 and only Eu-MOF-BTB will be investigated here. As shown in Figure 4.13, the Eu-MOF-BTB crystal is formed in the triginal crystal system, with space group *R32*, and lattice parameters of $a = 28.591(1)$Å, $b = 28.591(1)$Å, $c = 12.297(1)$Å, $\gamma = 120^{\circ}$. Substantial disorder of the DMF molecules and perhaps water can be observed in the cavities. Initially the disorder was modeled using difference Fourier peaks, which showed 12 to 15 DMF molecules per unit cell. However single crystal refinement could not produce reasonable model and therefore the SQUEEZE procedure was performed to account for the disordered solvent in the cavities. This yielded about 609 electrons per unit cell which corresponds to 15 DMF molecules per unit cell or 1.7 DMF per europium atom. Nevertheless there could be some water in the cavities as well, which could mean 12 DMF and 13 water molecules per unit cell or 1.33 DMF and 1.43 water molecules per europium atom. Each building unit is constructed by one nine-coordinated europium ions, one BTB ligand and one coordinated water molecule. The nine oxygen atoms coordinated on each europium ion consist of four carboxyl groups from different monodentated

benzoic-acid ligands, two bidentated carboxylic group and one terminal water molecule. The bond distances between Ho-O_{BTB} are in the range of 2.3570(16)-2.7494(14)Å and Ho-O_{water} bond distance is 2.438(3)Å. This 3-D framework has large 6.3 × 6.3Å 1-D hexagonal channels around along c axis which are shown in Figure 4.13 (taking into account the van der Waals radii of the atoms).

(a)

(b)
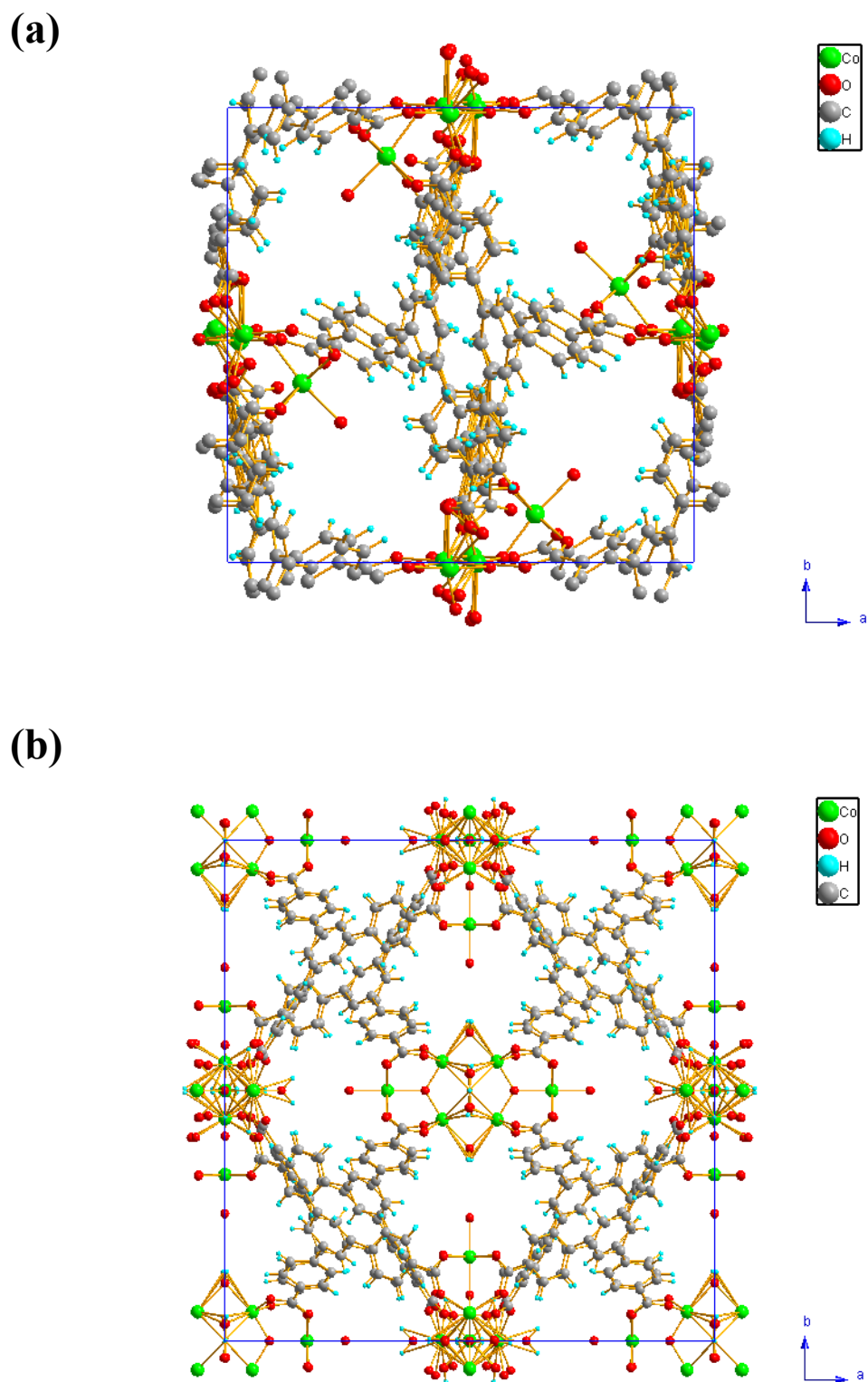
Figure 4.11 Illustrations of 3-D molecular structures for (a) Ho-MOF-BTB-plate and (b) Ho-MOF-BTB-cube crystals viewed along the *c* axis.

(a)
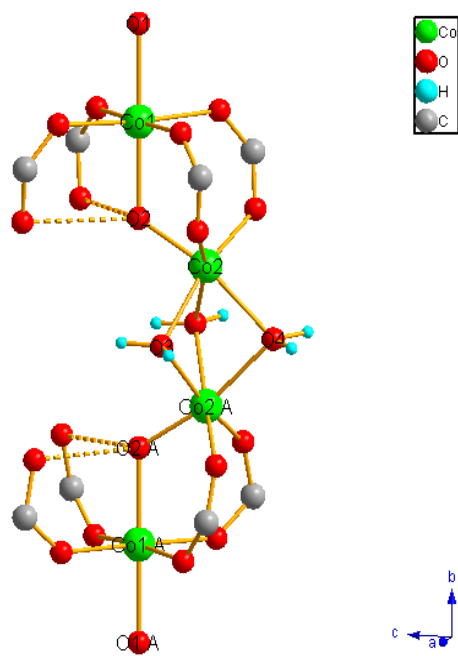
(b)
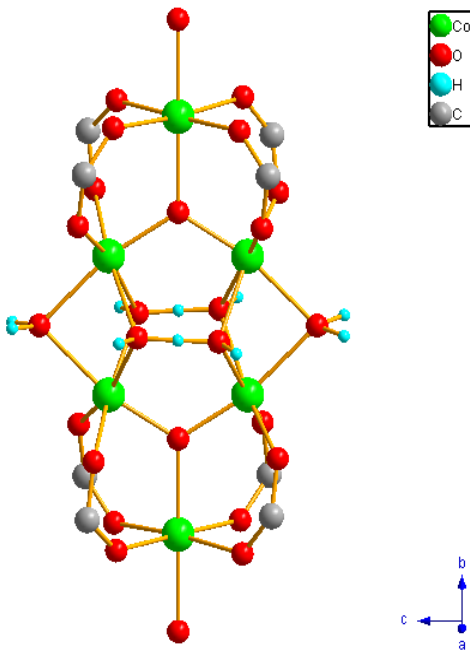
Figure 4.12 (a) Illustrations of ordered and (b) disordered cobalt core in the Ho-MOF-BTB-cube framework.
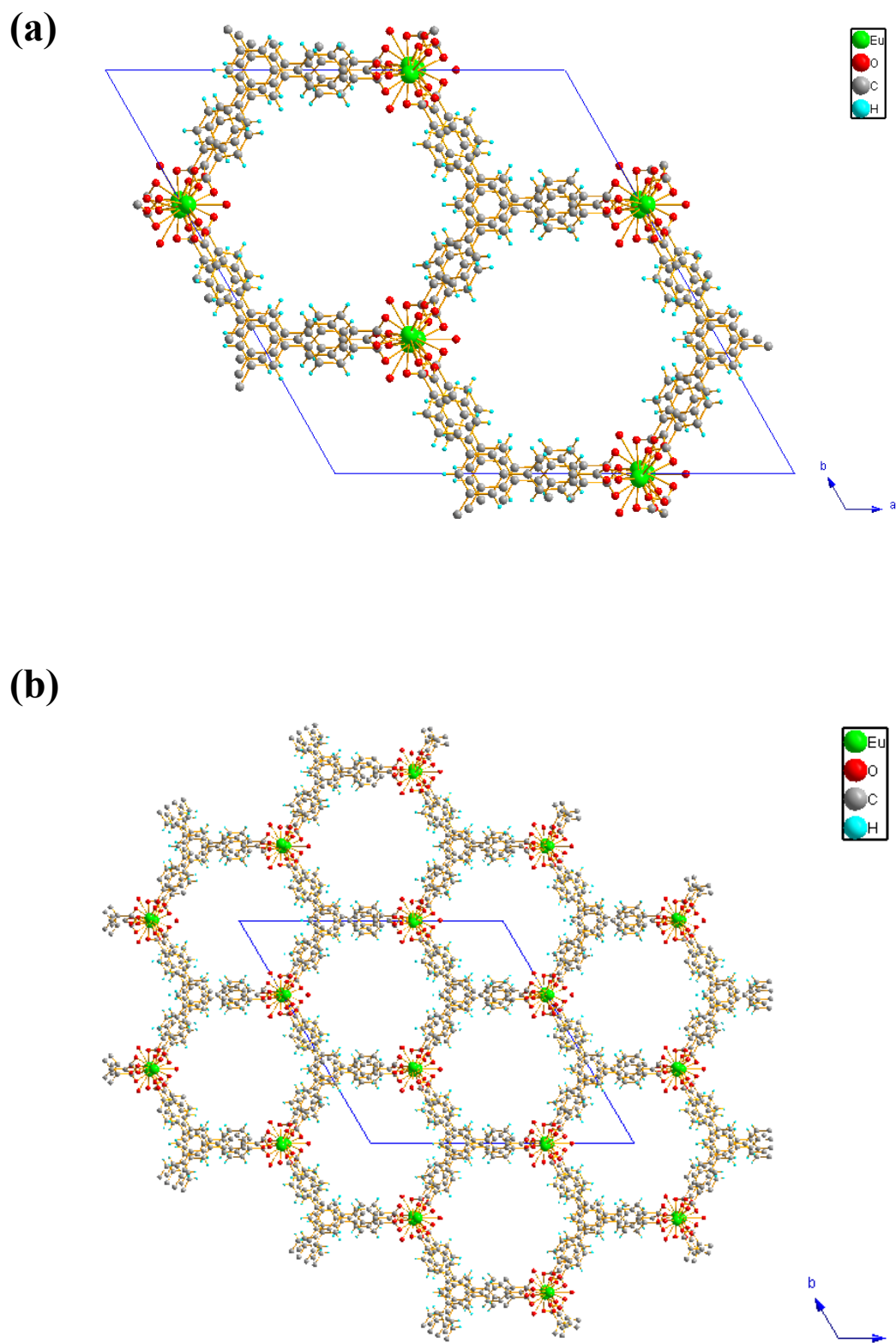
Figure 4.13 Illustration of Eu-MOF-BTB structure with (a) large cavities and (b) 1-D hexagonal channels along the *c* axis.

Systems	Co-MOF-BTB-plate	Co-MOF-BTB-cube
Empirical formula	$(C_{54}H_{36}O_{15}Co_3)\cdot 3C_3H_7NO\cdot 16.5H_2O$	$Co_3(BTB)_2(H2O)_{3.75}(DMF)_{1.5}]\cdot{\sim}9$ C_3H_7NO
Formula weight	2098.17 g/mole	1136.11 g/mole
Temperature	250(2) K	250(2) K
Wavelength	0.71073 Å	0.71073 Å
Crystal size	$0.48 \times 0.275 \times 0.045$ mm^3	$0.48 \times 0.41 \times 0.27$ mm^3
Crystal habit	purple plate	brown cube
Crystal system	Monoclinic	Cubic
Space group	$P2_1/n$	I23 or Im$\bar{3}$
Unit cell dimensions	a = 17.833(2)Å, $\alpha = 90°$	a = 27.227(3) Å, $\alpha = 90°$
	b = 17.666(2) Å, $\beta = 91.017(2)°$	b = 27.227(3) Å, $\beta = 90°$
	c = 27.405(3) Å, $\gamma = 90°$	c = 27.227(3) Å, $\gamma = 90°$
Volume	8632.1(18) Å^3	20183(4) Å^3
Z	4	8
Density, ρ_{calc}	1.614 g/cm^3	0.748 g/cm^3
Absorption coefficient, μ	0.693 mm^{-1}	0.525 mm^{-1}
θ range for data collection	1.78 to 25.00°	N/A
Index ranges	$-21 \le h \le 21, -20 \le k \le 20, -32 \le l \le 32$	$-26 \le h \le 2, -25 \le k \le 5, -22 \le l \le 14$
Reflections collected	106348	7237
Independent reflections	15150	3122
Observed reflection, $I>2\sigma(I)$	12222	2275
Data / restraints / parameters	15150 / 328 / 754	3122 / 165 / 238
Goodness-of-fit on F^2	1.006	1.226
Δ/σ_{max}	0.006	0.004
Final R indices:	$R_1, I > 2\sigma(I) = 0.0760$	$R_1, I > 2\sigma(I) = 0.0762$
	wR$_2$, all data = 0.1591	wR$_2$, all data = 0.1913
	$R_{int} = 0.0550$	$R_{int} = 0.0604$
	$R_{sig} = 0.0347$	$R_{sig} = 0.0434$
$R_1 = \Sigma||F_o|-|F_c||/\Sigma|F_o|, \quad wR_2 = [\Sigma w(F_o^2 - F_c^2)^2/\Sigma w(F_o^2)^2]^{1/2}$		

Table 4.5 The details of measured parameters, structural information and refinement results obtained from single crystal analyses of the Co-MOF-BTB systems.

Systems	Eu-MOF-BTB	Ho-MOF-BTB
Empirical formula	$[Eu(C_{27}H_{15}O_6)\cdot H_2O]\cdot 1.7C_3H_7NO$	$[(C_{27}H_{17}O_6)Ho(H_2O)_2]\cdot 3C_3H_7NO\cdot 2H_2O$
Formula weight	727.19 g/mole	891.67 g/mole
Temperature	220(2) K	250(2) K
Wavelength	0.71073 Å	0.71073 Å
Crystal size	$0.21 \times 0.14 \times 0.12$ mm^3	$0.33 \times 0.12 \times 0.09$ mm^3
Crystal habit	colorless needle	pink prism
Crystal system	Trigonal	Triclinic
Space group	R32	P$\bar{1}$
Unit cell dimensions	a = 28.5908(9) Å, $\quad$ α = 90°	a = 9.2435(10) Å, $\quad$ α = 106.733(2)°
	b = 28.5908(9) Å, $\quad$ β = 90°	b = 13.8346(14) Å, $\quad$ β = 96.244(2)°
	c = 12.2970(7) Å, $\quad$ γ = 120°	c = 15.3162(16) Å, $\quad$ γ = 94.620(2)°
Volume	8705.3(6) Å^3	1851.7(3) Å^3
Z	9	2
Density, ρ_{calc}	1.248 g/cm^3	1.599 g/cm^3
Absorption coefficient, μ	1.665 mm^{-1}	2.206 mm^{-1}
θ range for data collection	1.85 to 29.99°	2.23 to 27.50°
Index ranges	$-40 \leq h \leq 40$, $-40 \leq k \leq 40$, $-17 \leq l \leq 17$	$-12 \leq h \leq 12$, $-17 \leq k \leq 17$, $-19 \leq l \leq 19$
Reflections collected	34303	23547
Independent reflections	5656	8431
Observed reflection, $I>2\sigma(I)$	5526	7354
Data / restraints / parameters	5656 / 0 / 162	8431 / 442 / 641
Goodness-of-fit on F^2	1.000	0.982
Δ/σ$_{max}$	0.001	0.001
Final R indices:	$R_1, I > 2\sigma(I) = 0.0175$	$R_1, I > 2\sigma(I) = 0.0368$
	wR$_2$, all data = 0.0445	wR$_2$, all data = 0.0842
	R$_{int}$ = 0.0259	R$_{int}$ = 0.0365
	R$_{sig}$ = 0.0164	R$_{sig}$ = 0.0423
$R_1 = \Sigma ||F_o|-|F_c||/\Sigma|F_o|$, $\quad$ **$wR_2 = [\Sigma w(F_o^2 - F_c^2)^2/\Sigma w(F_o^2)^2]^{1/2}$**		

Table 4.6 The details of measured parameters, structural information and refinement results obtained from single crystal analyses of the Ln-MOF-BTB systems.

4.7 References

(1) A. L. Spek, *"PLATON/SQUEEZE - An Effective Tool for Taking the Contribution of Disordered Solvent into Account in Crystal Structure Refinement."* Bijvoet Center for Biomolecular Research, Utrecht University, Padualaan 8, 3584 CH Utrecht, Netherlands.
(2) van der Sluis, P. and Spek, A. L. *Acta Cryst.* **1990**, *A*, 194.

Chapter 5: Holmium Metal-Organic Framework Materials: Structural Dimensionality, Stability and Properties

5.1 Abstract

Two different structures of holmium metal-organic framework materials (Ho-MOFs) with rigid aromatic linkages 1, 3, 5-Benzene tricarboxylic acid (Ho-MOF-BTC) and 1, 3, 5-Tris(4-carboxyphenyl)benzene (Ho-MOF-BTB) have been successfully synthesized. The structure of Ho-MOF-BTC system identified by single crystal diffraction crystallizes in a tetragonal $P4_122$ space group, with lattice parameters of $a = 10.275(0)$Å, $b = 10.275(0)$Å, $c = 14.483(1)$Å, and in a triclinic $P\bar{1}$ space group, with lattice parameters of $a = 9.244(1)$Å, $b = 13.835(1)$Å, $c = 15.316(2)$Å, $\alpha = 106.733(2)^{o}$, $\beta = 96.244(2)^{o}$, $\gamma = 94.620(2)^{o}$ for the Ho-MOF-BTB_system. *In-situ* synchrotron powder X-ray (PXRD) diffraction, thermogravimetric analysis (TGA) and neutron diffraction results show that the three-dimensional (3-D) structure of Ho-MOF-BTC system robust up to 508°C. Moreover, a comparison of the *in-situ* Raman patterns of two-dimensional (2-D) Ho-MOF-BTB at ambient conditions and in its less crystalline state at elevated temperatures (ca. 116°C) demonstrate that the compound although disordered, still possesses structural integrity.

5.2 Introduction

In this chapter, we perform a systematic study between different framework dimensionalities with the same lanthanide ion. More specifically, we present the syntheses of 2-D and 3-D metal-organic framework complexes with holmium as the central metal, which coordinates with rigid organic ligands, 1, 3, 5-Benzene tricarboxylic

acid (Ho-MOF-BTC) and 1, 3, 5-tris(4-carboxphenyl)benzene (Ho-MOF-BTB). The experimental results show that dimensionality of the framework has a strong effect on the thermal/structural stability. Dynamic information on guest-host behavior has been measured by in-situ Raman spectroscopy.

5.3 Results

5.3.1 Crystal Structure of Ho-MOF-BTC System

The chemical formula of Ho-MOF-BTC, $2[(C_9H_3O_6)\ Ho(H_2O)]\cdot C_3H_7NO\cdot 0.5H_2O$, was determined by single crystal X-ray diffraction and thermogravimetric analysis. The X-ray diffraction result reveals that Ho-MOF-BTC crystal is a 3-D network containing 1-D channels, and crystallizes in the tetragonal crystal system, with space group $P4_122$, and lattice parameters of $a = 10.275(0)$Å, $b = 10.275(0)$Å, $c = 14.483(1)$Å. Each building unit is constructed by one seven-coordinated holmium ion, one BTC ligand and one water molecule. The guest DMF molecules are totally disordered in the crystal as determined by single crystal diffraction at 250(2)K. The seven oxygen atoms coordinated with each holmium ion consist of six carboxyl groups from different monodentated benzoic-acid ligands and one terminal water molecule. The bond distances between Ho-O_{BTC} are in the range 2.284(3)-2.297(3)Å and Ho-O_{water} bond distance is 2.381(5)Å. The crystal structure is similar to other reported metal-organic framework complexes[1-5] and forms 1-D ca. 6.6 × 6.6Å pseudo-circular channels along c direction, which are filled with coordinated water molecules and DMF solvent (taking into account the van der Waals radii of the atoms) as shown in Figure 5.1. Moreover, the details of measured parameters, structural information and refinement results for the single crystal analysis has been organized and tabulated in Table 5.1.
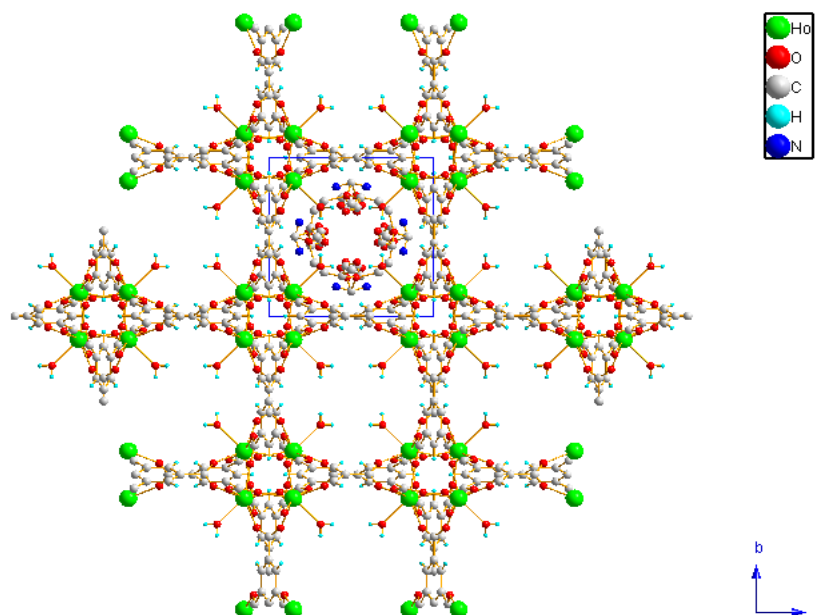
Figure 5.1 The as-synthesized Ho-MOF-BTC molecular structure viewed along the *c* axis.

5.3.2 Thermal and Structural Properties of Ho-MOF-BTC System

The data from a thermogravimetric experiment (TGA) shown in Figure 5.1 performed under N_2 flow 60ml/min and 2°C/min heating rate shows the weight of Ho-MOF-BTC complex is unstable above room temperature as the sample loses the free guest DMF solvent molecules immediately upon heating. Two obvious plateaus are observed, indicating that there are two possible stable phases from room temperature up to ca. 600°C. The weight loss for the first and second phase are 8.66 wt% and 5.28 wt%, respectively and comparable to the theoretical calculation of free DMF (8.48 wt%) and coordinated water molecules (5.22 wt%) based on the molecular formula. The dramatic weight loss above 508°C is attributed to the decomposition of the compound and the remaining weight of 44.67wt% is the oxide of holmium, Ho_2O_3, and is comparable to the

estimation of 43.8wt%[1].
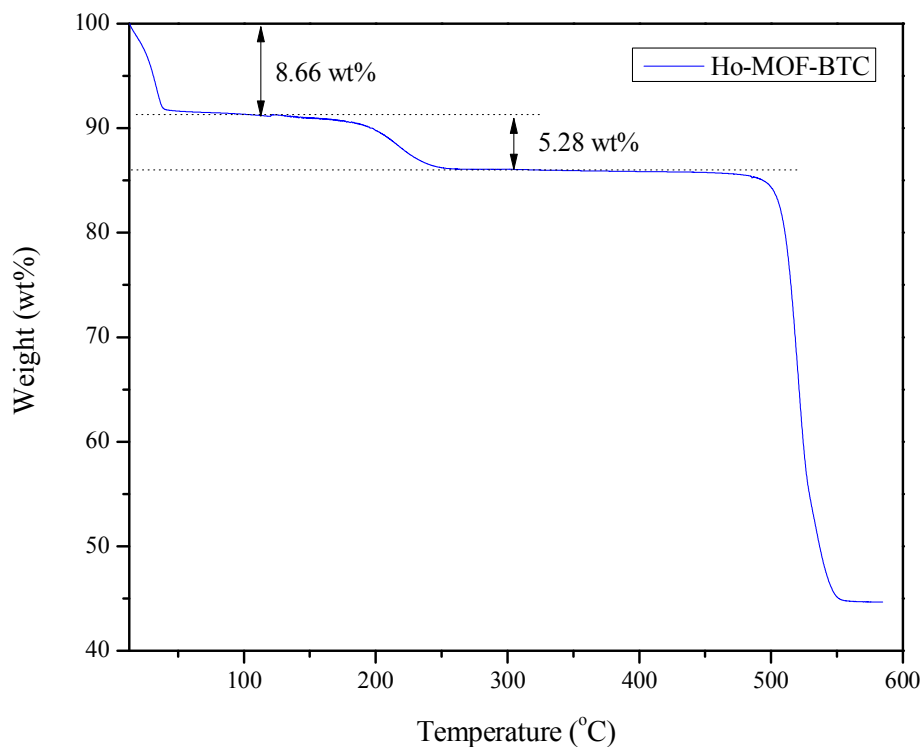
Figure 5.2 Thermogravimetric analysis (TGA) for the Ho-MOF-BTC system.

The structure stability is identified by *in-situ* synchrotron powder X-ray diffraction from 32.5 to 527.48°C as shown as Figure 5.3, showing the Bragg peak intensities are still maintained until 500°C. Furthermore, the PXRD pattern at 32.5°C can be extracted and well-refined by the as-synthesized structure using Rietveld method (Figure 5.4). The residual factor based on the entire powder pattern (weighted R factor, wR_p) is 3.65%, and the Bragg peak integrated intensities (R factor, R_p) is 2.73%, respectively. This result demonstrates that a highly pure phase can be obtained from the chemical synthesis which is an important property for applications. However, the experimental data at elevated temperatures possess too many impurity peaks caused by the decomposition of guest

molecules as this measurement was not performed under vacuum. Therefore, a high resolution powder neutron pattern (PND) in Figure 5.5 has been performed for a pre-dehydrated Ho-MOF-BTC system (at 250°C for 10 hours) and again refined by Rietveld method with wR_p = 4.16% and R_p = 3.43%. 3-D degassed structure can be reconstructed as shown as Figure 5.6. The structures are almost the same between as-synthesized and dehydrated sample with the lattice parameters changing from a = 10.279(0)Å, b = 10.279(0)Å, c = 14.453(1)Å to a = 10.293(0)Å, b = 10.293(0)Å, c = 13.818(1)Å. The data indicate that the structure does not collapse during the departure of the guest DMF solvent and coordinated water, and a permanent porous framework can be maintained until the whole structure is destroyed above 508°C. The high thermal/ structural stability of Ho-MOF-BTC system is so important to obtain the high porous structure at elevated temperatures then adsorbs H_2 gas at low temperatures.
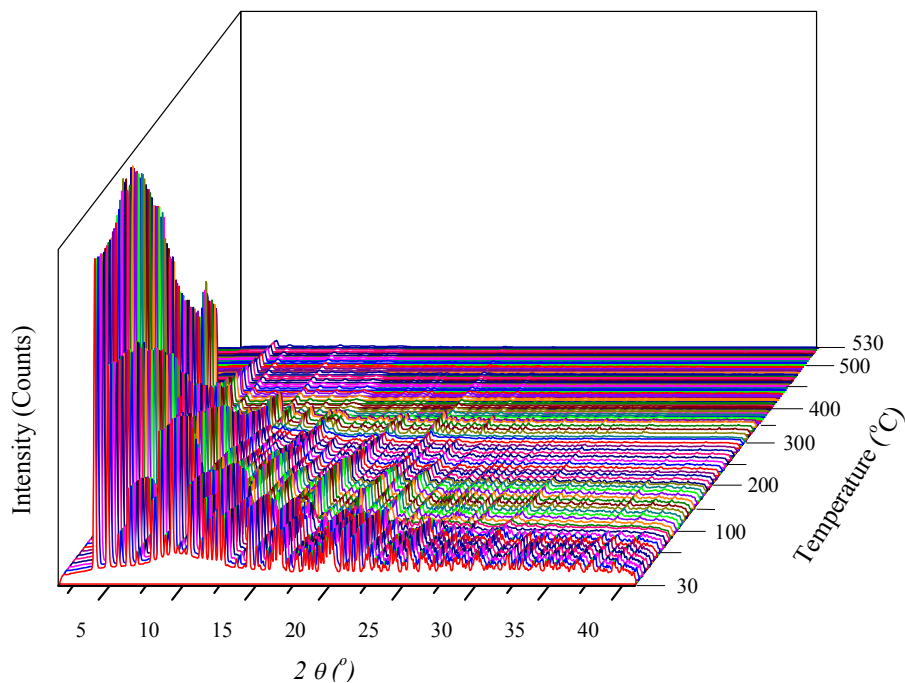
Figure 5.3 The 3-D *in-situ* synchrotron PXRD profile from 32.5 to 527.48°C for Ho-MOF-BTC system.
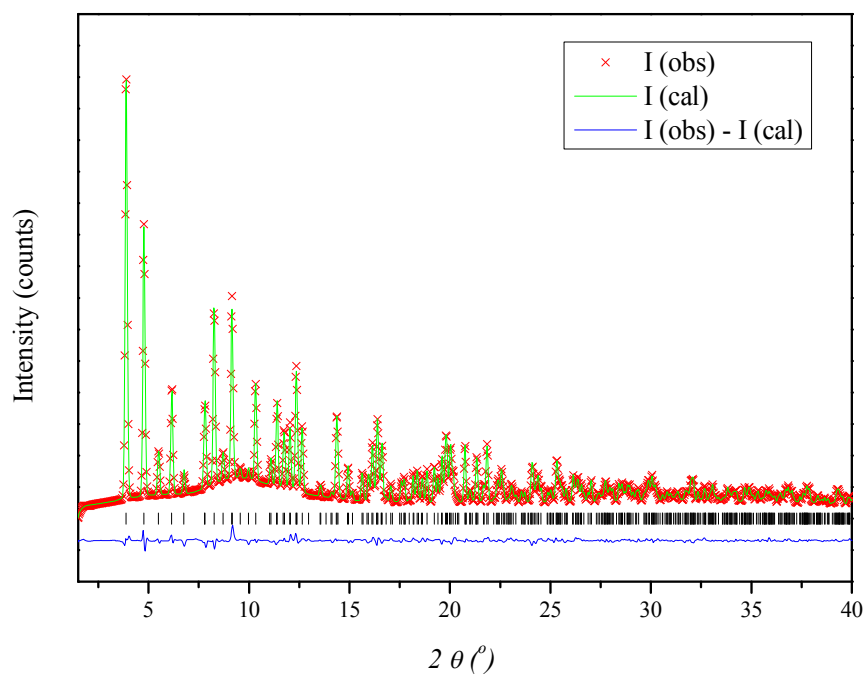
Figure 5.4 Rietveld refinement of synchrotron PXRD pattern for as-synthesized Ho-MOF-BTC system with $wR_p = 3.65\%$, and $R_p = 2.73\%$.
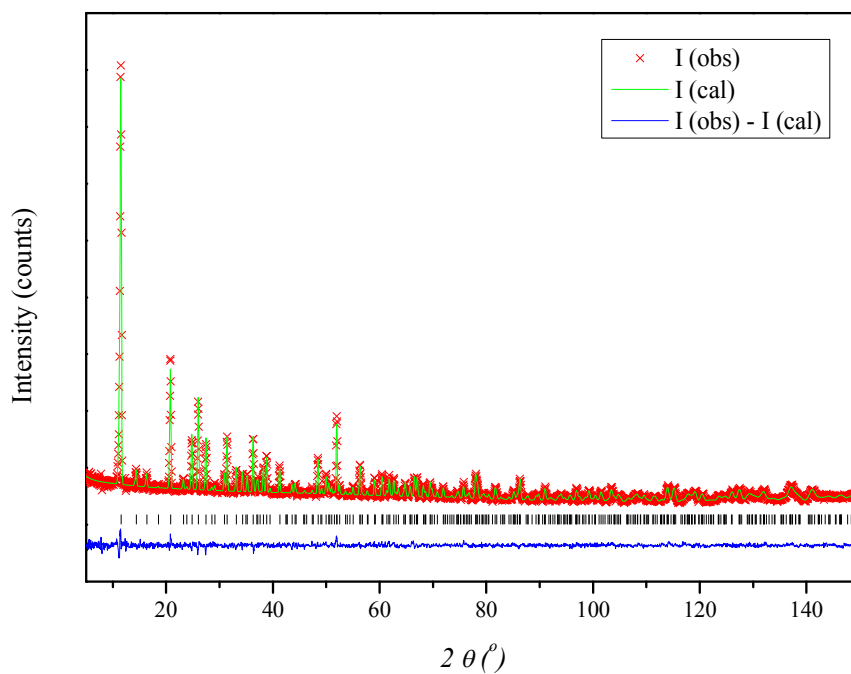
Figure 5.5 Rietveld refinement of PND pattern for dehydrated Ho-MOF-BTC system with $wR_p = 4.16\%$, $R_p = 3.43\%$.
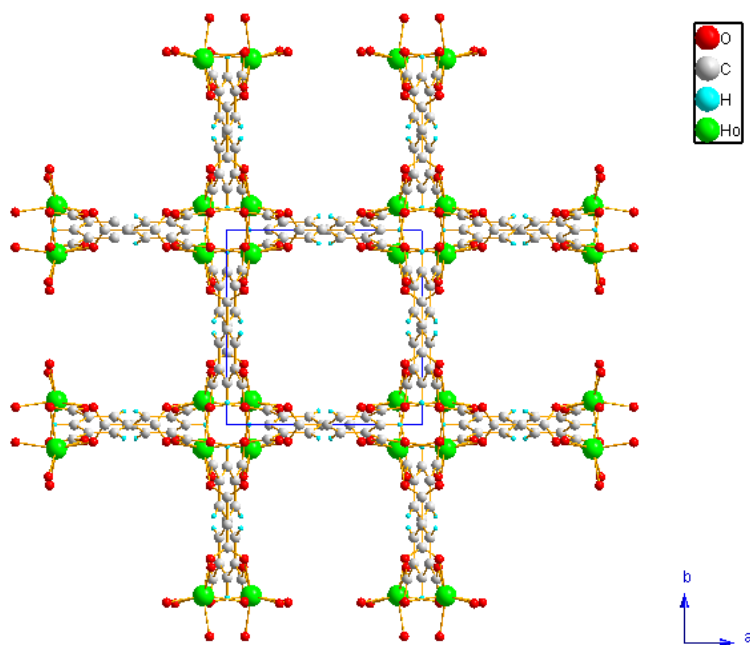
Figure 5.6 The 3-D dehydrated molecular structure of Ho-MOF-BTC system viewed along the *c* axis.

5.3.3 Crystal Structure of Ho-MOF-BTB System

Single crystal X-ray diffraction reveals the molecular formula for the as-synthesized Ho-MOF-BTB system is $[(C_{27}H_{17}O_6)Ho(H_2O)_2]\cdot 3C_3H_7NO\cdot 0.5H_2O$, and the crystal structure is a triclinic $P\bar{1}$ space group, with lattice parameters $a = 9.244(1)$Å, $b = 13.835(1)$Å, $c = 15.316(2)$Å, $\alpha = 106.733(2)^{\circ}$, $\beta = 96.244(2)^{\circ}$, $\gamma = 94.620(2)^{\circ}$. Each structural unit $((C_{27}H_{17}O_6)Ho(H_2O)_2)$ includes one nine-coordinated holmium ion, one BTB ligand and two terminal water molecules. The free space in crystal is occupied by disordered DMF solvent and water molecules. Nine oxygen atoms coordinate on the holmium ion and come from carboxyl groups belonging to three different BTB ligands, two terminal water molecules and one coordinated hydroxyl group as bridging atom to form a Ho-O-C-O-Ho linkage. The distances of Ho-O_{BTB} bonds are in the range of

2.334(3)-2.767(3)Å and the Ho-O$_{water}$ bond distance for first and second coordinated water molecules is 2.361(3) and 2.399(3)Å, respectively. As shown in Figure 5.7 (a)-(c), the crystal structure resembles a large cage with a high degree of porosity that is filled with free guest DMF solvent and water molecules. A quasi-honeycomb shaped channel structure (Figure 5.7 (c).) is observed along c axis. In addition, the details of measured parameters, structural information and refinement results for the single crystal analysis has been organized and tabulated in Table 5.1.

(a)

(b)

(c)

Figure 5.7 (a)-(c) The as-synthesized Ho-MOF-BTB molecular structure viewed along *a*, *b* and *c* axes, respectively.
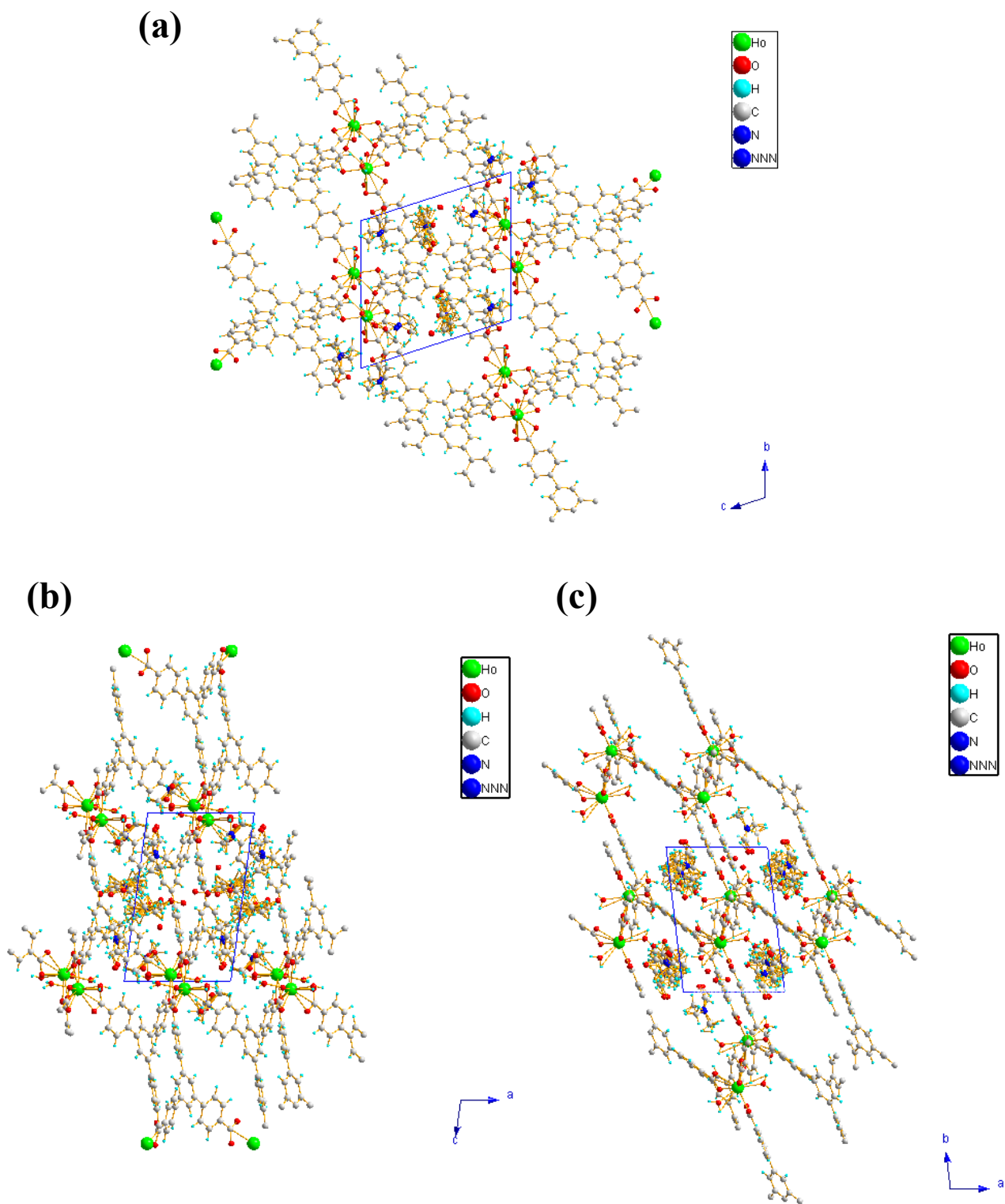
5.3.4 Thermal and Structural Properties of the Ho-MOF-BTB System

Thermogravimetric analysis (TGA) on the Ho-MOF-BTB system in Figure 5.8 is executed under the same conditions as the Ho-MOF-BTC system and a similar behavior is observed for the instability of the crystal at room temperature. There is one weight loss transition in the Ho-MOF-BTB system between ca. 65°C to 150°C. The corresponding weight loss of 22.79wt% is not consistent with the molecular weight ratio of DMF and water (28.63wt%) from single crystal identification. The discrepancy between the theoretical and experimental results is related to the crystal structure of Ho-MOF-BTB system. A large plateau over the wide temperature range from ca. 170°C to 400°C means that a very stable phase should be observed between these temperatures. However, a stable phase observed in the TGA data can not be assumed to be the same structural configuration as the as-synthesized state and needs to be verified by *in-situ* high temperature PXRD. A more comprehensive study and discussion will be proposed later in the discussion section. Similarly, decomposition of the sample occurs above 450°C resulting in a dramatic weight loss. *In-situ* synchrotron PXRD technique is used to examine the structural stability and shown by a 2-D contour plot in Figure 5.9. A well-refined PXRD pattern (Figure 5.10) at 32.3°C can be obtained (wR$_p$ = 3.08%, R$_p$ = 2.18%) from the Ho-MOF-BTB as-synthesized structure. Two small impurity peaks were ignored during the refinement. Surprisingly, the *in-situ* PXRD pattern at 116°C is the same as that at 169.2°C and reveals a total disappearance of crystallinity indicating the crystal structure collapses at 116°C. The major remaining peak ($d = 14.80$Å) indicates the size of Ho-BTB fragment that is calculated from PXRD pattern, and comparable to the molecular model ($d = 15.22$Å). The results show that the structure is totally collapsed and separated after the departure of the DMF and water molecules. No well defined structure

146

is observed at high temperature.
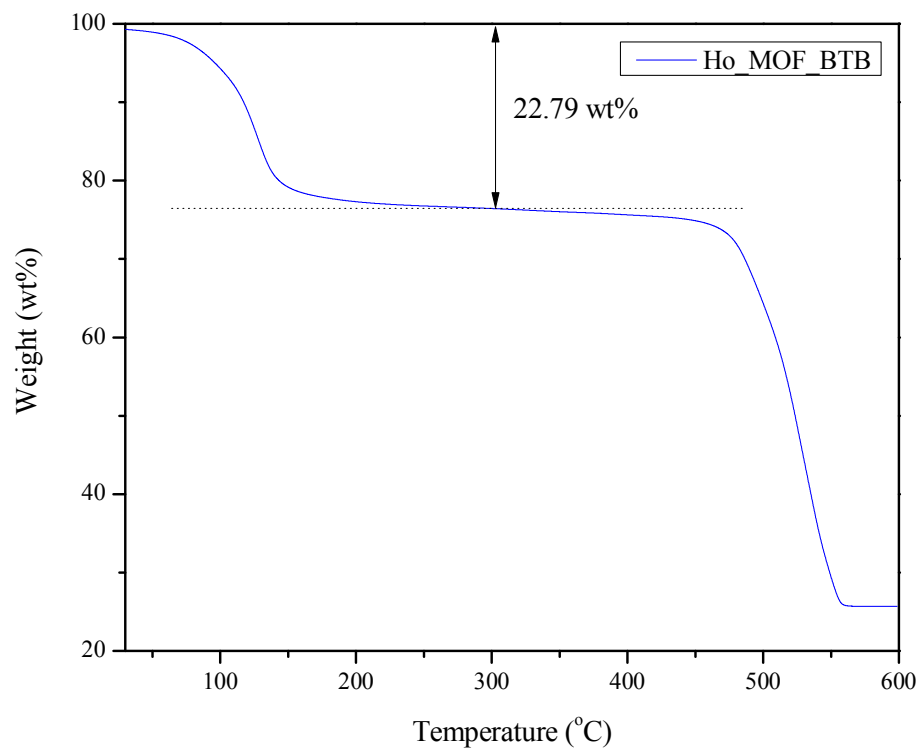
Figure 5.8 Thermogravimetric analysis (TGA) for the Ho-MOF-BTB system.
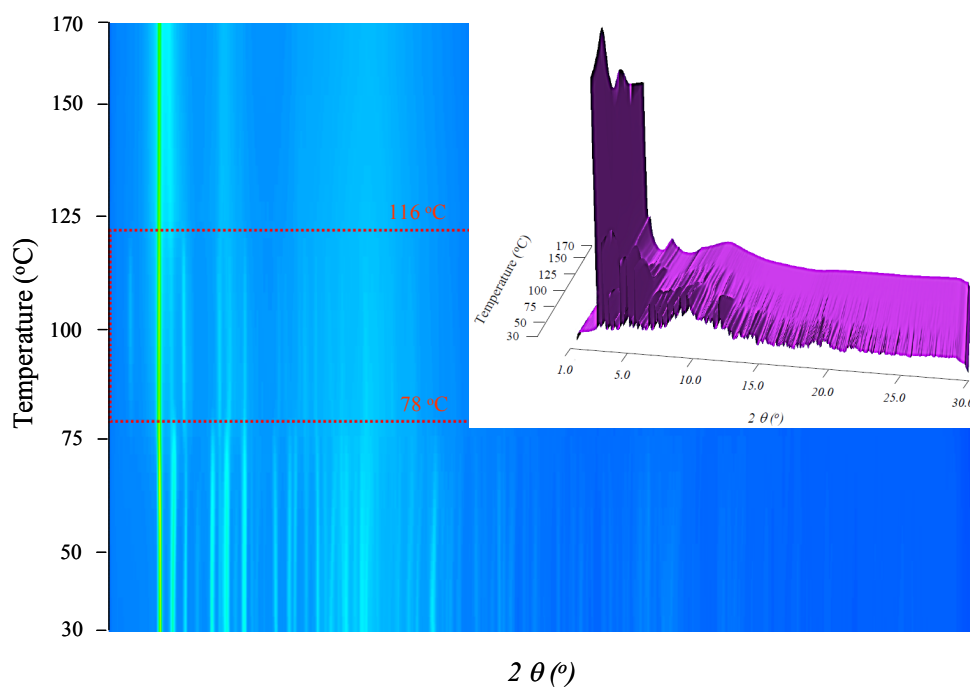
Figure 5.9 *In-situ* synchrotron PXRD from 32.3 to 169.2°C for Ho-MOF-BTB system.

Insert is a corresponding 3-D profile.
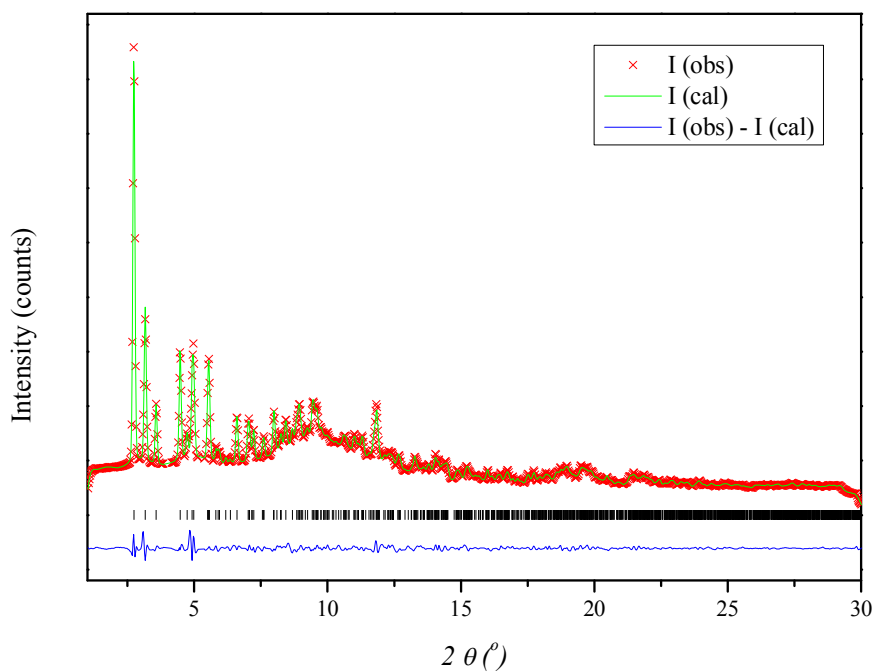
Figure 5.10 Rietveld refinement of synchrotron PXRD pattern for the as-synthesized

Ho-MOF-BTB system with $wR_p = 3.08\%$, $R_p = 2.18\%$.

Systems	Ho-MOF-BTC	Ho-MOF-BTB
Empirical formula	$2[(C_9H_3O_6)\ Ho(H_2O)]\cdot C_3H_7NO\cdot 0.5H_2O$	$[(C_{27}H_{17}O_6)Ho(H_2O)_2]\cdot 3C_3H_7NO\cdot 2H_2O$
Formula weight	862.23 g/mole	891.67 g/mole
Temperature	250(2) K	250(2) K
Wavelength	0.71073 Å	0.71073 Å
Crystal size	$0.51 \times 0.030 \times 0.025$ mm^3	$0.33 \times 0.12 \times 0.09$ mm^3
Crystal habit	colorless needle	pink prism
Crystal system	Tetragonal	Triclinic
Space group	$P4_122$	$P\bar{1}$
Unit cell dimensions	a = 10.2749(3) Å, $\alpha = 90°$	a = 9.2435(10) Å, $\alpha = 106.733(2)°$
	b = 10.2749(3) Å, $\beta = 90°$	b = 13.8346(14) Å, $\beta = 96.244(2)°$
	c = 14.4832(10) Å, $\gamma = 90°$	c = 15.3162(16) Å, $\gamma = 94.620(2)°$
Volume	1529.04(12) Å^3	1851.7(3) Å^3
Z	2	2
Density, ρ_{calc}	1.892 g/cm^3	1.599 g/cm^3
Absorption coefficient, μ	5.205 mm^{-1}	2.206 mm^{-1}
θ range for data collection	2.43 to 29.99°	2.23 to 27.50°
Index ranges	$-12 \leq h \leq 12,\ -17 \leq k \leq 17,\ -19 \leq l \leq 19$	$-12 \leq h \leq 12,\ -17 \leq k \leq 17,\ -19 \leq l \leq 19$
Reflections collected	5759	23547
Independent reflections	2172	8431
Observed reflection, I>2σ(I)	2060	7354
Data / restraints / parameters	2172 / 83 / 160	8431 / 442 / 641
Goodness-of-fit on F^2	0.986	0.982
Δ/σ$_{max}$	0	0.001
Final R indices:	R$_1$, I>2σ(I) = 0.0197	R$_1$, I>2σ(I) = 0.0368
	wR$_2$, all data = 0.0533	wR$_2$, all data = 0.0842

Table 5.1 The details of measured parameters, structural information and refinement obtained from the single crystal analyses of the Ho-MOF-BTC and Ho-MOF-BTB systems.

5.4 Discussions

5.4.1 Structure Differences and Comparison between the Ho-MOF-BTC and Ho-MOF-BTB Systems

The thermal and structural properties of holmium MOFs with different ligands are clearly sensitive to the specific ligand that controls the overall structural architecture. MOF materials always possess complicated framework structures and sometimes necessary to simplify the structures by geometric graphs using a quasi-topology method. In the Ho-MOF-BTC system, we have substituted the BTC ligand with a co-planar tripod because of the rigid benzene ring (Figure 5.11 (d)). There are three connected nodes corresponding to three different carboxylic groups. The simplified structures viewed along the *a*, *b* and *c* axes are shown in Figure 5.11 (a)-(c). It is straightforward to imagine the blue scaffold as "rigid bridge" between two lanthanide ions. From Figure 5.11 (c), the pseudo-circular channels are surrounded by the model tripods and form a stable structure at high temperature. Viewing along the *a* and *b* axes (Figure 5.11 (a) and (b).), the similar "Ho-O-hard bridge-O-Ho" chiral chain structure is observed. Each of the two lanthanide ions on the chain can be treated as a "pair" engaged by one rigid bridge and "each pair" is linked by another side rigid bridge that are alternatively perpendicular to each other along the *a* and *b* axes. Moreover, the co-planar scaffold changes up and down along the *c* axis (if viewed from *a* axis) as shown in Figure 5.11 (a). This will enhance the stability of the structure because each connected nodes join three different "lanthanide ion pairs" together. The 3-D interlocked network results in the robust framework for the dehydrated Ho-MOF-BTC system and helps to maintain the porosity until the decomposition temperature of $508^{o}C$, where the Ho-O-hard bridge-O-Ho chain and structure is lost.

For the Ho-MOF-BTB crystal structure, the BTB ligand can be imagined as a

co-planar tripod with a small amount of distortion because of the longer ligand length (Figure 5.12 (d).). A 2-D planer structure can be seen when viewed along the a and b axes (Figure 5.12 (a)-(b).). The rigid ligand bridges coordinate with each lanthanide ion pair with alternating bridges being above and below the plane when viewed along the b axis (Figure 5.12 (b).) and penetrate to each other to form a rhombic network. The crystal structure would appear stable if only viewed along these two directions, but this conclusion conflicts with the PXRD analysis which indicates that sample will lose crystallinity at elevated temperatures. From Figure 5.12 (c), an individual "double-layer sandwich" structure is observed if we rotate and view the structure along the (011) axis. There is no long lanthanide ion pair chain structure and a discontinuous and separated sheet structure as present. The crystal structure may be formed by weak interactions such as van der Waals forces, polarity and π-π interactions from the benzoic acid groups and solvent[6,7]. The structure in the Ho-MOF-BTB system has a strongly bonded 2-D network but weakly bound in the third dimension, as a result of the absence of continuous Ho-O-hard bridge-O-Ho linkage. The double layer units stack along the (010) axis without chemical bonding and form a 2-D planer structure. The open scaffold allows easy escape of solvent molecules and is consistent with the observed TGA behavior that will be discussed later.
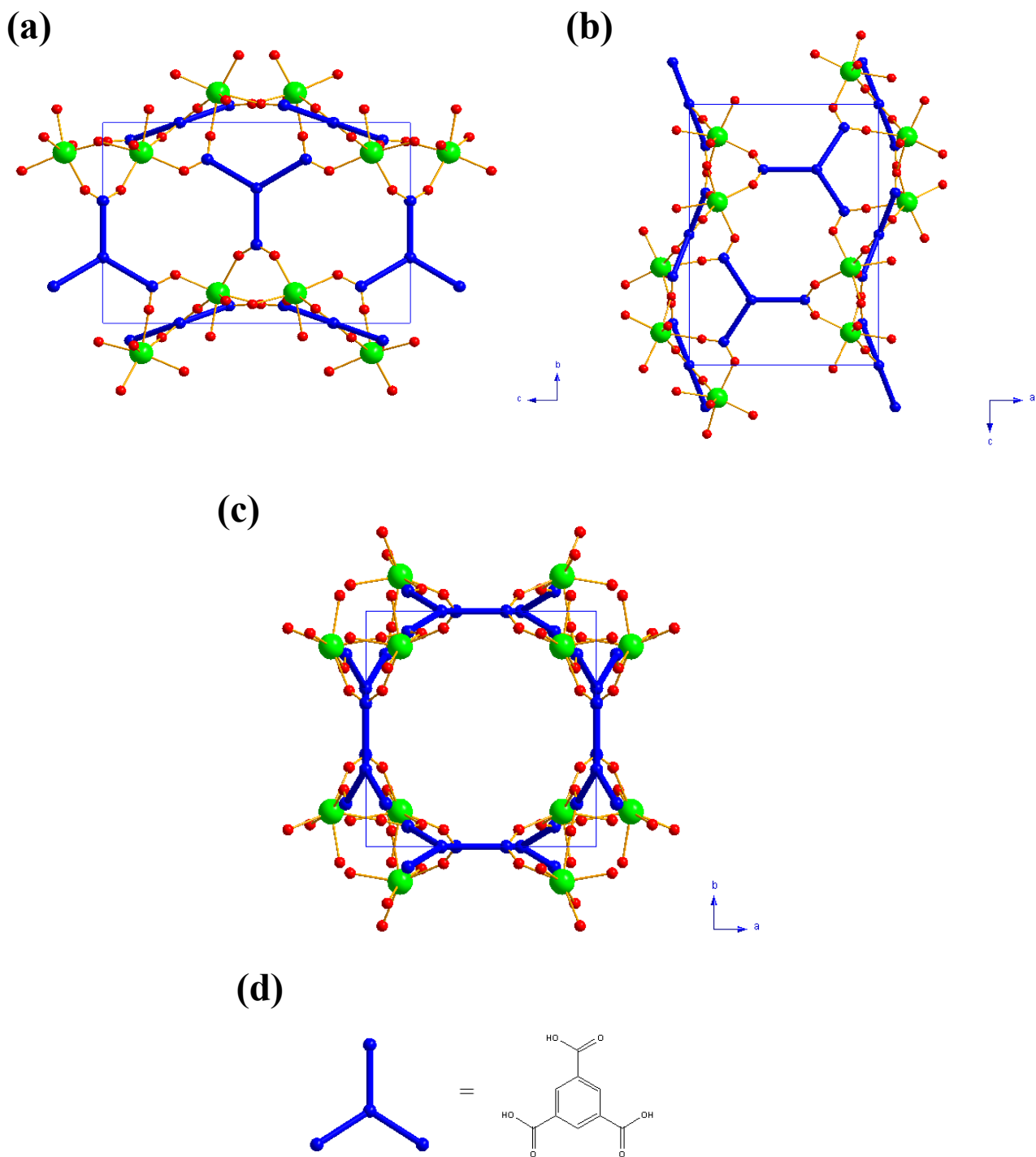
Figure 5.11 (a)-(c) The pseudo-topology analyses for the dehydrated Ho-MOF-BTC system along the *a*, *b* and *c* axes, respectively. Figure 5.11 (d) BTC ligand imaged as a co-plane tripod because of the rigid benzene ring.

(a)

(b)

(c)

(d)
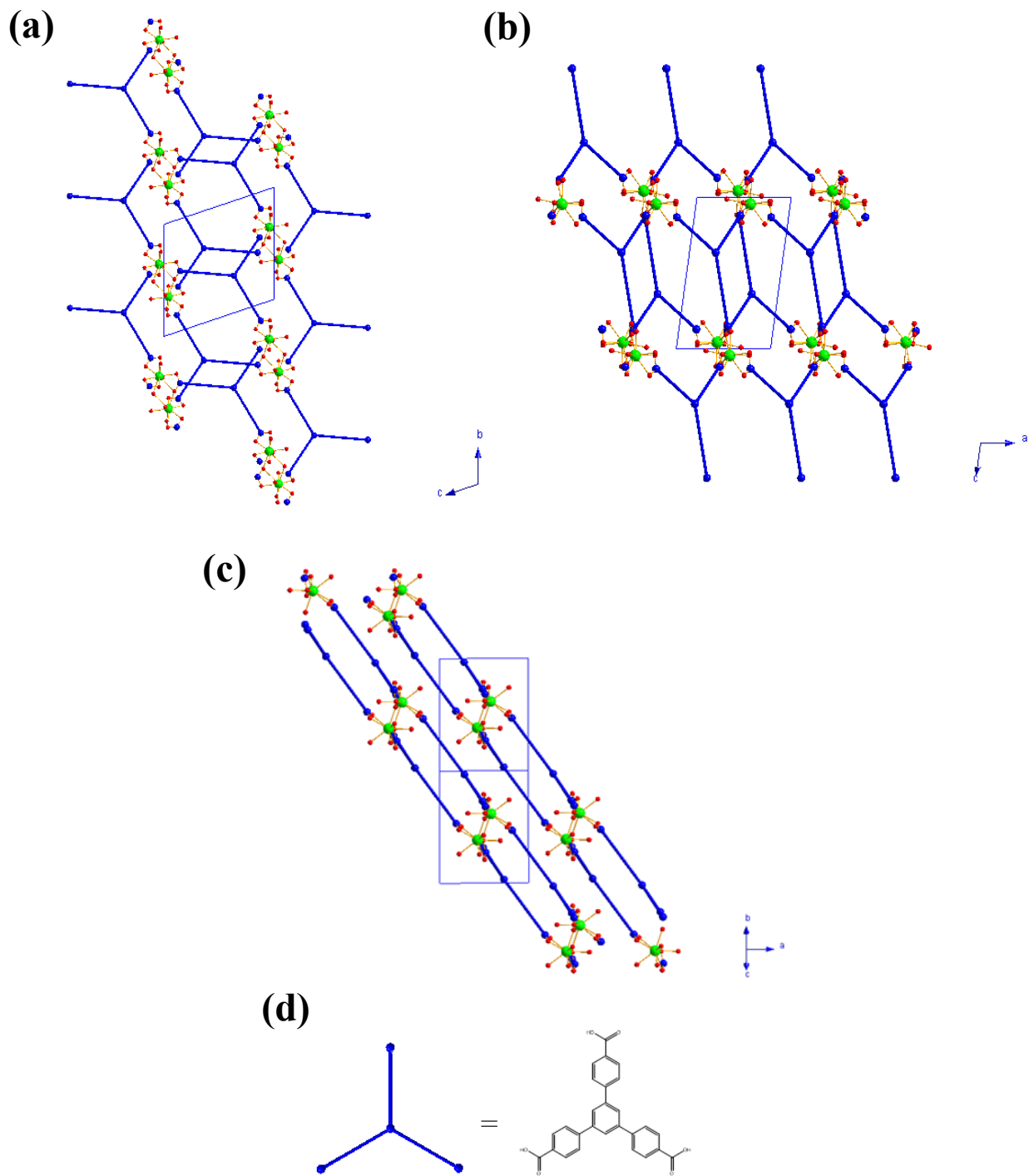
Figure 5.12 (a)-(b). The pseudo-topology analyses for the dehydrated Ho-MOF-BTB system along the *a* and *b* axes.   Figure 5.12 (c). shows the simplified structure along (011) axis. Figure 5.12 (d). The BTB ligand imaged as a co-plane tripod with a little distortion because of the longer ligand length.

5.4.2 Thermogravimetric Analysis (TGA) Studies

The TGA experimental results are consistent with the molecular formula from single crystal diffraction for the Ho-MOF-BTC system, but discrepancies are observed for TGA and single crystal diffraction experiments in the Ho-MOF-BTB case. The reason is due to the difference in the two crystal structures. A 3-D robust network is constructed for the Ho-MOF-BTC system, with a 1-D pseudo-circular channels. For the Ho-MOF-BTB system, a 2-D alternating-stack layer structure is observed for the as-synthesized sample which forms an amorphous phase at relatively low temperatures. It is easier to understand that the free guest solvents (i.e. DMF and water) can evaporate from small channels in the Ho-MOF-BTC system but relatively more difficult than from a sheet-like open structure in Ho-MOF-BTB system. The as-synthesized samples will keep losing free solvent after purification and so the weight of as-synthesized samples in both systems is unstable at room temperature. For the Ho-MOF-BTB system, it is reasonable to expect that some of the guest solvent molecules are lost prior to the TGA measurement. If the Ho-MOF-BTB crystals are stored in air at room temperature, the weight will gradually decrease, with the crystallinity disappearing. It is not possible to reliably identify the guest solvent molecules from the TGA results for Ho-MOF-BTB system because of the 2-D crystal structure. Another interesting behavior observed from the TGA data for the Ho-MOF-BTC system is that the first weight loss step is correlated with the loss of the DMF guest solvent molecules, even though the boiling temperature of DMF (b.p. $\approx$ 153°C) is higher than water (b.p. $\approx$ 100°C). This can be explained as that the DMF guest solvent is "free" in the channels of crystal structure and only bound by physical adsorption while water molecules "bond" with the lanthanide ions. The interaction strength of the water molecules is much higher than for the DMF molecules and hence

the DMF is lost before the water for the Ho-MOF-BTC system.

5.4.3 *In-situ* Raman Spectroscopy for the Ho-MOF-BTB System

The low structural stability of 2-D Ho-MOF-BTB crystal has been demonstrated by *in-situ* synchrotron PXRD with a combination of *in-situ* Raman spectroscopy, which offers information on guest molecules during the phase transformation. As shown in Figure 5.13, the Raman spectra at various temperatures exhibit a difference in the broad peak between 3100-4000cm^{-1} that is induced by different interactions between guest molecules and crystal structure. The comparison shows two decreasing peak intensities on ca.3337cm^{-1}, 3573cm^{-1} and an increasing peak intensity on ca.3629cm^{-1} for this sheet-like metal-organic framework from its well-defined structure to a less crystalline state at high temperatures, implying the escape of guest molecules and less motional hindrance from crystal. However, all major peaks caused by C=C bond vibration on aromatic rings perform the similar patterns, indicating no bond breaking occurs. The phenomenon can also be observed by high temperature *in-situ* synchrotron PXRD, which exhibits a strong, sharp peak and is corresponding to the repeated unit size of the layer structure.
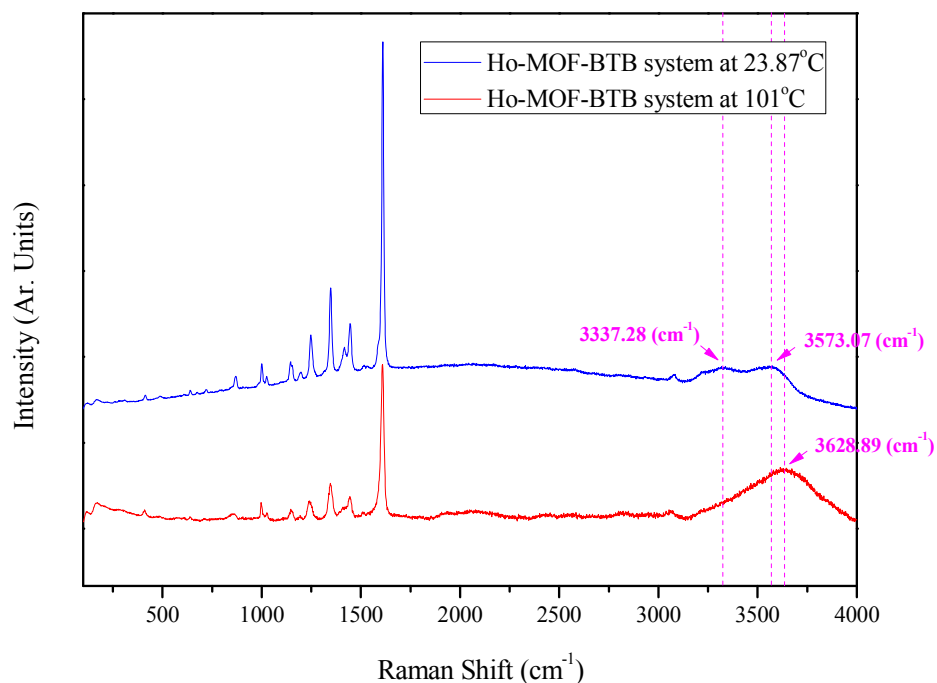
Figure 5.13 *In-situ* Raman spectroscopy for Ho-MOF-BTB system at 23.87 to 170°C.

5.4.4 Magnetic Properties for Ho-MOF-BTC System

Superconducting quantum interference device (SQUID) measurements have been performed on as-synthesized and dehydrated Ho-MOF-BTC systems. As shown in Figure 5.14 (a), the molar magnetic susceptibility, χ_M in as-synthesized Ho-MOF-BTC systems is increasing exponentially with decreasing temperature, revealing typical paramagnetic behavior. This weaker magnetic ordering is resulted from the long M-O-C-O-M distance (~7.058Å) along *c*-axis, and the super-exchange coupling is not effective. The Curie-Weiss law has been used between 50 to 300K and obtained the Curie constant and temperature, yielding 22.11(4)emuK/ mole and 0.5(1)K in the as-synthesized Ho-MOF-BTC system. However, a comparison of the curvature changing with temperature for dehydrated Ho-MOF-BTC system demonstrates that dehydrated

156

Ho-MOF-BTC presents a different magnetism. A plot of the temperature dependence $1/\chi_M$ exhibits a changing slope when temperature is decreasing, implying a weak ferromagnetic behavior, which can be evidenced by a Curie-Weiss calculation at same temperature range between 50 to 300K and yields the Curie constant and temperature 16.3(2)emuK/ mole and 17.4(7)K.
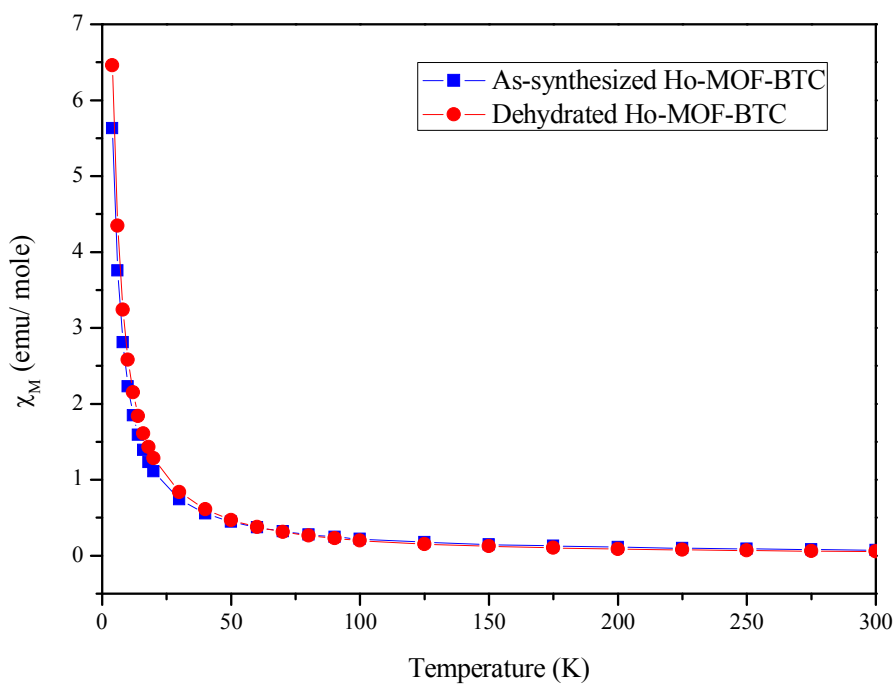
Figure 5.14 The SQUID measurements for as-synthesized and dehydrated Ho-MOF-BTC systems.

(a)
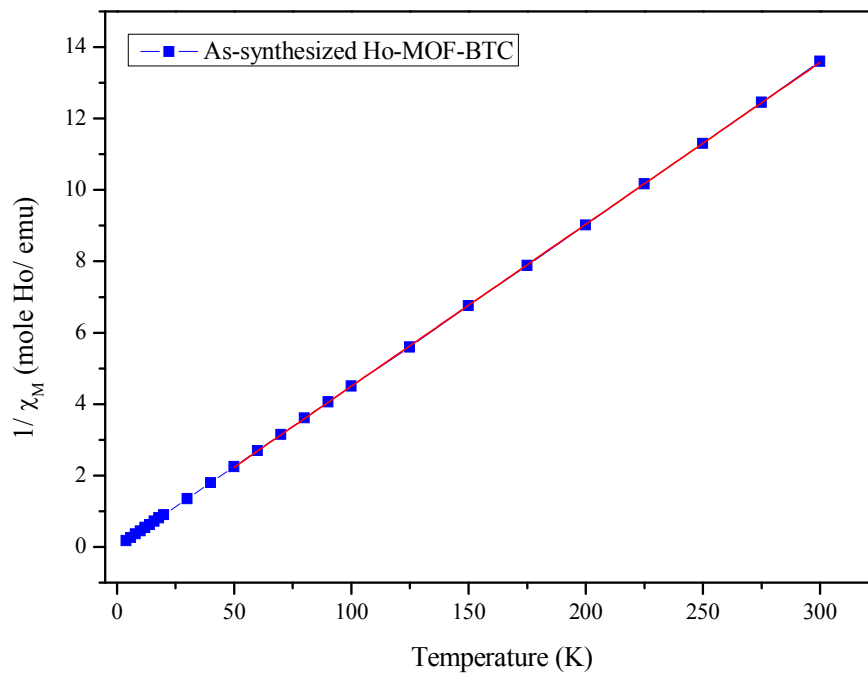
(b)
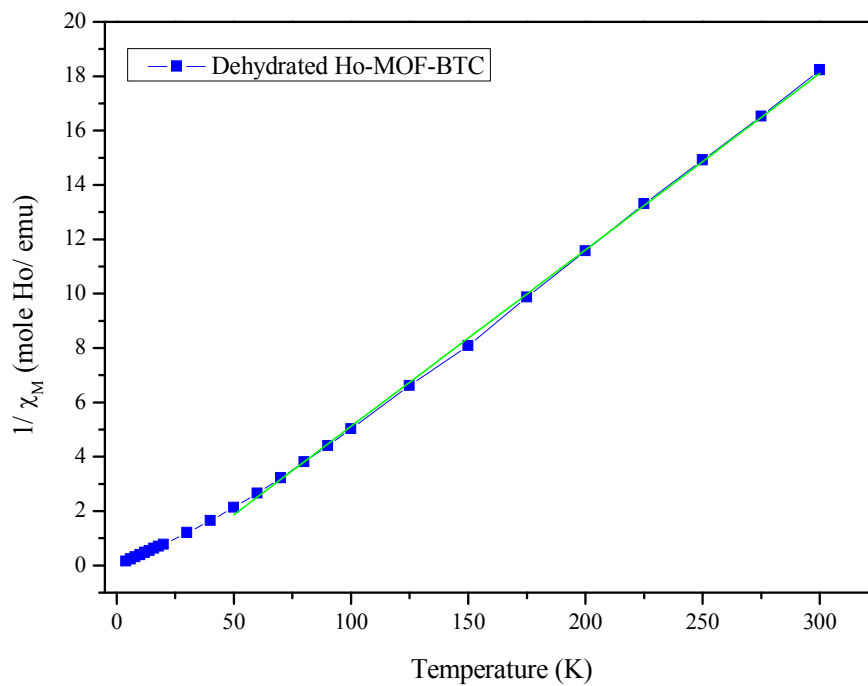
Figure 5.15 Temperature dependence of 1/ χ_M for (a) the as-synthesized and (b) dehydrated Ho-MOF-BTC systems.

5.5 Conclusions

Different structures of holmium MOF materials with different rigid benzoic ligands have been synthesized under mild hydrothermal and diffusion conditions. Single crystal X-ray diffraction reveals both 3-D network and 2-D "sheet-like" structures for the Ho-MOF-BTC and the Ho-MOF-BTB systems, respectively. Synchrotron powder X-ray diffraction (PXRD) results show Ho-MOF-BTC maintains a 1-D channel framework after all solvent and water depart up to $508^{o}C$. However, the structure of Ho-MOF-BTB system starts to collapse at ca. $80^{o}C$. A comprehensive investigation of the relationship between structural and thermal properties is proposed using pseudo-topology for these architectures. For the Ho-MOF-BTC system, the 1-D channel edges formed by the Ho-O-C-O-Ho 4-fold chiral chain along the c axis create a robust architecture because each holmium ion pair is fixed by the solid aromatic rings along three axis directions that are perpendicular to each other. In contrast, all the rigid benzoic ligands of the Ho-MOF-BTB system are parallel to each other and form a layer structure with a discontinuous ion-ion chain, suggesting that the dimensionality of molecular architecture dominates the structural stability of crystal frameworks. Furthermore, the *in-situ* Raman spectroscopy evidences that the 2-D Ho-MOF-BTB compound still keeps structural integrity although layers are disordered after dehydration. The SQUID data show a typical paramagnetic behavior in as-synthesized but maybe a weak ferromagnetism in dehydrated Ho-MOF-BTC system at low temperature. This phenomenon implies an appreciably magnetic hindrance from the guest solvent molecules since the major framework structure is almost identical; however, this assumption needs to be further verified by more experiments.

5.6 References

(1) Guo, X.; Zhu, G.; Li, Z.; Sun, F.; Yang, Z. and Qiu, S. *Chem. Commun.* **2006**, 3172.

(2) Gustafsson, M.; Bartoszewicz, A.; Martín-Matute, B.; Sun, J.; Grins, J.; Zhao, T.; Li, Z.; Zhu, G. and Zou X. *Chem. Mater.* **2010**, *22*, 3316.

(3) Luo, J.; Xu, H.; Liu, Y.; Zhao, Y.; Daemen, L. L.; Brown, C.; Timofeeva, T. V. ; Ma, S. and Zhou, H.-C. *J. Am. Chem. Soc.* **2008**, *130*, 9626.

(4) Rosi, N. L.; Kim, J.; Eddaoudi, M.; Chen, B.; O'Keeffe, M. and Yaghi, O. M. *J. Am. Chem. Soc.* **2005**, *2005*, 1504.

(5) Chen, B.; Yang, Y.; Zapata, F.; Lin, G.; Qian, G. and Lobkovsky, E. B. *Adv. Mater.* **2007**, 1693.

(6) Kitagawa, S. and Kondo, M. *Bull. Chem. Soc. Jpn.* **1998**, *71*, 1739.

(7) Serre, C.; Millange, F.; Thouvenot, C.; Gardant, N.; Pellé, F.; and Férey, G. *J. Mater. Chem.* **2004**, *14*, 1540.

Chapter 6: The Gas Adsorption Behaviors in Chiral Holmium Metal-Organic Framework Materials with Narrow Pore Size

6.1 Abstract

The holmium metal-organic framework material (MOF) with 4-fold chirality (space group $P4_122$) and high thermal/ structural stability that was used in chapter 5 is analyzed for its gas adsorption properties. The isotherm experiments of H_2, N_2 and CO_2 demonstrate a relatively high capacity of gas adsorption at low pressure range from 0 to 1atm. High resolution neutron powder diffractions have been used to identify the deuterium and deuterated methane adsorption sites in the analogous dehydrated structure, which exhibit a unique helical trajectory in 1-D channels, under high gas loading conditions, that is strongly related to the underlying chiral framework architecture. The distance between major deuterium adsorption sites (site **I** and site **II**) is 3.030 and 3.581Å, shorter than the intermolecular distance of solid deuterium (3.6Å) under the same measurement conditions, which is evidence for an extremely high hydrogen packing density in this dehydrated Ho-MOF-BTC system.

6.2 Introduction

Although there have been some chiral MOFs, gas adsorption within helical space group framework materials is very rare. In this chapter, the holmium metal-organic framework with chiral space group $P4_122$, as described in previous chapters, has been studied and its gas adsorption sites of deuterium (D_2) and deuterated methane (CD_4) identified. It is shown that a unique adsorption phenomenon within ca. 6.6 × 6.6Å 1-D channels occurs. It is strongly related to the pore size and helical metal ion-ion chain in

the structure.

6.3 Experimental Sections

6.3.1 Low Pressure H₂, N₂, and CO₂ Adsorption Isotherm Measurements

Low pressure gas adsorption isotherm experiments from 0 to 1atm were performed with a Quantachrome Instruments Autosorb-1-C surface area and pore size analyzer. The dehydrated sample was ground by agate mortar and pestle, degassed at 250^oC for 10 hours under high vacuum (10^{-6}torr) environment by heating rate 2^oC/min, and loaded in a quartz tube which is covered by a well-sealed lid within a helium-filled glovebox equipped with water and oxygen monitors. The sample 0.108g was used for these experiments, and all the sample, gas-lines and regulators will be automatically flushed and pumped to 10^{-3}torr about 10 times by Autosorb-1-C machine before measurement. A 1-minute leakage check was carried out to certify the well connection between the quartz tube (with sample) and instrument. Ultra high purity gases (UHP level) were used for each experiment. The temperature was maintained at 77K by liquid nitrogen bath for H_2 and N_2 measurement and at 273.15K by ice-water bath for CO_2 measurement.

6.3.2 Neutron Diffraction Experiments

Neutron powder diffraction data were obtained from the High Resolution Neutron Powder Diffractometer BT-1 in NIST Center for Neutron Research (NCNR). The neutron wavelength is 2.0782Å with 15' in-pile collimation (arc·min) and Ge(311) monochromator. The maximum beam size is about 15mm width × 50mm height. There are 32 sets of He-3 detectors at 5° intervals with 13 degree scan range covering 2θ from 0° to 167°.

6.3.2.1 Neutron Diffraction for Deuterium Loading Experiments

The process of sample preparation is exactly the same as for low pressure gas isotherm adsorption measurement. The sample weight was 1.0770g for the neutron diffraction experiments. The dehydrated powder filled 70% of a vanadium A-type can (6.0mm inner diameter and 1.5c.c. volume) and operated in the glovebox, then connected by a specific cover with a capillary gas-line and a packless valve that was then finally sealed with an indium O-ring. The sample can was fixed on the sample stick equipped with a stainless gas-line and an extra needle valve for the top-loading closed cycle refrigerator (TLCCR). Before starting the experiment, the sample was cooled to 4K in advance and kept pumping overnight until high vacuum (10^{-6} to 10^{-7}torr) was obtained. During this experiment, a known amount of hydrogen (deuterium, D_2) was loaded into sample step by step depending on the molar fraction between gas molecules and Holmium ion (Ho^{3+}) such as bare sample, 1 : 1, 2 : 1, 3 : 1 and 4 : 1. These ratios can be verified by Rietveld refinement for each of the loading. The loading gas temperature was set at 65K, 55K, 45K and 35K respectively for each ratio and held 1 to 2 minutes until no pressure drop was observed. The slack time before the beginning of each experiment set with different stoichiometry was ensured long enough (50 minutes) to reach and stabilize the temperature at 4K. All the experiments were measured at 4K for 2 hours to collect each run. For a set of experiments with different molar ratio would take 8 to 10 hours based on 4 or 5 times cycle runs. The Neutron scattering pattern of bare sample without any D_2 loading was first measured and analyzed by Rietveld refinement with the GSAS program, which was used as the starting model for the refinement of subsequently collected data. Deuterium molecules are observed as point scatters with double occupancy since they are

expected to be spherically averaged at ground state by quantum mechanical effects. The parameters such as coordinates for all atoms, thermal factor (Debye-Waller factor) varied during the refinement for each of the deuterium loading experiment. The difference of Fourier map for ordinal patterns can be calculated and used to indentify the deuterium adsorption position. Each Fourier difference map for previous gas loading pattern was served as the basis for successive scans and introduced new deuterium adsorption site from Rietveld calculation.

6.3.2.2 Neutron Diffraction for Deuterated Methane (CD_4) Loading Experiments

The process of neutron diffraction for deuterated methane (CD_4) is similar to that for deuterium. A known amount of CD_4 was loaded into sample step by step depending on the molar fraction between gas molecules and holmium ion (Ho^{3+}) such as bare sample, 0.8 : 1 and 1.6 : 1. The loading gas temperature was set at 140K and 120K respectively for each ratio. All the experiments were measured at 4 K for 2 hours to collect each cycle data.

6.4 Results and Discussions

6.4.1 Gas Adsorption Isotherms Experiment for Dehydrated Ho-MOF-BTC System

The gas adsorption-desorption properties for H_2, N_2 and CO_2 were investigated for Ho-MOF-BTC system at 0 to 1atm. Dehydrated Ho-MOF-BTC was prepared by heating up to $250^{o}C$ under a high vacuum 10^{-6}torr for 10 hours. The H_2 volumetric and gravimetric isotherm results are shown in Figure 6.1 (a)-(b), CO_2 volumetric isotherm data in Figure 6.2 and N_2 volumetric results in Figure 6.3, respectively. The type I adsorption isotherm curves for H_2 reveals a relatively high H_2 (at 77K) uptake amount

upon 1.46wt% (164.49ml/g) at standard temperature and pressure (STP, 1atm and 273.15K) by comparing to ca. 1.2wt% H_2 capacity of MOF-177[1] with larger specific surface area ($> 4000m^2/g$); and the Langmuir surface area is calculated by $879.1m^2/g$ in this dehydrated Ho-MOF-BTC system. The enthalpy of adsorption for isostructural Y-MOF-BTC system is ca. 7.3kJ/mole[2], which is comparable to the value of the dehydrated porous Prussian blue analogues with open transition metal sites[3], the hyper-crosslinked organic polymer and nanoporous slit-like carbon[4,5] based on physisorption (typically 4-10kJ/mole). The Ho-MOF-BTC system should possess similar adsorption heat of H_2 since the structure is as the same as Y-MOF-BTC system. The CO_2 adsorption curve is shown in Figure 6.2 and gives 15.2wt% (91.40ml/g) at 1atm and 273.15K. However, the adsorption isotherm curves in all H_2 ,N_2 and CO_2 cases show a continuously increasing uptake accompanied with the increasing of pressure and obviously the capacity doesn't reach the saturated state at 1.0atm. The N_2 (at 77K) adsorption isotherm behaviors are performed in Figure 6.3 and show that the N_2 uptake amount is 202.52ml/g. In addition, the calculated BET surface area for N_2 adsorption is $524.6m^2/g$. Interestingly, from experimental results, the measurement of N_2 isotherms at 77 K shows a hysteresis loops between adsorption and desorption behaviors; similar phenomenon has been recently proposed and discussed for H_2 isotherm case[6]. The much slower N_2 desorption kinetics may be caused by adjacent guests (kinetic trapping)[7] and related to the structural features of dehydrated Ho-MOF-BTC with unsaturated rare-earth metal ions. The gas isotherm behavior in this Ho-MOF-BTC system is different from degassed Dy-MOF-BTC with similar framework[8].

(a)

(b)
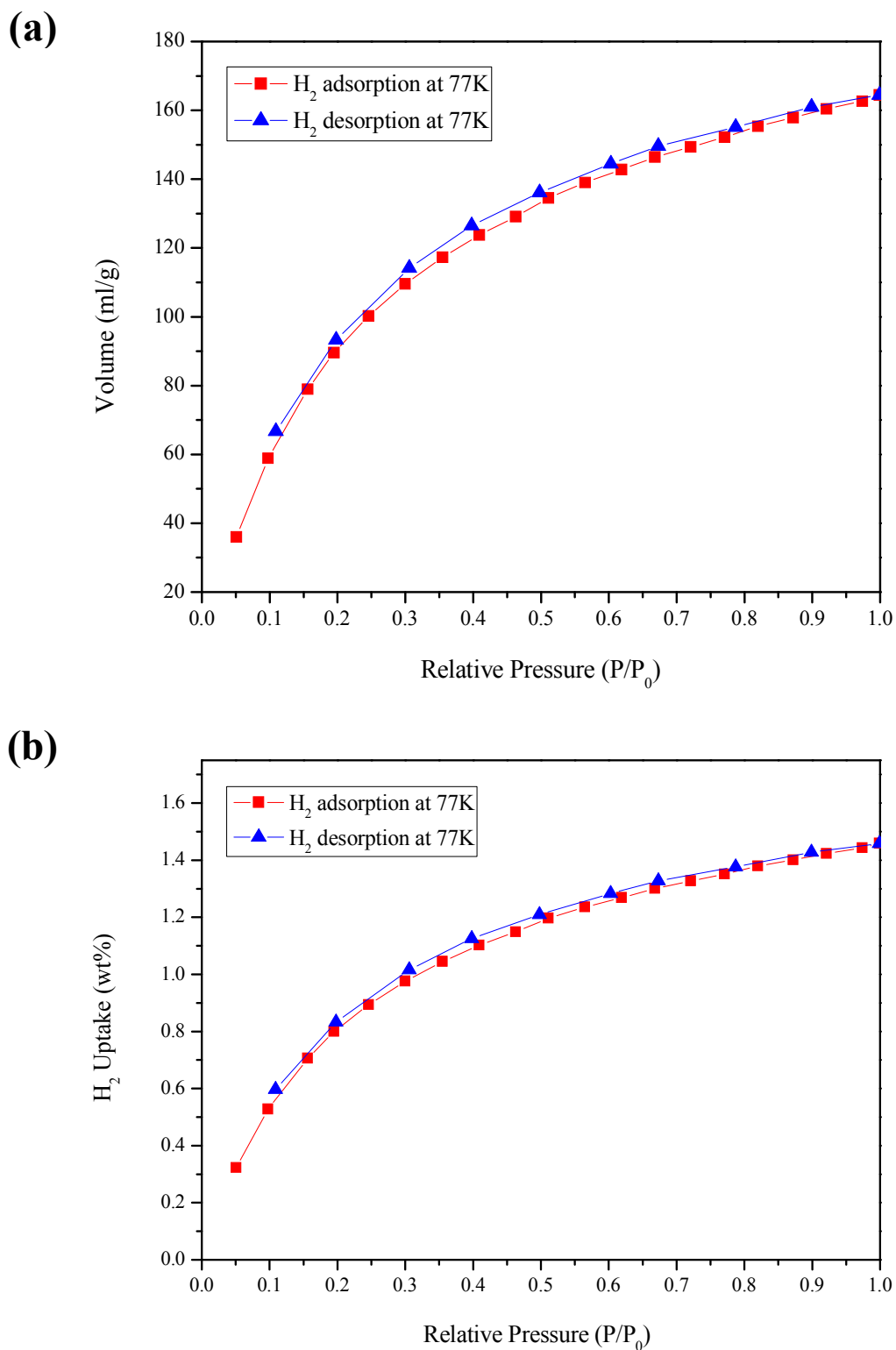
Figure 6.1 The H$_2$ adsorption isotherm experiment for dehydrated Ho-MOF-BTC system and excess amounts expressed by (a) volume and (b) weight percentage, respectively.
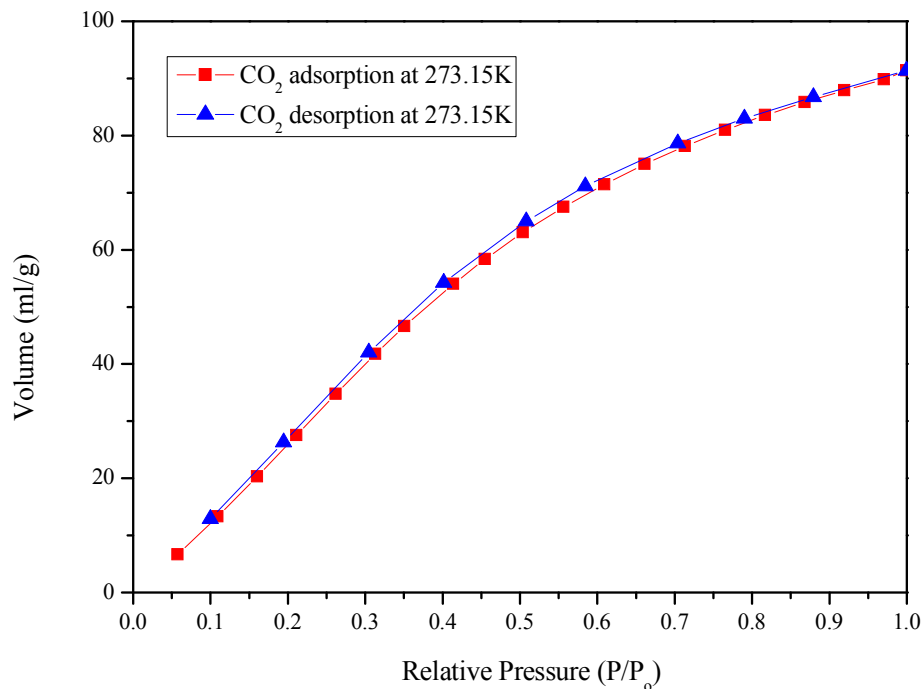
Figure 6.2 The CO_2 adsorption volumetric isotherm experiment for dehydrated Ho-MOF-BTC system
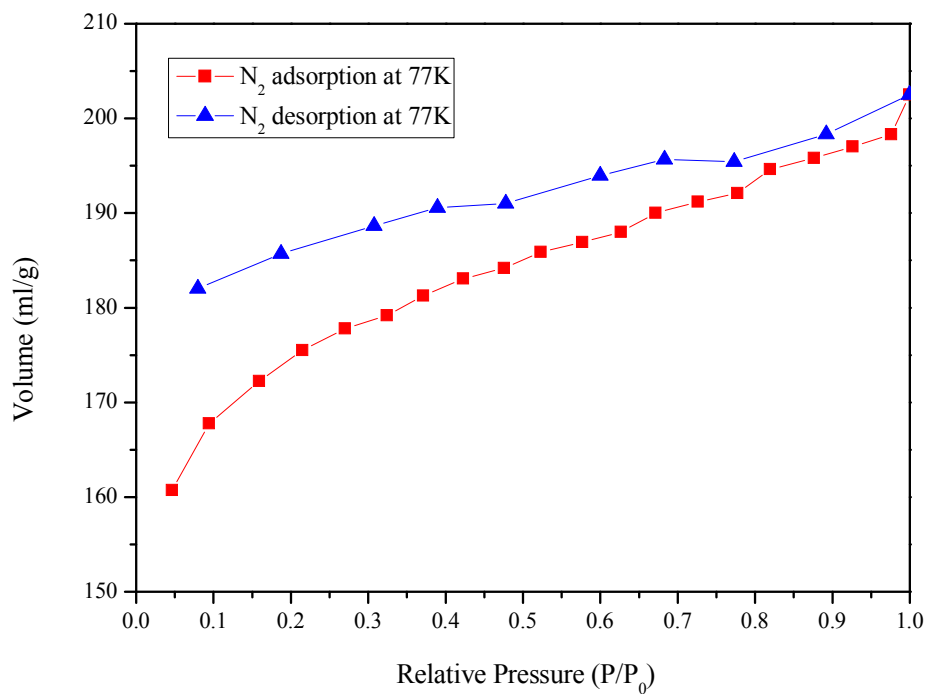
Figure 6.3 The N_2 adsorption volumetric isotherm experiment for dehydrated Ho-MOF-BTC system.

6.4.2 Neutron Diffraction Studies of Deuterium Adsorption Behaviors for Dehydrated Ho-MOF-BTC System

A series of high resolution powder neutron diffraction (PND) of dehydrated Ho-MOF-BTC under gas loading conditions have been achieved and analyzed to identify the deuterium (hydrogen) adsorption positions. The experiments start from the bare dehydrated sample that was prepared at $250^{\circ}C$ for 10hrs by heating rate $2^{\circ}C$/min. This powder pattern was well-refined by Rietveld method first and served as the model for the subsequently collected data. As shown in Figure 6.4 to Figure 6.8, the neutron powder diffraction patterns are the function of deuterium gas loading amount; the difference of Fourier map for ordinal patterns accurately determined the deuterium adsorption sites. The calculated results of weighted R factors (wR_p) and R factors (R_p) are 4.16% and 3.43% for bare sample, 3.54% and 2.19% for 1 : 1 ratio, 4.02% and 3.32% for 2 : 1 ratio, 3.19% and 2.62% for 3 : 1 ration, 3.16% and 2.58% for 4 : 1 ratio, respectively. In all of the cases, the R-factors show a high reliability and give a good fit to the data. In addition, the occupancy for every adsorption position can be estimated from the refinement results and the adsorption molar fractions (deuterium : metal ions) for all cases are identified as 1.04 : 1, 1.88 : 1, 2.94 : 1 and 4.26 : 1, respectively. These values are very comparable to the stoichiometry used in gas loading processes (e. g. 1 : 1, 2 : 1, 3 : 1, and 4 : 1). There are four probable adsorption positions that have been measured and classified by outer shell (first site **I** and second site **II**) with higher physisorption energy and inner shell (third site **III** and fourth site **IV**) with lower physisorption energy in the Ho-MOF-BTC channels. This phenomenon is very straightforward since the pore size is 6.6 × 6.6Å and larger than twice of kinetic diameter of deuterium (ca. 2.89Å). The distance between primary site (site **I**) and the unsaturated holmium ion is 4.226(13)Å, longer than that

between site **I** to the nearest carbon atom on BTC ligand by 3.243(15)Å (in 1 D_2/Ho^{3+} case), showing a stronger van der Waals interaction between the deuterium molecules and carbon-based linkers. A similar phenomenon had been observed and indicated a strong correlation to the dimensionality of pore[2]. The first two positions, site **I** (D1) and site **II** (D2), are close to the lanthanide ion. However, site **III** (D3) and site **IV** (D4) adopt positions far from the metals and adopt a unique "hydrogen helical" trajectory, as shown in Figure 6.7 and Figure 6.8. This feature corresponds to potential energy surface of unsaturated holmium ions reflecting the 4-fold spiral symmetry of the main chain. The distances between adjacent site **I** and site **II** are 3.030 and 3.581Å with 86.27% and 53.47% occupancy; between adjacent site **III** and site **IV** in pairs (1 × D4 with 2 × D3) is 1.658Å with 25.19% and 17.67% occupancy (in 3 D_2/Ho^{3+} case). Surprisingly, these distances are even shorter than the intermolecular distance of solid-state deuterium (3.6Å) under similar measurement conditions without applying any pressure that has been observed by Liu et. al. in MOF-74[1]. The results indicate that a very high hydrogen packing density can be obtained in this framework structure.

(a)

(b)

(c)
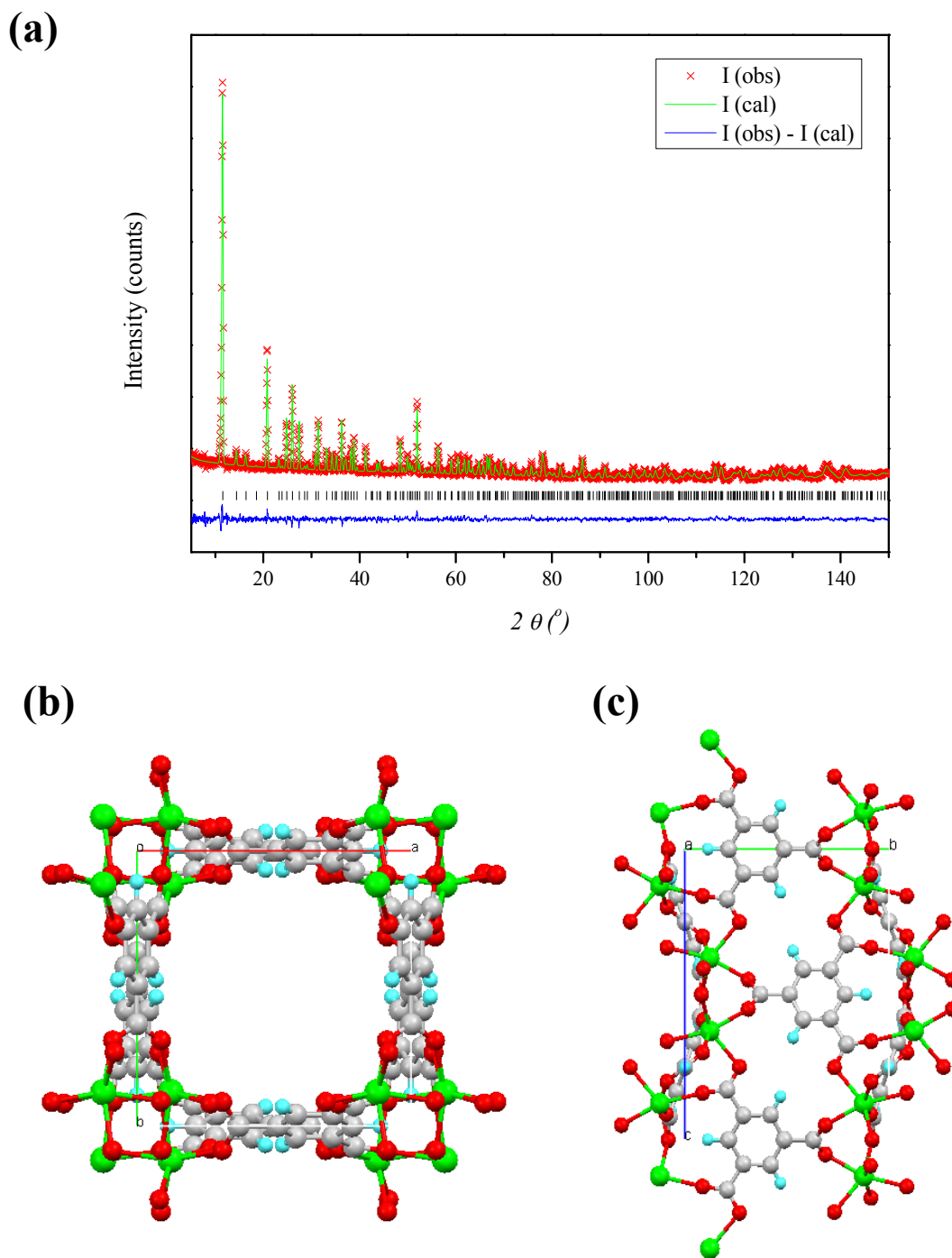
Figure 6.4 (a) The Rietveld refinement of high resolution PND pattern for bare sample without any deuterium loading, and Figure 6.4 (b)-(c) The viewed directions along *c* and *a* axis in 3-D molecular model.

(a)

(b)

(c)
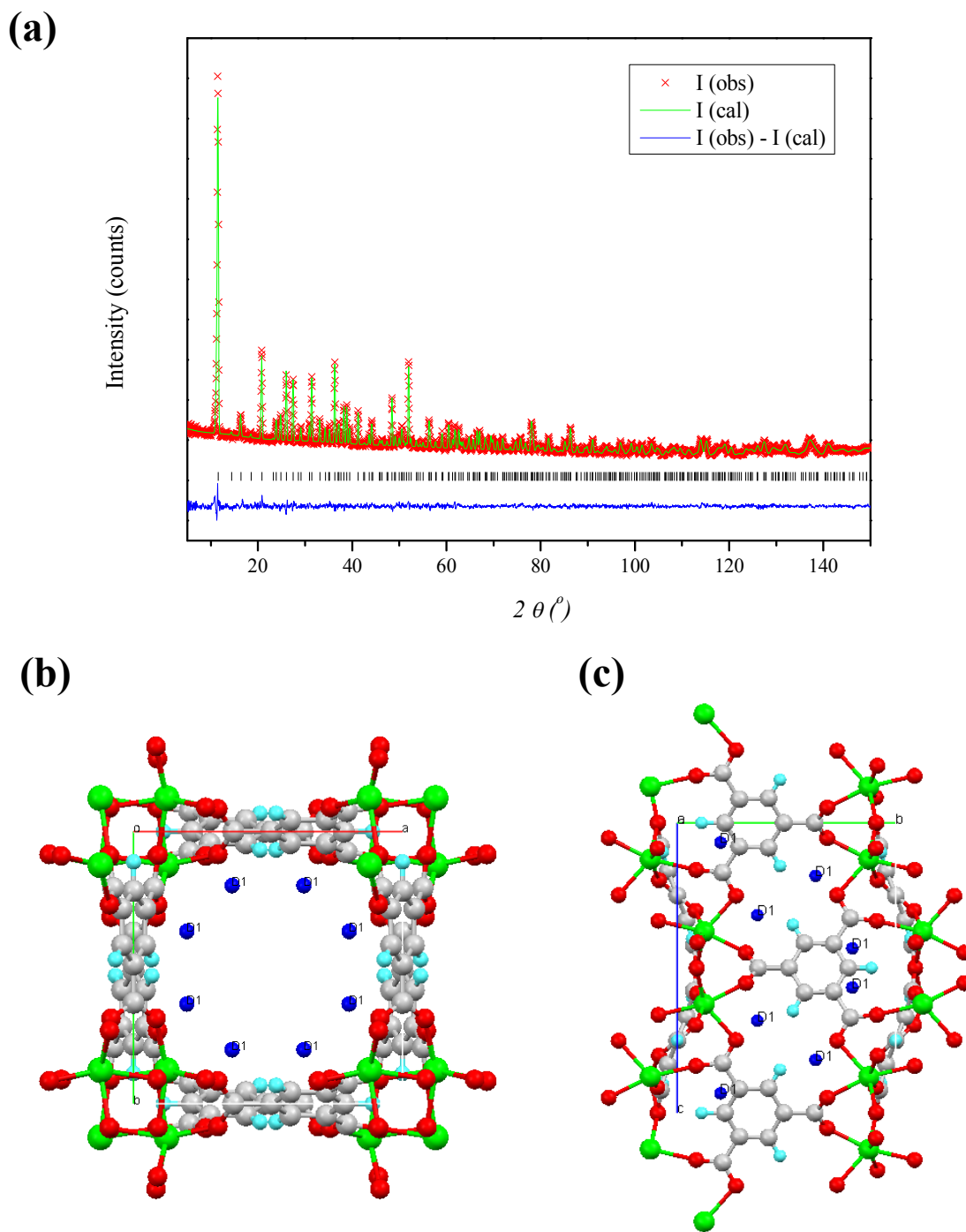
Figure 6.5 (a) The Rietveld refinement of high resolution PND pattern for deuterium :

Ho^{3+} = 1 : 1, and Figure 6.5 (b)-(c) The viewed directions along *c* and *a* axis in 3-D

molecular model, and the site **I** (D1) adsorption positions of deuterium.

(a)

(b)

(c)
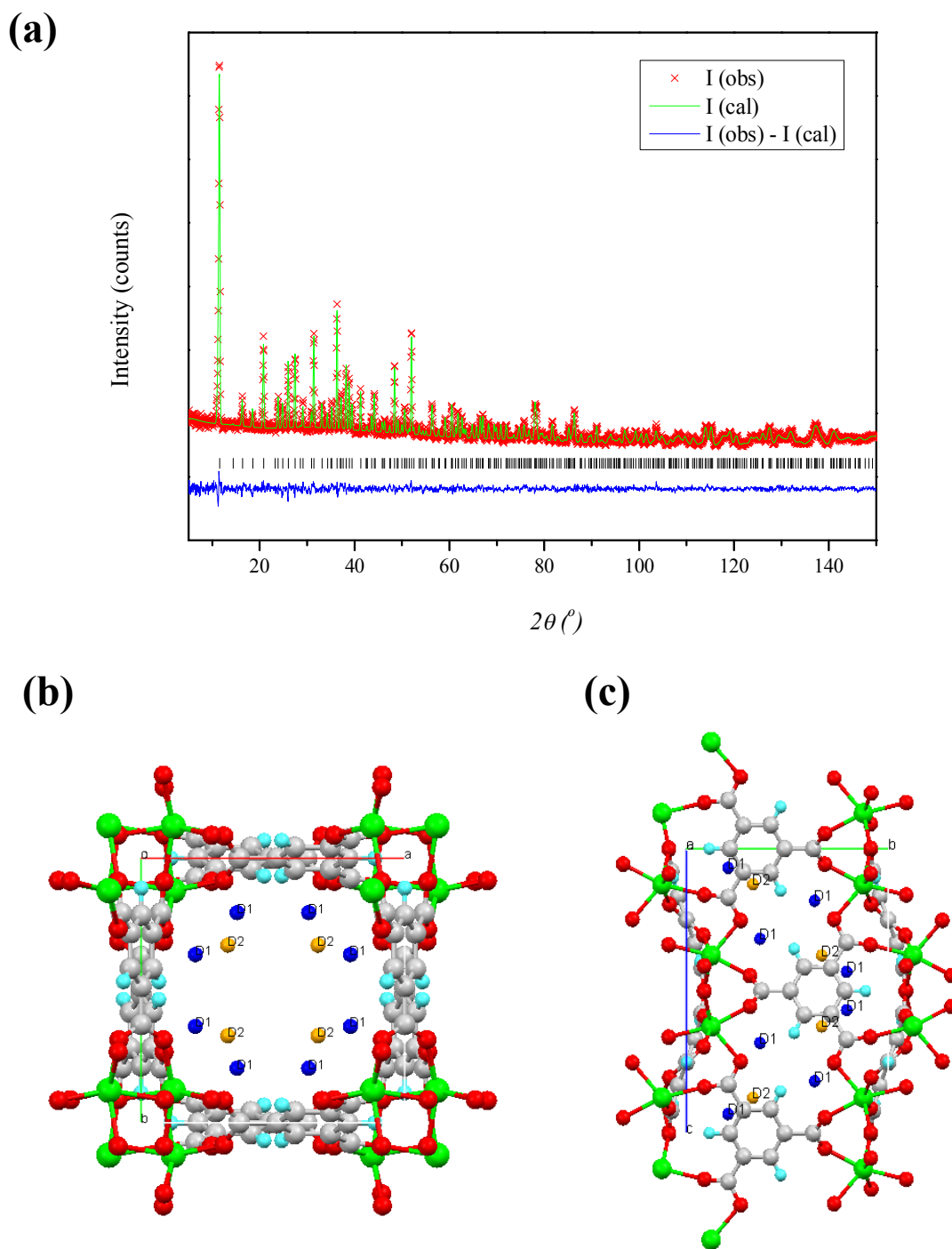
Figure 6.6 (a) The Rietveld refinement of high resolution PND pattern for deuterium :

Ho^{3+} = 2 : 1, and Figure 6.6 (b)-(c) The viewed directions along *c* and *a* axis in 3-D

molecular model, and the site **I** (D1) and site **II** (D2) adsorption positions of deuterium.

(a)

(b)

(c)
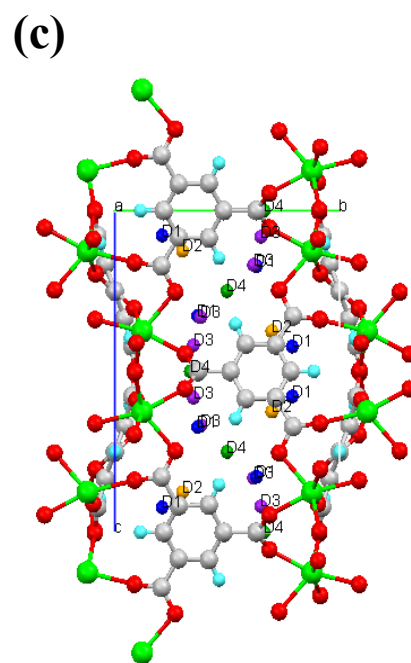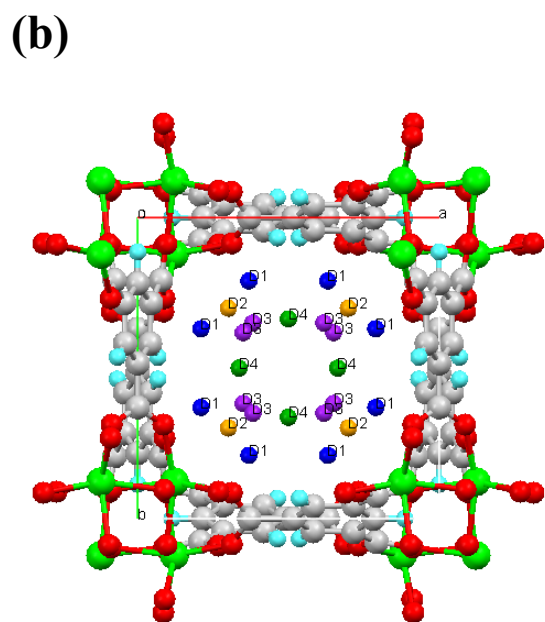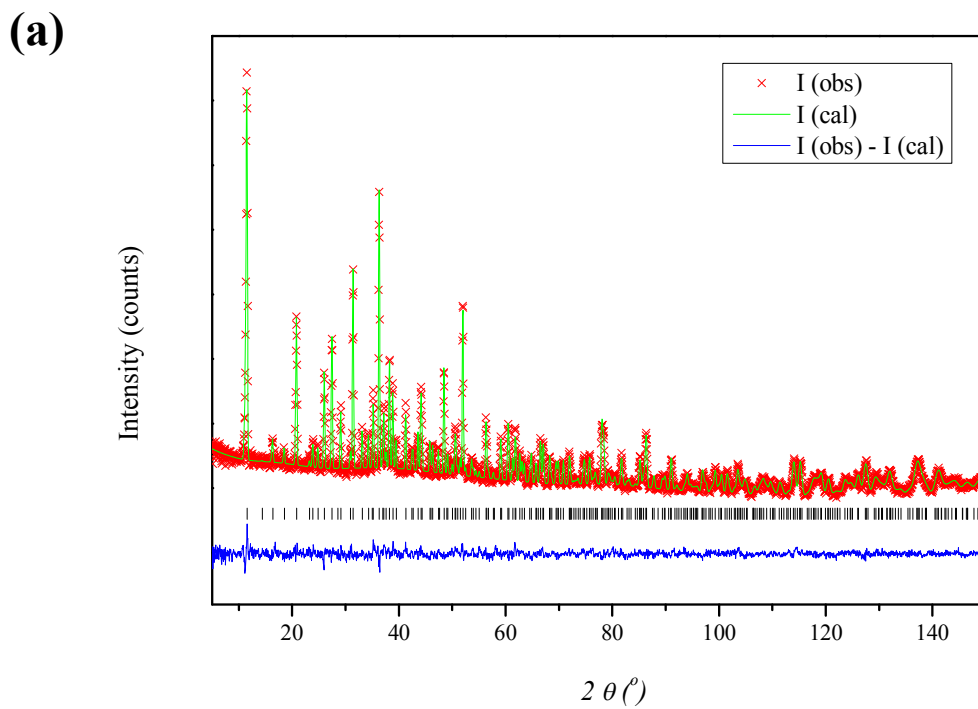
Figure 6.7 (a) The Rietveld refinement of high resolution PND pattern for deuterium : Ho^{3+} = 3 : 1, and Figure 6.7 (b)-(c) The viewed directions along *c* and *a* axis in 3-D molecular model, and the site **I** (D1), site **II** (D2), site **III** (D3) and site **IV** (D4) adsorption positions of deuterium.

(a)

(b)

(c)
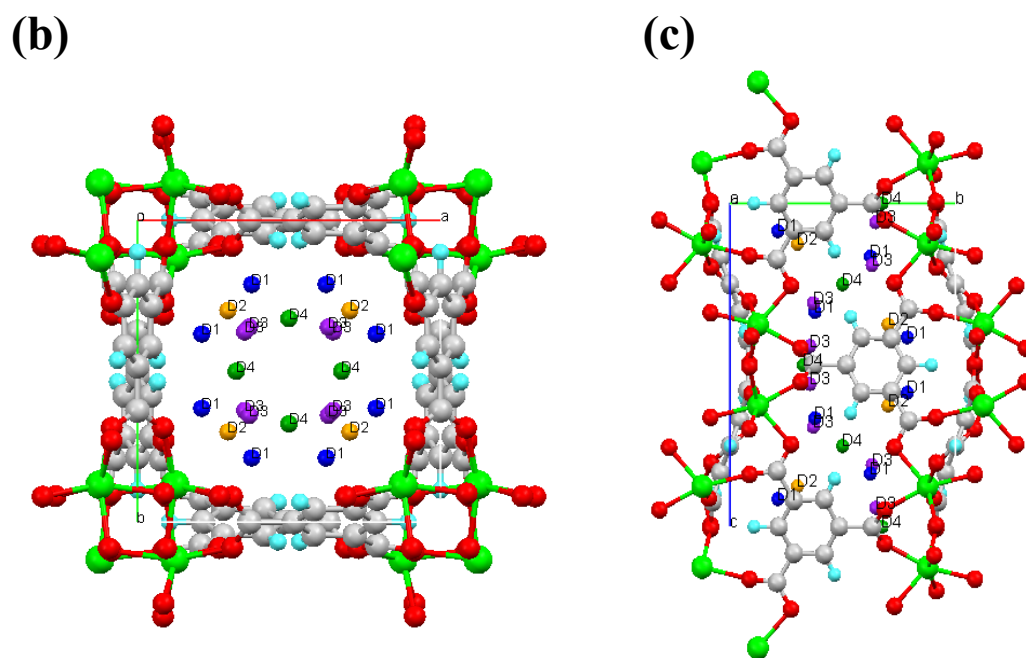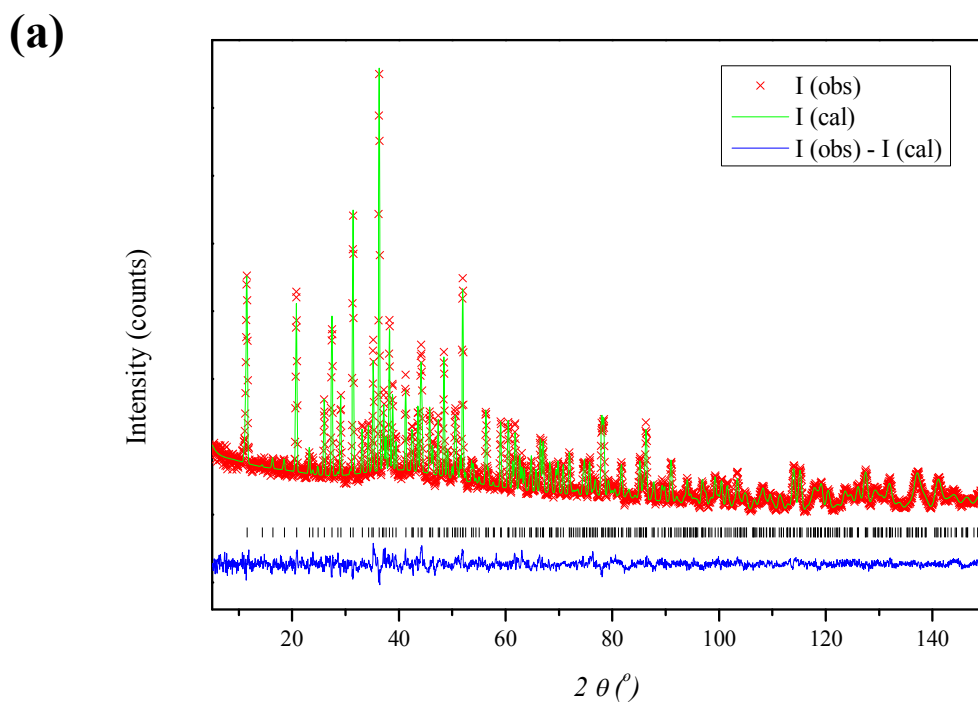
Figure 6.8 (a) The Rietveld refinement of high resolution PND pattern for deuterium : Ho^{3+} = 4 : 1, and Figure 6.8 (b)-(c) the viewed directions along *c* and *a* axis in 3-D molecular model, and the site **I** (D1), site **II** (D2), site **III** (D3) and site **IV** (D4) adsorption positions of deuterium.

6.4.3 Neutron Diffraction Studies of Deuterated Methane Adsorption behaviors for Dehydrated Ho-MOF-BTC System

To avoid the large incoherent neutron scattering length from H atoms in methane (CH_4), deuterated methane (CD_4) has been used to obtain high quality neutron diffraction patterns. The measurements were performed in a similar manner to those undertaken for deuterium; the collected data including bare sample, and that with different stoichiometry loadings (0.8 and 1.6/Ho^{3+} ion) are sequentially refined by full-profile Rietveld method as shown in Figure 6.9 and 6.10. The adsorption positions and orientations of CD_4 molecules can be clearly identified by using the difference Fourier maps. In Figure 6.9, the primary site of CD_4 can be observed in 0.8 CD_4/Ho^{3+} case, and the refinement results of wR_p and R_p are 4.81% and 4.06%, respectively. The calculated occupancy of CD_4 is 84.78%, very comparable to the expected values. The distance between the deuterated methane to unsaturated metal ion is 4.851(33)Å, much larger than the distance to nearest carbon atom on ligand at around 3.404(36)Å. In addition, the distance between two nearest-neighbor CD_4 molecules is 2.937(44)Å, much smaller than those found for solid methane (ca. 3.96Å)[9]. These results highlight some important issues in adsorption behaviors that should be noted: (i) The geometry of space. In this Ho-MOF-BTC system, the crystal structure contains a helical channel with 4-fold ion-ion chains on the edges. The open space of unsaturated holmium ions is restricted by the perpendicular organic linker walls that the approach of the CD_4 molecule to the metal ions on the corners. This steric hindrance is a major influence on the adsorption mechanism between the metal ions and guest molecules, and (ii) The dimension of the framework. The refinement results show that the distance between CD_4 molecules and the nearest carbon atom on ligand is 3.404(36)Å, very comparable to that of CH_4 on graphite surface, which is at 3.45Å[10],

suggesting that the aromatic rings on the organic ligands attract the methane gas molecules. On the other hand, the diameter of this 1-D channel is ca. 6.6×6.6Å, which is closed to 1.7 times of the kinetic diameter of methane gas molecule (ca. 3.8Å), which enhances the van der Waals interaction between CD_4 and organic linkers. The distance between two nearest-neighbor CD_4 molecules is 2.937(44)Å, much smaller than that of solid-state methane (ca. 3.96Å), implying that the highly encapsulated methane gas molecules in this Ho-MOF-BTC system is very tightly bound. As shown in Figure 6.10, the calculated results of wR_p and R_p in the high gas loading case (1.6 CD_4/Ho^{3+}) are 4.19% and 3.37%, respectively. However, the calculated occupancies of CD_4 for primary and secondary positions are 72.02% and 61.36%, slightly different from the totally experimental stoichiometry (1.33 from 1.6). Careful inspection of the high resolution PND pattern baseline shows a small hump that appears between ca. 20 to 40° in 2θ, implying that some of CD_4 gas molecules exist in this MOF system as an amorphous phase. In addition, the gas adsorption behavior is distinguishable from other MOF systems with larger pore sizes. In contrast to a number of other MOF systems, both of these two adsorption sites have similar occupancies and thermal parameters. Furthermore, the distance between the center carbon atom of the CD_4 molecule on primary site to the nearest-neighbor carbon atom on BTC ligand is 3.358(29)Å, which is similar to that of the CD_4 molecule on secondary site (3.650(37)Å). In both cases, the two distances are larger than their distances to unsaturated holmium metal ions at 4.275(30)Å and 5.016(34)Å, respectively. These findings demonstrate that (i) The CD_4 molecule adsorption behavior is not only affected by the unsaturated metal ion, but also strongly influenced by the space or geometric steric hindrance effect, and (ii) The space in Ho-MOF-BTC system is limited and close to the kinetic diameter of adsorbed CD_4 gas

molecule, which may cause a lack of distinction between the primary and secondary adsorption sites in terms of the energy of adsorption. Although in this section, the unusually small size and geometric effect from the framework has been emphasized, there is a high agreement from most researches that the gas adsorption positions in MOF system are the equilibrium locations between a balance of steric hindrance and energy effect. In addition, an interesting "helical CD_4" trajectory is identified once the primary and secondary sites are occupied. This phenomenon has not been observed for gas adsorption in any centrosymmetric MOF crystal structures before. This Ho-MOF-BTC system with non-centrosymmetric space group $P4_122$ shows a novel gas adsorption behavior, demonstrating an appreciable effect from 1-D chiral ion-ion chains on host framework.

(a)

(b)

(c)
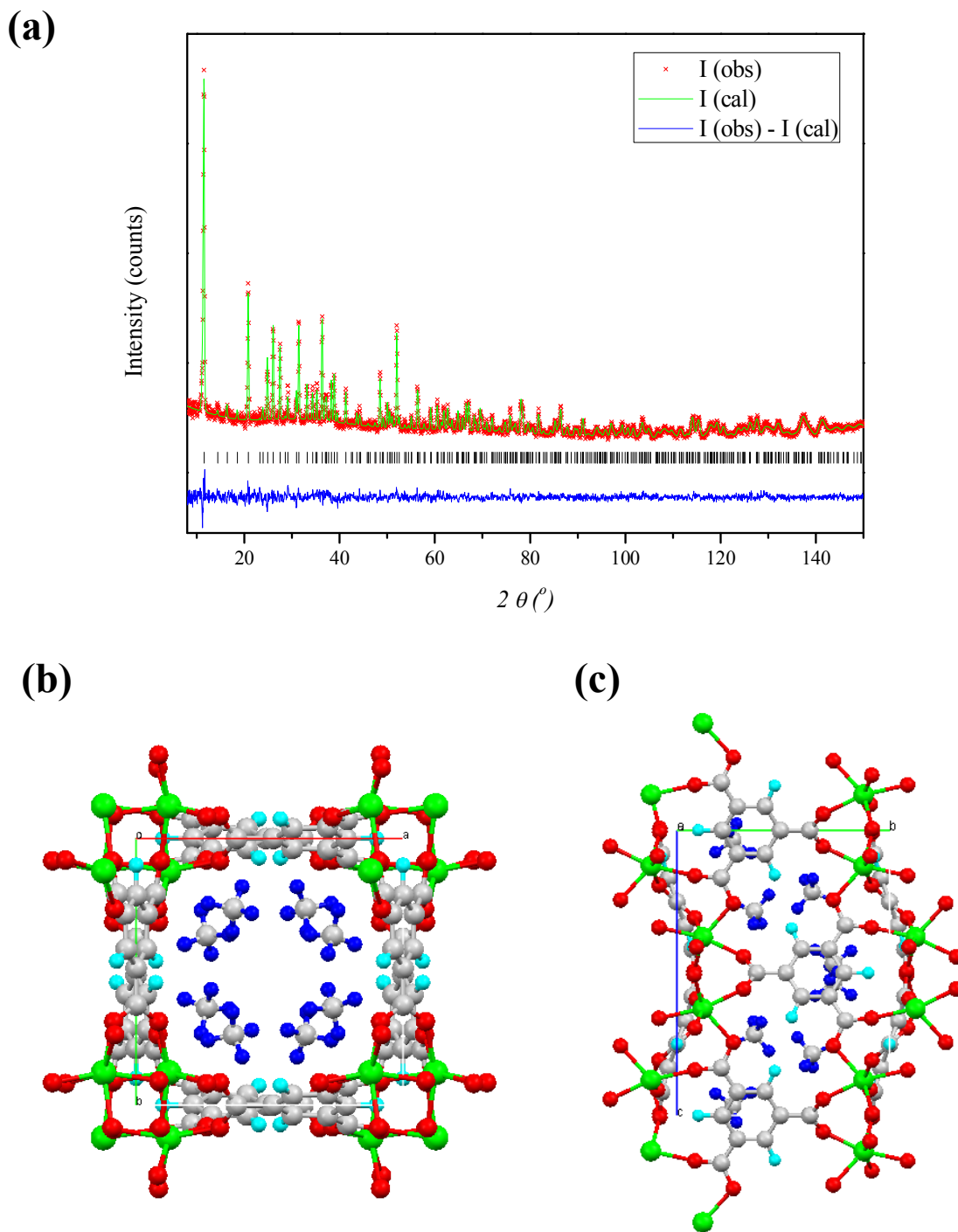
Figure 6.9 (a) The Rietveld refinement of high resolution PND pattern for deuterated methane : Ho^{3+} = 0.8 : 1, and Figure 6.9 (b)-(c) The viewed directions along c and a axis in 3-D molecular model with adsorption positions of first deuterated methane (blue atoms are the deuteriums on first deuterated methane).
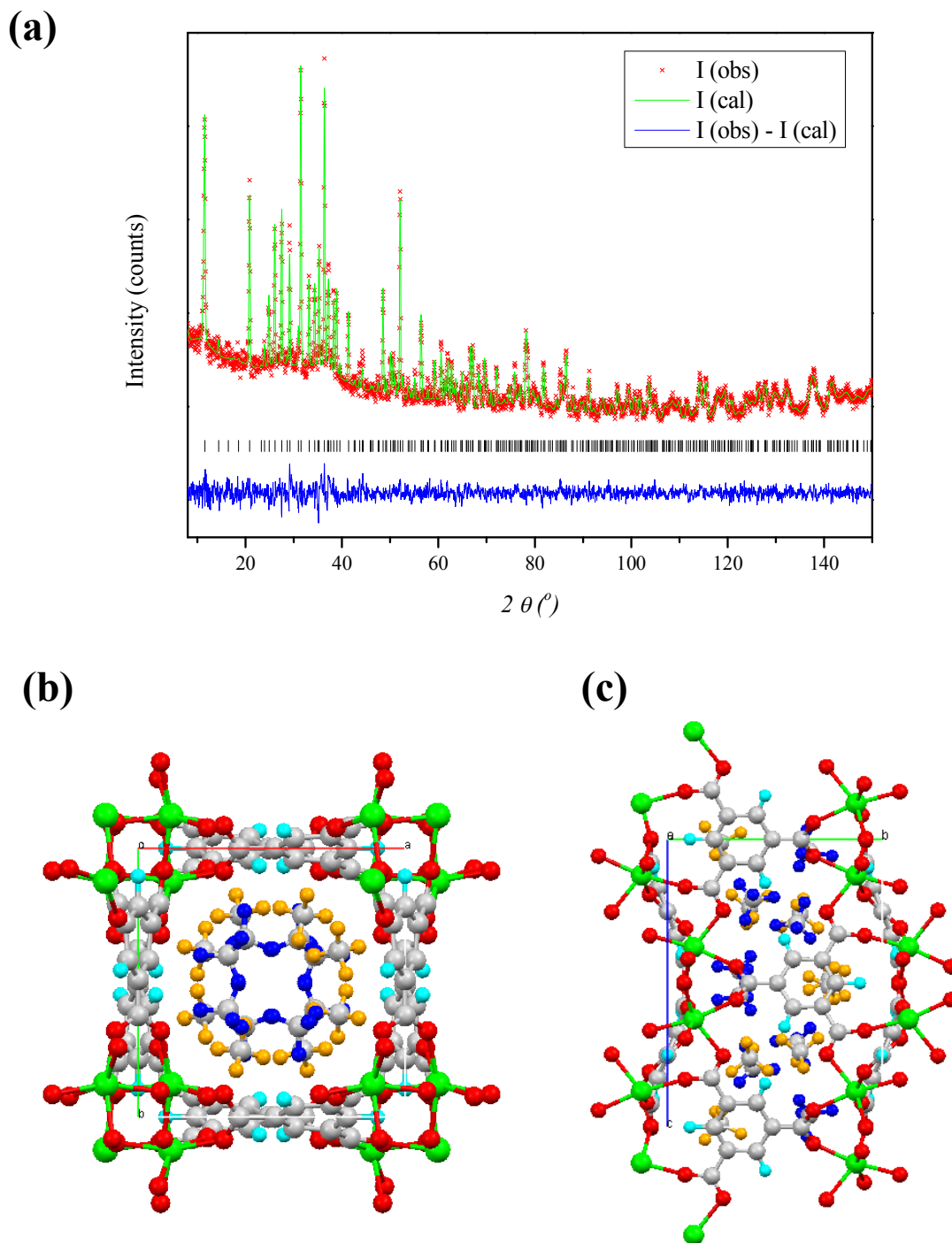
Figure 6.10 (a) The Rietveld refinement of high resolution PND pattern for deuterated methane : Ho^{3+} = 0.8 : 1, and Figure 6.9 (b)-(c) The viewed directions along *c* and *a* axis in 3-D molecular model with adsorption positions of first and second deuterated methane (orange atoms are the deuteriums on second deuterated methane).

6.4.4 Charge Flipping (CF) and Maximum Entropy Method (MEM) Calculation

A new *ab-initio* algorithm, named charge flipping has been developed recently to calculate and identify the unknown structure without the need for an initial model. As shown in Figure 6.11, the reconstruction of the nuclear scattering density using the charge flipping method reveals a distribution of deuterium guest molecules within central chiral channels. The helical density profile is easy to correlate with the chiral $P4_122$ symmetry of the lattice. However, the charge flipping calculation was performed starting from a random phase with $P1$ space group, in other word no assumption based on symmetry were taken before the analysis was performed. The charge flipping methodology offers a preliminary qualitative approach to construct the structure.

As a complementary strategy to reconstruct the nuclear scattering density, the maximum entropy method offers a more quantitative approach. Unlike the charge flipping calculation that assumes no model, the MEM method in these calculations is performed in the chiral $P4_122$ space group. A Le Bail or intensity extraction fit is shown in Figure 6.12 (a) that is used to assign intensities to each reflection ahead of the MEM routine. As shown in Figure 6.12 (b), the well-defined atom positions and framework structure obtained from the standard Rietveld refinement of high resolution PND in deuterium : Ho^{3+} = 4 : 1 system generally match well with the MEM reconstruction; all the atoms are surrounding by a nuclear scattering density. There is considerable diffusion around many of atoms that suggests even though the experiment was performed at 4K, there is still some considerable disorder. A very interesting distinction between deuterium sites should be emphasized; site (**I**) and site (**II**) of deuteriums located close to lanthanide positions are first observed therefore have higher adsorption energies. These deuterium have slightly more disorder than the framework, but very similar. However, site (**III**) and

site (**IV**) of deuteriums located at inner channel with low adsorption energies show considerable disorder; continuously helical density is observed that indicates the deuteriums at site (**III**) and site (**IV**) should be free to diffuse between almost continuous positions along the channels. This type of disorder is very common in lithium battery materials or materials with high ionic conductivity. They are often very difficult to identified or accurately determined through traditional Rietveld refinement since the atoms are defined by a specific location and a thermal parameter only. The MEM calculation is essential providing a quantitatively approach to the detail of the gas disorder within the channels.
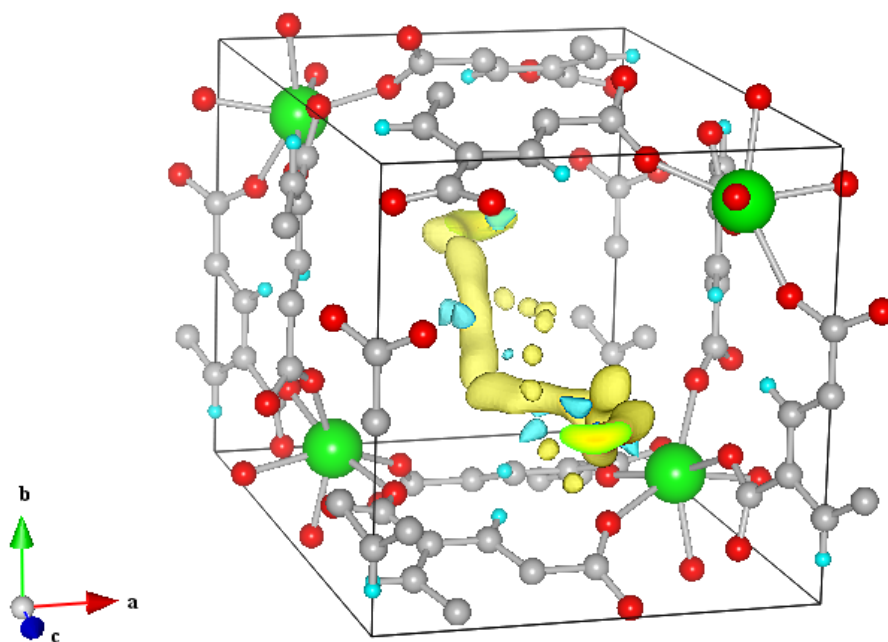
Figure 6.11 The charge flipping (CF) calculation for the nuclear scattering density distribution of guest molecules in deuterium : Ho^{3+} = 3 : 1 system.
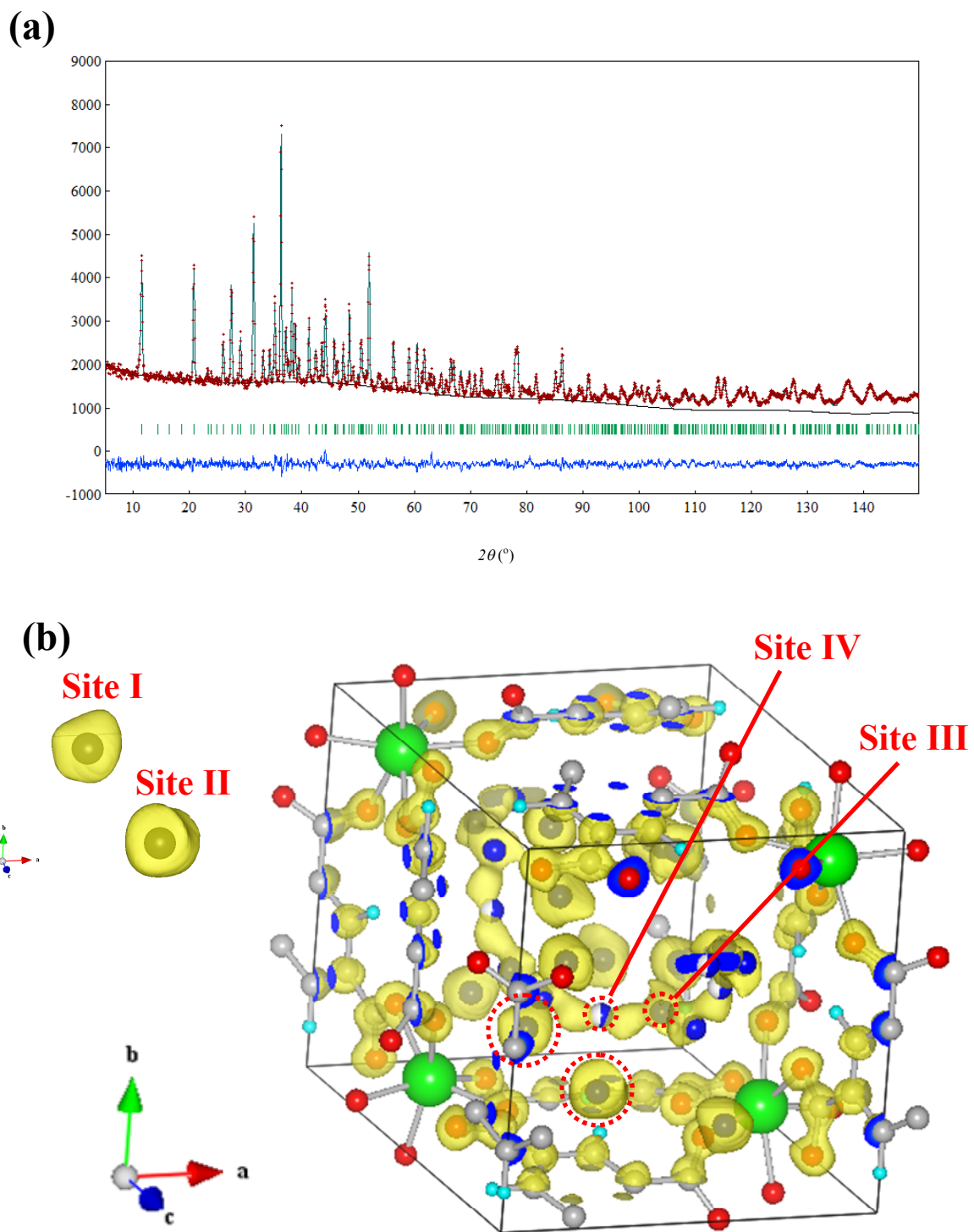
Figure 6.12 (a) The Le Bail refinement for maximum entropy method (MEM), and (b) The calculation of nuclear scattering density distribution in deuterium : Ho^{3+} = 4 : 1 system.

6.5 Conclusions

In summary, low pressure H_2, N_2 and CO_2 gas adsorption isotherm measurements have been achieved and analyzed. H_2 isotherm experiment shows that the dehydrated Ho-MOF-BTC system has a relatively high adsorption capacity 1.46wt% in mild storage condition (from 0 to 1atm). A series of high resolution neutron powder diffractions performed with deuterium and deuterated methane have been used to identify the adsorption positions in this special 4-fold chiral framework, showing that the extremely high gas packing density can be obtained. These properties can be explained by the optimal pore size in this MOF structure that enhances the van der Waals interaction between the organic ligands and guest gas molecules. A unique helical adsorption pattern is observed mirroring the chiral structure of the host material. Finally, an *ab-initio* charge flipping and maximum entropy (MEM) calculations provide qualitative and quantitative approaches to describe the thermal displacements, diffusion, and delocalization of deuterium molecules along the 1-D channels, evidencing a more realistic gas behavior from neutron diffraction experiments than that which could be achieved when relying on the Rietveld refinement.

6.6 References

(1) Liu, Y.; Kabbour, H.; Brown, C. M.; Neumann, D. A.andAhn, C. C. *Langmuir* **2008**, *24*, 4772.

(2) Luo, J.; Xu, H.; Liu, Y.; Zhao, Y.; Daemen, L. L.; Brown, C.; Timofeeva, T. V.; Ma, S. and Zhou, H.-C. *J. Am. Chem. Soc.* **2008**, *130*, 9626.

(3) Kaye, S. S. and Long, J. R. *J. Am. Chem. Soc.* **2005**, *127*, 6506.

(4) Wood, C. D.; Tan, B.; Trewin, A.; Niu, H.; Bradshaw, D.; Rosseinsky, M. J.; Khimyak, Y. Z.; Campbell, N. L.; Kirk, R.; Stöckel, E. and Cooper, A. I. *Chem. Mater.* **2007**, *19*, 2034.

(5) Kowalczyk, P.; Gauden, P. A.; Terzyk, A. P. and Bhatia, S. K. *Langmuir* **2007**, *23*, 3666.

(6) Navarro, J. A. R.; Barea, E.; Rodrguez-Diguez, A.; Salas, J. M.; Ania, C. O.; Parra, J. B.; Masciocchi, N.; Galli, S. and Sironi, A. *J. Am. Chem. Soc.* **2008**, *130*, 3978.

(7) Zhao, X.; Xiao, B.; Fletcher, A. J.; Thomas, K. M.; Bradshaw, D. and Rosseinsky, M. J. *Science* **2004**, *306*, 1012.

(8) Guo, X.; Zhu, G.; Li, Z.; Sun, F.; Yang, Z. and Qiu, S. *Chem. Commun.* **2006**, 3172.

(9) Wu, H.; Zhou, W. and Yildirim, T. *J. Am. Chem. Soc.* **2009**, *131*, 4995.

(10) Vidali, G.; Ihm, G.; Kim, H-Y. and Cole, M. W. *Surf. Sci. Rep.* **1991**, *12*, 133.

Chapter 7: A Flexible Holmium Metal-Organic Framework with 1, 4-Benzene Dicarboxylic Acid Ligand: Study of Phase Transitions

7.1 Abstract

A comprehensive structural study for a holmium with 1, 4-bicarboxylic acid (Ho-MOF-BDC) metal-organic framework (MOF) material has been performed using a combination of thermogravimetric analysis (TGA), *in-situ* Raman and synchrotron powder X-ray diffraction (PXRD) techniques. Although a structural collapse of crystal framework at elevated temperatures before decomposition was observed with diffraction, the *in-situ* Raman spectroscopy showed that the framework maintained its integrity. Crystallinity could be recovered by rehydration with solvent.

7.2 Results and Discussions

7.2.1 Crystal Structure of Ho-MOF-BDC System

Single crystal X-ray diffraction and thermogravimetric analysis have been used to determine the composition of Ho-MOF-BDC, which was found to be $Ho(C_8H_4O_4) \cdot [(CH_3)_2NCOH]_2 \cdot NO_3$. The molecular structure shown in Figure 7.1 exhibits that Ho-MOF-BDC has a three-dimensional (3-D) network with one-dimensional (1-D) channels along c axis. It crystallizes in the monoclinic crystal system, with space group *C2/c*, lattice parameters of $a = 17.058(2)$Å, $b = 10.673(1)$Å, $c = 10.572(1)$Å, $\beta = 96.116(2)°$. Each building unit consists of one eight-coordinated holmium ions, one BTC ligand, one DMF molecule and one nitrate group. The eight oxygen atoms coordinated with each holmium ion are from four carboxyl groups of different benzoic acid ligands, two monodentated DMF molecules and one bidentated nitrate group. The bond distances

between Ho-O_{BDC} are in the range 2.2434(14)-2.2913(14)Å, Ho-O_{DMF} bond distance is 2.3857(15)Å and Ho-$O_{nitrate}$ bond distance is 2.3856(15)Å. A similar lanthanide MOF structure has been proposed by Yaghi and his co-worker[1] and forms 1-D ca. 6.6 × 3Å rhombic channels along c axis, which are occupied by coordinated DMF solvents and nitrate group (taking into account the van der Waals radii of the atoms).
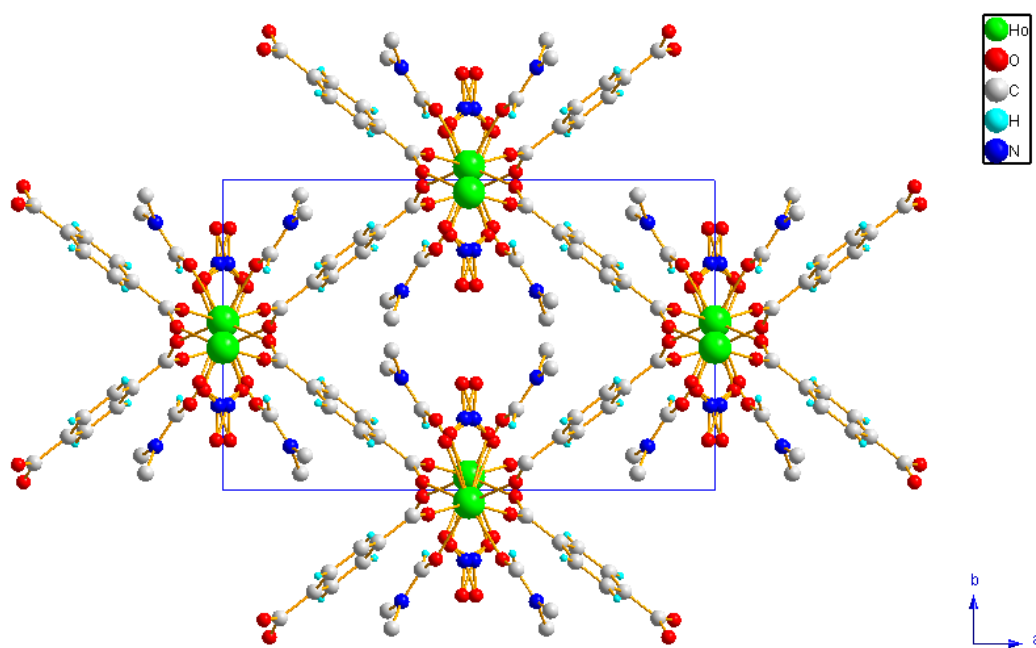
Figure 7.1 The 3-D molecular model of the as-synthesized Ho-MOF-BDC system viewed along c axis.

Systems	Ho-MOF-BDC
Empirical formula	$Ho(C_8H_4O_4) \cdot [(CH_3)_2NCOH]_2 \cdot NO_3$
Formula weight	537.24
Temperature	298(2) K
Wavelength	0.71073 Å
Crystal size	$0.29 \times 0.23 \times 0.20$ mm^3
Crystal habit	pink prism
Crystal system	Monoclinic
Space group	$C2/c$
Unit cell dimensions	a = 17.0583(14) Å, $\alpha = 90°$
	b = 10.6730(9) Å, $\beta = 96.116(2)°$
	c = 10.5721(9) Å, $\gamma = 90°$
Volume	1913.8(3) Å^3
Z	4
Density, ρ_{calc}	1.865 g/cm^3
Absorption coefficient, μ	4.185 mm^{-1}
θ range for data collection	2.25 to 27.50°
Index ranges	$-22 \le h \le 22, -13 \le k \le 13, -12 \le l \le 13$
Reflections collected	12749
Independent reflections	2198
Observed reflection, I>2σ(I)	2154
Data / restraints / parameters	2198 / 213 / 232
Goodness-of-fit on F^2	1.000
Δ/σ_{max}	0.001
Final R indices:	R_1, I>2 (I) = 0.0121
	wR$_2$, all data = 0.0288
	R_{int} = 0.0210
	R_{sig} = 0.0122
$R_1 = \Sigma ||F_o| - |F_c||/\Sigma |F_o|$, $wR_2 = [\Sigma w(F_o^2 - F_c^2)^2/\Sigma w(F_o^2)^2]^{1/2}$	

Table 7.1 The details of measured parameters, structural information and refinement results obtained from single crystal analysis on Ho-MOF-BDC systems.

7.2.2 Thermal and Structural Properties of Ho-MOF-BDC System

The TGA data is shown in Figure 7.2 that was performed under N_2 flow 60ml/min and 10^oC/min heating rate. A 4-step mass lose is evident with the first phase stable up to around 100^oC as a result of the strong chemical bonding present even in the solvent molecules. There are two obvious phase transitions between ca. 115 to 250^oC, which correspond to weight loss of 10.91wt% and 12.61wt%, respectively, which is equal to that expected from the loss of two DMF solvent molecules (e.g. 13.6wt% for each) per molecular formula. Another phase transition accompanies 12.82wt% loss at elevated temperature range between ca. 413 to 447^oC, corresponding to the decomposition of the nitrate group (theoretically 11.54wt%). Finally, the decomposition of the compound attributes a dramatic weight loss above ca. 500^oC, corresponding to a collapse of the structure to dense phase.
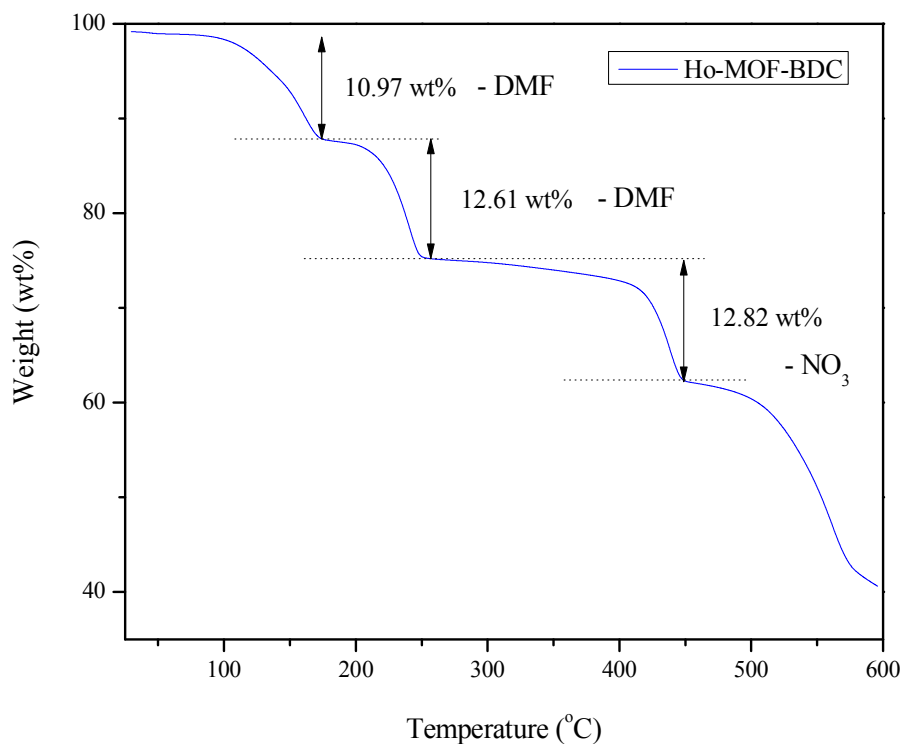
Figure 7.2 Thermogravimetric analysis (TGA) for the Ho-MOF-BDC system.

7.2.3 *In-situ* Synchrotron PXRD and Raman Spectroscopy

As shown in Figure 7.3, a very pure Ho-MOF-BDC phase can be obtained and structure determined by Rietveld refinement at 26.85°C of synchrotron X-ray diffraction data. Reliability factors based on the entire powder pattern (weighted R factor, wR_p) is 5.94%, and the Bragg peak integrated intensities (R factor, R_p) is 4.16%, respectively. In Figure 7.4, a two-dimensional (2-D) contour of the diffraction pattern as a function of heating from 26.85 to 526.85°C reveals very complex series of phase transitions. The different phases can be defined and identified as: (1) α phase: between temperature range of T1 = 26.85°C and T3 = 212.18°C. The structure contains four BDC ligands, two DMF solvent molecules and one nitrate group, (2) β phase: between T2 = 160.46°C and T4 = 276.83°C with four BDC ligands, one DMF solvent molecule and one nitrate group, (3) γ phase: between T4 = 276.83°C and T5 = 337.17°C with four BDC ligands and only one nitrate group, (4) δ phase: between T5 = 337.17°C and T6 = 449.23°C with four BDC ligands and only one nitrate group, and (5) ε phase: between T6 = 449.23°C and T7 = 526.85°C with four BDC ligands and starting decompose to dense phase. The transitions and bonding configurations shown in Figure 7.5 are roughly consistent with the observations from TGA analysis. However, from TGA result, there is only one large plateau between ca. 250°C and 415°C that corresponds to two phases in the PXRD results. These phases are hard to identify by diffraction due to the concomitant formation of impurity phases and the partial or total collapse of Ho-MOF-BDC framework structure. Meanwhile, as shown in Figure 7.6 (a)-(c), *in-situ* Raman spectroscopy was applied to monitor the bonding as a function of temperature. The results shown in Figure 7.6 (a)-(b) reveal strong Raman scattering peaks from BDC ligand (blue label), DMF molecules (red label) and nitrate group (green label) in α and β phase, implying that there are still strong

coordinated bondings with holmium cation. In Figure 7.6 (c), after the departure of both DMF, some Raman scattering still exists from BDC ligands within the framework, which means the integrity of the framework is maintained. The difference between γ and δ phase possibly results from the various orientations for nitrate group since there is no weight loss in the TGA experiments. Raman spectrum has no peaks for ε phase, demonstrating the framework decomposition (not show in here).
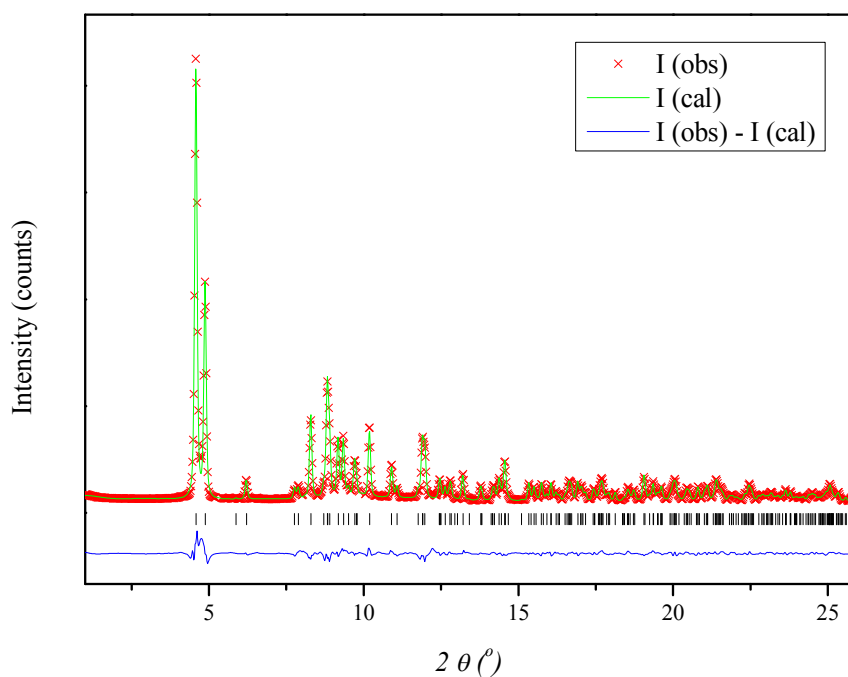
Figure 7.3 The Rietveld refinement of synchrotron PXRD for Ho-MOF-BDC system.
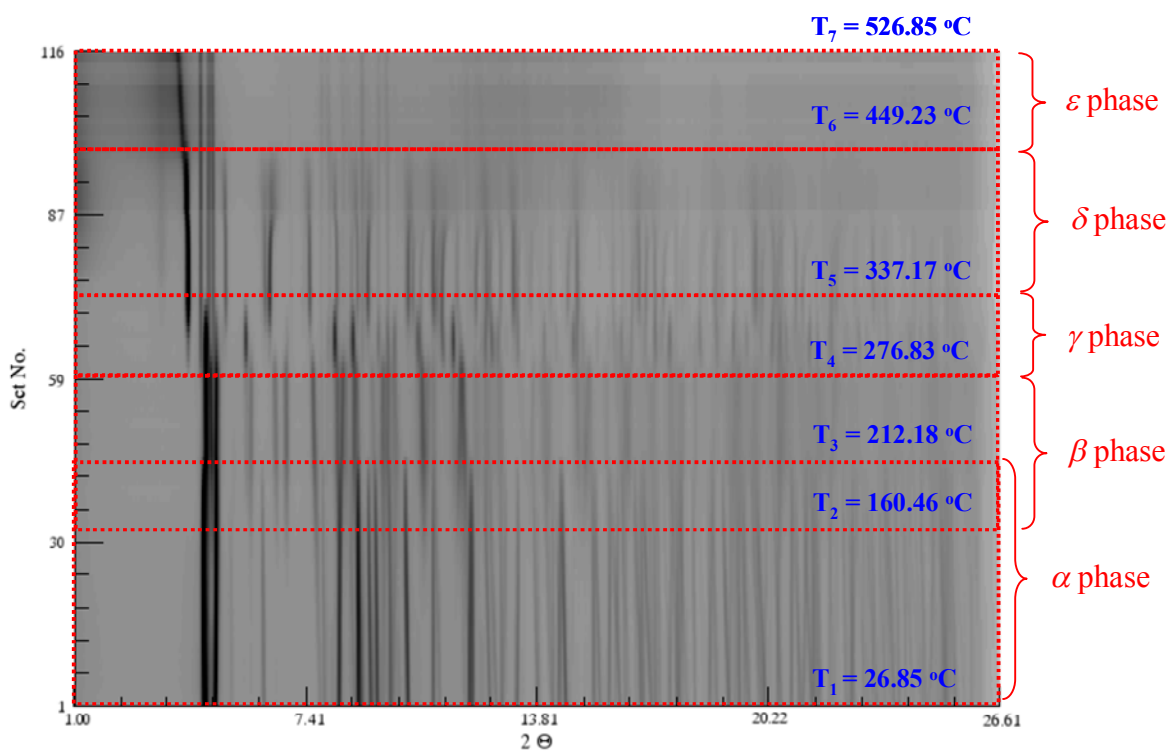
Figure 7.4 The 2-D contour of *in-situ* synchrotron PXRD for Ho-MOF-BDC system

between 26.85 to 526.85°C.

(a)

BDC ligand   *BDC ligand*

Nitrate

BDC ligand   *DMF*   *DMF*   *BDC ligand*

(b)

BDC ligand   *BDC ligand*

Nitrate

BDC ligand   *DMF*   *BDC ligand*
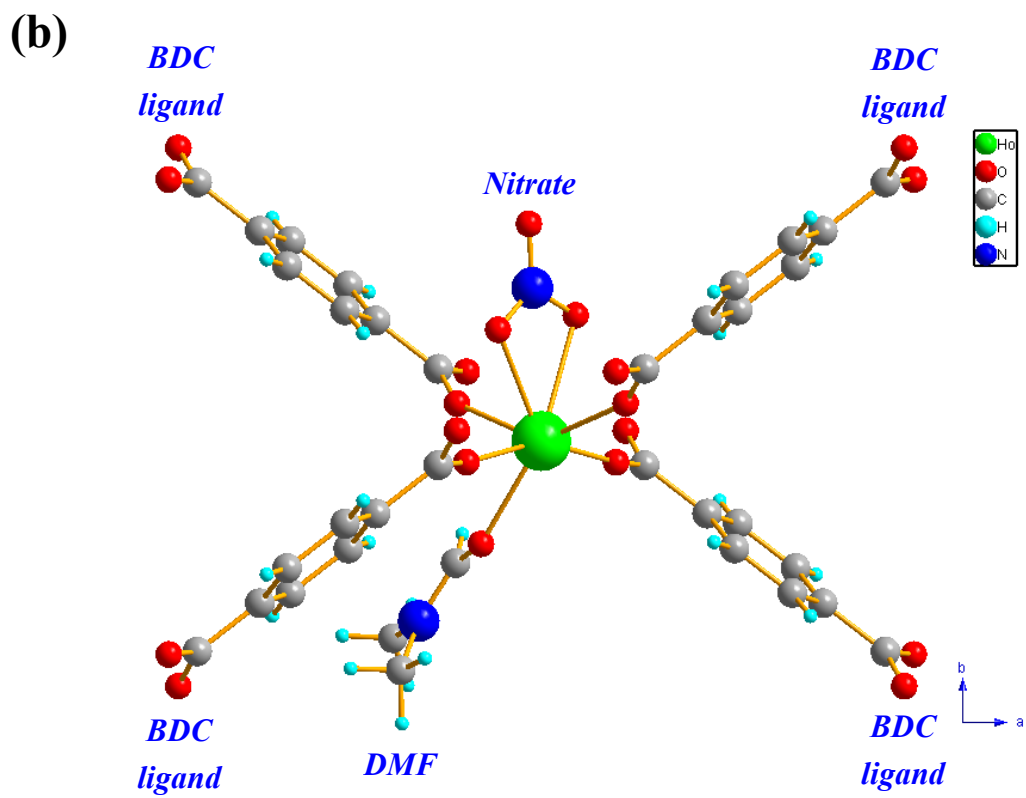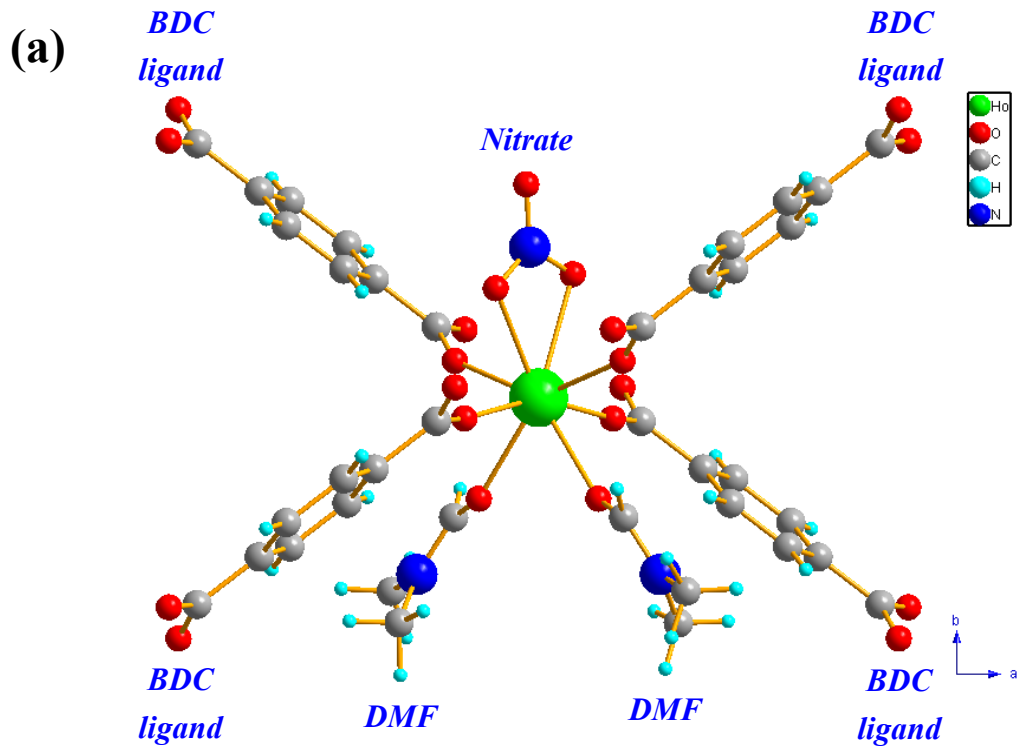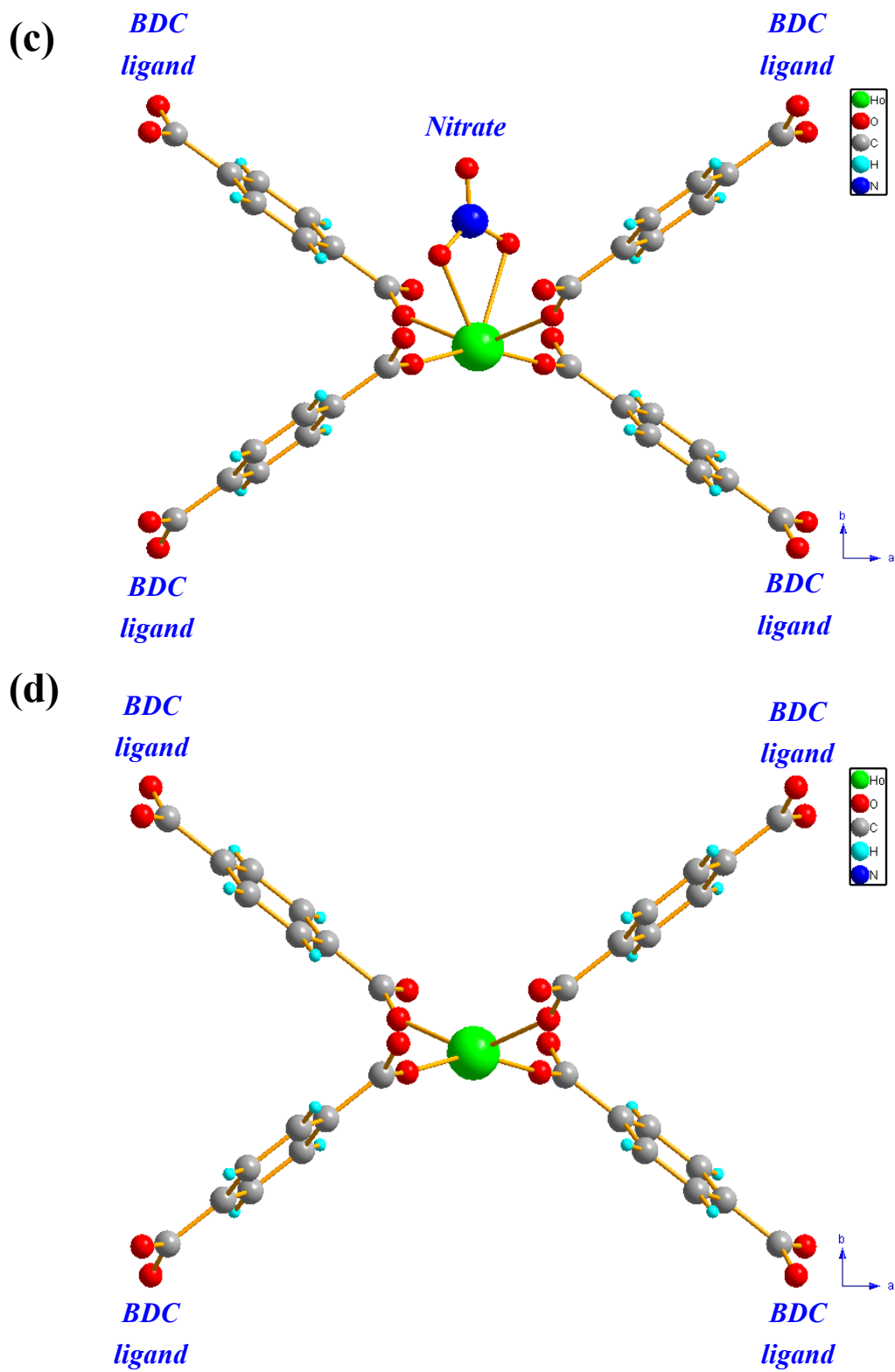
Figure 7.5 The bonding configurations for (a) α, (b) β, (c) γ and δ and (d) ε phase for Ho-MOF-BDC system.
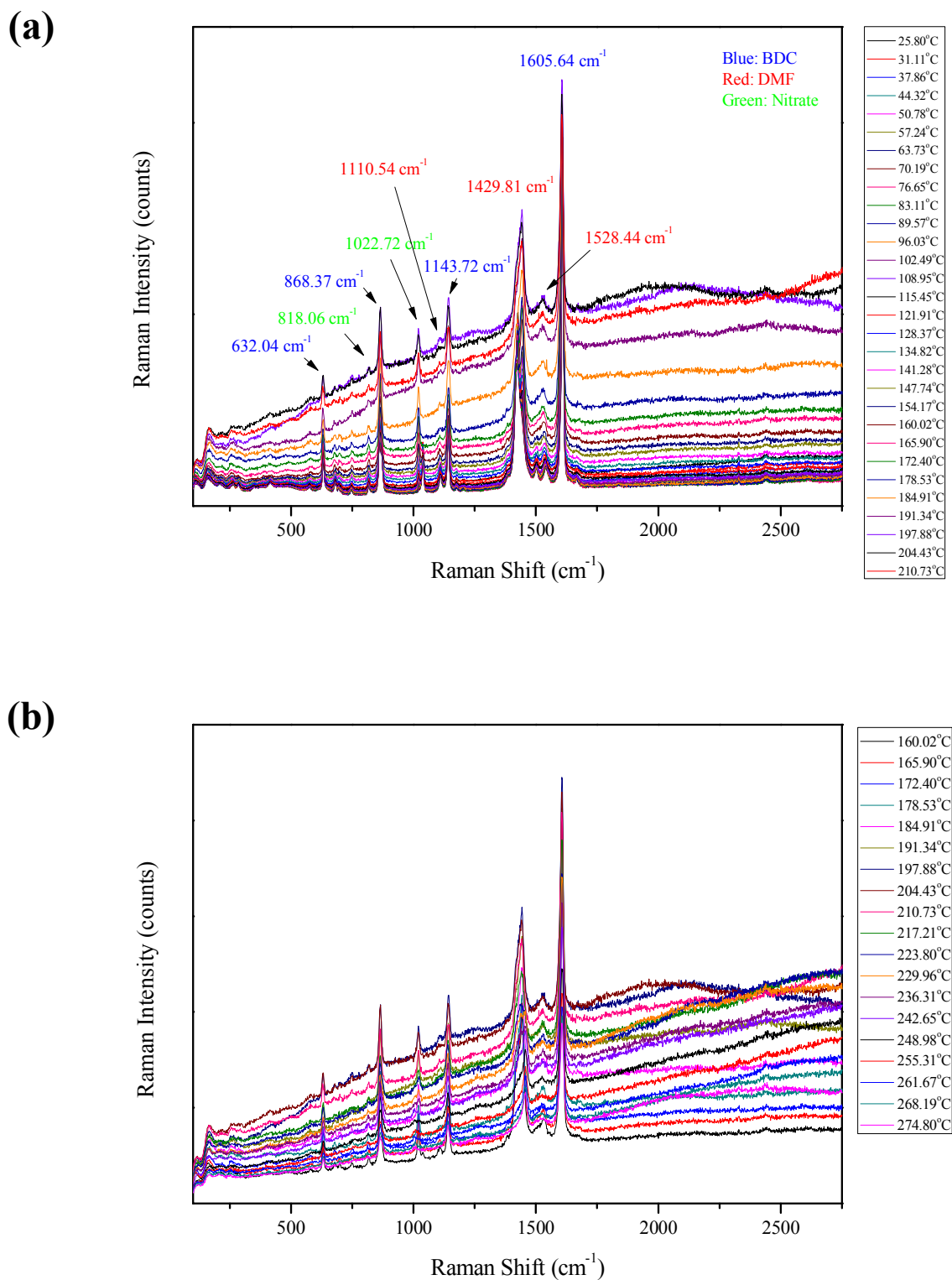
(a)

(b)

Figure 7.6 (a)-(b) *In-situ* Raman spectroscopy for α and β phases, and Figure 7.6 (c) For γ and δ phases of Ho-MOF-BDC system.

(c)
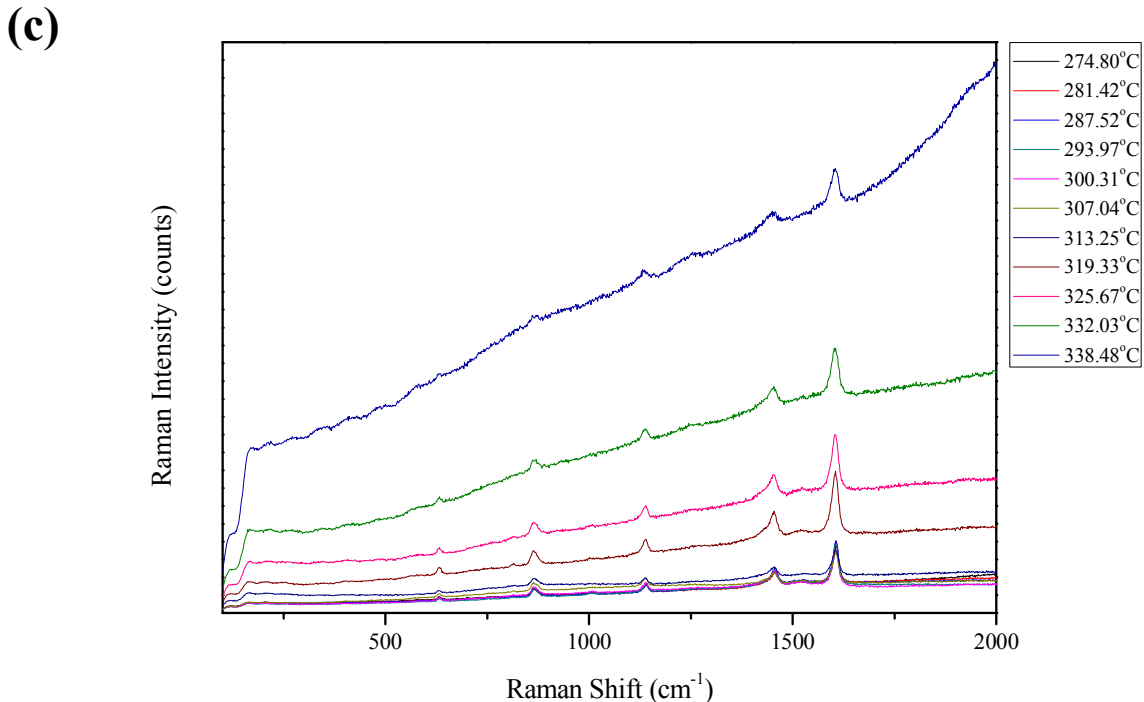
Figure 7.6 (a)-(b) *In-situ* Raman spectroscopy for α and β phases, and Figure 7.6 (c) For γ and δ phases of Ho-MOF-BDC system (continued).

7.2.4 Gas Isotherm experiments and Re-sorption Behavior for Dehydrated Ho-MOF-BDC System

The degassed Ho-MOF-BDC sample was prepared at $280^{o}C$ for 30 minutes under 10^{-6}torr vacuum and performed for the low pressure (0 to 1atm) gas isotherm experiment. The result from Figure 7.7 shows that excess adsorption volume of N_2 at 77K is only 5.0ml/g, and the calculated BET (Brunauer-Emmett-Teller) surface is $78.41m^2$/g, suggesting that the crystal framework has collapsed to an amorphous phase. However, the *in-situ* Raman spectra maintain the intensity of the chemical bonding within the high temperature range. In Figure 7.8 shows two X-ray patterns, the original structure and another obtained by immersing the dehydrated Ho-MOF-BDC powders in DMF solvent

for 3 days. The rehydrated sample shows a PXRD pattern that contains strong Bragg peaks and is consistent with the as-synthesized structure. This behavior is strong evidence that the framework was collapsed, but not destroyed when the coordinated solvent molecules/functional group are excluded, which is consistent with the *in-situ* Raman experimental results. It demonstrates that the structure can be recovered with DMF solvent.
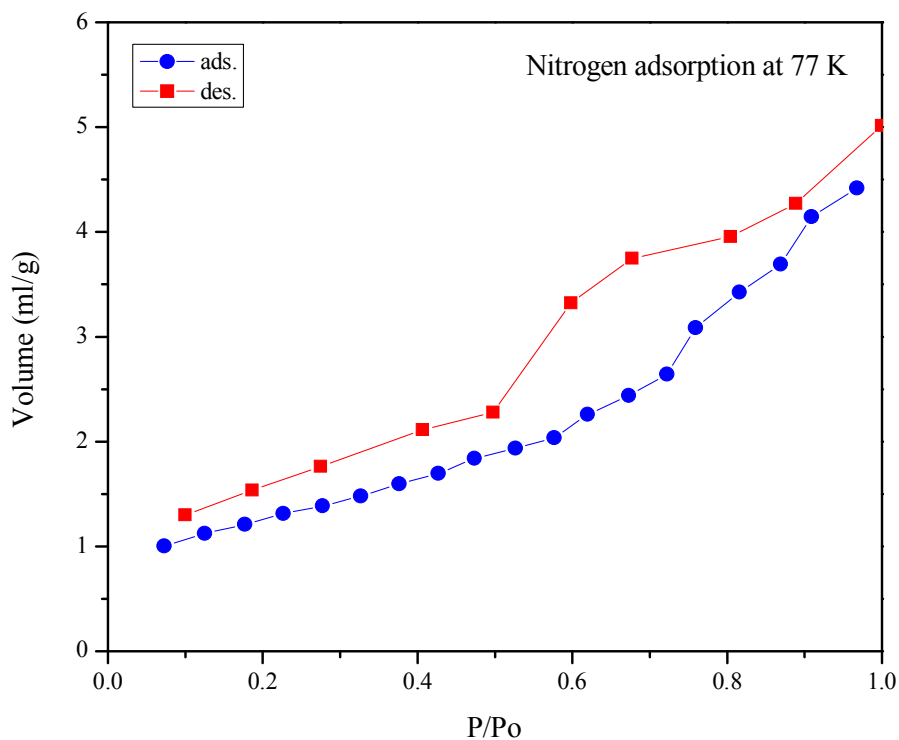
Figure 7.7 The N_2 adsorption volumetric isotherm experiment for dehydrated Ho-MOF-BDC system.
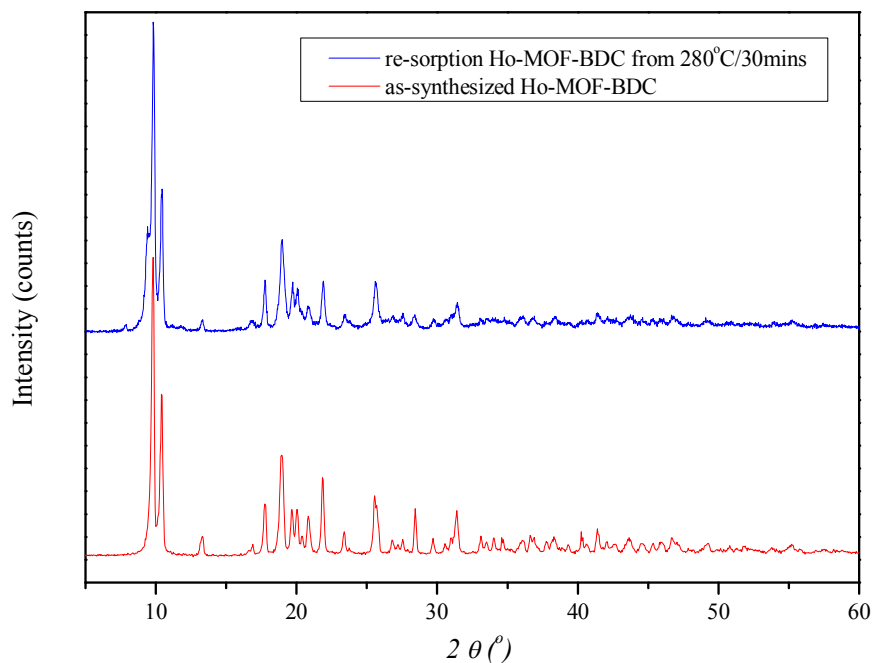
Figure 7.8 The comparison of PXRD patterns for as-synthesized (red) and re-sorption Ho-MOF-BDC (blue) systems.

7.3 Conclusions

A 3-D network Ho-MOF-BDC framework structure with 1-D rhombic channels along *c* axis has been synthesized and investigated. A complex series phase transitions are observed and studied via a combination with thermal analysis, *in-situ* synchrotron PXRD and Raman spectroscopy. Although a crystalline phase is not observed at elevated temperature range, Raman spectra confirm that the structural integrity is maintained, which finally can be verified by gas adsorption isotherm and re-sorption experiments.

7.4 References

(1) Reineke, T. M. ; Eddaoudi, M.; O'Keeffe, M. and Yaghi, O. M. *Angew. Chem. Int. Ed.* **1999**, *38*, 2590.

Chapter 8: Synthesis, Structure and Properties of Transition Metal (Manganese, Cobalt and Nickel) and Lanthanide (Cerium, Europium and Terbium) Formates

8.1 Introduction

Molecule-based magnets have received intense activity not only in terms of fundamental research on the magnetic exchanging interactions but the rich variety of systems allows detailed investigation into the correlations between structures and magnetisms. The major hindrance in the development of new magnetic MOF materials is ensuring sufficient magnetic coupling between magnetic ions. In general, magnetic exchange is promoted in shorter ligands. Recently, the formate anion ($HCOO^-$) has received particular attention and been used to synthesize a number of new molecular magnets because: (i) Formate is the smallest and simplest carboxylate and offers all the functionalities of carboxylates. It can adopt various bridging modes such as *syn-syn*, *anti-anti* and *syn-anti* as shown as Table 8.1[1] enable to link metal ions, (ii) Formate can work as a three- or one-atom connector providing significant magnetic coupling between spin moment carriers, and (iii) In contrast, formate has been less explored than other short ligands, such as cyanide (CN^-), azide (N_3^-), oxalate ($C_2O_4^{2-}$), acetate ($CH_3CO_2^-$) and dicyanamide ($N(CN)_2^-$)[2-20]. Specifically, the numbers in Table 8.1 refer to the Harris notation, which describes the binding mode as $[X.Y_1Y_2Y_3…..Y_n]$, where X is the overall number of metals bound by the whole ligand, and the Y value refers to the number of metal atoms attached to the different donor atoms. The ordering of Y is listed by the Cahn-Ingold-Prelog priority rules[1]. There are several reported systems using the

protonated amine cations (amineH$_n$) as an organic template solvent for chemical syntheses. The template effects of ammonium cations consist of (i) The hydrogen bonding interaction between the cation solvent molecules and the host framework, (ii) The contribution from the structural information, such as size and geometry of the cation on to the templated architecture, and (iii) The charge compensation and neutralization of the whole crystal system. In this chapter, three transition-metal formate and other three lanthanide formate crystals have been synthesized by solvothermal methods under several different conditions. The correlation between crystal structures, magnetic and optical properties is investigated and discussed below.
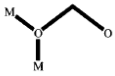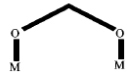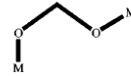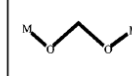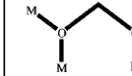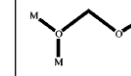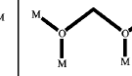
	syn-syn	syn-anti	anti-anti		
2.20				3.12	4.22
		2.11			

Table 8.1 The bridging modes for fromate (CHOO$^-$) anion.

8.2 Transition Metal Formates

In this series of synthesis, DMF played a very significant role not only to serve as the solvent for the crystals to be separated out because the compounds are very dissolvable in H$_2$O, but also acting as the source of formate and dimethylamine (DMA)[1,21-25].

8.2.1 Synthesis of [(CH$_3$)$_2$NH$_2$]M(HCO$_2$)$_3$ (M-formate-1) System

Two transition metal complexes **(M: Mn(1) and Co(2))** have been synthesized by solvothermal reaction. Transition metal (II) nitrate $(M(II)(NO_3)_2 \cdot xH_2O)$ was mixed with malonic acid powder at 1 : 1 molar fraction, dissolved in a mixed solvent which consisted of 3ml DMF, 3ml methanol and 6ml H_2O, then placed in a 20ml Teflon-lined steel autoclave under autogenous pressure at $160^{\circ}C$ for 3 days and naturally cooled to room temperature. Square-plate purple crystals were obtained by slowly evaporating the filtered clean solution at room temperature for 1 week after the reaction.

8.2.2 Synthesis of $[(CH_3)_2NH_2]Co(HCO_2)_3$ (Co-formate-2) System

This Co-formate-2 crystal was synthesized following the process that was described in section 8.2.1. The annealing temperature was changed to $180^{\circ}C$ for 3 days to obtain this structure.

8.2.3 Structure Identifications

Three transition-metal formate materials, called Co-formate-1, Co-formate-2 and Mn-formate have been synthesized and analyzed by single crystal X-ray diffraction. The detailed information on the crystal structure is summarized in Table 8.3. Co-formate-1 and Mn-formate are isostructural, whereas Co-formate-2 adopt a different configuration. Co-formate-1 crystallizes in the trigonal crystal system, with space group $R\bar{3}c$, and lattice parameters of a = 8.166(2)Å, b = 8.166(2)Å, c = 22.193(9)Å, γ = 120°, while the Co-formate-2 crystal is monoclinic with space group Cc, and lattice parameters of a = 14.155(2)Å, b = 8.182(1)Å, c = 8.697(1)Å, γ = $121.577(2)^{\circ}$. The cavities in both frameworks are filled with dimethyl ammonium (DMA) cations. However, the structure of Co-formate-2 can be thought as a distortion of the known trigonal structure of

Co-formate-1 system, which has been proposed and published before[1,26-29]. The relationship between the new structure to the cell of Co-formate-1 can be seen by transforming the monoclinic cell as shown in Table 8.2. Therefore, the Co-formate-2 system can be viewed as a pseudo-trigonal structure with non-orthogonal angles. Furthermore, if compared with the Co-formate-1 along [110] direction and the Co-formate-2 along [010] direction (Figure 8.1 (a) and (b) respectively) very similar frameworks are observed. One key difference is that the DMA cations simply because DMA cations are disordered in Co-formate-1 but perfectly ordered in Co-formate-2. In order to the order/ disorder of the DMA cations, inspection of the Co bond lengths shows very significant difference. Co-formate-1 with the disordered DMA cations, has 6 equal Co-O$_{formate}$ distances whereas the Co-formate-2 with the monoclinic cell and ordered cations, possesses two short Co-O$_{formate}$ bonds, two long Co-O$_{formate}$ bonds and two that are roughly equivalent to those in Co-formate-1. In both structures, each cobalt ion is bonded to six formate units, which construct a cubic framework, very much related to the perovskite structure commonly found in oxides. The bond distance Co-O$_{formate}$ for Co-formate-1 is 2.101(2)Å, whereas the bond distance Co-O$_{formate}$ for Co-formate-2 is in the range of 2.084(2)-2.124(2) Å. Co^{2+} ions are in the low spin electronic configuration for both structures (see magnetism section 8.2.4). The origin of the different bond distance for Co-formate-2 is the strong Jahn-Teller (J-T) distortion that occurs in the low spin d^7 electronic configuration. The absence of this distortion in the disordered Co-formae-1 that is also low spin is likely to be a result of the existence of a dynamical Jahn-Teller effect as opposed to the static effect that occurs in the ordered DMA structure.

	a	*b*	*c*	*α*	*β*	*γ*
Cell	8.1848	8.1886	22.2670	90.0043	91.1268	120.0408
Error (s. u.)	0.0029	0.0030	0.0083	0.0130	0.0123	0.0102

Table 8.2 The analytic transformation on the lattice parameters from monoclinic to trigonal crystal system in Co-formate case.

(a)

Co	
O	
C	
H	
N	

(b)

Co	
C	
H	
O	
N	
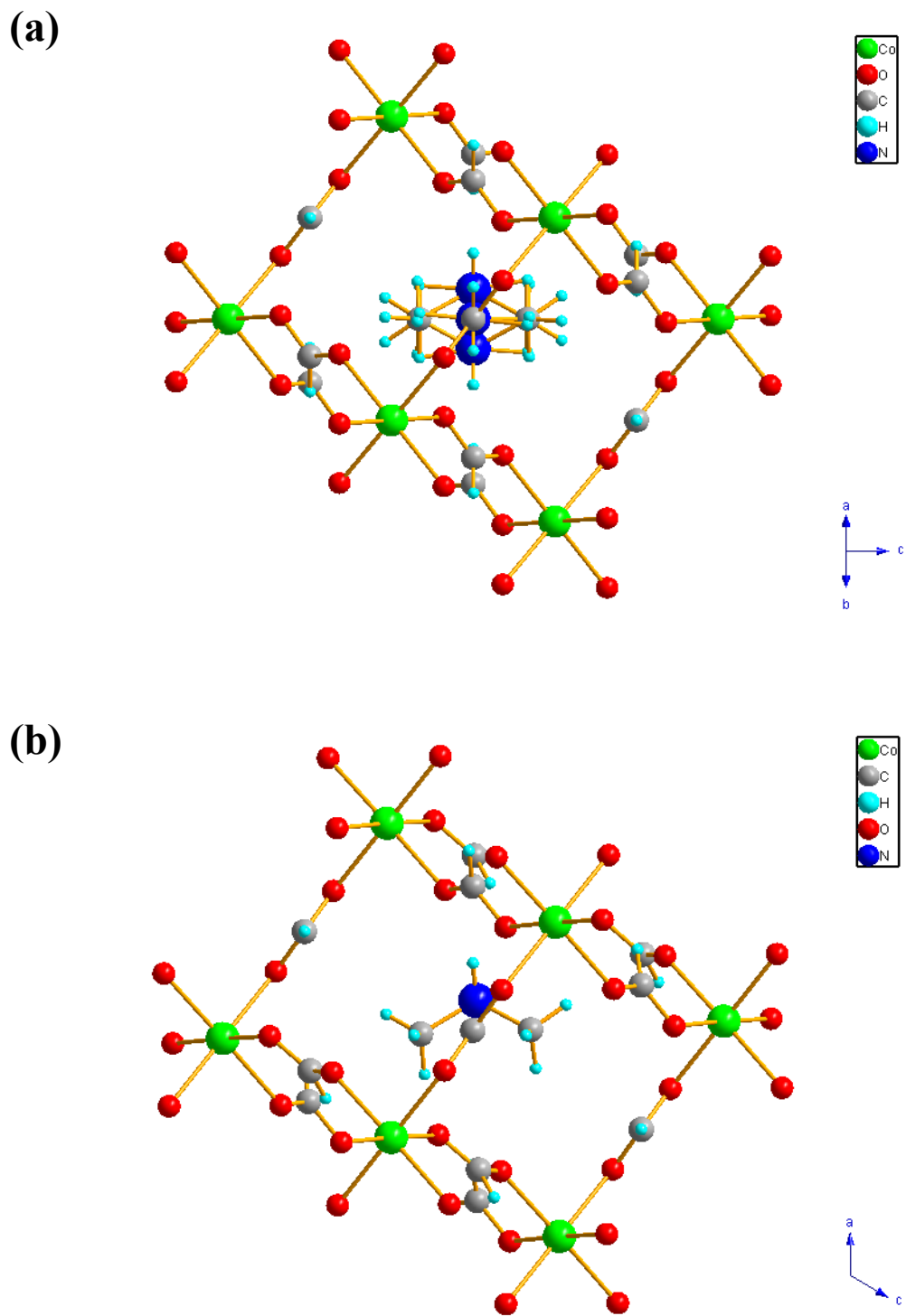
Figure 8.1 (a) Co-formate-1 system with disordered dimethyl ammonium (DMA) solvent viewed along [110] direction, and (b) Co-formate-2 system with ordered dimethyl ammonium (DMA) solvent viewed along [010] direction.

8.2.4 Magnetic Properties for Co-formate Systems

In both Co-formate-1 and Co-formate-2 systems, the cobalt ions are in the square lattice arrangement with magnetic exchanging taking place through formate ligands at 180°, which favors the antiferromagnetic coupling interaction[30-32]. This 3-D framework possesses the $(4^{12} \cdot 6^{3})$ network topology with cubic cavities inside[33] and can be described as metal-organic perovskite compounds of [amineH][Co(HCOO)$_3$] (ABX$_3$, A= amineH$^+$, B = Cobalt, and X=HCOO$^-$). The detailed investigations of structure and magnetic properties of Co-formate-1 have already been proposed[1,26-29]. However, in this section, a comparison between the ordered and disordered structures is investigated and discussed. It should be emphasized that all the measured conditions are identical for each experiment. Temperature dependence of the magnetic susceptibility χ_M (molecular susceptibility) from 4 to 300K in Figure 8.2 (a) was performed using some randomly orientated single crystals with a mass of 9.8 and 6.6m, respectively. It shows a peak in the susceptibility at 12K but which is stronger for the Co-formate-2 system. However, the increase in magnetic susceptibility below 12K is much greater for the Co-formate-1 compared to Co-formate-2. Furthermore, the temperature-dependent $1/\chi_M$ can be seen from Figure 8.2 (b), where the magnetic susceptibility obeys the Curie-Weiss law in the

range of 50-300K with a Curie constant (*C*) 3.99(2)emu K/ mole for Co-formate-1 and 3.97(3)emu K/ mole for Co-formate-2 which are close to the experimental value 3.0emu K/ mole for an octahedronal Co^{2+} ion[34]. The Weiss constants (θ) are found to be -47.9(7)K and -57(1)K for Co-formate-1 and Co-formate-2, respectively. In Figure 8.3, the magnetization for both the ZFC and FC curves measured in 100Oe increase below 15K. The magnetization values reach a plateau around 6K for Co-formate-1 before

increasing again below 4K. An interesting phenomenon is seen when comparing Co-formate-1 and Co-formate-2; the values of the magnetization are around five times greater for Co-formate-1. Moreover, a significantly magnetic hysteresis loop measured at 4K in Figure 8.4 can be observed for Co-formate-1 system, significant amounts of ferromagnetism in Co-formate-1 compared with Co-formate-2. These experiments suggest the following (i) Co-formate-1 and -2 are both low spin ($S = \frac{1}{2}$) with similar Weiss constants indicating similar antiferromagnetic exchange, (ii) Both Co-formate-1 and Co-formate-2 systems exhibit weak ferromagnetism at low-temperature state (below ca. 15K) as a result of spin canting. The difference between these two systems is likely to result from the ordering of the DMA cations; the disorder of the DMA in Co-formate-1 results in dynamical Jahn-Teller effect and enhancement of the orbital contribution, whereas the orbital contribution to the moment is reduced with the static Jahn-Teller effect, and (iii) The origin of the two-step transfer in ZFC-FC curves is still not clear, but this phenomenon might be caused by the move of the domain walls which results in the reorientation of the ordered spin state[35,36]. Although further work is required to clarify the electronic properties, the Co-formate-2 system possessing a non-centrosymmetric space group *Cc* and ordered DMA molecules results in a new multiferroic material, worthy of further investigation.

(a)

(b)
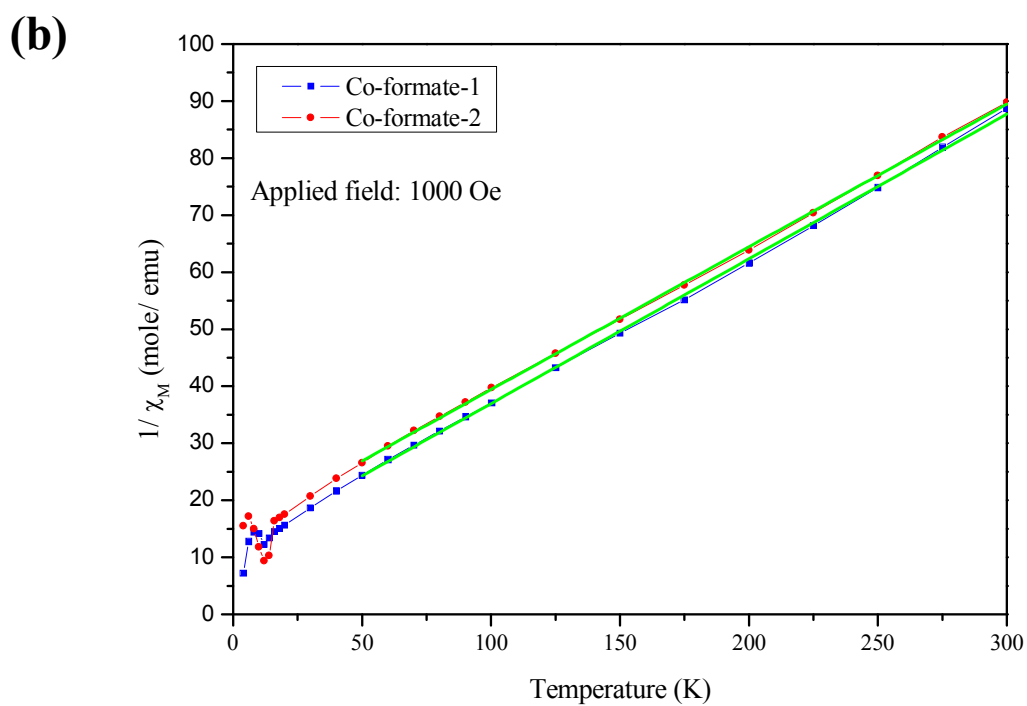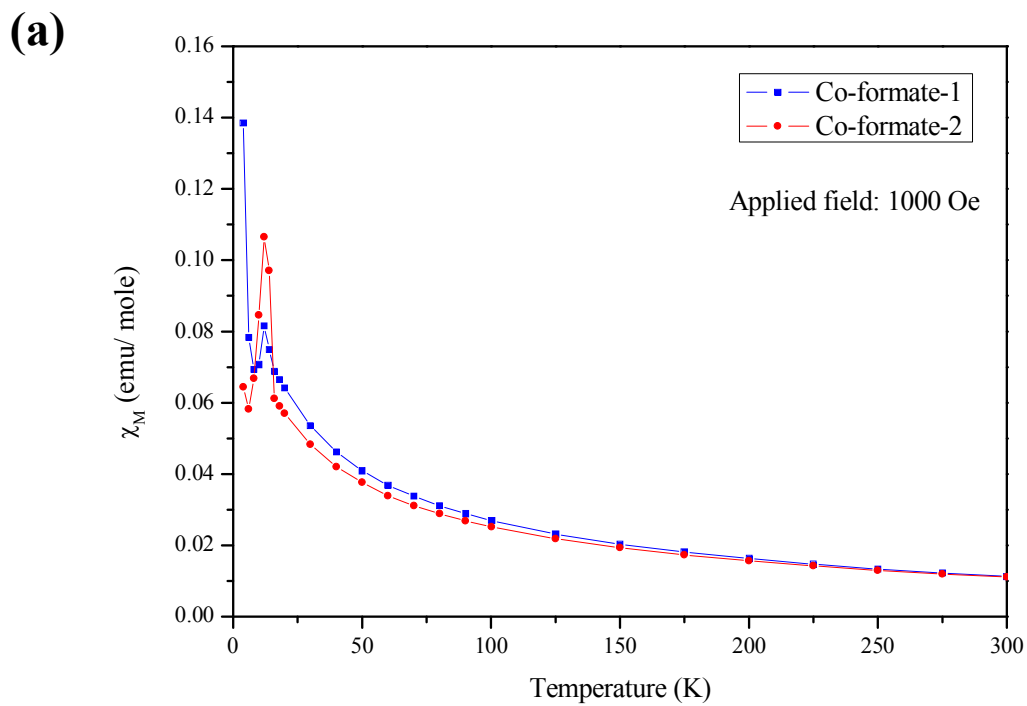
Figure 8.2 (a) Temperature dependence of molar susceptibilities (χ_M), and (b) of inverse molar susceptibilities ($1/\chi_M$) for Co-formate-1 and Co-formate-2 systems.
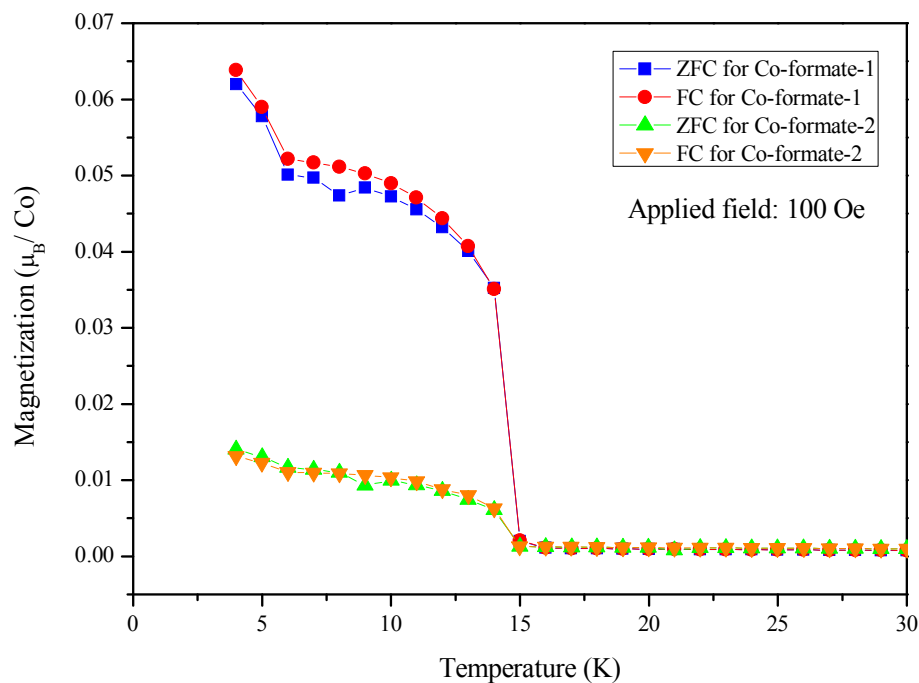
Figure 8.3 Temperature dependence of ZFC-FC (zero field cooling- field cooling) plots for Co-formate-1 and Co-formate-2 systems under 100Oe.
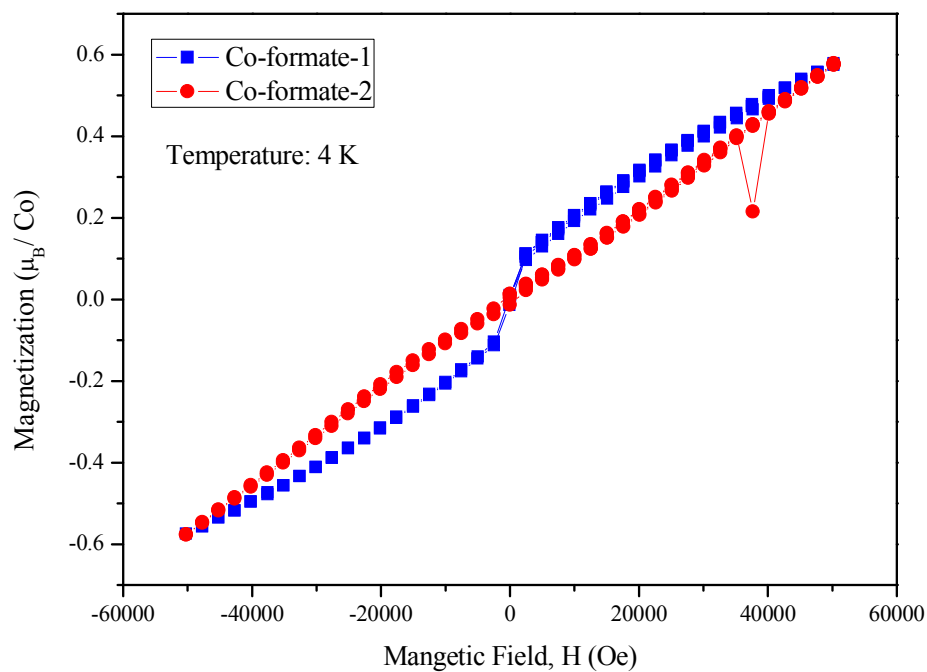
Figure 8.4 Illustrations of magnetic hysteresis for Co-formate-1 and Co-formate-2 systems between -50000Oe and 50000Oe magnetic field at 4K.

Systems	Co-formate-1	Co-formate-2
Empirical formula	$Co(HCOO)_3 \cdot [(CH_3)_2NH_2]$	$Co(HCOO)_3 \cdot [(CH_3)_2NH_2]$
Formula weight	240.08 g/mole	240.08 g/mole
Temperature	150(2) K	150(2) K
Wavelength	0.71073 Å	0.71073 Å
Crystal size	$0.33 \times 0.21 \times 0.14 \text{ mm}^3$	$0.27 \times 0.25 \times 0.05 \text{ mm}^3$
Crystal habit	purple prism	purple prism
Crystal system	Trigonal	Monoclinic
Space group	$R\bar{3}c$	Cc
Unit cell dimensions	$a = 8.1660(16)$ Å, $\quad \alpha = 90°$	$a = 14.1547(16)$ Å, $\quad \alpha = 90°$
	$b = 8.1660(16)$ Å, $\quad \beta = 90°$	$b = 8.1815(9)$ Å, $\quad \beta = 121.577(2)°$
	$c = 22.193(9)$ Å, $\quad \gamma = 120°$	$c = 8.6971(10)$ Å, $\quad \gamma = 90°$
Volume	$1281.6(6) \text{ Å}^3$	$858.06(17) \text{ Å}^3$
Z	6	4
Density, ρ_{calc}	1.866 g/cm^3	1.858 g/cm^3
Absorption coefficient, μ	2.008 mm^{-1}	1.999 mm^{-1}
θ range for data collection	2.75 to 31.90°	3.01 to 30.00°
Index ranges	$-11 \leq h \leq 11, -12 \leq k \leq 10, -32 \leq l \leq 27$	$-19 \leq h \leq 19, -11 \leq k \leq 11, -12 \leq l \leq 12$
Reflections collected	2832	6842
Independent reflections	478	2415
Observed reflection, $I>2\sigma(I)$	465	2323
Data / restraints / parameters	478 / 0 / 26	2415 / 2 / 127
Goodness-of-fit on F^2	1.000	1.000
Δ/σ_{max}	0.000	0.000
Final R indices:	$R_1, I > 2\sigma(I) = 0.0433$	$R_1, I > 2\sigma(I) = 0.0288$
	wR_2, all data = 0.1079	wR_2, all data = 0.0699
	$R_{int} = 0.0447$	$R_{int} = 0.0311$
	$R_{sig} = 0.0335$	$R_{sig} = 0.0316$
$R_1 = \Sigma||F_o|-|F_c||/\Sigma|F_o|, \quad wR_2 = [\Sigma w(F_o^2 -F_c^2)^2/\Sigma w(F_o^2)^2]^{1/2}$		

Table 8.3 The details of measured parameters, structural information and refinement results obtained from single crystal analyses of the transition-metal formate systems.

Systems	Mn-formate
Empirical formula	$[(CH_3)_2NH_2]Mn(HCO_2)_3$
Formula weight	236.09 g/mole
Temperature	200(2) K
Wavelength	0.71073 Å
Crystal size	$0.28 \times 0.15 \times 0.105$ mm^3
Crystal habit	colorless prism
Crystal system	Trigonal
Space group	R$\bar{3}$c
Unit cell dimensions	a = 8.3354(3) Å, $\alpha = 90°$
	b = 8.3354(3) Å, $\beta = 90°$
	c = 22.751(2) Å, $\gamma = 120°$
Volume	1368.95(14) Å^3
Z	6
Density, ρ_{calc}	1.718 g/cm^3
Absorption coefficient, μ	1.446 mm^{-1}
θ range for data collection	3.34 to 29.99°
Index ranges	$-11 \le h \le 10, -11 \le k \le 11, -31 \le l \le 31$
Reflections collected	4436
Independent reflections	449
Observed reflection, I>2σ(I)	436
Data / restraints / parameters	449 / 0 / 39
Goodness-of-fit on F^2	1.000
Δ/σ_{max}	0.000
Final R indices:	R$_1$, I > 2σ(I) = 0.0149
	wR$_2$, all data = 0.0360
	R$_{int}$ = 0.0150
	R$_{sig}$ = 0.0069
$R_1 = \Sigma||F_o|-|F_c||/\Sigma|F_o|$, $wR_2 = [\Sigma w(F_o^2 -F_c^2)^2/\Sigma\ w(F_o^2)^2]^{1/2}$	

Table 8.3 The details of measured parameters, structural information and refinement results obtained from single crystal analyses of the transition-metal formate systems (continued).

8.3 Lanthanide Formates and Tetraformate

8.3.1 Synthesis of Ln(HCO$_2$)$_3$ (Ln-formate) System

Two lanthanide complexes **(Ln: Ce(1) and Eu(2))** were synthesized by solvothermal reaction. Lanthanide nitrate (Ln(NO$_3$)$_3$·xH$_2$O) was dissolved in a mixed solvent system which consisted of 6ml DMF, and 6ml H$_2$O, then placed in a 20ml Teflon-lined steel autoclave under autogenous pressure at 140°C for 3 days and naturally cooled to the room temperature. Colorless needle-like crystals were obtained by slowly evaporating the filtered clean solution at room temperature for 1 week after the reaction.

8.3.2 Synthesis of [(CH$_3$)$_2$NH$_2$]$^+$[Tb(HCOO)$_4$]$^-$ (Tb-tetraformate) System

This Tb-tetraformate complex can be obtained via mixing terbium nitrate (Tb(NO$_3$)$_3$·5H$_2$O) with malonic acid powder at 1 : 1 molar fraction, dissolving in 6ml DMF and 6ml H$_2$O mixed solvent in a 20ml Teflon-lined steel autoclave under autogenous pressure at 180°C for 3 days and then naturally cooled to the room temperature. Colorless rod-like crystals were obtained by slowly evaporating the clean solution at 40°C for 3 days after the reaction.

8.3.3 Structure Identifications of Lanthanide Formates

Two isostructural lanthanide formate materials ((HCOO)$_3$Ln, Ln = Ce, Eu) have been synthesized and identified by single crystal X-ray diffractions. The details of crystal structure are given in Table 8.4. The Ce-formate crystallizes in the trigonal crystal system, with space group *R3m*, and lattice parameters of a = 10.689(1)Å, b = 10.689(1)Å, c = 4.113(1)Å, similar to the Eu-formate crystal where the lattice parameters are a = 10.495(1)Å, b = 10.495(1)Å, c = 4.005(0)Å. The difference in lattice parameters is a

result of the distinct ionic radii between Ce^{3+} (1.02Å) and Eu^{3+} (0.947Å). This lanthanide MOF crystal structure, showing in Figure 8.5, is a very condensed framework material absent any porosity. The Ln-formate coordination environment can be described as a tricapped trigonal prism of oxygen atoms. The metal centers are surrounded by nine carboxylate oxygen atoms: six carboxylate oxygen atoms from the formate anions bridging the lanthanide ions and forming the trigonal prism along c axis through Ln-O-Ln connection, and three oxygen atoms bonded to other three prisms by Ln-O-C-O-Ln connection along *ab* plane with **3.12** bridging mode[1]. The shortest distance between two lanthanide ions is 4.1133(5)Å and between adjacent chains is in range of 6.3218(3)-6.7531(3)Å. The Ce-O$_{formate}$ bond distance with the monodentated oxygen atom is in range of 2.5003(12)-2.5003(17)Å, and the bridging oxygen atom distances range from 2.5784(19) to 2.5960(19)Å. The Eu-O$_{formate}$ bond distance to the monodentated oxygen atom is in range of 2.4156(27)-2.4156(39)Å, and the bridging oxygen atom distance ranges from 2.5389(48) to 2.5090(47)Å. In this section, only Ce-formate will be investigated for magnetic property since europium ions possess half-filled *f* orbit (seven periphery occupied electrons) yielding no net magnetic moment. However, Eu-formate will be used in the photo-luminescent experiments because of its relatively high quantum-yield efficiency and emission spectrum in visible light wavelength (400-700nm).
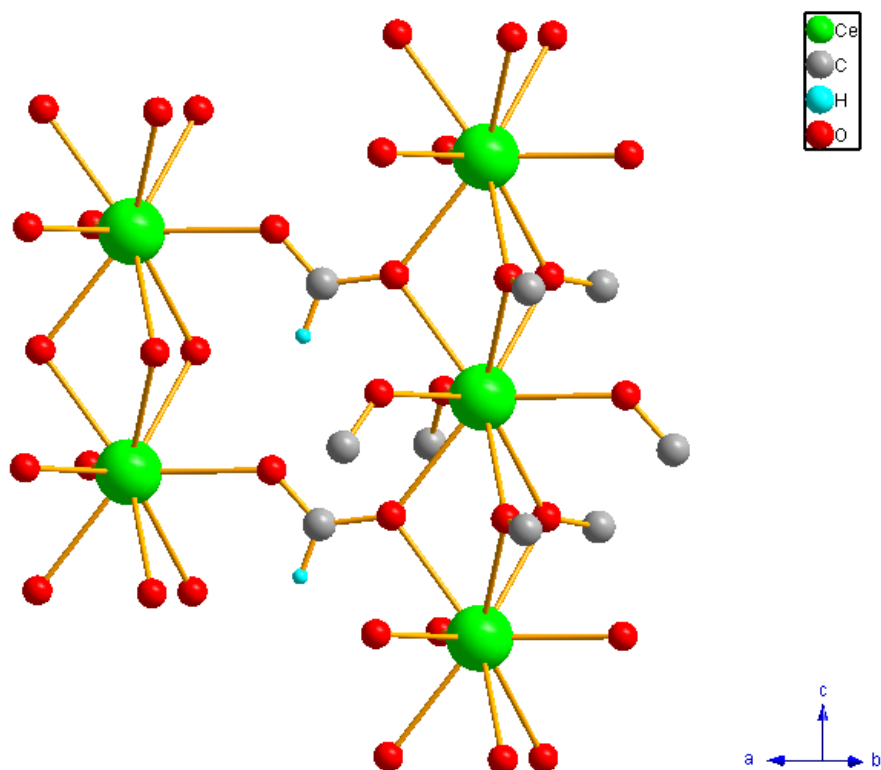
Figure 8.5 Illustration of 3-D molecular structure for Ce-formate which is isostructural with the Eu analogue.

8.3.4 The Magnetism for Ce-formate System

The temperature dependence of the magnetic susceptibility χ_M (molecular susceptibility) from 4 to 300K in Figure 8.6 (a) was measured using some randomly orientated single crystals with a mass of 8.0mg. The 1/ χ_M is shown in Figure 8.6 (b), where the magnetic susceptibility obeys the Curie-Weiss law in the range of 50-300K giving a Curie constant = 0.57(1)emu K/ mole and Weiss constants of 3(1)K. High resolution powder neutron diffraction has been performed at 1.5K to evaluate the magnetic structure for Ce-formate system as shown in Figure 8.7. Rietveld refinement

was performed using the initial model from single crystal X-ray diffraction, resulting in an excellent fit with R-factor $wR_p = 3.06\%$ and Bragg R-factor $R_p = 2.35\%$ which demonstrate the extremely high quality and purity for Ce-formate sample. However, this Rietveld refinement was achieved using only nuclear structure, therefore there was no magnetic scattering implying there is no long range magnetic order. This is consistent with the SQUID data, as there was only slight deviation from the Curie-Weiss law and no maximum in the susceptibility was observed.

8.3.5 Photoluminescence for Eu-formate System

Photoluminescence experiments were performed on the Eu-formate material. Around 10mg sample powders was uniformly spread out on a quartz slide to form thin film and covered by another thin quartz slide as a sandwich structure, which was amounted on the sample holder for solid-state fluorescence spectrometer. The power of xenon lamp voltage has been settled at 950V, the scanning speed 240nm/min and excitation slit = emission slit = 1nm. The background calibration has been performed before each experiment. Generally, UV/Vis spectroscopy should be applied to evaluate the maximum absorption wavelength, which will be used as excitation wavelength. However, for many molecule-based phosphors, the absorption spectra in ultra violet region (200–400nm) are very complicated and hard to define where the maximum absorption wavelength is. Therefore, each 5nm step of wavelength between 200 to 400nm have been tested as excitation wavelength (e. g. 200nm, 205nm…..395nm, 400nm), where the maximum intensity of emission spectra can be obtained. In Eu(III) compounds, the $^5D_0$-^7F_J transition series is the most obvious transition. In Particular, the ratio of the intensities between the ($^5D_0$-$^7F_2$) : ($^5D_0$-$^7F_1$) transitions is very sensitive to the local symmetry of the

Eu(III) ions. The $^5D_0$-$^7F_1$ transition has a prominent magnetic dipole and is relatively unaffected by the local environment. However, some transitions such as $^5D_0$-$^7F_2$ with ΔJ = ±2 are *hypersensitive* to the coordination environment because of their strong electric dipole characteristic[37]. Disparity allows the use of the relative intensities of these transitions to probe the nature of the linkage environment[37] especially when the single crystal analysis is not feasible. In this Eu-formate case, the maximum intensity of characteristic emission spectrum can be observed in Figure 8.8 when the excitation wavelength = 395nm has been chosen, and the relative ratio of intensities between $^7F_2$ and $^7F_2$ is large that supposes the coordinated environment of Eu(III) ions is basically asymmetric, which is consistent of our single crystal results. The europium compounds have been widely applied as red LED phosphors.

(a)
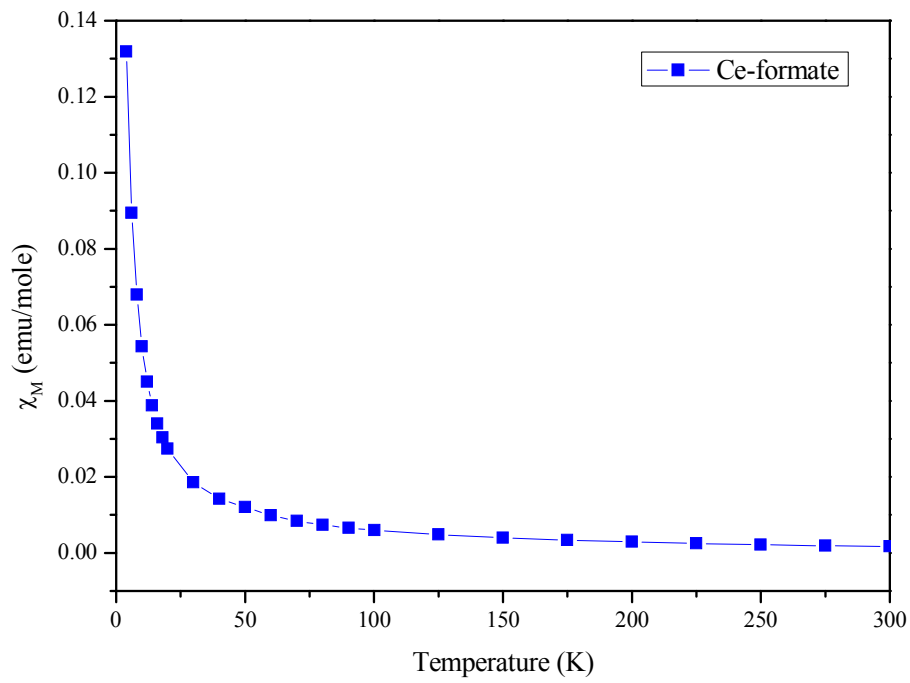
(b)
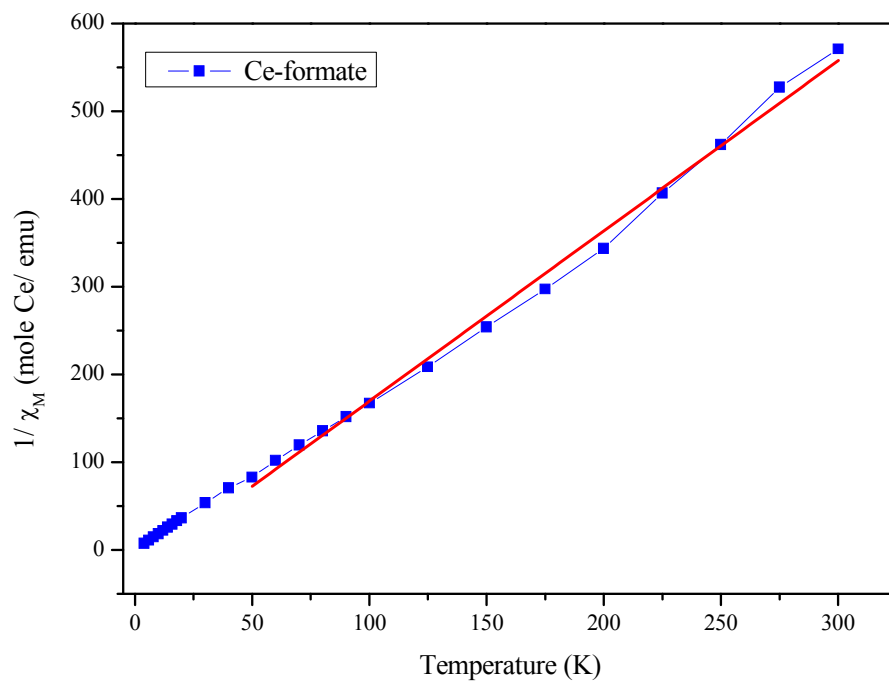
Figure 8.6 (a) Temperature dependence of molar susceptibilities (χ_M) and (b) Temperature dependence of inverse molar susceptibilities (1/ χ_M) for Ce-formate system.
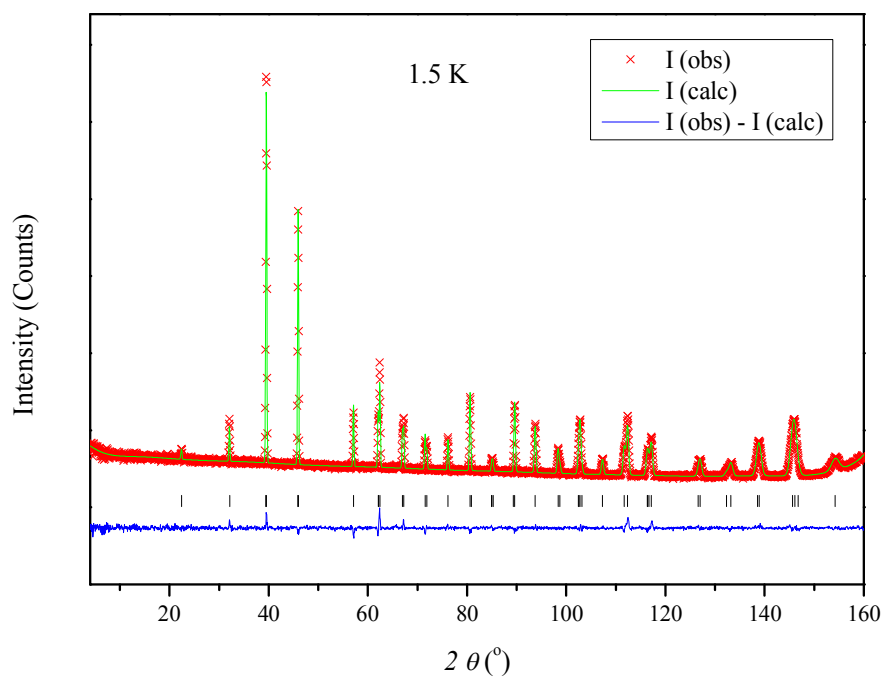
Figure 8.7 The neutron powder diffraction pattern at 1.5 K for Ce-formate system refined by the Rietveld method.
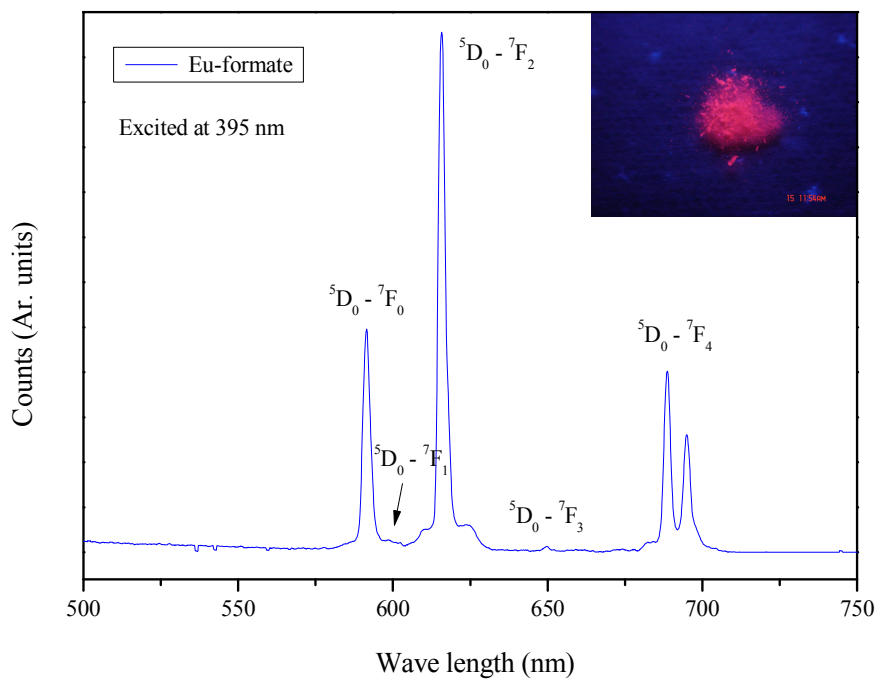
Figure 8.8 The characteristic solid-state emission spectrum for Eu-formate system excited at 390nm. Insert diagram shows the fluorescence under 365nm UV light.

Systems	Ce-formate	Eu-formate
Empirical formula	$(HCOO)_3Ce$	$(HCOO)_3Eu$
Formula weight	275.17 g/mole	287.01 g/mole
Temperature	200(2) K	200(2) K
Wavelength	0.71073 Å	0.71073 Å
Crystal size	N/A	$0.30 \times 0.14 \times 0.115$ mm^3
Crystal habit	colorless prism	colorless prism
Crystal system	Trigonal	Trigonal
Space group	R3m	R3m
Unit cell dimensions	a = 10.6890(6) Å, $\alpha = 90°$	a = 10.4948(5) Å, $\alpha = 90°$
	b = 10.6890(6) Å, $\beta = 90°$	b = 10.4948(5) Å, $\beta = 90°$
	c = 4.1133(5) Å, $\gamma = 120°$	c = 4.0054(4) Å, $\gamma = 120°$
Volume	407.00(6) Å^3	382.05(5) Å^3
Z	3	3
Density, ρ_{calc}	3.368 g/cm^3	3.742 g/cm^3
Absorption coefficient, μ	8.352 mm^{-1}	12.274 mm^{-1}
θ range for data collection	3.81 to 30.00°	3.88 to 29.98°
Index ranges	$-14 \leq h \leq 6, -13 \leq k \leq 12, -5 \leq l \leq 5$	$-14 \leq h \leq 14, -14 \leq k \leq 14, -5 \leq l \leq 5$
Reflections collected	660	1646
Independent reflections	286	291
Observed reflection, I>2σ(I)	1949	20362
Data / restraints / parameters	286 / 1 / 24	291 / 1 / 23
Goodness-of-fit on F^2	1.001	0.944
Δ/σ_{max}	0.001	0.000
Final R indices:	R_1, I > 2σ(I) = 0.0092	R_1, I > 2σ(I) = 0.0171
	wR$_2$, all data = 0.0211	wR$_2$, all data = 0.0419
	R_{int} = 0.0182	R_{int} = 0.0174
	R_{sig} = 0.0140	R_{sig} = 0.0249
$R_1 = \Sigma||F_o|-|F_c||/\Sigma|F_o|$, $wR_2 = [\Sigma w(F_o^2 - F_c^2)^2/\Sigma w(F_o^2)^2]^{1/2}$		

Table 8.4 The details of measured parameters, structural information and refinement results obtained from single crystal analyses of the Lanthanide formate systems.

8.3.6 The Magnetic and Optical Properties for Tb-tetraformate System

High quality crystals of Tb-tetraformate ($(HCOO)_4Tb$) have been synthesized and identified by single crystal X-ray diffraction. The detailed information of crystal structure is given in Table 8.5. It crystallizes in the orthorhombic crystal system, with the non-centrosymmetric space group ***Pna2₁***, and lattice parameters of a = 8.739(1)Å, b = 18.232(1)Å, c = 6.715(0)Å. Each structural unit includes one terbium metal ion, four fromate ligands and one free DMA guest molecule. As shown in Figure 8.9, the metal centers are surrounded by eight carboxylate oxygen atoms, all from the monodentated formate anions and form Tb-O-C-O-Tb connectively with *anti-anti* bridging mode. The short distance between two terbium ions is in the range of 6.6553(5)-6.8463(3) Å and the Tb-$O_{formate}$ bond distance is in range of 2.3402(11)-2.4646(13) Å. This structure is built by a 3-D network of 1-D cubic channels along c axis. The cavities in this framework are occupied by the ordered DMA ionic liquids acting as organic templates during the chemical synthesis, and offer strong hydrogen bonding interactions with the host material. The thermogravimetric analysis (TGA) shown in Figure 8.10 has been performed under nitrogen environment with 30ml/ min flow rate, and shows a poorly defined dehydrated phase between 200 to 300°C. Two high resolution powder neutron diffraction experiments have been performed at 1.5K and 20K to evaluate possible magnetic order, shown in Figure 8.11. The Rietveld refinement was achieved using the initial model from single crystal X-ray diffraction, yielding the weighted R-factor wR_p = 3.07% and Bragg R-factor R_p = 2.53% for 1.5K and wR_p = 3.46%, R_p = 2.91% for 20K. However, no additional magnetic scattering is apparent at 1.5K, showing no long ranged magnetic order.

The photoluminescence measurements of Tb-tetraformate were performed with

identical the experimental parameters and conditions to the Eu-formate experiments. As shown in Figure 8.12, the strongest emission spectra of Tb(III) compound have been identified from the $^5D_4$-^7F_J and $^5D_4$-$^7F_5$ transitions, which originate the strong green luminescence at 540–555nm. The maximum intensity of the emission spectrum is obtained when the excitation wavelength = 351 nm is chosen. However, unlike Eu(III) complexes , this Tb(III) ion does not possess any *hypersensitive* transitions, although the intensities of the $^7F_6$, $^7F_4$, and $^7F_2$ could be possibly sensitive to the coordination environment, which is not only correlated to the local symmetry but also to the nature of sample[37].
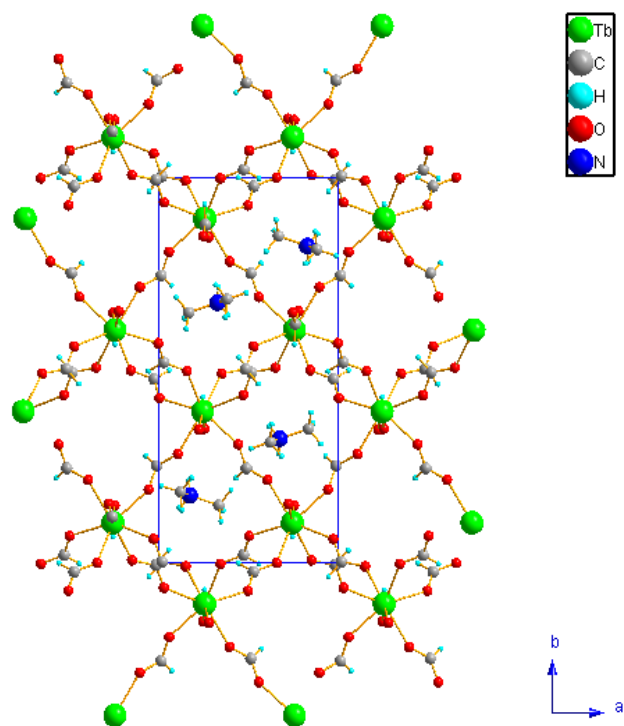
Figure 8.9 Illustration of 3-D molecular structure for Lanthanide tetraformate systems viewed along *c* axis.
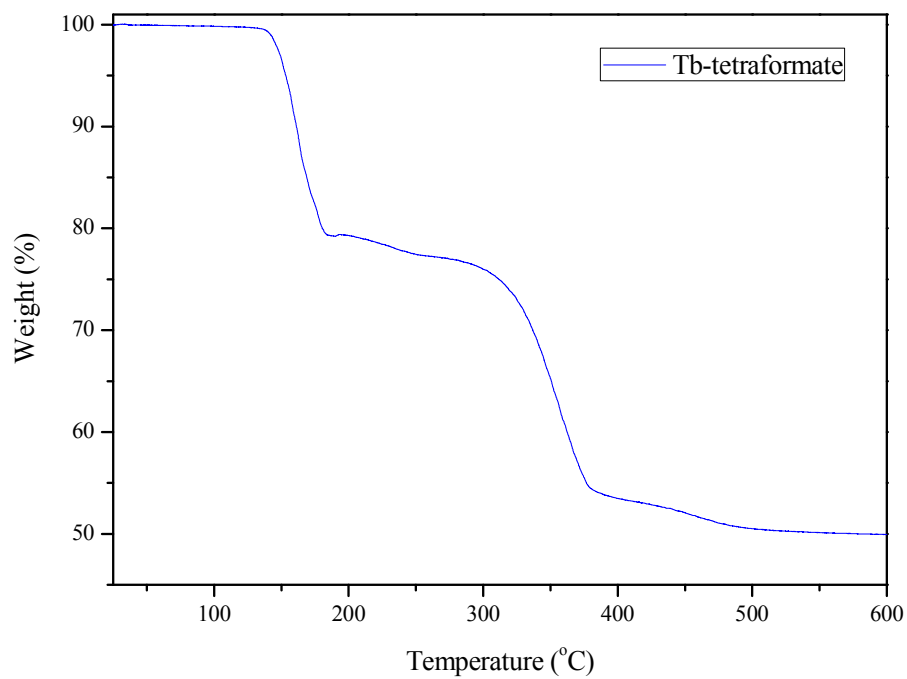
Figure 8.10 The thermogravimetric analysis (TGA) for Tb-tetraformate system.

(a)
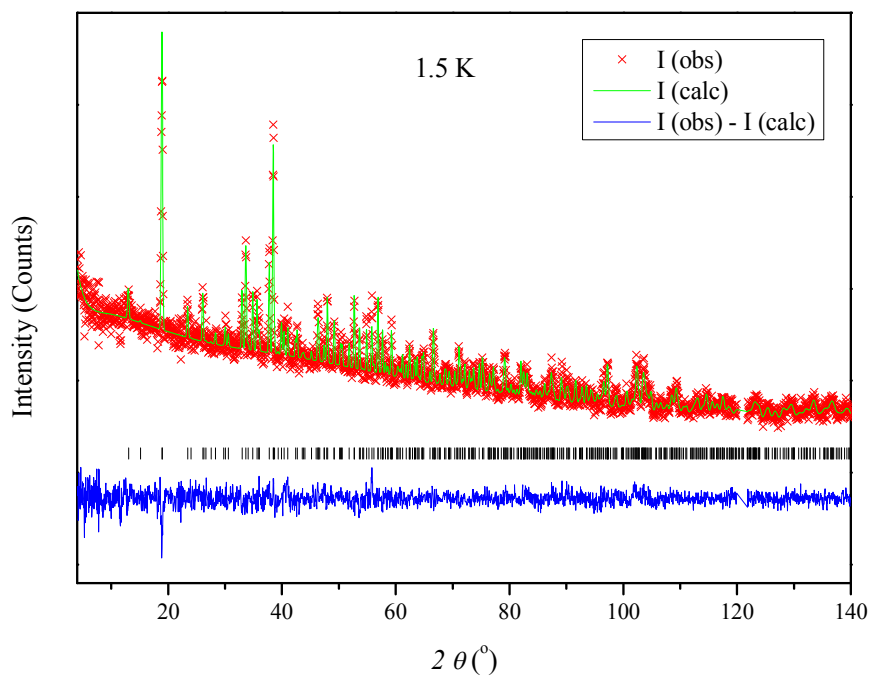
(b)
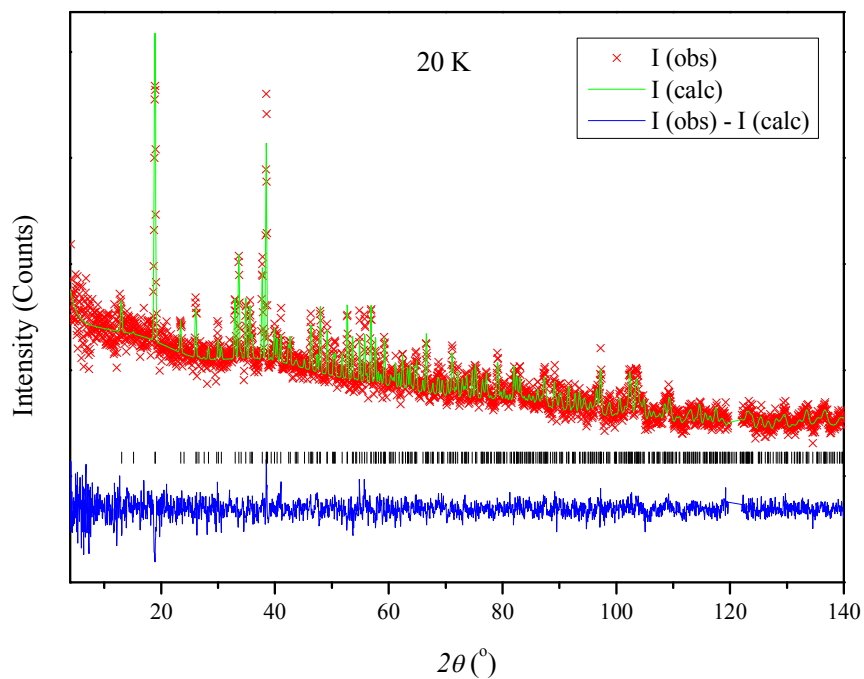
Figure 8.11(a) The neutron powder diffraction pattern at 1.5K and (b) at 20K for Tb-tetraformate system refined by the Rietveld method.

223
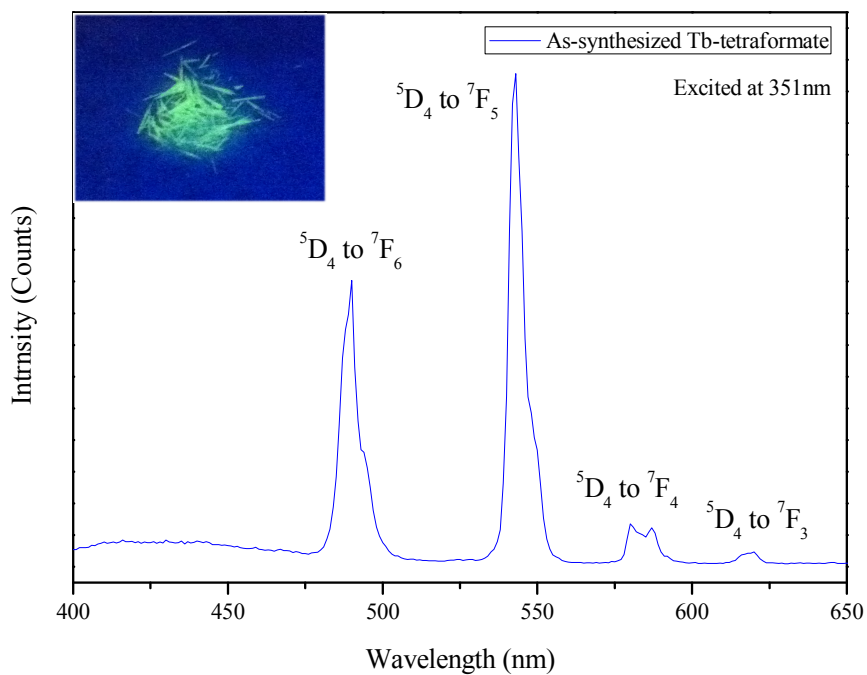
Figure 8.12 The characteristic solid-state emission spectrum for Tb-tetraformate system excited at 351nm. Insert diagram shows the fluorescence under 365nm UV light.

Systems	Tb-tetraformate
Empirical formula	$[(CH_3)_2NH_2]^+[Tb(HCOO)_4]^-$
Formula weight	385.09 g/mole
Temperature	150(2) K
Wavelength	0.71073 Å
Crystal size	$0.38 \times 0.12 \times 0.08 \ mm^3$
Crystal habit	colorless prism
Crystal system	Orthorhombic
Space group	$Pna2_1$
Unit cell dimensions	a = 8.7387(5) Å, $\alpha = 90°$
	b = 18.2328(11) Å, $\beta = 90°$
	c = 6.7147(4) Å, $\gamma = 90°$
Volume	$1912.0(3) \ Å^3$
Z	4
Density, ρ_{calc}	$2.391 \ g/cm^3$
Absorption coefficient, μ	$6.639 \ mm^{-1}$
θ range for data collection	2.23 to 30.00°
Index ranges	$-12 \le h \le 12, -25 \le k \le 25, -9 \le l \le 9$
Reflections collected	16529
Independent reflections	3126
Observed reflection, $I > 2\sigma(I)$	3078
Data / restraints / parameters	3126 / 5 / 160
Goodness-of-fit on F^2	1.000
Δ/σ_{max}	0.003
Final R indices:	$R_1, I > 2\sigma(I) = 0.0116$
	wR_2, all data = 0.0281
	$R_{int} = 0.0195$
	$R_{sig} = 0.0141$
$R_1 = \Sigma \|\|F_o\| - \|F_c\|\| / \Sigma \|F_o\|, \quad wR_2 = [\Sigma w(F_o^2 - F_c^2)^2 / \Sigma \ w(F_o^2)^2]^{1/2}$	

Table 8.5 The details of measured parameters, structural information and refinement results obtained from single crystal analysis of the Tb-tetraformate system.

8.4 References

(1) Wang, X.-Y.; Gan, L.; Zhang, S.-W. and Gao, S. *Inorg. Chem.* **2004**, *43*, 4615.

(2) Coronado, E. and Dunbar, K. R. *Inorg. Chem.* **2009**, *48*, 3293.

(3) Rovira, C. and Veciana, J. *Cryst. Eng. Commun.* **2009**, *11*, 2031.

(4) Kurmoo, M. *Chem. Soc. Rev.* **2009**, *38*, 1353.

(5) Maspoch, D.; Ruiz-Molina, D. and Veciana, J. *Chem. Soc. Rev.* **2007**, *36*, 770.

(6) Wang, X.-Y.; Wang, Z. M. and Gao, S. *Chem. Commun.* **2008**, 281.

(7) Coronado, E. and Day, P. *Chem. Rev.* **2004**, *104*, 5419.

(8) Coronado, E.; Galan-Máscarós, J. R.; Gómez-García, C. J. and Laukhin, V. *Nature* **2000**, *408*, 447.

(9) Sato, O. *Acc. Chem. Res.* **2003**, *36*, 692.

(10) Evans, J. S. O.; Bénard, S.; Yu, P. and Clément, R. *Chem. Mater.* **2001**, *13*, 3813.

(11) Sato, O.; Tao, J. and Zhang, Y. Z. *Angew. Chem. Int. Ed.* **2007**, *46*, 2152.

(12) Cheng, X.-N.; Zhang, W.-X.; Lin, Y.-Y.; Zheng, Y.-Z. and Chen, X.-M. *Adv. Mater.* **2007**, *19*, 1494.

(13) Kaye, S. S.; Choi, H. J. and Long, J. R. *J. Am. Chem. Soc.* **2008**, *130*, 16921.

(14) Kurmoo, M.; Kumagai, H.; Chapmanc, K. W. and Kepert, C. J. *Chem. Commun.* **2005**, 3012.

(15) Ohkoshi, S.-I.; Arai, K.-I.; Sato, Y. and Hashimoto, K. *Nat. Mater.* **2004**, *3*, 857.

(16) Maspoch, D.; Ruiz-Molina, D.; Wurst, K.; Domingo, N.; Cavallini, M.; Biscarini, F.; Tejada, J.; Rovira, C. and Veciana, J. *Nat. Mater.* **2003**, *2*, 190.

(17) Maspoch, D.; Domingo, N.; Ruiz-Molina, D.; Wurst, K.; Tejada, J.; Rovira, C. and Veciana, J. *C. R. Chimie* **2005**, *8*, 1213.

(18) Maspoch, D.; Ruiz-Molina, D. and Veciana, J. *J. Mater. Chem.* **2004**, 2713.

(19) Ohkoshi, S.-I.; Tokoro, H.; Matsuda, T.; Takahashi, H.; Irie, H. and Hashimoto, K. *Angew. Chem. Int. Ed.* **2007**, *46*, 3238.

(20) Bai, Y. L.; Tao, J.; Wernsdorfer, W.; Sato, O.; Huang, R. B. and Zheng, L. S. *J. Am. Chem. Soc.* **2006**, *128*, 16428.

(21) Burrows, A. D.; Cassar, K.; Friend, R. M. W.; Mahon, M. F.; Rigby, S. P. and Warren, J. E. *Cryst. Eng. Comm.* **2005**, *7*, 548.

(22) Chen, W.; Wang, J.; Chen, C.; Yue, Q.; Yuan, H.; Chen, J. and Wang, S. *Inorg. Chem.* **2003**, *42*, 944.

(23) He, J. H.; Yu, J. H.; Zhang, Y. T.; Pan, Q. H. and Xu, R. R. *Inorg. Chem.* **2005**, *44*, 9279.

(24) Juillard, J. *Pure Appl. Chem.* **1977**, *49*, 885.

(25) Xie, L; Liu, S.; Gao, B.; Zhang, C.; Sun, C.; Li, D. and Su, Z. *Chem. Commun.* **2005**, 2402.

(26) Wang, Z.; Zhang, B.; Otsuka, T.; Inoue, K.; Kobayashi, H. and Kurmoo, M. *Dalton Trans.* **2004**, 2209.

(27) Jain, P.; Dalal, N. S.; Toby, B. H.; Kroto, H. W. and Cheetham, A. K. *J. Am. Chem. Soc.* **2008**, *130*, 10450.

(28) Hu, K. L.; Kurmoo, M.; Wang, Z. M. and Gao, S. *Chem. Eur. J.* **2009**, *15*, 12050.

(29) Jain, P.; Ramachandran, V.; Clark, R. J.; Zhou, H. D.; Toby, B. H.; Dalal, N. S.; Kroto, H. W. and Cheetham, A. K. *J. Am. Chem. Soc.* **2009**, *131*, 13625.

(30) Colacio, E.; Ghaze, M.; Kivekäs, R. and Moreno, J. M. *Inorg. Chem.* **2000**, *39*, 2882.

(31) Pérez, C. R.; Sanchiz, J.; Molina, M. H.; Lloret, F. and Julve, M. *Inorg. Chem.* **2000**, *39*, 1363.

(32) Yolanda, R. M.; Catalina, R. P.; Joaquín, S.; Francesc, L. and Miguel, J. *Inorg. Chim. Acta* **2001**, *318*, 159.

(33) Batten, S. R. and Robson, R. *Angew. Chem. Int. Ed.* **1998**, *37*, 1460.

(34) *Magnetic Properties of Transition Metal Compounds*; Carlin, R. L. and Van-Duyneveldt, A. J., Ed.; Springer-Verlag: New York, 1977.

(35) Swüste, C. H. W.; Botterman, A. C.; Millenaar, J. and De Jonge, W. J. M. *J. Chem. Phys.* **1977**, 5021.

(36) Srinivasan, G. and Seehra, M. S. *Phys. Rev. B* **1983**, *28*, 1.

(37) Richardson, F. S. *Chem. Rev.* **1982**, *82*, 541.

Chapter 9: Conclusions and future works

9.1 Conclusions

The focus of this dissertation is to synthesize metal-organic frameworks with different geometry, chemical bonding configuration and dimensionality. This is achieved through different synthetic methods and is important to gain a better understanding of the relationship between the structural/ thermal stability and framework architecture. These new materials are investigated for their gas storage capabilities in sustainable energy applications. Particular emphasize is placed on new analysis methodology, implemented to extract as much information on gas adsorption mechanism as possible.

Twenty-two types of metal-organic framework materials have been synthesized by solvothermal reactions, diffusion and evaporation methods. The crystal structures of forty lanthanide MOFs and two transition metal MOFs possessing both 2-D and 3-D structures through linkage with different rigid carboxylate ligands such as 1, 4-Benzenedicarboxylic acid (H_2BDC), 1, 3, 5-Benzene tricarboxylic acid (H_3BTC), 1, 3, 5-tris(4-carboxphenyl)benzene (H_3BTB), 3, 5-Pyridinedicarboxylic acid (H_2PDC) and 2, 6-Naphthalenedicarboxylic acid (H_2NDC) have been resolved by single crystal X-ray diffraction. The most promising have been evaluated for their thermal/ structural stability by thermogravimetric analysis, powder neutron diffraction, *in-situ* and combined synchrotron powder X-ray and Raman spectroscopy.

The single crystal X-ray diffractions results show that the Ce-MOF-BTC and Ho-MOF-BTC have similar 3-D frameworks. The Ce-MOF-BTC compound undergoes mass loss and structure decomposes at ca. $350^{o}C$, in contrast to the Ho-MOF-BTC which is stable up to $508^{o}C$. A difference between these two structures is the presence of a μ_2 (shared) oxygen that is coordinated with two adjacent cerium

ions and one hard-bridged ligand in Ce compound but which is absent in the Ho system, which results in much longer metal-oxygen distances in the Ce-MOF-BTC structure compared with Ho-MOF-BTC. This phenomenon implies that the chemical bonding between Ce-O_{BTC} is easy to break thereby losing structural integrity at high temperatures, consisting with TGA results.

Another important comparison is between the 2-D Ho-MOF-BTB structure, which loses its crystallinity above $80^{o}C$, and the 3-D Ho-MOF-BTC framework, which is robust up to $508^{o}C$, as shown by *in-situ* synchrotron PXRD and TGA results. The complex structures are simplified using a quasi-topology method. For the Ho-MOF-BTC system, the 1-D channel edges formed by the Ho-O-C-O-Ho 4-fold chiral chain along the *c* axis create a robust architecture as a result of each holmium ion pair being fixed by the solid aromatic rings along three axis directions that are perpendicular to each other. In contrast, all the rigid benzoic ligands in the Ho-MOF-BTB system are parallel to each other forming layered structure with a discontinuous ion-ion chain, suggesting that the dimensionality of molecular architecture dominates the structural stability of crystal frameworks.

Ho-MOF-BTC system possessing a robust 3-D structure is shown to be suitable for gas loading applications. Low pressure H_2 isotherm experiment (from 0 to 1atm) shows that the dehydrated Ho-MOF-BTC system has a relatively high adsorption capacity 1.46wt% with $879.1 m^2/g$ specific surface area. In addition, a series of high resolution neutron powder diffractions performed with deuterium and deuterated methane have been used to identify the adsorption positions in this rare 4-fold chiral framework. For deuterium loading experiments, the distance between primary adsorption site (site **I**) and the unsaturated holmium ion is longer than that between site **I** to the nearest carbon atom on BTC ligand. Furthermore, the distances between adjacent site **I** and site **II**; adjacent site **III** and site **IV** in pairs ($1 \times D4$ with $2 \times D3$)

are shorter than the intermolecular distance of solid-state deuterium (3.6Å), showing that the extremely high gas packing density can be obtained. The deuterated methane loading experiments exhibit similar tendency as in the deuterium adsorption case. These properties can be explained by the optimal pore size (twice of kinetic diameter of adsorbed gas molecules) in this MOF structure that enhances the van der Waals interaction between the organic ligands and guest gas molecules. However, the adsorption behaviors are different between the deuterium and deuterated methane, as a result of their different molecular geometries and sizes. A unique helical adsorption pattern is also observed mirroring the chiral structure of the Ho-MOF-BTC material, as verified by an *ab-initio* charge flipping and maximum entropy (MEM) calculations, which provide qualitative and quantitative approaches to describe the thermal displacements, diffusion, and delocalization of deuterium molecules along the 1-D channels, providing a more accurate description of the gas behavior from neutron diffraction experiments than that which could be achieved with Rietveld refinement.

A 3-D network Ho-MOF-BDC framework structure with 1-D rhombic channels along *c* axis has been synthesized and investigated. A complex series phase transitions are observed by *in-situ* synchrotron PXRD patterns that correspond to sequential mass loss of two DMF molecules and one nitrate group. A crystalline-amorphous reversible reaction is observed by gas adsorption isotherm and re-sorption experiments, and in-situ Raman spectroscopy confirms that no chemical bonding break occurs before decomposition.

Two Co-formate systems, Co-formate-1 with disordered dimethyl ammonium (DMA) solvent molecules and Co-formate-2 with ordered DMA solvent molecules, have been synthesized and their relationship investigated. Co-formate-2 structure is monoclinic with *Cc* space group compared with the Co-formate-1 structure that crystallizes in the triginal *R$\bar{3}$c* symmetry. SQUID magnetometer shows that

Co-formate-1 and -2 are both low spin (S = $\frac{1}{2}$) with similar Weiss constants indicating similar antiferromagnetic exchange. In addition, both Co-formate-1 and Co-formate-2 systems exhibit weak ferromagnetism at low-temperature state (below ca. 15K) as a result of spin canting. The difference between these two systems is likely to result from the ordering of the DMA cations; the disorder of the DMA in Co-formate-1 results in dynamical Jahn-Teller effect and enhancement of the orbital contribution, whereas the orbital contribution to the moment is reduced with the static Jahn-Teller effect. The Co-formate-2 system possessing a non-centrosymmetric space group *Cc* and ordered DMA molecules results in a new multiferroic material.

In Eu-formate system, fluorescence measurements show the typical $^5D_0$-^7F_J transitions. The maximum intensity of characteristic emission spectrum can be obtained when the excitation wavelength = 395nm is chosen, and the relative ratio of intensities between $^7F_2$ and $^7F_2$ is large as a result of the coordinated environment around Eu(III) ions is asymmetric, which is consistent with the single crystal X-ray diffraction results. In Tb-tetraformate system, the strongest emission spectra have been identified from the $^5D_4$-^7F_J and $^5D_4$-$^7F_5$ transitions, which originate the strong green luminescence at 540–555nm. The maximum intensity of the emission spectrum is obtained when the excitation wavelength = 351 nm is chosen.

9.2 Future Works

The major deficiency in the application of MOFs as gas storage materials results from the low adsorption heat, typically between 4-10kJ/mole. Chapter 1 describes how several strategies have been proposed to improve this. Changes to the (i) Pore size, (ii) Pore geometry, (iii) Use of different kinds of metal ions, and (iv) Carbon-based ligands by inorganic ion doping. However, much progress still needs to

be made. In last decade, crystal engineering has played a significant role in the design, control, and optimization of structures by modifying the organic and inorganic components. Here, we propose extensions to the work developed in this dissertation to further enhance the adsorption properties.

The Eu-MOF-BTB system could be enhanced with the use of a long ligand that would increase the storage capacity of the MOF materials as well as reduce the adsorption rate in the linear (low pressure) region. The hexagonal pore geometry containing a $120^{o}C$ angle offers larger open space for the unsaturated metal cations compared with the Ho-MOF-BTC system that possesses pseudo-circle pore geometry with a $90^{o}C$ angle. The pore geometry effect could be evaluated by the measuring the adsorption positions and adsorption kinetics through neutron diffraction and isotherm experiments, respectively.

In addition, the Ho-MOF-PDC system possessing functional azaheterocyclic rings, which possess lone-pair electrons on nitrogen atoms, could be implemented to induce dipole/ induced-dipole or induced-dipole/ induced-dipole interactions thereby enhancing the attraction between gas molecules and MOF framework. Furthermore, the nitrogen positions are located towards the middle of the organic ligand thus provideing a large $180^{o}C$ angle that reduces the steric hindrance of gas molecules interacting with nitrogen. This framework structure provides the advantage of a combination the functionalized carbon-based ligand with the pore geometry for enhanced gas adsorption properties.

Appendix

10.1 Detailed Information for Y-MOF-BDC System from Single Crystal Analysis

Atom	x/a	y/b	z/c	U_{eq}
Y1	0.0000	0.457770(18)	0.7500	0.02794(7)
O1	0.08361(8)	0.42069(15)	0.60461(12)	0.0593(4)
O2	0.09389(7)	0.47563(12)	0.40572(12)	0.0456(3)
C1	0.11519(9)	0.41509(16)	0.50389(15)	0.0347(3)
C2	0.18530(8)	0.32914(14)	0.50183(14)	0.0304(3)
C3	0.21606(9)	0.26784(17)	0.61149(15)	0.0398(4)
C4	0.28048(9)	0.18938(16)	0.60977(15)	0.0392(4)
O11	-0.06713(9)	0.27592(13)	0.66438(13)	0.0602(4)
C11	-0.0943(10)	0.2389(10)	0.5645(9)	0.046(3)
N11	-0.1356(5)	0.1354(9)	0.5418(9)	0.0633(12)
C12	-0.1612(9)	0.1017(14)	0.4076(10)	0.113(6)
C13	-0.1578(10)	0.0518(13)	0.6387(13)	0.079(4)
O11A	-0.06713(9)	0.27592(13)	0.66438(13)	0.0602(4)
C11A	-0.0516(14)	0.198(2)	0.592(3)	0.063(3)
N11A	-0.0873(12)	0.0928(14)	0.5567(17)	0.078(2)
C12A	-0.1621(17)	0.062(3)	0.609(3)	0.098(10)
C13A	-0.058(2)	0.004(2)	0.470(3)	0.116(10)
O11B	-0.06713(9)	0.27592(13)	0.66438(13)	0.0602(4)
C11B	-0.0489(8)	0.1823(12)	0.6150(17)	0.063(3)
N11B	-0.0958(9)	0.1044(9)	0.5464(10)	0.078(2)
C12B	-0.1766(8)	0.1492(15)	0.5054(19)	0.106(6)
C13B	-0.0742(13)	-0.0190(12)	0.509(2)	0.116(7)
O11C	-0.06713(9)	0.27592(13)	0.66438(13)	0.0602(4)
C11C	-0.1105(11)	0.2575(12)	0.5715(11)	0.046(3)
N11C	-0.1396(6)	0.1473(10)	0.5354(10)	0.0633(12)
C12C	-0.1964(9)	0.1355(16)	0.4205(14)	0.099(5)
C13C	-0.1169(11)	0.0353(12)	0.6071(17)	0.127(7)
N21	0.0088(12)	0.7281(4)	0.7336(17)	0.068(5)

O21	-0.0387(10)	0.6787(14)	0.8029(13)	0.058(3)
O22	0.0482(11)	0.6556(15)	0.6697(15)	0.058(2)
O23	0.0167(8)	0.8421(3)	0.7306(16)	0.125(3)

[*] U_{eq} is defined as one third of the trace of the orthogonalized U_{ij} tensor.

Table 10.1 (a) Atomic coordinates and equivalent[*] isotropic atomic displacement parameters ($Å^2$) for Y-MOF-BDC System.

Atom	sof	Atom	sof	Atom	sof
O11 - C13	0.332(4)	O11A - C13A	0.146(6)		
O11B - C13B	0.229(7)	O11C - C13C	0.293(6)		
N21 - O23	0.50				

Table 10.1 (b) Site occupancy factors that deviate from unity for Y-MOF-BDC System.

10.2 Detailed Information for Ce-MOF-BDC System from Single Crystal Analysis

Atom	x/a	y/b	z/c	U_{eq}
Ce1	0.19834(2)	0.013479(13)	0.143184(7)	0.02032(5)
Ce2	0.24616(2)	0.288699(13)	0.120185(7)	0.01844(5)
Ce3	0.11692(2)	0.503548(12)	0.190593(7)	0.01782(5)
Ce4	0.10796(2)	0.795311(14)	0.210886(7)	0.02157(5)
Ce5	0.54635(2)	0.109693(13)	0.463862(7)	0.01907(5)
Ce6	0.56067(2)	0.389781(12)	0.465253(7)	0.01762(5)
O11	0.1427(3)	0.22833(19)	0.07194(10)	0.0330(7)
O12	0.0744(3)	0.12751(18)	0.10311(10)	0.0337(7)
O13	-0.1148(3)	0.0701(2)	-0.10065(11)	0.0378(8)
O14	-0.0476(3)	0.1694(2)	-0.13554(10)	0.0338(7)

C11	0.0408(4)	0.1678(2)	0.02671(12)	0.0200(8)
C12	-0.0159(4)	0.1088(3)	0.02377(14)	0.0278(9)
C13	-0.0512(4)	0.0964(3)	-0.01740(14)	0.0268(9)
C14	-0.0304(4)	0.1427(2)	-0.05628(13)	0.0226(8)
C15	0.0242(4)	0.2032(3)	-0.05351(14)	0.0277(9)
C16	0.0599(4)	0.2158(2)	-0.01180(14)	0.0257(8)
C17	0.0884(4)	0.1758(2)	0.07086(13)	0.0226(8)
C18	-0.0673(4)	0.1263(2)	-0.10100(13)	0.0254(9)
O21	0.3602(3)	0.0812(2)	0.13829(12)	0.0424(8)
O22	0.4370(3)	0.17632(17)	0.10563(10)	0.0303(7)
O23	1.0065(3)	-0.0064(2)	0.19011(11)	0.0405(8)
O24	0.9137(3)	-0.09178(18)	0.22863(11)	0.0357(7)
C21	0.5645(4)	0.0801(2)	0.15094(13)	0.0216(8)
C22	0.6735(4)	0.1044(2)	0.13498(14)	0.0252(8)
C23	0.7858(4)	0.0688(2)	0.15203(14)	0.0270(9)
C24	0.7896(4)	0.0089(2)	0.18513(13)	0.0224(8)
C25	0.6801(4)	-0.0141(2)	0.20146(14)	0.0271(9)
C26	0.5676(4)	0.0213(2)	0.18451(14)	0.0263(9)
C27	0.4447(4)	0.1151(2)	0.13039(14)	0.0248(8)
C28	0.9118(4)	-0.0324(3)	0.20259(13)	0.0251(8)
O31	-0.0441(3)	0.43122(18)	0.19108(10)	0.0278(6)
O32	0.0260(3)	0.30802(18)	0.16412(10)	0.0293(6)
O33	-0.5860(3)	0.35082(19)	0.11910(10)	0.0308(7)
O34	-0.6562(3)	0.47098(19)	0.14974(12)	0.0355(7)
C31	-0.1923(4)	0.3802(2)	0.16516(13)	0.0238(8)
C32	-0.2291(4)	0.3146(3)	0.15686(16)	0.0309(9)
C33	-0.3527(4)	0.3238(3)	0.14902(16)	0.0306(9)
C34	-0.4394(4)	0.3978(2)	0.14906(14)	0.0245(8)
C35	-0.4021(4)	0.4629(3)	0.15805(15)	0.0295(9)
C36	-0.2801(4)	0.4545(3)	0.16569(15)	0.0296(9)
C37	-0.0600(4)	0.3722(3)	0.17403(13)	0.0247(8)
C38	-0.5713(4)	0.4075(2)	0.13865(14)	0.0254(8)
O41	0.2912(3)	0.23331(18)	0.19960(10)	0.0345(7)
O42	0.2311(3)	0.36218(16)	0.20149(9)	0.0247(6)
O43	0.4536(3)	0.33556(18)	0.41411(10)	0.0308(7)
O44	0.4032(3)	0.22330(17)	0.42867(10)	0.0280(6)

C41	0.3097(4)	0.2926(2)	0.26761(13)	0.0220(8)
C42	0.3590(4)	0.3498(3)	0.28109(14)	0.0275(9)
C43	0.3941(4)	0.3450(2)	0.32461(13)	0.0254(8)
C44	0.3746(4)	0.2860(2)	0.35580(12)	0.0202(8)
C45	0.3238(4)	0.2294(2)	0.34284(13)	0.0265(9)
C46	0.2925(4)	0.2320(3)	0.29831(14)	0.0276(9)
C47	0.2754(4)	0.2957(2)	0.21995(13)	0.0230(8)
C48	0.4135(4)	0.2813(2)	0.40324(12)	0.0201(8)
O51	-0.0546(3)	0.72991(18)	0.21490(11)	0.0307(7)
O52	-0.0758(3)	0.60953(16)	0.21525(10)	0.0274(6)
O53	-0.6877(3)	0.7822(2)	0.15933(10)	0.0338(7)
O54	-0.6285(3)	0.89010(18)	0.13617(11)	0.0353(7)
C51	-0.2376(4)	0.7155(2)	0.19004(13)	0.0210(8)
C52	-0.3267(4)	0.6734(2)	0.19520(15)	0.0275(9)
C53	-0.4463(4)	0.7069(3)	0.18295(15)	0.0284(9)
C54	-0.4762(4)	0.7823(2)	0.16419(13)	0.0241(8)
C55	-0.3858(4)	0.8233(2)	0.15774(15)	0.0279(9)
C56	-0.2682(4)	0.7907(2)	0.17095(15)	0.0287(9)
C57	-0.1117(4)	0.6823(2)	0.20741(13)	0.0218(8)
C58	-0.6071(4)	0.8210(3)	0.15237(13)	0.0260(9)
O61	0.2238(3)	0.55259(18)	0.24385(10)	0.0331(7)
O62	0.2545(3)	0.67022(17)	0.23077(10)	0.0309(7)
O63	0.3713(3)	0.65983(17)	0.45831(10)	0.0319(7)
O64	0.4527(3)	0.53109(16)	0.45382(9)	0.0245(6)
C61	0.3625(4)	0.5993(2)	0.38938(13)	0.0218(8)
C62	0.3192(4)	0.5397(2)	0.37586(14)	0.0287(9)
C63	0.2835(4)	0.5444(2)	0.33236(14)	0.0275(9)
C64	0.2946(4)	0.6061(2)	0.30216(13)	0.0212(8)
C65	0.3389(4)	0.6651(2)	0.31606(14)	0.0274(9)
C66	0.3706(4)	0.6626(2)	0.35982(14)	0.0291(9)
C67	0.3974(4)	0.5970(2)	0.43677(13)	0.0223(8)
C68	0.2548(4)	0.6095(2)	0.25526(13)	0.0209(8)
O71	0.2115(3)	0.87011(19)	0.24872(11)	0.0356(7)
O72	0.2577(3)	0.97974(19)	0.22122(10)	0.0336(7)
O73	0.4465(3)	1.02690(19)	0.42993(11)	0.0351(7)
O74	0.3942(3)	0.9194(2)	0.45871(10)	0.0344(7)

C71	0.2939(4)	0.9379(2)	0.29726(13)	0.0222(8)
C72	0.3418(4)	1.0002(2)	0.30270(14)	0.0262(9)
C73	0.3785(4)	1.0098(2)	0.34442(13)	0.0250(8)
C74	0.3665(4)	0.9576(2)	0.38140(12)	0.0210(8)
C75	0.3192(4)	0.8951(2)	0.37599(13)	0.0245(8)
C76	0.2832(4)	0.8851(2)	0.33395(13)	0.0251(8)
C77	0.2514(4)	0.9281(2)	0.25225(13)	0.0247(8)
C78	0.4059(4)	0.9687(2)	0.42688(13)	0.0243(8)
O81	0.2825(3)	0.01538(18)	0.54447(11)	0.0345(7)
O82	0.3460(3)	0.1190(2)	0.51517(10)	0.0318(7)
O83	-0.2486(3)	0.28120(17)	0.44485(10)	0.0270(6)
O84	-0.2777(3)	0.16324(19)	0.45697(11)	0.0347(7)
C81	0.1368(4)	0.1172(2)	0.50946(13)	0.0221(8)
C82	0.1171(4)	0.1857(2)	0.48231(14)	0.0265(9)
C83	0.0008(4)	0.2178(2)	0.46774(14)	0.0249(8)
C84	-0.0963(4)	0.1818(2)	0.47960(13)	0.0212(8)
C85	-0.0774(4)	0.1143(3)	0.50737(15)	0.0286(9)
C86	0.0382(4)	0.0830(3)	0.52239(15)	0.0299(9)
C87	0.2646(4)	0.0809(2)	0.52402(13)	0.0250(9)
C88	-0.2174(4)	0.2116(2)	0.45966(13)	0.0222(8)
O91	0.2692(3)	0.54460(18)	0.53540(10)	0.0280(6)
O92	0.3394(3)	0.42117(17)	0.50804(11)	0.0299(7)
C91	0.1231(4)	0.4926(2)	0.50818(13)	0.0217(8)
C92	0.0899(4)	0.4268(2)	0.49798(15)	0.0268(9)
C93	-0.0319(4)	0.4340(2)	0.49041(15)	0.0267(9)
C97	0.2539(4)	0.4860(2)	0.51777(13)	0.0231(8)
O101	0.0324(4)	0.55063(19)	0.11567(10)	0.0395(8)
O102	0.1316(3)	0.42428(17)	0.10655(9)	0.0284(6)
C101	0.0329(4)	0.4945(2)	0.04415(13)	0.0246(8)
C102	0.0189(5)	0.4291(3)	0.02419(15)	0.0329(10)
C103	-0.0146(5)	0.4351(3)	-0.01976(15)	0.0332(10)
C107	0.0675(4)	0.4899(2)	0.09160(13)	0.0232(8)
C111	0.3420(5)	0.0587(3)	0.03373(16)	0.0370(11)
N111	0.3526(4)	0.0654(2)	-0.01187(12)	0.0333(9)
O111	0.3091(4)	0.0069(2)	0.05729(11)	0.0469(9)
C112	0.3224(6)	0.0127(4)	-0.0404(2)	0.0559(15)

237

C113	0.3898(6)	0.1324(3)	-0.0357(2)	0.0518(14)
C121	0.3457(5)	0.3783(3)	0.02047(15)	0.0354(10)
N121	0.3565(4)	0.4022(3)	-0.02328(14)	0.0426(10)
O121	0.3286(3)	0.31518(19)	0.03459(10)	0.0353(7)
C122	0.3467(8)	0.3538(4)	-0.05977(18)	0.0674(19)
C123	0.3732(7)	0.4794(4)	-0.0363(2)	0.0652(18)
C131	0.2995(6)	0.6936(4)	0.05346(19)	0.0520(14)
N131	0.3247(4)	0.7269(3)	0.01257(15)	0.0448(11)
O131	0.2667(5)	0.6325(3)	0.05948(13)	0.0666(13)
C132	0.3081(6)	0.6963(4)	-0.02966(19)	0.0625(17)
C133	0.3639(7)	0.7984(4)	0.0082(3)	0.079(2)
C141	0.0158(5)	0.0819(3)	0.29522(18)	0.0466(13)
N141	-0.0067(4)	0.0495(3)	0.33690(14)	0.0406(10)
O141	0.0548(4)	0.1411(2)	0.28792(13)	0.0567(11)
C142	0.0151(6)	0.0820(4)	0.37785(18)	0.0569(16)
C143	-0.0496(6)	-0.0205(4)	0.3433(3)	0.0678(19)
C151	0.6761(5)	0.1675(4)	0.35552(18)	0.0486(13)
N151	0.6859(4)	0.1763(3)	0.30994(13)	0.0403(10)
O151	0.6395(4)	0.1122(2)	0.37712(11)	0.0455(9)
C152	0.6572(9)	0.1244(5)	0.2818(2)	0.088(3)
C153	0.7254(7)	0.2434(4)	0.2871(3)	0.076(2)
C161	0.0113(4)	0.4069(3)	0.28885(14)	0.0303(9)
N161	-0.0040(4)	0.3819(2)	0.33253(13)	0.0346(9)
O161	0.0359(3)	0.46888(19)	0.27562(10)	0.0332(7)
C162	0.0129(7)	0.4252(4)	0.36976(17)	0.0567(16)
C163	-0.0319(6)	0.3077(3)	0.34503(19)	0.0498(14)
C171	-0.0053(5)	0.7215(3)	0.31681(16)	0.0387(11)
N171	-0.0188(4)	0.7080(3)	0.36212(14)	0.0443(11)
O171	0.0310(4)	0.7763(2)	0.29728(11)	0.0421(8)
C172	0.0107(9)	0.7575(4)	0.3929(2)	0.086(3)
C173	-0.0592(7)	0.6404(4)	0.3820(2)	0.078(2)
C181	0.6650(4)	0.4839(3)	0.36793(15)	0.0314(10)
N181	0.6811(4)	0.5093(2)	0.32438(13)	0.0350(9)
O181	0.6427(3)	0.42092(19)	0.38057(10)	0.0340(7)
C182	0.6686(7)	0.4650(4)	0.28648(17)	0.0567(16)
C183	0.7033(6)	0.5856(3)	0.31300(19)	0.0520(15)

C191	0.3673(5)	0.2009(3)	0.61355(16)	0.0393(11)
N191	0.3386(4)	0.1694(2)	0.65504(13)	0.0370(9)
O191	0.4068(4)	0.2589(2)	0.60618(12)	0.0479(9)
C192	0.3593(6)	0.1999(4)	0.69710(18)	0.0558(15)
C193	0.2932(6)	0.1004(4)	0.6603(2)	0.0568(16)
O1W	0.0952(4)	0.1334(3)	0.19399(12)	0.0614(12)
O2W	0.1851(3)	0.6235(2)	0.15225(9)	0.0331(8)
O3W	0.4804(3)	0.25504(18)	0.50860(10)	0.0320(7)

[*] U_{eq} is defined as one third of the trace of the orthogonalized U_{ij} tensor.

Table 10.2 (a) Atomic coordinates and equivalent[*] isotropic atomic displacement parameters (Å^2) for Ce-MOF-BDC System.

Ce1-O23#1	2.417(3)	Ce1-O21	2.419(3)	Ce1-O54#2	2.447(3)
Ce1-O12	2.457(3)	Ce1-O13#3	2.462(3)	Ce1-O72#4	2.476(3)
Ce1-O1W	2.525(5)	Ce1-O111	2.573(3)	Ce2-O102	2.420(3)
Ce2-O33#5	2.423(3)	Ce2-O22	2.440(3)	Ce2-O11	2.440(3)
Ce2-O32	2.479(3)	Ce2-O41	2.539(3)	Ce2-O121	2.561(3)
Ce2-O42	2.732(3)	Ce3-O52	2.425(3)	Ce3-O61	2.456(3)
Ce3-O31	2.487(3)	Ce3-O42	2.491(3)	Ce3-O34#5	2.495(3)
Ce3-O101	2.535(3)	Ce3-O161	2.580(3)	Ce3-O2W	2.590(3)
Ce3-O102	2.856(3)	Ce4-O51	2.400(3)	Ce4-O14#6	2.408(3)
Ce4-O71	2.419(3)	Ce4-O53#5	2.437(3)	Ce4-O62	2.449(3)
Ce4-O24#7	2.475(3)	Ce4-O171	2.543(3)	Ce5-O84#5	2.384(3)
Ce5-O82	2.409(3)	Ce5-O73#4	2.432(3)	Ce5-O74#8	2.452(3)
Ce5-O81#9	2.456(3)	Ce5-O44	2.475(3)	Ce5-O151	2.553(3)
Ce5-O3W	2.804(3)	Ce6-O83#5	2.418(3)	Ce6-O92	2.461(3)
Ce6-O43	2.463(3)	Ce6-O64	2.477(3)	Ce6-O91#8	2.491(3)
Ce6-O63#8	2.512(3)	Ce6-O181	2.556(3)	Ce6-O64#8	2.779(3)
Ce6-O3W	2.932(3)	O11-C17	1.256(5)	O12-C17	1.253(5)
O13-C18	1.258(5)	O14-C18	1.254(5)	C11-C12	1.386(6)
C11-C16	1.391(5)	C11-C17	1.508(5)	C12-C13	1.379(5)
C13-C14	1.385(6)	C14-C15	1.393(6)	C14-C18	1.506(5)
C15-C16	1.397(5)	O21-C27	1.237(5)	O22-C27	1.259(5)
O23-C28	1.256(5)	O24-C28	1.259(5)	C21-C26	1.385(5)
C21-C22	1.393(5)	C21-C27	1.510(5)	C22-C23	1.390(6)
C23-C24	1.390(6)	C24-C25	1.388(6)	C24-C28	1.505(5)
C25-C26	1.390(6)	O31-C37	1.258(5)	O32-C37	1.264(5)
O33-C38	1.252(5)	O34-C38	1.255(5)	C31-C36	1.391(6)
C31-C32	1.392(6)	C31-C37	1.503(6)	C32-C33	1.394(6)
C33-C34	1.384(6)	C34-C35	1.391(6)	C34-C38	1.509(6)
C35-C36	1.377(6)	O41-C47	1.242(5)	O42-C47	1.267(5)
O43-C48	1.253(5)	O44-C48	1.253(5)	C41-C42	1.393(6)
C41-C46	1.393(6)	C41-C47	1.501(5)	C42-C43	1.386(5)
C43-C44	1.385(5)	C44-C45	1.389(5)	C44-C48	1.515(5)
C45-C46	1.399(5)	O51-C57	1.247(5)	O52-C57	1.256(5)
O53-C58	1.264(5)	O54-C58	1.259(5)	C51-C52	1.387(6)
C51-C56	1.388(6)	C51-C57	1.517(5)	C52-C53	1.390(6)
C53-C54	1.388(6)	C54-C55	1.384(6)	C54-C58	1.508(6)
C55-C56	1.381(6)	O61-C68	1.241(5)	O62-C68	1.257(5)
O63-C67	1.246(5)	O64-C67	1.272(5)	C61-C62	1.387(6)
C61-C66	1.389(6)	C61-C67	1.498(5)	C62-C63	1.388(5)
C63-C64	1.385(5)	C64-C65	1.390(5)	C64-C68	1.506(5)
C65-C66	1.380(5)	O71-C77	1.251(5)	O72-C77	1.257(5)
O73-C78	1.257(5)	O74-C78	1.253(5)	C71-C72	1.390(6)
C71-C76	1.391(5)	C71-C77	1.511(5)	C72-C73	1.388(5)
C73-C74	1.393(5)	C74-C75	1.388(5)	C74-C78	1.513(5)
C75-C76	1.394(5)	O81-C87	1.255(5)	O82-C87	1.263(5)
O83-C88	1.255(5)	O84-C88	1.248(5)	C81-C86	1.386(6)
C81-C82	1.395(6)	C81-C87	1.504(5)	C82-C83	1.384(6)
C83-C84	1.390(5)	C84-C85	1.392(6)	C84-C88	1.504(5)
C85-C86	1.381(6)	O91-C97	1.257(5)	O92-C97	1.268(5)
C91-C92	1.387(6)	C91-C93#11	1.395(6)	C91-C97	1.499(5)
C92-C93	1.379(6)	C93-C91#11	1.395(6)	O101-C107	1.246(5)
O102-C107	1.274(5)	C101-C103#6	1.381(6)	C101-C102	1.393(6)
C101-C107	1.494(5)	C102-C103	1.389(6)	C103-C101#6	1.380(6)
C111-O111	1.217(6)	C111-N111	1.314(6)	N111-C112	1.436(6)
N111-C113	1.468(6)	C121-O121	1.226(6)	C121-N121	1.316(6)
N121-C122	1.448(7)	N121-C123	1.456(7)	C131-O131	1.236(7)
C131-N131	1.319(7)	N131-C132	1.439(7)	N131-C133	1.450(7)
C141-O141	1.243(7)	C141-N141	1.326(7)	N141-C142	1.445(7)
N141-C143	1.448(7)	C151-N151	1.317(6)	N151-C152	1.410(8)
N151-C153	1.470(7)	C161-O161	1.234(5)	C161-N161	1.321(5)
N161-C162	1.438(6)	N161-C163	1.451(6)	C171-O171	1.231(6)
C171-N171	1.317(6)	N171-C172	1.435(8)	N171-C173	1.454(7)
C181-O181	1.237(5)	C181-N181	1.320(5)	N181-C182	1.446(6)
N181-C183	1.455(6)	C191-O191	1.226(6)	C191-N191	1.326(6)
N191-C193	1.448(7)	N191-C192	1.452(6)		
O23#1-Ce1-O21	144.71(12)	O23#1-Ce1-O54#2	110.24(12)	O21-Ce1-O54#2	87.53(12)
O23#1-Ce1-O12	91.92(12)	O21-Ce1-O12	87.50(12)	O54#2-Ce1-O12	147.26(10)
O23#1-Ce1-O13#3	70.55(11)	O21-Ce1-O13#3	144.56(12)	O54#2-Ce1-O13#3	77.89(11)

240

O23#1-Ce1-O13#3	70.55(11)	O21-Ce1-O13#3	144.56(12)	O54#2-Ce1-O13#3	77.89(11)
O12-Ce1-O13#3	87.79(11)	O23#1-Ce1-O72#4	76.45(11)	O21-Ce1-O72#4	80.74(11)
O54#2-Ce1-O72#4	72.31(11)	O12-Ce1-O72#4	138.34(10)	O13#3-Ce1-O72#4	123.56(11)
O23#1-Ce1-O1W	73.04(13)	O21-Ce1-O1W	74.58(13)	O54#2-Ce1-O1W	142.43(12)
O12-Ce1-O1W	65.98(11)	O13#3-Ce1-O1W	133.85(13)	O72#4-Ce1-O1W	72.37(12)
O23#1-Ce1-O111	139.43(12)	O21-Ce1-O111	73.63(12)	O54#2-Ce1-O111	74.51(11)
O12-Ce1-O111	73.04(11)	O13#3-Ce1-O111	71.40(12)	O72#4-Ce1-O111	138.53(11)
O1W-Ce1-O111	128.40(12)	O102-Ce2-O33#5	79.73(11)	O102-Ce2-O22	151.11(10)
O33#5-Ce2-O22	78.58(11)	O102-Ce2-O11	97.22(10)	O33#5-Ce2-O11	144.41(10)
O22-Ce2-O11	89.52(11)	O102-Ce2-O32	74.20(10)	O33#5-Ce2-O32	135.45(10)
O22-Ce2-O32	134.53(10)	O11-Ce2-O32	75.24(10)	O102-Ce2-O41	123.88(9)
O33#5-Ce2-O41	86.77(11)	O22-Ce2-O41	73.61(10)	O11-Ce2-O41	122.08(11)
O32-Ce2-O41	78.92(10)	O102-Ce2-O121	75.30(10)	O33#5-Ce2-O121	72.89(10)
O22-Ce2-O121	80.21(10)	O11-Ce2-O121	72.08(11)	O32-Ce2-O121	131.37(10)
O41-Ce2-O121	149.57(11)	O102-Ce2-O42	76.13(9)	O33#5-Ce2-O42	66.04(9)
O22-Ce2-O42	111.50(9)	O11-Ce2-O42	148.12(10)	O32-Ce2-O42	72.94(9)
O41-Ce2-O42	48.97(9)	O121-Ce2-O42	133.15(10)		
O52-Ce3-O31	81.06(10)	O61-Ce3-O31	141.10(10)	O52-Ce3-O42	145.42(9)
O61-Ce3-O42	94.96(10)	O31-Ce3-O42	74.30(10)	O52-Ce3-O34#5	144.80(10)
O61-Ce3-O34#5	76.60(11)	O31-Ce3-O34#5	129.31(10)	O42-Ce3-O34#5	68.86(10)
O52-Ce3-O101	75.95(10)	O61-Ce3-O101	136.42(10)	O31-Ce3-O101	77.41(11)
O42-Ce3-O101	120.44(9)	O34#5-Ce3-O101	92.36(11)	O52-Ce3-O161	75.19(10)
O61-Ce3-O161	70.06(10)	O31-Ce3-O161	71.04(10)	O42-Ce3-O161	74.08(9)
O34#5-Ce3-O161	126.86(11)	O101-Ce3-O161	139.85(11)	O52-Ce3-O2W	79.19(10)
O61-Ce3-O2W	71.03(9)	O31-Ce3-O2W	141.65(9)	O42-Ce3-O2W	134.46(10)
O34#5-Ce3-O2W	65.79(11)	O101-Ce3-O2W	66.07(10)	O161-Ce3-O2W	133.16(10)
O52-Ce3-O102	117.02(9)	O61-Ce3-O102	149.49(10)	O31-Ce3-O102	63.58(9)
O42-Ce3-O102	72.77(8)	O34#5-Ce3-O102	72.92(10)	O101-Ce3-O102	47.71(9)
O161-Ce3-O102	129.18(9)	O2W-Ce3-O102	97.35(9)	O51-Ce4-O14#6	80.07(11)
O51-Ce4-O71	149.44(11)	O14#6-Ce4-O71	122.72(11)	O51-Ce4-O53#5	133.11(11)
O14#6-Ce4-O53#5	76.80(10)	O71-Ce4-O53#5	75.75(11)	O51-Ce4-O62	88.81(10)
O14#6-Ce4-O62	125.62(10)	O71-Ce4-O62	92.02(11)	O53#5-Ce4-O62	73.09(11)
O51-Ce4-O24#7	79.79(11)	O14#6-Ce4-O24#7	77.03(11)	O71-Ce4-O24#7	85.75(11)
O53#5-Ce4-O24#7	131.99(11)	O62-Ce4-O24#7	152.65(10)	O51-Ce4-O171	74.20(11)
O14#6-Ce4-O171	146.22(11)	O71-Ce4-O171	76.42(11)	O53#5-Ce4-O171	136.97(11)
O62-Ce4-O171	75.80(11)	O24#7-Ce4-O171	77.18(11)	O84#5-Ce5-O82	138.60(11)
O84#5-Ce5-O73#4	147.22(11)	O82-Ce5-O73#4	74.13(11)	O84#5-Ce5-O74#8	78.57(11)
O82-Ce5-O74#8	76.02(10)	O73#4-Ce5-O74#8	121.08(11)	O84#5-Ce5-O81#9	82.54(11)
O82-Ce5-O81#9	120.48(11)	O73#4-Ce5-O81#9	78.75(11)	O74#8-Ce5-O81#9	74.59(11)
O84#5-Ce5-O44	96.43(10)	O82-Ce5-O44	79.38(10)	O73#4-Ce5-O44	87.07(10)
O74#8-Ce5-O44	134.54(10)	O81#9-Ce5-O44	150.29(10)	O84#5-Ce5-O151	72.92(12)
O82-Ce5-O151	140.66(11)	O73#4-Ce5-O151	77.12(12)	O74#8-Ce5-O151	142.90(12)
O81#9-Ce5-O151	78.57(11)	O44-Ce5-O151	72.84(11)	O84#5-Ce5-O3W	67.29(10)
O82-Ce5-O3W	74.51(10)	O73#4-Ce5-O3W	139.83(10)	O74#8-Ce5-O3W	73.89(10)
O81#9-Ce5-O3W	139.81(10)	O44-Ce5-O3W	62.92(9)	O151-Ce5-O3W	114.56(11)
O83#5-Ce6-O92	142.15(10)	O83#5-Ce6-O43	89.41(10)	O92-Ce6-O43	77.62(10)
O83#5-Ce6-O64	146.63(10)	O92-Ce6-O64	71.03(10)	O43-Ce6-O64	97.91(10)
O83#5-Ce6-O91#8	78.86(10)	O92-Ce6-O91#8	130.91(10)	O43-Ce6-O91#8	143.02(10)
O64-Ce6-O91#8	75.82(10)	O83#5-Ce6-O63#8	75.13(10)	O92-Ce6-O63#8	86.63(11)
O43-Ce6-O63#8	130.62(10)	O64-Ce6-O63#8	120.71(9)	O91#8-Ce6-O63#8	80.23(10)
O83#5-Ce6-O181	77.24(10)	O92-Ce6-O181	129.17(10)	O43-Ce6-O181	71.44(10)
O64-Ce6-O181	74.45(10)	O91#8-Ce6-O181	71.79(10)	O63#8-Ce6-O181	143.78(11)
O83#5-Ce6-O64#8	115.25(9)	O92-Ce6-O64#8	71.75(9)	O43-Ce6-O64#8	149.37(10)
O64-Ce6-O64#8	71.90(9)	O91#8-Ce6-O64#8	64.03(9)	O63#8-Ce6-O64#8	48.87(9)
O181-Ce6-O64#8	129.34(9)	O83#5-Ce6-O3W	77.55(9)	O92-Ce6-O3W	64.61(9)
O43-Ce6-O3W	68.22(9)	O64-Ce6-O3W	135.32(9)	O91#8-Ce6-O3W	140.01(9)
O63#8-Ce6-O3W	62.75(9)	O181-Ce6-O3W	132.07(9)	O64#8-Ce6-O3W	98.28(8)
C17-O11-Ce2	144.3(3)	C17-O12-Ce1	141.1(3)	C18-O13-Ce1#3	149.0(3)
C18-O14-Ce4#6	140.6(3)	C12-C11-C16	119.9(3)	C12-C11-C17	119.2(3)
C16-C11-C17	120.8(4)	C13-C12-C11	120.4(4)	C13-C12-H12	119.8
C11-C12-H12	119.8	C12-C13-C14	120.3(4)	C12-C13-H13	119.8
C14-C13-H13	119.8	C13-C14-C15	119.8(3)	C13-C14-C18	119.0(4)
C15-C14-C18	121.2(4)	C14-C15-C16	119.8(4)	C14-C15-H15	120.1
C16-C15-H15	120.1	C11-C16-C15	119.7(4)	C11-C16-H16	120.1
C15-C16-H16	120.1	O12-C17-O11	125.0(4)	O12-C17-C11	117.2(4)
O11-C17-C11	117.7(4)	O14-C18-O13	125.4(4)	O14-C18-C14	117.5(4)
O13-C18-C14	117.2(4)	C27-O21-Ce1	172.8(3)	C27-O22-Ce2	120.0(3)
C28-O23-Ce1#5	159.6(3)	C28-O24-Ce4#2	115.3(3)	C26-C21-C22	119.9(4)
C26-C21-C27	119.7(4)	C22-C21-C27	120.4(4)	C23-C22-C21	120.2(4)
C23-C22-H22	119.9	C21-C22-H22	119.9	C22-C23-C24	120.0(4)

241

C22-C23-H23	120.0	C24-C23-H23	120.0	C25-C24-C23	119.5(4)
C25-C24-C28	119.8(4)	C23-C24-C28	120.7(4)	C24-C25-C26	120.7(4)
C24-C25-H25	119.7	C26-C25-H25	119.7	C21-C26-C25	119.7(4)
C21-C26-H26	120.1	C25-C26-H26	120.1	O21-C27-O22	123.6(4)
O21-C27-C21	118.0(4)	O22-C27-C21	118.4(4)	O23-C28-O24	123.5(4)
O23-C28-C24	118.4(4)	O24-C28-C24	118.1(4)	C37-O31-Ce3	142.3(3)
C37-O32-Ce2	127.9(3)	C38-O33-Ce2#1	137.4(3)	C38-O34-Ce3#1	133.5(3)
C36-C31-C32	119.4(4)	C36-C31-C37	119.5(4)	C32-C31-C37	121.2(4)
C31-C32-C33	119.8(4)	C31-C32-H32	120.1	C33-C32-H32	120.1
C34-C33-C32	120.7(4)	C34-C33-H33	119.7	C32-C33-H33	119.7
C33-C34-C35	118.9(4)	C33-C34-C38	120.2(4)	C35-C34-C38	120.8(4)
C36-C35-C34	120.9(4)	C36-C35-H35	119.6	C34-C35-H35	119.6
C35-C36-C31	120.3(4)	C35-C36-H36	119.8	C31-C36-H36	119.8
O31-C37-O32	125.0(4)	O31-C37-C31	116.3(4)	O32-C37-C31	118.7(4)
O33-C38-O34	125.5(4)	O33-C38-C34	116.4(4)	O34-C38-C34	118.1(4)
C47-O41-Ce2	99.3(2)	C47-O42-Ce3	162.5(3)	C47-O42-Ce2	89.5(2)
Ce3-O42-Ce2	106.43(9)	C48-O43-Ce6	150.7(3)	C48-O44-Ce5	137.5(3)
C42-C41-C46	120.0(3)	C42-C41-C47	120.4(3)	C46-C41-C47	119.6(4)
C43-C42-C41	119.9(4)	C43-C42-H42	120.1	C41-C42-H42	120.1
C44-C43-C42	120.5(4)	C44-C43-H43	119.7	C42-C43-H43	119.7
C43-C44-C45	119.9(3)	C43-C44-C48	120.0(3)	C45-C44-C48	120.0(3)
C44-C45-C46	120.0(4)	C44-C45-H45	120.0	C46-C45-H45	120.0
C41-C46-C45	119.6(4)	C41-C46-H46	120.2	C45-C46-H46	120.2
O41-C47-O42	121.7(3)	O41-C47-C41	119.3(3)	O42-C47-C41	119.0(3)
O44-C48-O43	124.9(3)	O44-C48-C44	117.5(3)	O43-C48-C44	117.6(3)
C57-O51-Ce4	161.4(3)	C57-O52-Ce3	135.2(3)	C58-O53-Ce4#1	135.1(3)
C58-O54-Ce1#7	138.8(3)	C52-C51-C56	118.9(4)	C52-C51-C57	121.0(4)
C56-C51-C57	120.1(4)	C51-C52-C53	120.7(4)	C51-C52-H52	119.6
C53-C52-H52	119.6	C54-C53-C52	119.9(4)	C54-C53-H53	120.1
C52-C53-H53	120.1	C55-C54-C53	119.3(4)	C55-C54-C58	119.8(4)
C53-C54-C58	120.8(4)	C56-C55-C54	120.7(4)	C56-C55-H55	119.7
C54-C55-H55	119.7	C55-C56-C51	120.5(4)	C55-C56-H56	119.8
C51-C56-H56	119.8	O51-C57-O52	124.9(4)	O51-C57-C51	117.3(3)
O52-C57-C51	117.7(4)	O54-C58-O53	124.5(4)	O54-C58-C54	117.5(4)
O53-C58-C54	118.0(4)	C68-O61-Ce3	146.2(3)	C68-O62-Ce4	140.7(3)
C67-O63-Ce6#8	101.2(2)	C67-O64-Ce6	164.0(3)	C67-O64-Ce6#8	87.8(2)
Ce6-O64-Ce6#8	108.11(9)	C62-C61-C66	120.6(4)	C62-C61-C67	120.1(3)
C66-C61-C67	119.3(4)	C61-C62-C63	119.1(4)	C61-C62-H62	120.5
C63-C62-H62	120.5	C64-C63-C62	120.7(4)	C64-C63-H63	119.7
C62-C63-H63	119.7	C63-C64-C65	119.6(4)	C63-C64-C68	119.3(3)
C65-C64-C68	121.1(3)	C66-C65-C64	120.3(4)	C66-C65-H65	119.9
C64-C65-H65	119.9	C65-C66-C61	119.7(4)	C65-C66-H66	120.1
C61-C66-H66	120.1	O63-C67-O64	122.0(4)	O63-C67-C61	119.0(3)
O64-C67-C61	119.0(3)	O63-C67-Ce6#8	54.9(2)	O64-C67-Ce6#8	67.2(2)
C61-C67-Ce6#8	172.9(3)	O61-C68-O62	124.9(4)	O61-C68-C64	117.8(3)
O62-C68-C64	117.3(3)	C77-O71-Ce4	153.2(3)	C77-O72-Ce1#10	138.2(3)
C78-O73-Ce5#10	156.9(3)	C78-O74-Ce5#8	136.3(3)	C72-C71-C76	119.5(4)
C72-C71-C77	120.5(4)	C76-C71-C77	120.0(4)	C73-C72-C71	120.3(4)
C73-C72-H72	119.8	C71-C72-H72	119.8	C72-C73-C74	120.3(4)
C72-C73-H73	119.9	C74-C73-H73	119.9	C75-C74-C73	119.5(3)
C75-C74-C78	120.5(3)	C73-C74-C78	120.0(4)	C74-C75-C76	120.2(4)
C74-C75-H75	119.9	C76-C75-H75	119.9	C71-C76-C75	120.2(4)
C71-C76-H76	119.9	C75-C76-H76	119.9	O71-C77-O72	124.9(4)
O71-C77-C71	118.1(4)	O72-C77-C71	117.0(4)	O74-C78-O73	125.3(4)
O74-C78-C74	117.1(4)	O73-C78-C74	117.6(4)	C87-O81-Ce5#9	135.0(3)
C87-O82-Ce5	138.2(3)	C88-O83-Ce6#1	131.8(3)	C88-O84-Ce5#1	159.4(3)
C86-C81-C82	119.4(4)	C86-C81-C87	120.7(4)	C82-C81-C87	119.9(4)
C83-C82-C81	119.9(4)	C83-C82-H82	120.1	C81-C82-H82	120.1
C82-C83-C84	120.4(4)	C82-C83-H83	119.8	C84-C83-H83	119.8
C83-C84-C85	119.6(4)	C83-C84-C88	120.4(4)	C85-C84-C88	119.8(4)
C86-C85-C84	119.8(4)	C86-C85-H85	120.1	C84-C85-H85	120.1
C85-C86-C81	120.8(4)	C85-C86-H86	119.6	C81-C86-H86	119.6
O81-C87-O82	124.6(4)	O81-C87-C81	117.9(4)	O82-C87-C81	117.5(4)
O84-C88-O83	124.1(4)	O84-C88-C84	116.8(4)	O83-C88-C84	119.1(4)
C97-O91-Ce6#8	139.3(3)	C97-O92-Ce6	132.2(3)	C92-C91-C93#11	118.8(4)
C92-C91-C97	121.4(4)	C93#11-C91-C97	119.9(4)	C93-C92-C91	120.4(4)
C93-C92-H92	119.8	C91-C92-H92	119.8	C92-C93-C91#11	120.8(4)
C92-C93-H93	119.6	C91#11-C93-H93	119.6	O91-C97-O92	125.5(4)
O91-C97-C91	117.4(4)	O92-C97-C91	117.2(4)	C107-O101-Ce3	103.4(2)
C107-O102-Ce2	167.9(3)	C107-O102-Ce3	87.3(2)	Ce2-O102-Ce3	104.67(9)

C103#6-C101-C102	119.5(4)	C103#6-C101-C107	119.4(4)	C102-C101-C107	121.1(4)
C103-C102-C101	119.9(4)	C103-C102-H102	120.0	C101-C102-H102	120.0
C101#6-C103-C102	120.5(4)	C101#6-C103-H103	119.7	C102-C103-H103	119.7
O101-C107-O102	121.6(3)	O101-C107-C101	119.0(4)	O102-C107-C101	119.4(3)
O111-C111-N111	125.4(5)	O111-C111-H111	117.3	N111-C111-H111	117.3
C111-N111-C112	123.6(5)	C111-N111-C113	119.6(4)	C112-N111-C113	116.7(4)
C111-O111-Ce1	127.8(3)	O121-C121-N121	125.5(5)	O121-C121-H121	117.2
N121-C121-H121	117.2	C121-N121-C122	120.8(5)	C121-N121-C123	121.2(5)
C122-N121-C123	117.9(4)	C121-O121-Ce2	123.1(3)	O131-C131-N131	124.9(5)
O131-C131-H131	117.6	N131-C131-H131	117.6	C131-N131-C132	121.4(5)
C131-N131-C133	121.7(6)	C132-N131-C133	116.8(5)	O141-C141-N141	124.3(5)
O141-C141-H141	117.8	N141-C141-H141	117.8	C141-N141-C142	120.7(5)
C141-N141-C143	122.0(5)	C142-N141-C143	117.3(5)	O151-C151-N151	122.3(5)
O151-C151-H151	118.8	N151-C151-H151	118.8	C151-N151-C152	122.5(5)
C151-N151-C153	119.6(5)	C152-N151-C153	117.9(5)	C151-O151-Ce5	126.1(3)
O161-C161-N161	125.5(4)	O161-C161-H161	117.3	N161-C161-H161	117.3
C161-N161-C162	121.3(4)	C161-N161-C163	121.9(4)	C162-N161-C163	116.7(4)
C161-O161-Ce3	125.6(3)	O171-C171-N171	124.4(5)	O171-C171-H171	117.8
N171-C171-H171	117.8	C171-N171-C172	121.2(5)	C171-N171-C173	120.6(5)
C172-N171-C173	118.2(5)	C171-O171-Ce4	128.6(3)	N171-C172-H17A	109.5
O181-C181-H181	117.4	N181-C181-H181	117.4	C181-N181-C182	121.2(4)
C181-N181-C183	121.3(4)	C182-N181-C183	117.3(4)	C181-O181-Ce6	123.4(3)
O191-C191-N191	125.8(5)	O191-C191-H191	117.1	N191-C191-H191	117.1
C191-N191-C193	121.8(4)	C191-N191-C192	121.2(5)	C193-N191-C192	116.9(5)
Ce5-O3W-Ce6	122.53(10)				

Symmetry transformation codes: #1 x-1,y,z #2 x+1,y-1,z #3 -x,-y,-z #4 x,y-1,z #5 x+1,y,z #6 -x,-y+1,-z #7 x-1,y+1,z #8 -x+1,-y+1,-z+1 #9 -x+1,-y,-z+1 #10 x,y+1,z #11 -x,-y+1,-z+1

Table 10.2 (b) Bond lengths (Å) and angles (°) for Ce-MOF-BDC System.

10.3 Detailed Information for Pr-MOF-BDC System from Single Crystal Analysis

Atom	x/a	y/b	z/c	U_{eq}
Pr1	0.93995(3)	0.109809(18)	0.534539(10)	0.01729(7)
Pr2	0.95445(3)	0.390236(18)	0.535774(10)	0.01852(7)
Pr3	0.61606(3)	0.003137(18)	0.190640(10)	0.01763(7)
Pr4	0.60843(3)	0.295397(19)	0.210832(10)	0.02116(8)
Pr5	0.69786(3)	0.513007(18)	0.143172(10)	0.02026(8)
Pr6	0.74394(3)	-0.210836(18)	0.120694(10)	0.01807(7)
C1A	0.6227(5)	-0.0070(3)	0.50793(18)	0.0195(12)
C2A	0.5322(5)	0.0661(4)	0.5092(2)	0.0263(13)
C3A	0.4106(6)	0.0725(4)	0.5016(2)	0.0270(13)
C4A	0.7549(5)	-0.0134(3)	0.51739(19)	0.0226(12)
O1A	0.7699(4)	0.0453(2)	0.53465(14)	0.0271(9)
O2A	0.8408(4)	-0.0778(2)	0.50754(15)	0.0304(10)

C1B	0.5977(5)	0.3182(3)	0.51969(18)	0.0212(12)
C2B	0.5772(6)	0.3861(4)	0.4922(2)	0.0290(14)
C3B	0.4610(6)	0.4174(4)	0.4776(2)	0.0297(14)
C4B	0.3633(5)	0.3827(3)	0.49050(19)	0.0228(12)
C5B	0.3836(5)	0.3140(3)	0.5177(2)	0.0256(13)
C6B	0.5012(5)	0.2821(3)	0.53201(19)	0.0235(12)
C7B	0.7199(5)	0.2885(3)	0.53934(19)	0.0227(12)
C8B	0.2342(6)	0.4189(4)	0.47625(19)	0.0255(13)
O1B	0.7796(4)	0.3375(3)	0.54225(15)	0.0346(10)
O2B	0.7518(4)	0.2189(2)	0.55450(13)	0.0266(9)
O3B	0.2151(4)	0.4846(2)	0.45592(15)	0.0341(10)
O4B	0.1530(4)	0.3811(3)	0.48542(14)	0.0310(10)
C1C	0.5324(5)	-0.0062(3)	0.04442(19)	0.0246(13)
C2C	0.5151(7)	0.0651(4)	0.0198(2)	0.0336(15)
C3C	0.4833(6)	0.0707(4)	-0.0244(2)	0.0335(15)
C4C	0.5661(5)	-0.0102(4)	0.09191(19)	0.0250(13)
O1C	0.5299(5)	0.0505(3)	0.11647(14)	0.0388(11)
O2C	0.6319(4)	-0.0758(2)	0.10713(13)	0.0276(9)
C1D	0.7939(5)	0.1060(3)	0.30182(19)	0.0219(12)
C2D	0.7832(6)	0.0444(4)	0.3321(2)	0.0290(14)
C3D	0.8196(6)	0.0396(4)	0.3755(2)	0.0280(13)
C4D	0.8626(5)	0.0993(3)	0.38934(18)	0.0213(12)
C5D	0.8718(6)	0.1621(4)	0.3594(2)	0.0287(14)
C6D	0.8387(6)	0.1652(4)	0.3156(2)	0.0285(13)
C7D	0.7534(5)	0.1092(3)	0.2552(2)	0.0228(12)
C8D	0.8988(5)	0.0969(3)	0.43671(19)	0.0225(12)
O1D	0.7227(4)	0.0522(2)	0.24337(14)	0.0326(10)
O2D	0.7517(4)	0.1702(2)	0.23021(14)	0.0295(10)
O3D	0.9530(4)	0.0312(2)	0.45401(13)	0.0253(9)
O4D	0.8715(4)	0.1596(2)	0.45858(14)	0.0315(10)
C1E	0.2639(5)	0.2151(3)	0.18961(19)	0.0225(12)
C2E	0.2328(6)	0.2907(3)	0.1706(2)	0.0289(14)
C3E	0.1144(6)	0.3231(4)	0.1574(2)	0.0291(14)
C4E	0.0243(5)	0.2822(3)	0.16402(19)	0.0231(12)
C5E	0.0551(6)	0.2065(4)	0.1831(2)	0.0288(13)
C6E	0.1749(6)	0.1731(4)	0.1951(2)	0.0283(13)

244

C7E	0.3904(5)	0.1822(3)	0.20702(18)	0.0218(12)
C8E	-0.1082(6)	0.3208(4)	0.15256(19)	0.0279(14)
O1E	0.4475(4)	0.2306(2)	0.21417(15)	0.0297(9)
O2E	0.4268(4)	0.1097(2)	0.21561(13)	0.0257(9)
O3E	-0.1296(4)	0.3899(3)	0.13622(15)	0.0366(11)
O4E	-0.1885(4)	0.2825(3)	0.16002(14)	0.0339(10)
C1F	0.5309(5)	0.3570(3)	0.05629(19)	0.0229(12)
C2F	0.5523(6)	0.4030(4)	0.01757(19)	0.0265(13)
C3F	0.5172(6)	0.3908(4)	-0.0239(2)	0.0268(13)
C4F	0.4602(5)	0.3319(3)	-0.02720(18)	0.0208(12)
C5F	0.4413(6)	0.2839(3)	0.01116(19)	0.0252(13)
C6F	0.4769(6)	0.2964(4)	0.05317(19)	0.0268(13)
C7F	0.5677(5)	0.3734(4)	0.10126(19)	0.0258(13)
C8F	0.4122(5)	0.3243(3)	-0.07139(18)	0.0226(12)
O1F	0.6150(4)	0.4298(3)	0.10098(15)	0.0370(11)
O2F	0.5487(4)	0.3297(3)	0.13555(13)	0.0339(10)
O3F	0.4267(4)	0.3732(2)	-0.10348(14)	0.0324(10)
O4F	0.3587(4)	0.2718(3)	-0.07319(14)	0.0310(10)
C1G	0.2896(5)	0.5095(3)	0.18496(18)	0.0216(12)
C2G	0.2837(6)	0.5699(4)	0.1521(2)	0.0269(13)
C3G	0.1707(5)	0.6050(3)	0.1352(2)	0.0252(13)
C4G	0.0625(5)	0.5800(3)	0.15123(19)	0.0207(12)
C5G	0.0685(5)	0.5204(4)	0.1847(2)	0.0270(13)
C6G	0.1810(5)	0.4856(4)	0.2012(2)	0.0260(13)
C7G	0.4133(5)	0.4685(4)	0.20184(19)	0.0254(13)
C8G	-0.0572(5)	0.6144(4)	0.13098(19)	0.0247(13)
O1G	0.5062(4)	0.4956(3)	0.18956(15)	0.0391(11)
O2G	0.4174(4)	0.4088(3)	0.22789(15)	0.0360(11)
O3G	-0.0681(4)	0.6759(2)	0.10657(14)	0.0292(10)
O4G	-0.1410(4)	0.5789(3)	0.13875(17)	0.0461(13)
C1H	0.7939(5)	0.4378(3)	0.29700(18)	0.0230(12)
C2H	0.7837(6)	0.3849(3)	0.3342(2)	0.0252(13)
C3H	0.8196(5)	0.3957(3)	0.37588(19)	0.0242(12)
C4H	0.8671(5)	0.4582(3)	0.38125(19)	0.0218(12)
C5H	0.8783(6)	0.5098(4)	0.3441(2)	0.0255(13)
C6H	0.8417(6)	0.4997(3)	0.30255(19)	0.0251(13)

C7H	0.7507(5)	0.4274(4)	0.25196(19)	0.0248(13)
C8H	0.9065(5)	0.4698(4)	0.4267(2)	0.0248(13)
O1H	0.7097(4)	0.3700(3)	0.24890(15)	0.0355(11)
O2H	0.7577(4)	0.4790(3)	0.22086(14)	0.0339(10)
O3H	0.8952(4)	0.4201(3)	0.45870(13)	0.0339(10)
O4H	0.9470(4)	0.5279(3)	0.42967(15)	0.0359(11)
C1I	0.3059(5)	-0.1197(4)	0.1653(2)	0.0251(13)
C2I	0.2181(6)	-0.0456(4)	0.1656(2)	0.0300(14)
C3I	0.0955(6)	-0.0370(4)	0.1580(2)	0.0288(13)
C4I	0.0593(5)	-0.1025(4)	0.14943(19)	0.0240(12)
C5I	0.1470(6)	-0.1767(4)	0.1498(2)	0.0329(14)
C6I	0.2697(6)	-0.1854(4)	0.1576(2)	0.0324(14)
C7I	0.4394(5)	-0.1269(4)	0.17389(19)	0.0255(13)
C8I	-0.0734(5)	-0.0933(4)	0.1393(2)	0.0278(14)
O1I	0.4545(4)	-0.0676(3)	0.19098(14)	0.0291(9)
O2I	0.5255(4)	-0.1914(2)	0.16405(14)	0.0282(9)
O3I	-0.1584(4)	-0.0296(3)	0.15029(16)	0.0342(10)
O4I	-0.0882(4)	-0.1507(3)	0.11998(15)	0.0307(10)
C1J	0.8082(5)	-0.2071(3)	0.26810(19)	0.0226(12)
C2J	0.7921(6)	-0.2678(4)	0.2987(2)	0.0282(13)
C3J	0.8233(6)	-0.2700(3)	0.34321(19)	0.0253(13)
C4J	0.8744(5)	-0.2139(3)	0.35625(18)	0.0199(12)
C5J	0.8928(6)	-0.1544(3)	0.32481(19)	0.0255(13)
C6J	0.8570(6)	-0.1502(3)	0.28141(19)	0.0261(13)
C7J	0.7725(5)	-0.2042(3)	0.22028(19)	0.0237(12)
C8J	0.9142(5)	-0.2183(3)	0.40365(18)	0.0198(12)
O1J	0.7896(4)	-0.2666(2)	0.19982(13)	0.0330(10)
O2J	0.7284(4)	-0.1376(2)	0.20144(13)	0.0237(9)
O3J	0.9038(4)	-0.2770(2)	0.42927(13)	0.0271(9)
O4J	0.9537(4)	-0.1639(2)	0.41461(13)	0.0282(9)
C1K	0.8357(6)	0.0166(4)	0.6318(2)	0.0303(14)
C2K	0.8331(8)	0.0356(5)	0.7134(2)	0.056(2)
C3K	0.7958(8)	-0.0845(4)	0.6868(3)	0.050(2)
N1K	0.8190(5)	-0.0086(3)	0.67516(17)	0.0332(12)
O1K	0.8583(4)	0.0798(3)	0.61877(14)	0.0320(10)
C1L	0.8254(7)	0.3328(5)	0.6439(2)	0.0463(17)

C2L	0.8431(11)	0.3762(6)	0.7177(3)	0.084(3)
C3L	0.7749(9)	0.2582(6)	0.7122(3)	0.078(3)
N1L	0.8147(5)	0.3244(3)	0.68930(19)	0.0396(13)
O1L	0.8618(5)	0.3876(3)	0.62184(15)	0.0429(12)
C1M	0.4965(6)	0.2217(4)	0.3164(2)	0.0378(15)
C2M	0.5114(11)	0.2586(6)	0.3924(3)	0.082(3)
C3M	0.4423(9)	0.1413(6)	0.3814(3)	0.078(3)
N1M	0.4827(6)	0.2090(4)	0.3615(2)	0.0461(14)
O1M	0.5323(5)	0.2766(3)	0.29657(15)	0.0411(11)
C1N	0.8414(6)	0.5578(4)	0.0336(2)	0.0376(15)
C2N	0.8225(8)	0.5115(5)	-0.0405(3)	0.055(2)
C3N	0.8897(8)	0.6309(5)	-0.0352(3)	0.0526(19)
N1N	0.8521(5)	0.5642(3)	-0.01135(17)	0.0328(11)
O1N	0.8062(5)	0.5068(3)	0.05736(16)	0.0489(13)
C1O	0.8429(6)	-0.1216(4)	0.0209(2)	0.0344(14)
C2O	0.8423(10)	-0.1465(5)	-0.0593(3)	0.064(2)
C3O	0.8726(10)	-0.0214(5)	-0.0361(3)	0.067(2)
N1O	0.8542(6)	-0.0983(4)	-0.02279(19)	0.0431(14)
O1O	0.8251(4)	-0.1851(3)	0.03560(14)	0.0356(10)
C1P	0.5114(6)	-0.0929(4)	0.2891(2)	0.0327(15)
C2P	0.5124(8)	-0.0736(5)	0.3699(2)	0.056(2)
C3P	0.4681(8)	-0.1919(5)	0.3450(3)	0.052(2)
N1P	0.4953(5)	-0.1173(3)	0.33278(18)	0.0342(12)
O1P	0.5362(4)	-0.0314(3)	0.27551(14)	0.0337(10)
C1Q	0.1336(6)	0.2987(4)	0.3861(2)	0.0368(14)
C2Q	0.1417(9)	0.3000(5)	0.3024(2)	0.056(2)
C3Q	0.2072(8)	0.3994(5)	0.3392(3)	0.060(2)
N1Q	0.1626(5)	0.3299(3)	0.34464(18)	0.0354(12)
O1Q	0.0933(5)	0.2409(3)	0.39336(16)	0.0483(12)
C1R	0.5161(7)	0.5822(5)	0.2950(3)	0.0476(16)
C2R	0.5142(9)	0.5830(5)	0.3782(3)	0.058(2)
C3R	0.4503(8)	0.4800(5)	0.3431(4)	0.069(2)
N1R	0.4936(5)	0.5501(4)	0.3370(2)	0.0425(13)
O1R	0.5561(6)	0.6411(3)	0.28789(18)	0.0583(14)
C1S	0.7997(8)	0.1925(5)	0.0533(3)	0.0527(18)
C2S	0.8090(9)	0.1961(5)	-0.0299(3)	0.065(2)

C3S	0.8653(9)	0.2970(5)	0.0088(4)	0.084(3)
N1S	0.8260(6)	0.2253(4)	0.0124(2)	0.0444(13)
O1S	0.7658(6)	0.1314(4)	0.05877(18)	0.0666(17)
O1W	1.0174(4)	0.2452(3)	0.49114(15)	0.0352(10)
O2W	0.6827(4)	0.1232(3)	0.15197(13)	0.0305(10)
O3W	0.5990(6)	0.6307(3)	0.19340(16)	0.0524(13)

---

[*] U_{eq} is defined as one third of the trace of the orthogonalized U_{ij} tensor.

Table 10.3 (a) Atomic coordinates and equivalent[*] isotropic atomic displacement parameters (Å^2) for Pr-MOF-BDC System

Pr1-O2B	2.400(4)	Pr1-O2A#1	2.438(4)	Pr1-O4J#1	2.445(4)
Pr1-O3D#1	2.464(4)	Pr1-O1A	2.480(4)	Pr1-O4D	2.493(4)
Pr1-O1K	2.540(4)	Pr1-O3D	2.761(4)	Pr1-O1W	2.927(5)
Pr2-O1B	2.366(4)	Pr2-O4B#2	2.386(4)	Pr2-O4H#3	2.414(4)
Pr2-O3H	2.434(4)	Pr2-O3B#4	2.443(4)	Pr2-O3J#1	2.452(4)
Pr2-O1L	2.536(4)	Pr2-O1W	2.798(5)	Pr3-O2E	2.407(4)
Pr3-O1D	2.437(4)	Pr3-O2J	2.469(4)	Pr3-O1I	2.473(4)
Pr3-O3I#2	2.481(4)	Pr3-O1C	2.516(4)	Pr3-O1P	2.573(4)
Pr3-O2W	2.588(4)	Pr3-O2C	2.833(4)	Pr4-O1E	2.378(4)
Pr4-O2F	2.395(4)	Pr4-O1H	2.397(4)	Pr4-O4E#2	2.421(4)
Pr4-O2D	2.423(4)	Pr4-O2G	2.453(4)	Pr4-O1M	2.524(4)
Pr5-O4G#2	2.392(4)	Pr5-O1G	2.398(4)	Pr5-O3E#2	2.435(4)
Pr5-O1F	2.442(4)	Pr5-O3F#5	2.442(4)	Pr5-O2H	2.461(4)
Pr5-O3W	2.480(5)	Pr5-O1N	2.566(4)	Pr6-O2C	2.397(4)
Pr6-O4I#2	2.401(4)	Pr6-O4F#6	2.420(4)	Pr6-O3G#7	2.424(4)
Pr6-O2I	2.461(4)	Pr6-O1J	2.528(4)	Pr6-O1O	2.543(4)
Pr6-O2J	2.710(4)				
C1A-C3A#8	1.377(8)	C1A-C2A	1.384(8)	C1A-C4A	1.511(7)
C2A-C3A	1.377(8)	C3A-C1A#8	1.377(8)	C4A-O1A	1.249(7)
C4A-O2A	1.264(7)	O2A-Pr1#1	2.438(4)	C1B-C6B	1.388(8)
C1B-C2B	1.391(8)	C1B-C7B	1.504(8)	C2B-C3B	1.376(8)
C3B-C4B	1.384(8)	C4B-C5B	1.395(8)	C4B-C8B	1.509(8)
C5B-C6B	1.389(8)	C7B-O1B	1.252(7)	C7B-O2B	1.257(7)
C8B-O3B	1.252(7)	C8B-O4B	1.259(7)	O3B-Pr2#4	2.443(4)
O4B-Pr2#9	2.386(4)	C1C-C3C#6	1.383(9)	C1C-C2C	1.396(8)
C1C-C4C	1.488(7)	C2C-C3C	1.384(8)	C3C-C1C#6	1.383(9)
C4C-O1C	1.253(7)	C4C-O2C	1.279(7)	C1D-C2D	1.383(8)
C1D-C6D	1.395(8)	C1D-C7D	1.498(8)	C2D-C3D	1.383(8)
C3D-C4D	1.391(8)	C4D-C5D	1.388(8)	C4D-C8D	1.499(7)
C5D-C6D	1.383(8)	C7D-O1D	1.244(7)	C7D-O2D	1.263(7)
C8D-O4D	1.246(7)	C8D-O3D	1.265(7)	O3D-Pr1#1	2.464(4)
C1E-C6E	1.386(8)	C1E-C2E	1.389(8)	C1E-C7E	1.518(8)
C2E-C3E	1.384(8)	C3E-C4E	1.380(8)	C4E-C5E	1.393(8)
C4E-C8E	1.514(8)	C5E-C6E	1.385(8)	C7E-O1E	1.254(7)
C7E-O2E	1.254(7)	C8E-O4E	1.255(7)	C8E-O3E	1.259(7)
O3E-Pr5#9	2.435(4)	O4E-Pr4#9	2.421(4)	C1F-C2F	1.379(8)
C1F-C6F	1.390(8)	C1F-C7F	1.508(7)	C2F-C3F	1.380(8)
C3F-C4F	1.387(8)	C4F-C5F	1.388(8)	C4F-C8F	1.506(7)
C5F-C6F	1.400(8)	C7F-O2F	1.252(7)	C7F-O1F	1.260(7)
C8F-O4F	1.253(7)	C8F-O3F	1.258(7)	O3F-Pr5#5	2.442(4)
O4F-Pr6#6	2.420(4)	C1G-C2G	1.386(8)	C1G-C6G	1.389(8)
C1G-C7G	1.505(8)	C2G-C3G	1.388(8)	C3G-C4G	1.394(8)
C4G-C5G	1.388(8)	C4G-C8G	1.497(8)	C5G-C6G	1.377(8)
C7G-O1G	1.249(7)	C7G-O2G	1.260(7)	C8G-O4G	1.251(7)
C8G-O3G	1.253(7)	O3G-Pr6#10	2.424(4)	O4G-Pr5#9	2.392(4)
C1H-C6H	1.382(8)	C1H-C2H	1.399(8)	C1H-C7H	1.513(7)
C2H-C3H	1.384(8)	C3H-C4H	1.389(8)	C4H-C5H	1.386(8)
C4H-C8H	1.511(8)	C5H-C6H	1.381(8)	C7H-O1H	1.246(7)
C7H-O2H	1.257(7)	C8H-O4H	1.253(7)	C8H-O3H	1.259(7)
O4H-Pr2#3	2.414(4)	C1I-C6I	1.383(8)	C1I-C2I	1.386(8)
C1I-C7I	1.513(8)	C2I-C3I	1.380(8)	C3I-C4I	1.387(8)
C4I-C5I	1.389(8)	C4I-C8I	1.513(8)	C5I-C6I	1.383(8)
C7I-O1I	1.257(7)	C7I-O2I	1.265(7)	C8I-O3I	1.255(7)
C8I-O4I	1.259(7)	O3I-Pr3#9	2.481(4)	O4I-Pr6#9	2.401(4)
C1J-C6J	1.382(8)	C1J-C2J	1.387(8)	C1J-C7J	1.509(8)
C2J-C3J	1.395(8)	C2J-H2J	0.9400	C3J-C4J	1.384(8)
C4J-C5J	1.391(8)	C4J-C8J	1.513(7)	C5J-C6J	1.382(8)
C7J-O1J	1.239(7)	C7J-O2J	1.270(7)	C8J-O4J	1.250(7)
C8J-O3J	1.264(7)	O3J-Pr2#1	2.452(4)	O4J-Pr1#1	2.445(4)
O1W-H11W	0.821(10)	O1W-H12W	0.821(10)	O2W-H21W	0.810(10)
O2W-H22W	0.807(10)	O3W-H31W	0.808(10)	O3W-H32W	0.813(10)

Table 10.3 (b) Bond lengths (Å) for Pr-MOF-BDC System

O2B-Pr1-O2A#1	141.88(14)	O2B-Pr1-O4J#1	88.86(14)	O2A#1-Pr1-O4J#1	77.73(14)
O2B-Pr1-O3D#1	147.01(13)	O2A#1-Pr1-O3D#1	70.90(13)	O4J#1-Pr1-O3D#1	98.26(13)
O2B-Pr1-O1A	79.21(14)	O2A#1-Pr1-O1A	130.80(14)	O4J#1-Pr1-O1A	143.30(13)
O3D#1-Pr1-O1A	75.94(13)	O2B-Pr1-O4D	75.00(14)	O2A#1-Pr1-O4D	86.82(14)
O4J#1-Pr1-O4D	130.37(13)	O3D#1-Pr1-O4D	120.74(13)	O1A-Pr1-O4D	79.95(14)
O2B-Pr1-O1K	77.15(13)	O2A#1-Pr1-O1K	129.22(14)	O4J#1-Pr1-O1K	71.39(14)
O3D#1-Pr1-O1K	74.80(13)	O1A-Pr1-O1K	72.15(13)	O4D-Pr1-O1K	143.59(14)
O2B-Pr1-O3D	115.56(12)	O2A#1-Pr1-O3D	71.60(13)	O4J#1-Pr1-O3D	149.33(13)
O3D#1-Pr1-O3D	71.79(13)	O1A-Pr1-O3D	64.01(12)	O4D-Pr1-O3D	49.00(12)
O1K-Pr1-O3D	129.68(13)	O2B-Pr1-O1W	76.59(13)	O2A#1-Pr1-O1W	65.30(13)
O4J#1-Pr1-O1W	68.39(12)	O3D#1-Pr1-O1W	135.93(13)	O1A-Pr1-O1W	139.17(13)
O4D-Pr1-O1W	62.32(13)	O1K-Pr1-O1W	131.78(13)	O3D-Pr1-O1W	98.14(12)
O1B-Pr2-O4B#2	138.83(15)	O1B-Pr2-O4H#3	146.82(16)	O4B#2-Pr2-O4H#3	74.29(15)
O1B-Pr2-O3H	78.73(15)	O4B#2-Pr2-O3H	76.11(14)	O4H#3-Pr2-O3H	121.18(15)
O1B-Pr2-O3B#4	82.77(15)	O4B#2-Pr2-O3B#4	120.28(15)	O4H#3-Pr2-O3B#4	78.38(15)
O3H-Pr2-O3B#4	74.63(15)	O1B-Pr2-O3J#1	96.36(14)	O4B#2-Pr2-O3J#1	79.39(14)
O4H#3-Pr2-O3J#1	87.10(14)	O3H-Pr2-O3J#1	134.60(14)	O3B#4-Pr2-O3J#1	150.23(14)
O1B-Pr2-O1L	72.81(16)	O4B#2-Pr2-O1L	140.61(15)	O4H#3-Pr2-O1L	76.80(16)
O3H-Pr2-O1L	142.83(15)	O3B#4-Pr2-O1L	78.47(15)	O3J#1-Pr2-O1L	72.94(14)
O1B-Pr2-O1W	66.77(14)	O4B#2-Pr2-O1W	75.20(14)	O4H#3-Pr2-O1W	140.55(14)
O3H-Pr2-O1W	73.93(14)	O3B#4-Pr2-O1W	139.62(14)	O3J#1-Pr2-O1W	63.09(13)
O1L-Pr2-O1W	114.31(15)	O2E-Pr3-O1D	88.15(14)	O2E-Pr3-O2J	145.52(13)
O1D-Pr3-O2J	95.48(13)	O2E-Pr3-O1I	81.45(14)	O1D-Pr3-O1I	141.38(14)
O2J-Pr3-O1I	74.42(13)	O2E-Pr3-O3I#2	144.27(14)	O1D-Pr3-O3I#2	76.47(15)
O2J-Pr3-O3I#2	69.05(14)	O1I-Pr3-O3I#2	129.70(14)	O2E-Pr3-O1C	76.16(14)
O1D-Pr3-O1C	136.18(14)	O2J-Pr3-O1C	120.45(13)	O1I-Pr3-O1C	76.97(15)
O3I#2-Pr3-O1C	92.83(15)	O2E-Pr3-O1P	75.05(13)	O1D-Pr3-O1P	70.19(14)
O2J-Pr3-O1P	74.06(13)	O1I-Pr3-O1P	71.19(14)	O3I#2-Pr3-O1P	126.71(14)
O1C-Pr3-O1P	139.56(15)	O2E-Pr3-O2W	78.58(14)	O1D-Pr3-O2W	71.12(13)
O2J-Pr3-O2W	134.93(14)	O1I-Pr3-O2W	140.90(13)	O3I#2-Pr3-O2W	66.01(14)
O1C-Pr3-O2W	65.80(14)	O1P-Pr3-O2W	133.30(14)	O2E-Pr3-O2C	118.23(12)
O1D-Pr3-O2C	149.00(14)	O2J-Pr3-O2C	72.36(12)	O1I-Pr3-O2C	64.07(13)
O3I#2-Pr3-O2C	72.56(13)	O1C-Pr3-O2C	48.18(12)	O1P-Pr3-O2C	129.42(13)
O2W-Pr3-O2C	96.98(12)	O1E-Pr4-O2F	79.69(15)	O1E-Pr4-O1H	149.34(15)
O2F-Pr4-O1H	123.07(15)	O1E-Pr4-O4E#2	133.08(15)	O2F-Pr4-O4E#2	76.77(14)
O1H-Pr4-O4E#2	75.97(15)	O1E-Pr4-O2D	88.03(14)	O2F-Pr4-O2D	124.64(15)
O1H-Pr4-O2D	93.18(14)	O4E#2-Pr4-O2D	73.45(14)	O1E-Pr4-O2G	80.54(15)
O2F-Pr4-O2G	77.31(15)	O1H-Pr4-O2G	84.85(15)	O4E#2-Pr4-O2G	131.28(15)
O2D-Pr4-O2G	153.09(14)	O1E-Pr4-O1M	74.46(15)	O2F-Pr4-O1M	146.33(15)
O1H-Pr4-O1M	76.14(16)	O4E#2-Pr4-O1M	136.89(15)	O2D-Pr4-O1M	75.99(14)
O2G-Pr4-O1M	77.49(15)	O4G#2-Pr5-O1G	144.30(17)	O4G#2-Pr5-O3E#2	87.09(17)
O1G-Pr5-O3E#2	111.16(16)	O4G#2-Pr5-O1F	144.58(17)	O1G-Pr5-O1F	70.96(15)
O3E#2-Pr5-O1F	77.69(16)	O4G#2-Pr5-O3F#5	88.11(16)	O1G-Pr5-O3F#5	90.93(15)
O3E#2-Pr5-O3F#5	147.41(14)	O1F-Pr5-O3F#5	87.99(15)	O4G#2-Pr5-O2H	80.47(15)
O1G-Pr5-O2H	76.71(14)	O3E#2-Pr5-O2H	72.31(15)	O1F-Pr5-O2H	123.31(15)
O3F#5-Pr5-O2H	138.27(14)	O4G#2-Pr5-O3W	74.4(2)	O1G-Pr5-O3W	72.65(18)
O3E#2-Pr5-O3W	141.92(17)	O1F-Pr5-O3W	134.55(18)	O3F#5-Pr5-O3W	66.27(15)
O2H-Pr5-O3W	71.99(16)	O4G#2-Pr5-O1N	73.96(18)	O1G-Pr5-O1N	139.22(16)
O3E#2-Pr5-O1N	74.71(15)	O1F-Pr5-O1N	71.25(17)	O3F#5-Pr5-O1N	72.98(15)
O2H-Pr5-O1N	138.88(16)	O3W-Pr5-O1N	128.38(16)	O2C-Pr6-O4I#2	79.80(14)
O2C-Pr6-O4F#6	98.18(14)	O4I#2-Pr6-O4F#6	144.77(14)	O2C-Pr6-O3G#7	151.40(14)
O4I#2-Pr6-O3G#7	78.79(15)	O4F#6-Pr6-O3G#7	88.62(14)	O2C-Pr6-O2I	74.57(14)
O4I#2-Pr6-O2I	135.80(14)	O4F#6-Pr6-O2I	75.12(14)	O3G#7-Pr6-O2I	133.85(14)
O2C-Pr6-O1J	123.90(13)	O4I#2-Pr6-O1J	86.49(15)	O4F#6-Pr6-O1J	121.39(14)
O3G#7-Pr6-O1J	73.36(13)	O2I-Pr6-O1J	79.01(14)	O2C-Pr6-O1O	75.40(14)
O4I#2-Pr6-O1O	73.25(14)	O4F#6-Pr6-O1O	72.26(14)	O3G#7-Pr6-O1O	80.41(14)
O2I-Pr6-O1O	131.28(14)	O1J-Pr6-O1O	149.53(15)	O2C-Pr6-O2J	75.70(12)
O4I#2-Pr6-O2J	66.32(13)	O4F#6-Pr6-O2J	147.75(13)	O3G#7-Pr6-O2J	112.07(12)
O2I-Pr6-O2J	72.73(13)	O1J-Pr6-O2J	49.27(12)	O1O-Pr6-O2J	133.47(13)
C3A#8-C1A-C2A	118.9(5)	C3A#8-C1A-C4A	121.5(5)	C2A-C1A-C4A	119.6(5)
C3A-C2A-C1A	120.2(5)	C1A#8-C3A-C2A	120.9(5)	O1A-C4A-O2A	125.5(5)
O1A-C4A-C1A	117.2(5)	O2A-C4A-C1A	117.4(5)	C4A-O1A-Pr1	139.2(4)
C4A-O2A-Pr1#1	133.0(4)	C6B-C1B-C2B	119.7(5)	C6B-C1B-C7B	120.4(5)
C2B-C1B-C7B	119.6(5)	C3B-C2B-C1B	119.7(5)	C2B-C3B-C4B	120.9(5)
C3B-C4B-C5B	119.7(5)	C3B-C4B-C8B	120.9(5)	C5B-C4B-C8B	119.5(5)

C2B-C1B-C7B	119.6(5)	C3B-C2B-C1B	119.7(5)	C2B-C3B-C4B	120.9(5)
C3B-C4B-C5B	119.7(5)	C3B-C4B-C8B	120.9(5)	C5B-C4B-C8B	119.5(5)
C6B-C5B-C4B	119.4(5)	C1B-C6B-C5B	120.5(5)	O1B-C7B-O2B	123.9(5)
O1B-C7B-C1B	116.8(5)	O2B-C7B-C1B	119.1(5)	O3B-C8B-O4B	124.4(6)
O3B-C8B-C4B	117.8(5)	O4B-C8B-C4B	117.8(5)	C7B-O1B-Pr2	158.9(4)
C7B-O2B-Pr1	132.4(3)	C8B-O3B-Pr2#4	135.6(4)	C8B-O4B-Pr2#9	138.8(4)
C3C#6-C1C-C2C	119.4(5)	C3C#6-C1C-C4C	121.9(5)	C2C-C1C-C4C	118.7(5)
C3C-C2C-C1C	120.0(6)	C1C#6-C3C-C2C	120.6(6)	O1C-C4C-O2C	120.8(5)
O1C-C4C-C1C	119.8(5)	O2C-C4C-C1C	119.4(5)	C4C-O1C-Pr3	103.4(3)
C4C-O2C-Pr6	166.9(4)	C4C-O2C-Pr3	87.6(3)	Pr6-O2C-Pr3	105.12(13)
C2D-C1D-C6D	119.6(5)	C2D-C1D-C7D	119.3(5)	C6D-C1D-C7D	121.1(5)
C1D-C2D-C3D	120.8(6)	C2D-C3D-C4D	119.4(5)	C5D-C4D-C3D	120.2(5)
C5D-C4D-C8D	119.3(5)	C3D-C4D-C8D	120.5(5)	C6D-C5D-C4D	120.0(5)
C5D-C6D-C1D	120.0(5)	O1D-C7D-O2D	123.8(5)	O1D-C7D-C1D	118.3(5)
O2D-C7D-C1D	117.9(5)	O4D-C8D-O3D	121.7(5)	O4D-C8D-C4D	119.1(5)
O3D-C8D-C4D	119.2(5)	C7D-O1D-Pr3	146.7(4)	C7D-O2D-Pr4	141.5(4)
C8D-O3D-Pr1#1	163.7(4)	C8D-O3D-Pr1	88.0(3)	Pr1#1-O3D-Pr1	108.22(13)
C8D-O4D-Pr1	101.3(3)	C6E-C1E-C2E	119.2(5)	C6E-C1E-C7E	121.1(5)
C2E-C1E-C7E	119.6(5)	C3E-C2E-C1E	120.0(6)	C4E-C3E-C2E	121.0(5)
C3E-C4E-C5E	119.1(5)	C3E-C4E-C8E	120.3(5)	C5E-C4E-C8E	120.5(5)
C6E-C5E-C4E	120.0(6)	C5E-C6E-C1E	120.7(5)	O1E-C7E-O2E	124.7(5)
O1E-C7E-C1E	117.2(5)	O2E-C7E-C1E	118.0(5)	O4E-C8E-O3E	124.6(6)
O4E-C8E-C4E	118.5(5)	O3E-C8E-C4E	116.9(6)	C7E-O1E-Pr4	161.7(4)
C7E-O2E-Pr3	135.3(4)	C8E-O3E-Pr5#9	138.6(4)	C8E-O4E-Pr4#9	136.0(4)
C2F-C1F-C6F	119.7(5)	C2F-C1F-C7F	118.9(5)	C6F-C1F-C7F	121.4(5)
C1F-C2F-C3F	120.5(6)	C2F-C3F-C4F	120.4(5)	C3F-C4F-C5F	119.6(5)
C3F-C4F-C8F	119.5(5)	C5F-C4F-C8F	120.7(5)	C4F-C5F-C6F	119.8(5)
C1F-C6F-C5F	119.9(5)	O2F-C7F-O1F	125.8(5)	O2F-C7F-C1F	117.2(6)
O1F-C7F-C1F	117.0(5)	O4F-C8F-O3F	125.0(5)	O4F-C8F-C4F	118.3(5)
O3F-C8F-C4F	116.6(5)	C7F-O1F-Pr5	149.1(4)	C7F-O2F-Pr4	140.1(4)
C8F-O3F-Pr5#5	140.6(4)	C8F-O4F-Pr6#6	145.6(4)	C2G-C1G-C6G	119.4(5)
C2G-C1G-C7G	120.4(5)	C6G-C1G-C7G	120.1(5)	C1G-C2G-C3G	120.1(5)
C2G-C3G-C4G	120.2(5)	C5G-C4G-C3G	119.4(5)	C5G-C4G-C8G	120.2(5)
C3G-C4G-C8G	120.4(5)	C6G-C5G-C4G	120.1(5)	C5G-C6G-C1G	120.8(5)
O1G-C7G-O2G	123.4(6)	O1G-C7G-C1G	118.5(5)	O2G-C7G-C1G	118.1(5)
O4G-C8G-O3G	123.1(5)	O4G-C8G-C4G	117.8(5)	O3G-C8G-C4G	119.1(5)
C7G-O1G-Pr5	158.5(4)	C7G-O2G-Pr4	116.6(4)	C8G-O3G-Pr6#10	122.0(4)
C8G-O4G-Pr5#9	172.7(4)	C6H-C1H-C2H	118.9(5)	C6H-C1H-C7H	121.1(5)
C2H-C1H-C7H	119.9(5)	C3H-C2H-C1H	120.0(5)	C2H-C3H-C4H	120.7(5)
C5H-C4H-C3H	119.0(5)	C5H-C4H-C8H	120.4(5)	C3H-C4H-C8H	120.7(5)
C6H-C5H-C4H	120.6(5)	C5H-C6H-C1H	120.8(5)	O1H-C7H-O2H	125.5(5)
O1H-C7H-C1H	118.1(5)	O2H-C7H-C1H	116.4(5)	O4H-C8H-O3H	125.5(5)
O4H-C8H-C4H	117.7(5)	O3H-C8H-C4H	116.8(5)	C7H-O1H-Pr4	152.9(4)
C7H-O2H-Pr5	138.1(4)	C8H-O3H-Pr2	136.7(4)	C8H-O4H-Pr2#3	156.2(4)
C6I-C1I-C2I	119.6(5)	C6I-C1I-C7I	121.4(5)	C2I-C1I-C7I	119.0(5)
C3I-C2I-C1I	120.5(6)	C2I-C3I-C4I	120.3(6)	C3I-C4I-C5I	119.1(5)
C3I-C4I-C8I	120.6(5)	C5I-C4I-C8I	120.3(5)	C6I-C5I-C4I	120.7(6)
C1I-C6I-C5I	119.9(6)	O1I-C7I-O2I	125.5(5)	O1I-C7I-C1I	116.3(5)
O2I-C7I-C1I	118.2(5)	O3I-C8I-O4I	125.7(5)	O3I-C8I-C4I	117.9(5)
O4I-C8I-C4I	116.4(5)	C7I-O1I-Pr3	141.5(4)	C7I-O2I-Pr6	127.9(4)
C8I-O3I-Pr3#9	133.5(4)	C8I-O4I-Pr6#9	137.1(4)	C6J-C1J-C2J	120.1(5)
C6J-C1J-C7J	120.5(5)	C2J-C1J-C7J	119.4(5)	C1J-C2J-C3J	119.5(6)
C4J-C3J-C2J	120.4(5)	C3J-C4J-C5J	119.4(5)	C3J-C4J-C8J	120.5(5)
C5J-C4J-C8J	120.0(5)	C6J-C5J-C4J	120.3(5)	C1J-C6J-C5J	120.2(5)
O1J-C7J-O2J	121.5(5)	O1J-C7J-C1J	119.3(5)	O2J-C7J-C1J	119.1(5)
O4J-C8J-O3J	125.1(5)	O4J-C8J-C4J	117.9(5)	O3J-C8J-C4J	117.0(5)
C7J-O1J-Pr6	99.1(3)	C7J-O2J-Pr3	162.0(4)	C7J-O2J-Pr6	89.6(3)
Pr3-O2J-Pr6	106.82(13)	C8J-O3J-Pr2#1	137.6(4)	C8J-O4J-Pr1#1	150.8(3)
Pr2-O1W-Pr1	122.91(16)	Pr2-O1W-H11W	119(5)	Pr1-O1W-H11W	116(5)
Pr2-O1W-H12W	90(5)	Pr1-O1W-H12W	90(5)	H11W-O1W-H12W	105(3)
Pr3-O2W-H21W	111(5)	Pr3-O2W-H22W	83(5)	H21W-O2W-H22W	105(3)
Pr5-O3W-H31W	143(5)	Pr5-O3W-H32W	102(3)	H31W-O3W-H32W	110(3)

Symmetry transformation codes:#1 -x+2,-y,-z+1   #2 x+1,y,z   #3 -x+2,-y+1,-z+1   #4 -x+1,-y+1,-z+1   #5 -x+1,-y+1,-z   #6 x+1,-y,-z   #7 x+1,y-1,z   #8 -x+1,-y,-z+1   #9 x-1,y,z   #10 x-1,y+1,z

Table 10.3 (c) Bond angles (°) for Pr-MOF-BDC System.

D—H···A*	d(D—H)	d(H···A)	d(D···A)	∠(DHA)
O1W—H11W···O1Q#2	0.821(10)	2.000(12)	2.820(6)	178(6)
O1W—H12W···O3J#1	0.821(10)	2.25(5)	2.762(6)	121(5)
O2W—H21W···O1S	0.810(10)	1.99(3)	2.715(6)	148(5)
O2W—H22W···O3I#2	0.807(10)	2.14(5)	2.763(6)	134(6)
O3W—H31W···O1R	0.808(10)	2.05(4)	2.715(7)	139(6)
O3W—H32W···O3F#5	0.813(10)	2.21(4)	2.691(6)	118(4)

* D - donor atom, H - hydrogen, A - acceptor.
Symmetry transformation codes:
#1 -x+2,-y,-z+1   #2 x+1,y,z   #3 -x+2,-y+1,-z+1   #4 -x+1,-y+1,-z+1   #5 -x+1,-y+1,-z   #6 -x+1,-y,-z   #7 x+1,y-1,z   #8 -x+1,-y,-z+1   #9 x-1,y,z   #10 x-1,y+1,z

Table 10.3 (d) Hydrogen bond information (Å and °) for Pr-MOF-BDC System.

10.4 Detailed Information for Gd-MOF-BDC System from Single Crystal Analysis

Atom	x/a	y/b	z/c	U_{eq}
Gd1	0.0000	0.455890(10)	0.7500	0.02542(4)
O1	0.08358(10)	0.4179(2)	0.60143(16)	0.0622(5)
O2	0.09584(9)	0.47629(15)	0.40510(15)	0.0446(3)
C1	0.11603(10)	0.41388(19)	0.50249(18)	0.0343(4)
C2	0.18563(9)	0.32869(16)	0.50129(16)	0.0283(3)
C3	0.21539(11)	0.26677(19)	0.61074(17)	0.0362(4)
C4	0.27968(11)	0.18844(19)	0.60963(16)	0.0351(4)
O11	-0.06770(11)	0.27003(16)	0.66367(16)	0.0569(4)
C11	-0.0934(7)	0.2342(11)	0.5623(8)	0.040(2)
N11	-0.1358(5)	0.1331(9)	0.5378(9)	0.0625(14)
C12	-0.1616(10)	0.1028(14)	0.4022(10)	0.080(4)
C13	-0.1602(10)	0.0471(14)	0.6315(13)	0.059(3)
O11A	-0.06770(11)	0.27003(16)	0.66367(16)	0.0569(4)

C11A	-0.0563(14)	0.187(2)	0.592(3)	0.064(3)
N11A	-0.0994(13)	0.0914(15)	0.5516(18)	0.071(2)
C12A	-0.169(2)	0.058(4)	0.619(4)	0.087(8)
C13A	-0.085(2)	0.014(3)	0.445(3)	0.099(7)
O11B	-0.06770(11)	0.27003(16)	0.66367(16)	0.0569(4)
C11B	-0.0445(6)	0.1779(11)	0.6137(15)	0.064(3)
N11B	-0.0862(7)	0.0954(8)	0.5443(8)	0.071(2)
C12B	-0.1688(7)	0.1360(15)	0.5078(19)	0.102(5)
C13B	-0.0586(10)	-0.0238(10)	0.5041(14)	0.095(4)
O11C	-0.06770(11)	0.27003(16)	0.66367(16)	0.0569(4)
C11C	-0.1120(6)	0.2554(9)	0.5706(7)	0.040(2)
N11C	-0.1432(5)	0.1469(9)	0.5354(8)	0.0625(14)
C12C	-0.1991(7)	0.1385(12)	0.4190(11)	0.079(3)
C13C	-0.1251(10)	0.0322(11)	0.6066(15)	0.097(5)
N21	0.0111(10)	0.7313(4)	0.7340(15)	0.069(2)
O21	-0.0381(7)	0.6800(7)	0.8007(8)	0.0581(16)
O22	0.0464(8)	0.6602(9)	0.6661(8)	0.0614(17)
O23	0.0171(12)	0.8456(4)	0.7287(18)	0.133(4)

* U_{eq} is defined as one third of the trace of the orthogonalized U_{ij} tensor.

Table 10.4 (a) Atomic coordinates and equivalent[*] isotropic atomic displacement parameters (Å^2) for Gd-MOF-BDC System.

Atom	sof	Atom	sof	Atom	sof
O11 - C13	0.275(4)	O11A - C13A	0.140(6)		
O11B - C13B	0.269(7)	O11C - C13C	0.316(6)		
N21 - O23	0.50				

Table 10.4 (b) Site occupancy factors that deviate from unity for Gd-MOF-BDC System.

Gd1-O1#1	2.2823(15)	Gd1-O1	2.2824(15)	Gd1-O2#2	2.3257(14)
Gd1-O2#3	2.3258(14)	Gd1-O11	2.4237(16)	Gd1-O11#1	2.4237(16)
O1-C1	1.242(2)	O2-C1	1.248(2)	O2-Gd1#2	2.3258(14)
C1-C2	1.505(2)	C2-C3	1.387(2)	C2-C4#4	1.388(2)
C3-C4	1.388(2)	C4-C2#4	1.389(2)	O11-C11	1.185(7)
C11-N11	1.310(7)	N11-C13	1.445(10)	N11-C12	1.499(8)
N21-O23	1.220(5)	N21-O22	1.245(7)	N21-O21	1.283(9)
O1#1-Gd1-O1	159.68(11)	O1#1-Gd1-O2#2	95.21(7)	O1-Gd1-O2#2	91.05(6)
O1#1-Gd1-O2#3	91.05(6)	O1-Gd1-O2#3	95.21(7)	O2#2-Gd1-O2#3	143.96(8)
O1#1-Gd1-O11	78.69(6)	O1-Gd1-O11	84.79(8)	O2#2-Gd1-O11	72.75(6)
O2#3-Gd1-O11	143.12(6)	O1#1-Gd1-O11#1	84.79(8)	O1-Gd1-O11#1	78.69(6)
O2#2-Gd1-O11#1	143.12(6)	O2#3-Gd1-O11#1	72.75(6)	O11-Gd1-O11#1	71.11(8)
C1-O1-Gd1	164.68(14)	C1-O2-Gd1#2	150.40(14)	O1-C1-O2	124.90(17)
O1-C1-C2	117.28(17)	O2-C1-C2	117.81(16)	C3-C2-C4#4	119.69(15)
C3-C2-C1	120.27(15)	C4#4-C2-C1	120.04(15)	C2-C3-C4	120.23(15)
C3-C4-C2#4	120.08(16)	C11-O11-Gd1	136.6(6)	O11-C11-N11	126.4(9)
C11-N11-C13	125.2(8)	C11-N11-C12	118.1(8)	C13-N11-C12	116.7(8)
O23-N21-O22	121.8(7)	O23-N21-O21	120.8(7)	O22-N21-O21	117.0(4)
N21-O21-Gd1	94.6(5)	N21-O22-Gd1	97.1(6)		

Symmetry transformation codes:#1 -x,y,-z+3/2　#2 -x,-y+1,-z+1　#3 x,-y+1,z+1/2　#4 -x+1/2,-y+1/2,-z+1

Table 10.4 (c) Bond lengths (Å) and angles (°) for Gd-MOF-BDC System.

10.5 Detailed Information for Ho-MOF-BDC System from Single Crystal Analysis

Atom	x/a	y/b	z/c	U_{eq}
Ho1	0.0000	0.457488(9)	0.7500	0.02904(5)
O1	0.08356(10)	0.41988(18)	0.60432(15)	0.0632(5)
O2	0.09430(8)	0.47592(14)	0.40610(14)	0.0472(3)
C1	0.11533(10)	0.41485(18)	0.50395(17)	0.0361(4)
C2	0.18527(9)	0.32919(16)	0.50190(16)	0.0316(3)
C3	0.21587(11)	0.26730(19)	0.61143(17)	0.0410(4)
C4	0.28043(11)	0.18875(19)	0.60978(17)	0.0404(4)
O11	-0.06727(11)	0.27547(15)	0.66423(15)	0.0622(4)
C11	-0.0958(8)	0.2417(10)	0.5638(8)	0.046(3)
N11	-0.1371(5)	0.1393(9)	0.5391(9)	0.0646(13)
C12	-0.1659(10)	0.1088(16)	0.4046(10)	0.106(6)
C13	-0.1574(11)	0.0521(11)	0.6320(12)	0.078(4)
O11A	-0.06727(11)	0.27547(15)	0.66423(15)	0.0622(4)
C11A	-0.0611(18)	0.200(2)	0.585(3)	0.066(3)
N11A	-0.0998(17)	0.0972(17)	0.555(2)	0.081(2)

254

C12A	-0.156(4)	0.048(4)	0.642(4)	0.115(14)
C13A	-0.092(3)	0.026(3)	0.442(3)	0.124(12)
O11B	-0.06727(11)	0.27547(15)	0.66423(15)	0.0622(4)
C11B	-0.0470(6)	0.1839(8)	0.6137(11)	0.066(3)
N11B	-0.0915(8)	0.1027(8)	0.5468(8)	0.081(2)
C12B	-0.1750(8)	0.1410(16)	0.513(2)	0.132(7)
C13B	-0.0655(11)	-0.0159(10)	0.5061(16)	0.127(6)
O11C	-0.06727(11)	0.27547(15)	0.66423(15)	0.0622(4)
C11C	-0.1120(13)	0.2569(13)	0.5731(13)	0.046(3)
N11C	-0.1394(7)	0.1464(12)	0.5364(11)	0.0646(13)
C12C	-0.1993(11)	0.136(2)	0.4243(16)	0.090(6)
C13C	-0.1133(14)	0.0342(13)	0.601(2)	0.109(7)
N21	0.010(2)	0.7282(4)	0.737(3)	0.074(3)
O21	-0.0384(14)	0.6797(12)	0.813(2)	0.073(2)
O22	0.0484(13)	0.6543(12)	0.6798(18)	0.0652(17)
O23	0.0139(15)	0.8415(3)	0.728(2)	0.136(4)

[*] U_{eq} is defined as one third of the trace of the orthogonalized U_{ij} tensor.

Table 10.5 (a) Atomic coordinates and equivalent[*] isotropic atomic displacement parameters ($Å^2$) for Ho-MOF-BDC System.

Atom	sof	Atom	sof	Atom	sof
O11 - C13	0.355(4)	O11A - C13A	0.124(7)		
O11B - C13B	0.273(7)	O11C - C13C	0.249(7)		
N21 - O23	0.50				

Table 10.5 (b) Site occupancy factors that deviate from unity for Ho-MOF-BDC System.

Ho1-O1#1	2.2433(14)	Ho1-O1	2.2434(14)	Ho1-O2#2	2.2913(14)
Ho1-O2#3	2.2913(14)	Ho1-O11C#1	2.3856(15)	Ho1-O11B#1	2.3856(15)
Ho1-O11A#1	2.3856(15)	Ho1-O11#1	2.3856(15)	Ho1-O11	2.3857(15)
O1-C1	1.243(2)	O2-C1	1.243(2)	O2-Ho1#3	2.2913(14)
C1-C2	1.505(2)	C2-C4#4	1.386(2)	C2-C3	1.386(2)
C3-C4	1.386(2)	C4-C2#4	1.386(2)	O11-C11	1.176(6)
C11-N11	1.311(6)	N11-C13	1.423(9)	N11-C12	1.490(8)
N21-O23	1.215(5)	N21-O22	1.222(9)	N21-O21	1.319(13)
O1#1-Ho1-O1	159.38(10)	O1#1-Ho1-O2#2	90.55(5)	O1-Ho1-O2#2	95.82(6)
O1#1-Ho1-O2#3	95.82(6)	O1-Ho1-O2#3	90.55(5)	O2#2-Ho1-O2#3	143.86(8)
O1#1-Ho1-O11C#1	84.74(7)	O1-Ho1-O11C#1	78.47(6)	O2#2-Ho1-O11C#1	72.93(6)
O2#3-Ho1-O11C#1	143.00(6)	O1#1-Ho1-O11B#1	84.74(7)	O1-Ho1-O11B#1	78.47(6)
O2#2-Ho1-O11B#1	72.93(6)	O2#3-Ho1-O11B#1	143.00(6)	O11C#1-Ho1-O11B#1	0.00(9)
O1#1-Ho1-O11A#1	84.74(7)	O1-Ho1-O11A#1	78.47(6)	O2#2-Ho1-O11A#1	72.93(6)
O2#3-Ho1-O11A#1	143.00(6)	O11C#1-Ho1-O11A#1	0.00(9)	O11B#1-Ho1-O11A#1	0.00(9)
O1#1-Ho1-O11#1	84.74(7)	O1-Ho1-O11#1	78.47(6)	O2#2-Ho1-O11#1	72.93(6)
O2#3-Ho1-O11#1	143.00(6)	O11C#1-Ho1-O11#1	0.00(9)	O11B#1-Ho1-O11#1	0.00(9)
O11A#1-Ho1-O11#1	0.00(9)	O1#1-Ho1-O11	78.47(6)	O1-Ho1-O11	84.74(7)
O2#2-Ho1-O11	143.00(6)	O2#3-Ho1-O11	72.93(6)	O11C#1-Ho1-O11	70.96(8)
O11B#1-Ho1-O11	70.96(8)	O11A#1-Ho1-O11	70.96(8)	O11#1-Ho1-O11	70.96(8)
C1-O1-Ho1	163.84(13)	C1-O2-Ho1#3	151.69(14)	O2-C1-O1	125.06(17)
O2-C1-C2	117.75(15)	O1-C1-C2	117.18(16)	C4#4-C2-C3	119.37(15)
C4#4-C2-C1	120.23(15)	C3-C2-C1	120.40(15)	C4-C3-C2	120.46(16)
C3-C4-C2#4	120.17(16)	C11-O11-Ho1	136.8(5)	O11-C11-N11	126.7(8)
C11-N11-C13	125.0(7)	C11-N11-C12	119.2(7)	C13-N11-C12	115.8(7)
O23-N21-O22	124.5(9)	O23-N21-O21	118.8(8)	O22-N21-O21	116.7(4)
N21-O21-Ho1	90.7(10)	N21-O22-Ho1	101.1(11)		
O1#1-Ho1-O1-C1	118.0(6)	O2#2-Ho1-O1-C1	-134.6(6)	O2#3-Ho1-O1-C1	9.8(6)
O11C#1-Ho1-O1-C1	154.2(6)	O11B#1-Ho1-O1-C1	154.2(6)	O11A#1-Ho1-O1-C1	154.2(6)
O11#1-Ho1-O1-C1	154.2(6)	O11-Ho1-O1-C1	82.6(6)	Ho1#3-O2-C1-O1	-51.7(4)
Ho1#3-O2-C1-C2	129.1(2)	Ho1-O1-C1-O2	12.5(8)	Ho1-O1-C1-C2	-168.2(5)
O2-C1-C2-C4#4	-6.0(3)	O1-C1-C2-C4#4	174.8(2)	O2-C1-C2-C3	174.19(19)
O1-C1-C2-C3	-5.1(3)	C4#4-C2-C3-C4	0.4(3)	C1-C2-C3-C4	-179.77(18)
C2-C3-C4-C2#4	-0.4(3)	O1#1-Ho1-O11-C11	135.4(11)	O1-Ho1-O11-C11	-56.6(11)
O2#2-Ho1-O11-C11	-149.3(11)	O2#3-Ho1-O11-C11	35.6(11)	O11C#1-Ho1-O11-C11	-136.2(11)
O11B#1-Ho1-O11-C11	-136.2(11)	O11A#1-Ho1-O11-C11	-136.2(11)	O11#1-Ho1-O11-C11	-136.2(11)
Ho1-O11-C11-N11	-173.4(5)	O11-C11-N11-C13	2.6(14)	O11-C11-N11-C12	-177.4(14)
O23-N21-O21-Ho1	178(4)	O22-N21-O21-Ho1	-1(4)	O1#1-Ho1-O21-N21	177(2)
O1-Ho1-O21-N21	-3(3)	O2#2-Ho1-O21-N21	83(2)	O2#3-Ho1-O21-N21	-83(2)
O11C#1-Ho1-O21-N21	112(2)	O11B#1-Ho1-O21-N21	112(2)	O11A#1-Ho1-O21-N21	112(2)
O11#1-Ho1-O21-N21	112(2)	O11-Ho1-O21-N21	-125(2)	O23-N21-O22-Ho1	-178(4)
O21-N21-O22-Ho1	1(4)	O1#1-Ho1-O22-N21	-5(3)	O1-Ho1-O22-N21	176(2)
O2#2-Ho1-O22-N21	-82(2)	O2#3-Ho1-O22-N21	80(2)	O11C#1-Ho1-O22-N21	-129(2)
O11B#1-Ho1-O22-N21	-129(2)	O11A#1-Ho1-O22-N21	-129(2)	O11#1-Ho1-O22-N21	-129(2)
O11-Ho1-O22-N21	119(2)				

Symmetry transformation codes:#1 -x,y,-z+3/2   #2 x,-y+1,z+1/2   #3 -x,-y+1,-z+1   #4 -x+1/2,-y+1/2,-z+1

Table 10.5 (c) Bond lengths (Å), valence and torsion angles (°) for Ho-MOF-BDC System.

10.6 Detailed Information for Ce-MOF-BTC System from Single Crystal Analysis

Atom	x/a	y/b	z/c	U_{eq}
Ce1	0.62480(2)	0.50015(4)	0.119748(19)	0.01129(7)
C1A	0.7595(5)	0.2405(5)	0.2500	0.018(2)
C2A	0.7691(5)	0.1829(5)	0.3281(5)	0.0212(16)
C3A	0.8365(5)	0.1191(6)	0.3291(4)	0.0186(15)
C4A	0.8917(5)	0.1083(5)	0.2500	0.015(2)
C5A	0.6892(5)	0.3108(5)	0.2500	0.017(2)
O1A	0.7022(4)	0.3784(4)	0.1979(3)	0.0231(12)
C6A	0.8512(5)	0.0630(5)	0.4188(5)	0.0192(16)
O2A	0.7997(4)	0.0758(4)	0.4898(3)	0.0253(11)
O3A	0.9153(3)	0.0085(4)	0.4229(3)	0.0188(11)
C1B	0.7623(5)	0.7623(5)	0.0000	0.017(2)
C2B	0.8018(5)	0.7902(5)	0.0864(5)	0.0205(16)
C3B	0.8672(5)	0.8551(5)	0.0869(4)	0.0179(15)
C4B	0.8949(5)	0.8949(5)	0.0000	0.019(2)
C5B	0.6913(5)	0.6913(5)	0.0000	0.018(2)
O1B	0.6782(4)	0.6499(4)	0.0780(3)	0.0235(13)
C6B	0.9103(5)	0.8825(6)	0.1789(5)	0.0198(15)
O2B	0.9913(4)	0.9103(3)	0.1781(3)	0.0183(11)
O3B	0.8682(4)	0.8728(4)	0.2567(3)	0.0229(13)
O1C	-0.0817(5)	0.6058(5)	1.0214(5)	0.0482(19)
C1C	-0.0143(7)	0.5737(6)	0.9850(7)	0.043(2)
N1C	0.0636(6)	0.6142(7)	0.9783(6)	0.051(2)
C2C	0.0738(9)	0.7043(9)	1.0184(11)	0.080(4)
C3C	0.1391(9)	0.5699(10)	0.9304(13)	0.114(7)
O1W	0.7746(4)	0.4934(5)	0.0437(4)	0.0269(13)
O2W	0.8760(5)	0.6129(5)	0.2204(5)	0.0424(17)

[*] U_{eq} is defined as one third of the trace of the orthogonalized U_{ij} tensor.

Table 10.6 (a) Atomic coordinates and equivalent[*] isotropic atomic displacement parameters (Å^2) for Ce-MOF-BTC System.

Ce1-O1A	2.426(5)	Ce1-O1B	2.457(5)	Ce1-O3A#1	2.487(5)
Ce1-O1W	2.489(5)	Ce1-O2B#2	2.505(5)	Ce1-O3B#3	2.532(5)
Ce1-O2A#4	2.532(5)	Ce1-O2B#3	2.726(4)	Ce1-O3A#4	2.955(4)
C1A-C2A	1.398(9)	C1A-C2A#5	1.398(9)	C1A-C5A	1.494(15)
C2A-C3A	1.394(11)	C3A-C4A	1.389(8)	C3A-C6A	1.523(9)
C4A-C3A#5	1.389(8)	C5A-O1A#5	1.263(7)	C5A-O1A	1.263(7)
C6A-O3A	1.264(9)	C6A-O2A	1.271(8)	O2A-Ce1#6	2.532(5)
O3A-Ce1#7	2.487(5)	O3A-Ce1#6	2.954(4)	C1B-C2B#8	1.406(9)
C1B-C2B	1.406(9)	C1B-C5B	1.509(15)	C2B-C3B	1.384(10)
C3B-C4B	1.413(8)	C3B-C6B	1.493(9)	C4B-C3B#8	1.413(8)
C5B-O1B	1.268(7)	C5B-O1B#8	1.268(7)	C6B-O3B	1.263(8)
C6B-O2B	1.286(9)	C6B-Ce1#9	2.985(7)	O2B-Ce1#10	2.505(5)
O2B-Ce1#9	2.726(4)	O3B-Ce1#9	2.532(5)	O1C-C1C	1.231(11)
C1C-N1C	1.322(13)	N1C-C2C	1.472(14)	N1C-C3C	1.474(15)
O1W-H11W	0.83(3)	O2W-H21W	0.82(3)	O2W-H22W	0.82(3)
O1A-Ce1-O1B	129.77(19)	O1A-Ce1-O3A#1	82.30(17)	O1B-Ce1-O3A#1	143.38(18)
O1A-Ce1-O1W	74.16(19)	O1B-Ce1-O1W	69.0(2)	O3A#1-Ce1-O1W	146.5(2)
O1A-Ce1-O2B#2	155.26(17)	O1B-Ce1-O2B#2	72.96(17)	O3A#1-Ce1-O2B#2	73.13(15)
O1W-Ce1-O2B#2	129.21(18)	O1A-Ce1-O3B#3	71.50(16)	O1B-Ce1-O3B#3	124.34(16)
O3A#1-Ce1-O3B#3	78.20(17)	O1W-Ce1-O3B#3	72.0(2)	O2B#2-Ce1-O3B#3	105.43(17)
O1A-Ce1-O2A#4	77.06(19)	O1B-Ce1-O2A#4	68.06(17)	O3A#1-Ce1-O2A#4	111.14(15)
O1W-Ce1-O2A#4	86.70(18)	O2B#2-Ce1-O2A#4	108.88(19)	O3B#3-Ce1-O2A#4	145.7(2)
O1A-Ce1-O2B#3	119.73(16)	O1B-Ce1-O2B#3	82.86(16)	O3A#1-Ce1-O2B#3	96.37(15)
O1W-Ce1-O2B#3	75.86(16)	O2B#2-Ce1-O2B#3	67.09(16)	O3B#3-Ce1-O2B#3	49.81(16)
O2A#4-Ce1-O2B#3	150.04(16)	O1A-Ce1-O3A#4	71.96(15)	O1B-Ce1-O3A#4	105.02(16)
O3A#1-Ce1-O3A#4	64.32(17)	O1W-Ce1-O3A#4	127.02(16)	O2B#2-Ce1-O3A#4	94.27(14)
O3B#3-Ce1-O3A#4	130.16(16)	O2A#4-Ce1-O3A#4	46.82(14)	O2B#3-Ce1-O3A#4	157.10(12)
C2A-C1A-C2A#5	118.6(10)	C2A-C1A-C5A	120.7(5)	C2A#5-C1A-C5A	120.7(5)
C3A-C2A-C1A	120.5(7)	C4A-C3A-C2A	120.4(7)	C4A-C3A-C6A	120.0(7)
C2A-C3A-C6A	119.6(6)	C3A#5-C4A-C3A	119.4(10)	O1A#5-C5A-O1A	125.5(10)
O1A#5-C5A-C1A	117.3(5)	O1A-C5A-C1A	117.3(5)	C5A-O1A-Ce1	142.1(6)
O3A-C6A-O2A	121.7(6)	O3A-C6A-C3A	120.4(6)	O2A-C6A-C3A	117.8(7)
C2B#8-C1B-C2B	118.8(10)	C2B#8-C1B-C5B	120.6(5)	C2B-C1B-C5B	120.6(5)
C3B-C2B-C1B	120.9(7)	C2B-C3B-C4B	120.1(7)	C2B-C3B-C6B	120.4(6)
C4B-C3B-C6B	119.5(7)	C3B#8-C4B-C3B	119.0(10)	O1B-C5B-O1B#8	125.6(10)
O1B-C5B-C1B	117.2(5)	O1B#8-C5B-C1B	117.2(5)	O3B-C6B-O2B	121.2(6)
O3B-C6B-C3B	119.3(7)	O2B-C6B-C3B	119.4(6)	O1C-C1C-N1C	125.2(9)
C1C-N1C-C2C	119.2(9)	C1C-N1C-C3C	120.3(10)	C2C-N1C-C3C	120.4(10)
Ce1-O1W-H11W	112(4)	H21W-O2W-H22W	113(4)		
C2A#5-C1A-C2A-C3A	1.9(5)	C5A-C1A-C2A-C3A	-178.1(5)	C1A-C2A-C3A-C4A	-3.8(11)
C1A-C2A-C3A-C6A	174.3(6)	C2A-C3A-C4A-C3A#5	1.9(6)	C6A-C3A-C4A-C3A#5	-176.2(8)
C2A-C1A-C5A-O1A#5	-24.7(5)	C2A#5-C1A-C5A-O1A#5	155.3(5)	C2A-C1A-C5A-O1A	155.3(5)
C2A#5-C1A-C5A-O1A	-24.7(5)	C4A-C3A-C6A-O3A	2.3(11)	C2A-C3A-C6A-O3A	-175.8(7)
C4A-C3A-C6A-O2A	179.3(6)	C2A-C3A-C6A-O2A	1.2(12)	C2B#8-C1B-C2B-C3B	-0.2(6)
C5B-C1B-C2B-C3B	179.8(6)	C1B-C2B-C3B-C4B	0.4(12)	C1B-C2B-C3B-C6B	-178.5(6)
C2B-C3B-C4B-C3B#8	-0.2(6)	C6B-C3B-C4B-C3B#8	178.7(8)	C2B#8-C1B-C5B-O1B	170.4(5)
C2B-C1B-C5B-O1B	-9.6(5)	C2B#8-C1B-C5B-O1B#8	-9.6(5)	C2B-C1B-C5B-O1B#8	170.4(5)
O1B#8-C5B-O1B-Ce1	28.4(4)	C1B-C5B-O1B-Ce1	-151.6(4)	C2B-C3B-C6B-O3B	-25.7(12)
C4B-C3B-C6B-O3B	155.5(7)	C2B-C3B-C6B-O2B	150.1(8)	C4B-C3B-C6B-O2B	-28.7(11)
O1C-C1C-N1C-C2C	1.4(17)	O1C-C1C-N1C-C3C	-178.2(12)		

Symmetry transformation codes:#1 -y+1/2,x-1/2,z-1/4   #2 x-1/2,-y+3/2,-z+1/4   #3 -y+3/2,x-1/2,z-1/4   #4 -x+3/2,y+1/2,-z+3/4   #5 -y+1,-x+1,-z+1/2   #6 -x+3/2,y-1/2,-z+3/4   #7 y+1/2,-x+1/2,z+1/4   #8 y,x,-z   #9 y+1/2,-x+3/2,z+1/4   #10 x+1/2,-y+3/2,-z+1/4

Table 10.6 (b) Bond lengths (Å), valence and torsion angles (°) for Ce-MOF-BTC System.

D—H···A*	d(D—H)	d(H···A)	d(D···A)	∠(DHA)
O1W—H11W···O1C#11	0.83(3)	2.04(3)	2.758(9)	144(5)
O2W—H21W···O1W#9	0.82(3)	2.01(3)	2.648(9)	134(5)
O2W—H22W···O2A#4	0.82(3)	1.99(3)	2.753(9)	154(7)

* D - donor atom, H - hydrogen, A - acceptor.
Symmetry transformation codes: #1 -y+1/2,x-1/2,z-1/4   #2 x-1/2,-y+3/2,-z+1/4   #3 -y+3/2,x-1/2,z-1/4   #4 -x+3/2,y+1/2,-z+3/4   #5 -y+1,-x+1,-z+1/2   #6 -x+3/2,y-1/2,-z+3/4   #7 y+1/2,-x+1/2,z+1/4   #8 y,x,-z   #9 y+1/2,-x+3/2,z+1/4   #10 x+1/2,-y+3/2,-z+1/4   #11 x+1,y,z-1

Table 10.6 (c) Hydrogen bond (Å and °) information for Ce-MOF-BTC System.

10.7 Detailed Information for Ho-MOF-BTC System from Single Crystal Analysis

Atom	x/a	y/b	z/c	U_{eq}
Ho1	0.149212(13)	0.149212(13)	0.3750	0.01102(6)
O1	0.0716(3)	0.3366(3)	0.44171(19)	0.0332(7)
C1	0.0000	0.3907(5)	0.5000	0.0215(10)
C2	0.0000	0.5378(5)	0.5000	0.0178(10)
C3	0.0433(4)	0.6052(3)	0.4228(2)	0.0187(7)
H3	0.0727	0.5593	0.3707	0.022
C4	0.0432(4)	0.7406(3)	0.4225(2)	0.0158(6)
C5	0.0000	0.8075(5)	0.5000	0.0184(10)
H5	0.0000	0.8990	0.5000	0.022
C6	0.0866(3)	0.8170(3)	0.3398(2)	0.0188(7)
O2	0.0938(3)	0.7591(3)	0.26391(17)	0.0316(7)
O3	0.1122(3)	0.9328(3)	0.3501(2)	0.0389(8)
O1W	0.3131(3)	0.3131(3)	0.3750	0.074(2)
H1W	0.384(4)	0.314(4)	0.346(5)	0.088
O2W	0.564(3)	0.302(3)	0.445(2)	0.062(8)
O3W	0.659(5)	0.535(4)	0.494(3)	0.069(12)
O1S	0.7578(18)	0.5280(19)	0.3110(13)	0.067(4)
N1S	0.815(3)	0.408(3)	0.2707(17)	0.076(5)

C1S	0.842(4)	0.5000	0.2500	0.070(5)
C2S	0.725(4)	0.665(4)	0.319(3)	0.059(7)
C3S	0.746(4)	0.444(4)	0.373(4)	0.058(6)
C4S	0.709(6)	0.502(6)	0.475(4)	0.063(8)
C5S	0.685(4)	0.466(5)	0.438(3)	0.055(7)

* U_{eq} is defined as one third of the trace of the orthogonalized U_{ij} tensor.

Table 10.7 (a) Atomic coordinates and equivalent* isotropic atomic displacement parameters (Å^2) for Ho-MOF-BTC System.

Atom	sof	Atom	sof	Atom	sof
O2W	0.13	O3W	0.12	O1S	0.25
N1S	0.25	C1S	0.30	C2S	0.15
C3S	0.15	C4S	0.15	C5S	0.15

Table 10.7 (b) Site occupancy factors that deviate from unity for Ho-MOF-BTC System.

D—H⋯A*	d(D—H)	d(H⋯A)	d(D⋯A)	∠(DHA)
O1W—H1W⋯O3W#7	0.838(10)	2.16(5)	2.98(5)	165(8)
O1W—H1W⋯O2W	0.838(10)	2.34(8)	2.77(3)	112(6)

* D - donor atom, H - hydrogen, A - acceptor.
Symmetry transformation codes:
#1 y-1,x,-z+3/4   #2 x,y-1,z   #3 x,-y+1,-z+1/2   #4 -y+1,x,z+1/4   #5 y,x,-z+3/4   #6 -x,y,-z+1   #7 y,-x+1,z-1/4
#8 x,y+1,z

Table 10.7 (c) Hydrogen bond (Å and °) information for Ho-MOF-BTC System.

Ho1-O3#1	2.284(3)	Ho1-O3#2	2.284(3)	Ho1-O2#3	2.293(2)
Ho1-O2#4	2.293(2)	Ho1-O1	2.297(3)	Ho1-O1#5	2.297(3)
Ho1-O1W	2.381(5)	O1-C1	1.250(3)	C1-O1#6	1.250(3)
C1-C2	1.512(7)	C2-C3	1.388(4)	C2-C3#6	1.388(4)
C3-C4	1.392(5)	C4-C5	1.389(4)	C4-C6	1.500(4)
C5-C4#6	1.389(4)	C6-O3	1.228(4)	C6-O2	1.251(4)
O2-Ho1#7	2.293(2)	O3-Ho1#8	2.284(3)	O1W-H1W	0.838(10)
O3#1-Ho1-O3#2	72.57(17)	O3#1-Ho1-O2#3	88.02(12)	O3#2-Ho1-O2#3	102.69(12)
O3#1-Ho1-O2#4	102.69(12)	O3#2-Ho1-O2#4	88.02(12)	O2#3-Ho1-O2#4	166.81(17)
O3#1-Ho1-O1	74.66(12)	O3#2-Ho1-O1	145.53(11)	O2#3-Ho1-O1	86.48(10)
O2#4-Ho1-O1	88.94(11)	O3#1-Ho1-O1#5	145.53(11)	O3#2-Ho1-O1#5	74.66(12)
O2#3-Ho1-O1#5	88.94(11)	O2#4-Ho1-O1#5	86.48(10)	O1-Ho1-O1#5	139.35(16)
O3#1-Ho1-O1W	143.71(8)	O3#2-Ho1-O1W	143.71(9)	O2#3-Ho1-O1W	83.40(8)
O2#4-Ho1-O1W	83.40(8)	O1-Ho1-O1W	69.68(8)	O1#5-Ho1-O1W	69.68(8)
C1-O1-Ho1	149.4(3)	O1-C1-O1#6	127.2(5)	O1-C1-C2	116.4(2)
O1#6-C1-C2	116.4(2)	C3-C2-C3#6	120.2(5)	C3-C2-C1	119.9(2)
C3#6-C2-C1	119.9(2)	C2-C3-C4	120.1(3)	C5-C4-C3	119.5(3)
C5-C4-C6	118.8(3)	C3-C4-C6	121.7(3)	C4-C5-C4#6	120.7(5)
O3-C6-O2	123.7(3)	O3-C6-C4	118.3(3)	O2-C6-C4	118.1(3)
C6-O2-Ho1#7	126.2(3)	C6-O3-Ho1#8	176.6(3)	Ho1-O1W-H1W	128.5(14)
O3#1-Ho1-O1-C1	39.6(5)	O3#2-Ho1-O1-C1	21.1(6)	O2#3-Ho1-O1-C1	128.6(5)
O2#4-Ho1-O1-C1	-63.8(5)	O1#5-Ho1-O1-C1	-147.2(5)	O1W-Ho1-O1-C1	-147.2(5)
Ho1-O1-C1-O1#6	1.7(4)	Ho1-O1-C1-C2	-178.3(4)	O1-C1-C2-C3	19.4(3)
O1#6-C1-C2-C3	-160.6(3)	O1-C1-C2-C3#6	-160.6(3)	O1#6-C1-C2-C3#6	19.4(3)
C3#6-C2-C3-C4	-0.1(3)	C1-C2-C3-C4	179.9(3)	C2-C3-C4-C5	0.3(5)
C2-C3-C4-C6	-178.8(3)	C3-C4-C5-C4#6	-0.1(3)	C6-C4-C5-C4#6	178.9(4)
C5-C4-C6-O3	17.1(5)	C3-C4-C6-O3	-163.9(4)	C5-C4-C6-O2	-162.3(3)
C3-C4-C6-O2	16.7(6)	O3-C6-O2-Ho1#7	-1.9(6)	C4-C6-O2-Ho1#7	177.5(2)

Symmetry transformation codes:

#1 y-1,x,-z+3/4   #2 x,y-1,z   #3 x,-y+1,-z+1/2   #4 -y+1,x,z+1/4   #5 y,x,-z+3/4   #6 -x,y,-z+1   #7 y,-x+1,z-1/4   #8 x,y+1,z

Table 10.7 (d) Bond lengths (Å) and angles (°) for Ho-MOF-BTC System.

10.8 Detailed Information for Ho-MOF-PDC System from Single Crystal Analysis

Atom	x/a	y/b	z/c	U_{eq}
Ho1	0.523532(19)	0.417432(6)	0.199786(11)	0.02242(6)
O1	0.5813(4)	0.39404(13)	0.06057(19)	0.0446(8)
C1	0.5541(5)	0.41000(19)	-0.0101(3)	0.0387(10)
N1	0.529(2)	0.3856(3)	-0.0761(5)	0.056(3)
C2	0.537(3)	0.3337(4)	-0.0794(11)	0.144(10)
C3	0.501(4)	0.4126(4)	-0.1542(4)	0.078(4)
N1A	0.493(4)	0.3877(4)	-0.0737(4)	0.056(3)
C2A	0.431(4)	0.3413(4)	-0.0487(4)	0.144(10)
C3A	0.505(6)	0.4007(10)	-0.1629(9)	0.078(4)

C11	0.3321(5)	0.33930(14)	0.2660(3)	0.0277(8)
O11	0.4362(4)	0.33964(11)	0.2102(2)	0.0380(7)
O12	0.2691(3)	0.37720(10)	0.29213(19)	0.0304(6)
C12	0.3333(7)	0.2500	0.2662(4)	0.0300(12)
C13	0.2883(4)	0.29254(14)	0.3032(3)	0.0271(8)
C14	0.2058(5)	0.29063(15)	0.3780(3)	0.0330(9)
N15	0.1645(7)	0.2500	0.4161(3)	0.0380(12)
C21	0.3258(5)	0.49267(15)	0.3239(3)	0.0302(9)
O21	0.4061(4)	0.48248(11)	0.2612(2)	0.0423(8)
O22	0.1908(4)	0.47731(11)	0.3400(2)	0.0412(8)
C22	0.3300(5)	0.57458(15)	0.6047(2)	0.0276(8)
O23	0.1869(3)	0.56550(12)	0.61358(19)	0.0383(7)
O24	0.4203(4)	0.59004(14)	0.65985(19)	0.0432(8)
C23	0.3241(4)	0.53630(14)	0.4619(2)	0.0253(8)
C24	0.3966(4)	0.52644(14)	0.3860(3)	0.0271(8)
C25	0.5426(5)	0.54712(18)	0.3712(3)	0.0384(10)
N26	0.6170(5)	0.57559(17)	0.4250(3)	0.0481(11)
C27	0.5458(5)	0.58357(18)	0.4984(3)	0.0389(10)
C28	0.3991(4)	0.56517(15)	0.5201(2)	0.0271(8)

[*] U_{eq} is defined as one third of the trace of the orthogonalized U_{ij} tensor.

Table 10.8 (a) Atomic coordinates and equivalent[*] isotropic atomic displacement parameters ($Å^2$) for Ho-MOF-PDC System.

Atom	sof	Atom	sof	Atom	sof
N1 – C3	0.589(17)	N1A – C3A	0.411(17)		

Table 10.8 (b) Site occupancy factors that deviate from unity for Ho-MOF-PDC System.

Ho1-O22#1	2.292(3)	Ho1-O21	2.300(3)	Ho1-O24#2	2.301(3)
Ho1-O23#3	2.309(3)	Ho1-O11	2.312(3)	Ho1-O1	2.369(3)
Ho1-O12#1	2.378(3)	Ho1-O12	2.852(3)	O1-C1	1.236(5)
C1-N1	1.274(10)	N1-C2	1.461(9)	N1-C3	1.478(12)
C11-O11	1.257(5)	C11-O12	1.262(5)	C11-C13	1.488(6)
O12-Ho1#4	2.378(3)	C12-C13#5	1.386(5)	C12-C13	1.386(5)
C13-C14	1.385(6)	C14-N15	1.340(5)	N15-C14#5	1.340(5)
C21-O21	1.245(5)	C21-O22	1.254(5)	C21-C24	1.498(6)
O22-Ho1#4	2.292(3)	C22-O24	1.247(5)	C22-O23	1.251(5)
C22-C28	1.495(5)	O23-Ho1#6	2.308(3)	O24-Ho1#2	2.301(3)
C23-C28	1.388(6)	C23-C24	1.388(5)	C24-C25	1.391(6)
C25-N26	1.332(6)	N26-C27	1.338(6)	C27-C28	1.395(6)
O22#1-Ho1-O21	78.81(12)	O22#1-Ho1-O24#2	102.02(13)	O21-Ho1-O24#2	75.35(13)
O22#1-Ho1-O23#3	99.43(12)	O21-Ho1-O23#3	75.69(12)	O24#2-Ho1-O23#3	139.52(11)
O22#1-Ho1-O11	155.75(11)	O21-Ho1-O11	125.40(11)	O24#2-Ho1-O11	84.88(12)
O23#3-Ho1-O11	89.40(12)	O22#1-Ho1-O1	79.28(13)	O21-Ho1-O1	135.23(12)
O24#2-Ho1-O1	147.72(12)	O23#3-Ho1-O1	70.06(11)	O11-Ho1-O1	82.67(12)
O22#1-Ho1-O12#1	79.50(11)	O21-Ho1-O12#1	137.30(11)	O24#2-Ho1-O12#1	73.84(11)
O23#3-Ho1-O12#1	144.30(11)	O11-Ho1-O12#1	80.22(10)	O1-Ho1-O12#1	74.76(11)
O22#1-Ho1-O12	154.81(10)	O21-Ho1-O12	76.37(10)	O24#2-Ho1-O12	67.54(10)
O23#3-Ho1-O12	78.57(10)	O11-Ho1-O12	49.10(9)	O1-Ho1-O12	122.20(11)
O12#1-Ho1-O12	116.79(9)	C1-O1-Ho1	135.8(3)	O1-C1-N1	126.3(6)
C1-N1-C2	123.9(8)	C1-N1-C3	116.7(10)	C2-N1-C3	119.2(10)
O11-C11-O12	121.8(4)	O11-C11-C13	117.8(4)	O12-C11-C13	120.4(4)
C11-O11-Ho1	106.5(3)	C11-O12-Ho1#4	142.3(3)	C11-O12-Ho1	80.8(2)
Ho1#4-O12-Ho1	120.45(11)	C13#5-C12-C13	118.9(5)	C14-C13-C12	118.3(4)
C14-C13-C11	120.3(4)	C12-C13-C11	121.4(4)	N15-C14-C13	123.9(4)
C14-N15-C14#5	116.7(5)	O21-C21-O22	126.1(4)	O21-C21-C24	117.1(4)
O22-C21-C24	116.7(4)	C21-O21-Ho1	139.7(3)	C21-O22-Ho1#4	139.8(3)
O24-C22-O23	126.1(4)	O24-C22-C28	117.2(4)	O23-C22-C28	116.7(4)
C22-O23-Ho1#6	141.2(3)	C22-O24-Ho1#2	141.7(3)	C28-C23-C24	119.8(4)
C23-C24-C25	117.5(4)	C23-C24-C21	121.7(4)	C25-C24-C21	120.7(4)
N26-C25-C24	124.4(4)	C25-N26-C27	116.7(4)	N26-C27-C28	124.1(4)
C23-C28-C27	117.4(4)	C23-C28-C22	121.8(4)	C27-C28-C22	120.7(4)

Symmetry transformation codes:#1 x+1/2,y,-z+1/2 #2 -x+1,-y+1,-z+1 #3 -x+1/2,-y+1,z-1/2 #4 x-1/2,y,-z+1/2 #5 x,-y+1/2,z #6 -x+1/2,-y+1,z+1/2

Table 10.8 (c) Bond lengths (Å) and angles (°) for Ho-MOF-PDC System.

10.9 Detailed Information for Ho-MOF-NDC-1 System from Single Crystal Analysis

Atom	x/a	y/b	z/c	U_{eq}
Ho1	0.250772(9)	0.356060(19)	0.219819(10)	0.01916(4)
Ho2	0.250272(9)	0.267502(19)	0.470344(9)	0.01874(4)
O11	0.16352(15)	0.3724(4)	0.26400(16)	0.0323(8)
O12	0.17402(13)	0.3040(4)	0.37839(17)	0.0346(8)
C13	0.14524(19)	0.3630(5)	0.3228(2)	0.0242(9)
C14	0.08532(19)	0.4250(5)	0.3266(2)	0.0230(9)

C15	0.0592(2)	0.5354(5)	0.2775(2)	0.0295(10)
C16	0.0064(2)	0.5980(6)	0.2841(2)	0.0312(10)
C17	0.0563(2)	0.3774(5)	0.3792(2)	0.0255(9)
C18	-0.00007(18)	0.4355(5)	0.3851(2)	0.0222(9)
O21	-0.20129(14)	0.6769(4)	0.35207(17)	0.0326(7)
O22	-0.17596(14)	0.6498(4)	0.47049(17)	0.0331(8)
C23	-0.1669(2)	0.6354(5)	0.4081(2)	0.0240(9)
C24	-0.10891(19)	0.5655(5)	0.3992(2)	0.0224(9)
C25	-0.0845(2)	0.4504(5)	0.4454(2)	0.0282(10)
C26	-0.0316(2)	0.3865(5)	0.4381(2)	0.0303(10)
C27	-0.07994(19)	0.6135(5)	0.3464(2)	0.0243(9)
C28	-0.02511(18)	0.5517(5)	0.3381(2)	0.0231(8)
O31	0.32255(14)	0.1497(4)	0.65251(16)	0.0307(7)
O32	0.33827(14)	0.2055(4)	0.54397(16)	0.0327(7)
C33	0.35464(19)	0.1554(5)	0.6059(2)	0.0228(9)
C34	0.41808(19)	0.1000(5)	0.6261(2)	0.0239(9)
C35	0.4350(2)	0.0138(5)	0.6891(2)	0.0305(10)
C36	0.4917(2)	-0.0414(6)	0.7073(3)	0.0352(11)
C37	0.4589(2)	0.1305(5)	0.5844(2)	0.0285(10)
C38	0.51866(19)	0.0775(5)	0.6030(2)	0.0273(10)
O41	0.71876(13)	-0.1417(3)	0.72027(16)	0.0252(7)
O42	0.72658(13)	-0.0894(3)	0.60661(16)	0.0282(7)
C43	0.6974(2)	-0.0934(5)	0.6576(2)	0.0247(9)
C44	0.6357(2)	-0.0315(5)	0.6407(2)	0.0258(9)
C45	0.6183(2)	0.0558(6)	0.5789(3)	0.0354(11)
C46	0.5615(2)	0.1105(6)	0.5604(3)	0.0361(11)
C47	0.5946(2)	-0.0644(5)	0.6826(2)	0.0275(10)
C48	0.5350(2)	-0.0104(5)	0.6653(2)	0.0268(10)
O51	0.33945(14)	0.4123(4)	0.29959(16)	0.0320(8)
O52	0.30428(14)	0.3949(4)	0.39991(17)	0.0327(7)
C53	0.34583(19)	0.4141(5)	0.3663(2)	0.0258(9)
C54	0.40857(19)	0.4393(5)	0.4082(2)	0.0266(10)
C55	0.4576(2)	0.4184(6)	0.3740(2)	0.0341(11)
C56	0.5145(2)	0.4423(6)	0.4105(2)	0.0370(12)
C57	0.4166(2)	0.4818(5)	0.4781(2)	0.0288(10)
C58	0.47535(19)	0.5103(5)	0.5175(2)	0.0266(9)

264

O61	0.19546(15)	0.0172(4)	0.62194(16)	0.0337(8)
O62	0.21275(13)	0.0580(3)	0.51140(16)	0.0279(7)
C63	0.17899(19)	0.0293(5)	0.5551(2)	0.0239(9)
C64	0.11328(19)	0.0104(5)	0.5244(2)	0.0248(9)
C65	0.0947(2)	-0.0151(6)	0.4499(2)	0.0352(11)
C66	0.0355(2)	-0.0293(6)	0.4203(2)	0.0367(11)
C67	0.0708(2)	0.0240(5)	0.5667(2)	0.0277(10)
C68	0.0090(2)	0.0138(5)	0.5375(2)	0.0254(9)
O71	0.24686(17)	0.5970(4)	0.25728(19)	0.0436(8)
C72	0.2113(3)	0.6998(6)	0.2481(3)	0.0423(13)
N73	0.1940(2)	0.7772(5)	0.2991(2)	0.0422(11)
C74	0.2144(3)	0.7369(7)	0.3741(3)	0.0587(17)
C75	0.1534(3)	0.9002(8)	0.2835(3)	0.0617(19)
O81	0.27966(17)	0.4932(4)	0.5295(2)	0.0484(10)
C82	0.2994(2)	0.5253(6)	0.5936(3)	0.0393(12)
N83	0.3187(2)	0.6573(4)	0.6160(2)	0.0374(10)
C84	0.3201(4)	0.7757(7)	0.5658(3)	0.073(2)
C85	0.3429(3)	0.6865(7)	0.6911(3)	0.0540(15)

---

[*] U_{eq} is defined as one third of the trace of the orthogonalized U_{ij} tensor.

Table 10.9 (a) Atomic coordinates and equivalent[*] isotropic atomic displacement parameters ($Å^2$) for Ho-MOF-NDC-1 System.

Ho1-O31#1	2.260(3)	Ho1-O21#2	2.278(3)
Ho1-O41#3	2.294(3)	Ho1-O11	2.306(3)
Ho1-O71	2.308(3)	Ho1-O61#1	2.338(3)
Ho1-O51	2.339(3)	Ho2-O12	2.240(3)
Ho2-O62	2.283(3)	Ho2-O32	2.285(3)
Ho2-O52	2.295(3)	Ho2-O42#3	2.306(3)
Ho2-O22#4	2.328(3)	Ho2-O81	2.371(4)
O11-C13	1.265(5)	O12-C13	1.251(5)
C13-C14	1.492(6)	C14-C17	1.368(6)
C14-C15	1.419(6)	C15-C16	1.358(6)
C16-C28	1.423(6)	C17-C18	1.414(6)
C18-C26	1.415(6)	C18-C28	1.428(6)
O21-C23	1.252(5)	O21-Ho1#5	2.278(3)
O22-C23	1.246(5)	O22-Ho2#4	2.328(3)
C23-C24	1.505(6)	C24-C27	1.371(6)
C24-C25	1.409(6)	C25-C26	1.369(6)
C27-C28	1.407(6)	O31-C33	1.251(5)
O31-Ho1#6	2.260(3)	O32-C33	1.248(5)
C33-C34	1.510(6)	C34-C37	1.360(6)
C34-C35	1.419(6)	C35-C36	1.369(6)
C36-C48	1.410(6)	C37-C38	1.424(6)
C38-C46	1.413(6)	C38-C48	1.416(6)
O41-C43	1.273(5)	O41-Ho1#3	2.294(3)
O42-C43	1.274(5)	O42-Ho2#3	2.306(3)
C43-C44	1.492(6)	C44-C47	1.372(6)
C44-C45	1.407(6)	C45-C46	1.368(6)
C47-C48	1.423(6)	O51-C53	1.245(5)
O52-C53	1.251(5)	C53-C54	1.515(6)
C54-C57	1.359(6)	C54-C55	1.409(6)
C55-C56	1.366(6)	C56-C58#7	1.408(6)
C57-C58	1.428(6)	C58-C56#7	1.408(6)
C58-C58#7	1.422(8)	O61-C63	1.256(5)
O61-Ho1#6	2.338(3)	O62-C63	1.262(5)
C63-C64	1.510(6)	C64-C67	1.376(6)
C64-C65	1.415(6)	C65-C66	1.363(7)
C66-C68#8	1.414(6)	C67-C68	1.416(6)
C68-C66#8	1.415(6)	C68-C68#8	1.424(8)
O71-C72	1.227(6)	C72-N73	1.315(7)
N73-C75	1.446(7)	N73-C74	1.455(7)
O81-C82	1.248(6)	C82-N83	1.319(6)
N83-C85	1.450(6)	N83-C84	1.441(7)
O31#1-Ho1-O21#2	88.56(11)	O31#1-Ho1-O41#3	94.38(11)
O21#2-Ho1-O41#3	76.05(11)	O31#1-Ho1-O11	167.07(11)
O21#2-Ho1-O11	84.27(12)	O41#3-Ho1-O11	94.32(11)
O31#1-Ho1-O71	105.69(13)	O21#2-Ho1-O71	144.84(12)
O41#3-Ho1-O71	132.70(12)	O11-Ho1-O71	74.97(13)
O31#1-Ho1-O61#1	84.39(12)	O21#2-Ho1-O61#1	75.30(12)
O41#3-Ho1-O61#1	151.34(11)	O11-Ho1-O61#1	83.38(12)
O71-Ho1-O61#1	74.38(12)	O31#1-Ho1-O51	74.95(11)
O21#2-Ho1-O51	144.21(12)	O41#3-Ho1-O51	73.88(12)
O11-Ho1-O51	116.76(11)	O71-Ho1-O51	70.92(13)
O61#1-Ho1-O51	132.42(12)	O12-Ho2-O62	95.91(12)
O12-Ho2-O32	166.58(11)	O62-Ho2-O32	85.92(11)
O12-Ho2-O52	84.00(12)	O62-Ho2-O52	153.66(11)
O32-Ho2-O52	88.48(11)	O12-Ho2-O42#3	81.30(11)
O62-Ho2-O42#3	77.12(11)	O32-Ho2-O42#3	86.18(11)
O52-Ho2-O42#3	76.83(11)	O12-Ho2-O22#4	78.42(11)
O62-Ho2-O22#4	75.52(12)	O32-Ho2-O22#4	114.83(11)
O52-Ho2-O22#4	129.69(12)	O42#3-Ho2-O22#4	143.79(12)
O12-Ho2-O81	110.35(14)	O62-Ho2-O81	130.52(12)
O32-Ho2-O81	77.77(14)	O52-Ho2-O81	72.84(13)
O42#3-Ho2-O81	145.84(12)	O22#4-Ho2-O81	70.06(13)
C13-O11-Ho1	140.2(3)	C13-O12-Ho2	157.5(3)
O12-C13-O11	124.3(4)	O12-C13-C14	117.3(4)
O11-C13-C14	118.4(4)	C17-C14-C15	120.1(4)
C17-C14-C13	119.3(4)	C15-C14-C13	120.6(4)
C16-C15-C14	120.2(4)	C15-C16-C28	121.4(4)
C14-C17-C18	120.9(4)	C17-C18-C26	122.1(4)
C17-C18-C28	119.2(4)	C26-C18-C28	118.6(4)
C23-O21-Ho1#5	151.8(3)	C23-O22-Ho2#4	139.4(3)
O22-C23-O21	125.7(4)	O22-C23-C24	117.4(4)
O21-C23-C24	117.0(4)	C27-C24-C25	120.1(4)
C27-C24-C23	120.2(4)	C25-C24-C23	119.6(4)
C26-C25-C24	120.2(4)	C25-C26-C18	121.0(4)
C24-C27-C28	121.1(4)	C27-C28-C16	123.0(4)
C27-C28-C18	118.9(4)	C16-C28-C18	118.1(4)
C33-O31-Ho1#6	169.7(3)	C33-O32-Ho2	137.3(3)
O32-C33-O31	124.7(4)	O32-C33-C34	117.3(4)
O31-C33-C34	117.9(4)	C37-C34-C35	119.7(4)
C37-C34-C33	120.9(4)	C35-C34-C33	119.3(4)
C36-C35-C34	120.4(4)	C35-C36-C48	121.0(4)
C34-C37-C38	121.1(4)	C46-C38-C48	119.7(4)
C46-C38-C37	121.4(4)	C48-C38-C37	118.9(4)
C43-O41-Ho1#3	141.3(3)	C43-O42-Ho2#3	132.5(3)
O41-C43-O42	123.8(4)	O41-C43-C44	120.5(4)
O42-C43-C44	115.7(4)	C47-C44-C45	119.3(4)
C47-C44-C43	120.9(4)	C45-C44-C43	119.7(4)
C46-C45-C44	121.4(4)	C45-C46-C38	120.0(4)
C44-C47-C48	121.3(4)	C36-C48-C38	118.9(4)
C36-C48-C47	122.8(4)	C38-C48-C47	118.3(4)
C53-O51-Ho1	125.3(3)	C53-O52-Ho2	155.5(3)
O51-C53-O52	124.3(4)	O51-C53-C54	116.7(4)
O52-C53-C54	119.0(4)	C57-C54-C55	121.1(4)
C57-C54-C53	119.5(4)	C55-C54-C53	119.4(4)
C56-C55-C54	120.4(4)	C55-C56-C58#7	120.3(4)
C58#7-C56-H56	119.8	C54-C57-C58	120.0(4)
C56#7-C58-C58#7	119.6(5)	C56#7-C58-C57	121.8(4)
C58#7-C58-C57	118.6(5)	C63-O61-Ho1#6	140.3(3)
C63-O62-Ho2	135.4(3)	O61-C63-O62	125.4(4)
O61-C63-C64	117.6(4)	O62-C63-C64	117.0(4)
C67-C64-C65	119.1(4)	C67-C64-C63	121.5(4)
C65-C64-C63	119.4(4)	C66-C65-C64	120.7(4)
C65-C66-C68#8	121.2(4)	C68#8-C66-H66	119.4
C64-C67-C68	121.7(4)	C66#8-C68-C67	122.7(4)
C66#8-C68-C68#8	118.8(5)	C67-C68-C68#8	118.5(5)
C72-O71-Ho1	137.8(4)	O71-C72-N73	125.8(5)
C72-N73-C75	122.2(5)	C72-N73-C74	120.0(5)
C75-N73-C74	117.8(5)	C82-O81-Ho2	132.8(4)
O81-C82-N83	124.2(5)		

C66#8-C68-C68#8	118.8(5)	C67-C68-C68#8	118.5(5)	C72-O71-Ho1	137.8(4)
O71-C72-N73	125.8(5)	C72-N73-C75	122.2(5)	C72-N73-C74	120.0(5)
C75-N73-C74	117.8(5)	C82-O81-Ho2	132.8(4)	O81-C82-N83	124.2(5)
C82-N83-C84	120.9(5)	C82-N83-C85	121.5(5)	C84-N83-C85	117.4(4)
O31#1-Ho1-O11-C13	179.6(5)	O21#2-Ho1-O11-C13	123.0(5)	O41#3-Ho1-O11-C13	47.5(5)
O71-Ho1-O11-C13	-85.7(5)	O61#1-Ho1-O11-C13	-161.2(5)	O51-Ho1-O11-C13	-26.6(5)
O62-Ho2-O12-C13	-174.1(8)	O32-Ho2-O12-C13	-76.9(11)	O52-Ho2-O12-C13	-20.6(8)
O42#3-Ho2-O12-C13	-98.2(8)	O22#4-Ho2-O12-C13	112.0(8)	O81-Ho2-O12-C13	48.6(8)
Ho2-O12-C13-O11	59.2(10)	Ho2-O12-C13-C14	-121.2(7)	Ho1-O11-C13-O12	-17.8(8)
Ho1-O11-C13-C14	162.6(3)	O12-C13-C14-C17	-20.3(6)	O11-C13-C14-C17	159.2(4)
O12-C13-C14-C15	157.9(4)	O11-C13-C14-C15	-22.6(6)	C17-C14-C15-C16	2.3(7)
C13-C14-C15-C16	-175.8(4)	C14-C15-C16-C28	-2.3(7)	C15-C14-C17-C18	0.7(7)
C13-C14-C17-C18	178.9(4)	C14-C17-C18-C26	178.9(4)	C14-C17-C18-C28	-3.8(7)
Ho2#4-O22-C23-O21	4.5(8)	Ho2#4-O22-C23-C24	-177.1(3)	Ho1#5-O21-C23-O22	63.2(9)
Ho1#5-O21-C23-C24	-115.3(6)	O22-C23-C24-C27	-143.7(4)	O21-C23-C24-C27	34.8(6)
O22-C23-C24-C25	36.3(6)	O21-C23-C24-C25	-145.2(4)	C27-C24-C25-C26	0.4(7)
C23-C24-C25-C26	-179.6(4)	C24-C25-C26-C18	0.8(7)	C17-C18-C26-C25	176.2(5)
C28-C18-C26-C25	-1.1(7)	C25-C24-C27-C28	-1.3(7)	C23-C24-C27-C28	178.7(4)
C24-C27-C28-C16	179.9(4)	C24-C27-C28-C18	0.9(6)	C15-C16-C28-C27	-179.8(5)
C15-C16-C28-C18	-0.8(7)	C17-C18-C28-C27	-177.2(4)	C26-C18-C28-C27	0.3(6)
C17-C18-C28-C16	3.8(6)	C26-C18-C28-C16	-178.8(4)	O12-Ho2-O32-C33	-139.8(5)
O62-Ho2-O32-C33	-41.4(5)	O52-Ho2-O32-C33	164.4(5)	O42#3-Ho2-O32-C33	-118.7(5)
O22#4-Ho2-O32-C33	30.6(5)	O81-Ho2-O32-C33	91.6(5)	Ho2-O32-C33-O31	-14.5(8)
Ho2-O32-C33-C34	166.5(3)	Ho1#6-O31-C33-O32	19(2)	Ho1#6-O31-C33-C34	-162.1(15)
O32-C33-C34-C37	13.1(6)	O31-C33-C34-C37	-166.0(4)	O32-C33-C34-C35	-166.4(4)
O31-C33-C34-C35	14.4(6)	C37-C34-C35-C36	-1.5(7)	C33-C34-C35-C36	178.0(4)
C34-C35-C36-C48	2.0(8)	C35-C34-C37-C38	0.0(7)	C33-C34-C37-C38	-179.5(4)
C34-C37-C38-C46	-179.2(5)	C34-C37-C38-C48	1.1(7)	Ho1#3-O41-C43-O42	-69.0(7)
Ho1#3-O41-C43-C44	113.5(5)	Ho2#3-O42-C43-O41	78.7(6)	Ho2#3-O42-C43-C44	-103.6(4)
O41-C43-C44-C47	-20.1(7)	O42-C43-C44-C47	162.1(4)	O41-C43-C44-C45	163.2(4)
O42-C43-C44-C45	-14.6(6)	C47-C44-C45-C46	1.1(8)	C43-C44-C45-C46	177.9(5)
C44-C45-C46-C38	-1.1(8)	C48-C38-C46-C45	0.9(8)	C37-C38-C46-C45	-178.8(5)
C45-C44-C47-C48	-0.9(7)	C43-C44-C47-C48	-177.6(4)	C35-C36-C48-C38	-0.9(7)
C35-C36-C48-C47	179.4(5)	C46-C38-C48-C36	179.6(5)	C37-C38-C48-C36	-0.6(7)
C46-C38-C48-C47	-0.7(7)	C37-C38-C48-C47	179.1(4)	C44-C47-C48-C36	-179.7(5)
C44-C47-C48-C38	0.6(7)	O31#1-Ho1-O51-C53	-166.9(4)	O21#2-Ho1-O51-C53	-101.6(4)
O41#3-Ho1-O51-C53	-67.7(4)	O11-Ho1-O51-C53	19.0(4)	O71-Ho1-O51-C53	80.2(4)
O61#1-Ho1-O51-C53	125.6(4)	O12-Ho2-O52-C53	-123.6(7)	O62-Ho2-O52-C53	-32.4(8)
O32-Ho2-O52-C53	45.3(7)	O42#3-Ho2-O52-C53	-41.1(7)	O22#4-Ho2-O52-C53	166.9(7)
O81-Ho2-O52-C53	123.0(7)	Ho1-O51-C53-O52	-4.8(7)	Ho1-O51-C53-C54	174.4(3)
Ho2-O52-C53-O51	107.1(7)	Ho2-O52-C53-C54	-72.0(9)	O51-C53-C54-C57	162.3(5)
O52-C53-C54-C57	-18.5(7)	O51-C53-C54-C55	-17.6(7)	O52-C53-C54-C55	161.6(5)
C57-C54-C55-C56	-0.7(8)	C53-C54-C55-C56	179.2(5)	C54-C55-C56-C58#7	-0.7(8)
C55-C54-C57-C58	1.9(7)	C53-C54-C57-C58	-178.0(4)	C54-C57-C58-C56#7	178.6(5)
C54-C57-C58-C58#7	-1.5(8)	O12-Ho2-O62-C63	-89.1(4)	O32-Ho2-O62-C63	104.3(4)
O52-Ho2-O62-C63	-177.5(4)	O42#3-Ho2-O62-C63	-168.7(4)	O22#4-Ho2-O62-C63	-12.7(4)
O81-Ho2-O62-C63	34.2(5)	Ho1#6-O61-C63-O62	50.7(7)	Ho1#6-O61-C63-C64	-128.3(4)
Ho2-O62-C63-O61	-84.6(6)	Ho2-O62-C63-C64	94.4(5)	O61-C63-C64-C67	19.3(6)
O62-C63-C64-C67	-159.8(4)	O61-C63-C64-C65	-163.7(4)	O62-C63-C64-C65	17.2(6)
C67-C64-C65-C66	-1.4(7)	C63-C64-C65-C66	-178.5(5)	C64-C65-C66-C68#8	2.3(8)
C65-C64-C67-C68	-0.4(7)	C63-C64-C67-C68	176.7(4)	C64-C67-C68-C66#8	-179.1(5)
C64-C67-C68-C68#8	1.1(8)	O31#1-Ho1-O71-C72	114.4(6)	O21#2-Ho1-O71-C72	3.7(7)
O41#3-Ho1-O71-C72	-134.0(5)	O11-Ho1-O71-C72	-52.2(6)	O61#1-Ho1-O71-C72	35.0(6)
O51-Ho1-O71-C72	-178.1(6)	Ho1-O71-C72-N73	127.8(5)	O71-C72-N73-C75	177.8(6)
O71-C72-N73-C74	-4.2(9)	O12-Ho2-O81-C82	145.9(4)	O62-Ho2-O81-C82	28.4(5)
O32-Ho2-O81-C82	-45.3(5)	O52-Ho2-O81-C82	-137.5(5)	O42#3-Ho2-O81-C82	-109.1(5)
O22#4-Ho2-O81-C82	77.1(5)	Ho2-O81-C82-N83	173.5(4)	O81-C82-N83-C84	-2.0(9)
O81-C82-N83-C85	-178.0(5)				

Symmetry transformation codes:#1 x,-y+1/2,z-1/2   #2 -x,y-1/2,-z+1/2   #3 -x+1,-y,-z+1   #4 -x,-y+1,-z+1   #5 -x,y+1/2,-z+1/2
#6 x,-y+1/2,z+1/2   #7 -x+1,-y+1,-z+1   #8 -x,-y,-z+1

Table 10.9 (b) Bond lengths (Å), valence and torsion angles (°) for Ho-MOF-NDC-1 System.

10.10 Detailed Information for Ho-MOF-NDC-2 System from Single Crystal Analysis

Atom	x/a	y/b	z/c	U_{eq}
Ho1	0.25510(3)	0.990033(19)	0.527039(18)	0.01748(6)
O11	0.3090(4)	0.8220(3)	0.5404(3)	0.0303(8)
O12	0.5420(4)	0.8844(3)	0.5105(3)	0.0288(8)
C11	0.4281(6)	0.8059(4)	0.5228(4)	0.0251(10)
C12	0.4301(7)	0.6823(5)	0.5134(5)	0.0299(11)
C13	0.5642(6)	0.6644(5)	0.5121(5)	0.0307(11)
C14	0.5691(7)	0.5494(5)	0.5042(5)	0.0319(12)
C15	0.7062(7)	0.5286(5)	0.5023(6)	0.0381(14)
C16	0.7063(7)	0.4157(5)	0.4939(6)	0.0398(14)
O21	0.035(3)	0.8073(14)	0.3725(16)	0.024(3)
O22	0.255(2)	0.870(2)	0.327(2)	0.022(3)
C21	0.116(2)	0.7924(13)	0.3023(11)	0.019(2)
C22	0.048(2)	0.6809(14)	0.1869(12)	0.026(3)
C23	0.1429(15)	0.6334(9)	0.1384(8)	0.029(2)
C24	0.0819(14)	0.5276(10)	0.0293(8)	0.022(3)
C25	0.1781(12)	0.4765(9)	-0.0228(9)	0.038(3)
C26	0.1142(12)	0.3742(9)	-0.1289(8)	0.034(3)
O21A	0.025(3)	0.7790(13)	0.3852(15)	0.024(3)
O22A	0.241(2)	0.857(2)	0.339(2)	0.022(3)
C21A	0.1083(19)	0.7711(12)	0.3151(10)	0.019(2)
C22A	0.0491(19)	0.6572(14)	0.2026(11)	0.026(3)
C23A	0.1157(12)	0.6620(10)	0.1143(7)	0.029(2)
C24A	0.0613(14)	0.5555(11)	0.0063(8)	0.030(3)
C25A	0.1276(12)	0.5568(9)	-0.0872(8)	0.039(3)
C26A	0.0728(12)	0.4515(9)	-0.1896(8)	0.037(3)
O31	0.1035(5)	1.0452(4)	0.4112(3)	0.0371(9)
O32	-0.1155(4)	1.0626(4)	0.3498(3)	0.0303(8)
C31	0.0051(6)	1.0495(5)	0.3345(4)	0.0247(10)
C32	0.0300(7)	1.0353(6)	0.2155(5)	0.0368(14)
C33	-0.0857(7)	1.0215(7)	0.1248(5)	0.0484(18)

C34	-0.0709(7)	1.0024(8)	0.0103(5)	0.0510(19)
C35	-0.1893(7)	0.9876(9)	-0.0851(5)	0.059(2)
C36	-0.1704(7)	0.9691(8)	-0.1952(5)	0.0491(18)
O1A	0.4240(11)	0.9174(10)	-0.1741(9)	0.053(3)
C2A	0.2988(16)	0.8226(13)	-0.2172(13)	0.046(3)
N3A	0.2437(15)	0.7587(12)	-0.1546(11)	0.055(3)
C4A	0.321(2)	0.7917(15)	-0.0322(14)	0.062(4)
C5A	0.092(2)	0.6526(19)	-0.2098(19)	0.094(6)
O1B	0.4825(14)	0.8674(14)	0.0668(10)	0.087(4)
C2B	0.540(2)	0.8021(18)	0.0162(16)	0.080(5)
N3B	0.516(2)	0.7619(14)	-0.1030(14)	0.088(4)
C4B	0.419(3)	0.799(2)	-0.1742(15)	0.100(6)
C5B	0.614(4)	0.683(4)	-0.143(4)	0.168(14)
O1C	0.4529(13)	0.3954(9)	-0.1786(12)	0.079(4)
C2C	0.5821(19)	0.4530(14)	-0.1862(15)	0.066(4)
N3C	0.6389(17)	0.5683(13)	-0.1808(13)	0.069(4)
C4C	0.533(3)	0.641(2)	-0.180(2)	0.083(6)
C5C	0.796(2)	0.6341(17)	-0.1789(18)	0.077(5)
O1D	0.2501(4)	1.1842(4)	0.6461(3)	0.0359(9)
C2D	0.3594(18)	1.2998(15)	0.7427(14)	0.051(4)
C3D	0.340(2)	1.2977(19)	0.8586(17)	0.068(6)
O1W	0.4638(4)	1.0797(4)	0.7049(3)	0.0337(9)

[*] U_{eq} is defined as one third of the trace of the orthogonalized U_{ij} tensor.

Table 10.10 (a) Anisotropic atomic displacement parameters[*] (Å^2) for Ho-MOF-NDC-2 System.

Ho1-O12#1	2.255(3)	Ho1-O31	2.288(4)	Ho1-O32#2	2.289(4)
Ho1-O11	2.351(3)	Ho1-O1W	2.377(4)	Ho1-O1D	2.425(4)
Ho1-O21	2.45(2)	Ho1-O22	2.47(2)	O11-C11	1.258(6)
O12-C11	1.257(6)	O12-Ho1#1	2.255(3)	C11-C12	1.505(6)
C12-C13	1.371(7)	C12-C16#3	1.413(8)	C13-C14	1.415(7)
C14-C15	1.417(8)	C14-C14#3	1.425(10)	C15-C16	1.370(7)
C16-C12#3	1.413(8)	O21-C21	1.266(6)	O22-C21	1.260(6)
C21-C22	1.503(8)	C22-C23	1.361(11)	C22-C26#4	1.41(2)
C23-C24	1.424(9)	C24-C25	1.413(10)	C24-C24#4	1.43(2)
C25-C26	1.380(10)	C26-C22#4	1.41(2)	O31-C31	1.252(6)
O32-C31	1.249(6)	O32-Ho1#2	2.289(4)	C31-C32	1.505(7)
C32-C33	1.367(8)	C32-C36#5	1.417(8)	C33-C34	1.409(8)
C34-C35	1.418(8)	C34-C34#5	1.432(11)	C35-C36	1.369(8)
C36-C32#5	1.418(8)	O1A-C2A	1.244(16)	C2A-N3A	1.320(16)
N3A-C4A	1.442(19)	N3A-C5A	1.46(2)	O1B-C2B	1.20(2)
C2B-N3B	1.36(2)	N3B-C4B	1.46(3)	N3B-C5B	1.59(4)
O1C-C2C	1.233(18)	C2C-N3C	1.32(2)	N3C-C5C	1.43(2)
N3C-C4C	1.56(2)	O1D-C2D	1.451(15)	O1D-H11D	0.814(15)
O1D-H12D	0.817(15)	C2D-C3D	1.49(3)	O1W-H11W	0.823(15)
O1W-H12W	0.816(15)				
O12#1-Ho1-O31	85.69(13)	O12#1-Ho1-O32#2	152.78(14)	O31-Ho1-O32#2	104.47(14)
O12#1-Ho1-O11	107.81(12)	O31-Ho1-O11	143.78(15)	O32#2-Ho1-O11	78.98(11)
O12#1-Ho1-O1W	75.73(14)	O31-Ho1-O1W	140.78(15)	O32#2-Ho1-O1W	80.86(13)
O11-Ho1-O1W	75.38(14)	O12#1-Ho1-O1D	84.00(14)	O31-Ho1-O1D	70.50(14)
O32#2-Ho1-O1D	76.09(15)	O11-Ho1-O1D	142.52(15)	O1W-Ho1-O1D	73.39(13)
O12#1-Ho1-O21	123.5(3)	O31-Ho1-O21	68.1(5)	O32#2-Ho1-O21	83.6(3)
O11-Ho1-O21	76.7(5)	O1W-Ho1-O21	150.1(5)	O1D-Ho1-O21	127.0(5)
O12#1-Ho1-O22	73.6(5)	O31-Ho1-O22	78.5(8)	O32#2-Ho1-O22	132.7(5)
O11-Ho1-O22	73.8(8)	O1W-Ho1-O22	126.5(6)	O1D-Ho1-O22	142.9(8)
O21-Ho1-O22	53.1(3)	C11-O11-Ho1	124.0(3)	C11-O12-Ho1#1	174.4(3)
O12-C11-O11	124.4(4)	O12-C11-C12	118.8(4)	O11-C11-C12	116.8(4)
C13-C12-C16#3	119.8(5)	C13-C12-C11	120.1(5)	C16#3-C12-C11	120.1(5)
C12-C13-C14	121.1(5)	C13-C14-C15	122.1(5)	C13-C14-C14#3	118.8(6)
C15-C14-C14#3	119.0(6)	C16-C15-C14	120.5(5)	C15-C16-C12#3	120.7(5)
C21-O21-Ho1	93.1(10)	C21-O22-Ho1	92.4(11)	O22-C21-O21	121.1(9)
O22-C21-C22	118.5(8)	O21-C21-C22	120.4(9)	O22-C21-Ho1	61.1(10)
O21-C21-Ho1	60.2(9)	C22-C21-Ho1	175.0(7)	C23-C22-C26#4	120.1(10)
C23-C22-C21	119.7(10)	C26#4-C22-C21	120.2(9)	C22-C23-C24	121.1(10)
C25-C24-C23	122.2(9)	C25-C24-C24#4	119.2(10)	C23-C24-C24#4	118.6(10)
C26-C25-C24	120.3(9)	C25-C26-C22#4	120.7(9)	C31-O31-Ho1	167.1(4)
C31-O32-Ho1#2	129.6(3)	O32-C31-O31	123.9(4)	O32-C31-C32	117.3(4)
O31-C31-C32	118.7(5)	C33-C32-C36#5	119.6(5)	C33-C32-C31	120.0(5)
C36#5-C32-C31	120.4(5)	C32-C33-C34	122.2(5)	C33-C34-C35	123.2(5)
C33-C34-C34#5	118.2(6)	C35-C34-C34#5	118.6(6)	C36-C35-C34	121.4(5)
C35-C36-C32#5	120.0(5)	O1A-C2A-N3A	121.8(14)	C2A-N3A-C4A	123.8(13)
C2A-N3A-C5A	118.4(14)	C4A-N3A-C5A	117.7(13)	O1B-C2B-N3B	122(2)
O1B-C2B-H2B	118.8	N3B-C2B-H2B	118.8	C2B-N3B-C4B	120.2(18)
C2B-N3B-C5B	111(2)	C4B-N3B-C5B	129(2)	O1C-C2C-N3C	126.8(16)
O1C-C2C-H2C	116.6	N3C-C2C-H2C	116.6	C2C-N3C-C5C	124.1(15)
C2C-N3C-C4C	120.7(16)	C5C-N3C-C4C	115.2(15)	C2D-O1D-Ho1	136.8(7)
C2D-O1D-H11D	102(4)	Ho1-O1D-H11D	121(4)	C2D-O1D-H12D	50(8)
Ho1-O1D-H12D	108(6)	H11D-O1D-H12D	107(3)	O1D-C2D-C3D	110.8(14)
Ho1-O1W-H11W	96(4)	Ho1-O1W-H12W	109(4)	H11W-O1W-H12W	104(3)

Symmetry transformation codes:#1 -x+1,-y+2,-z+1   #2 -x,-y+2,-z+1   #3 -x+1,-y+1,-z+1   #4 -x,-y+1,-z   #5 -x,-y+2,-z

Table 10.10 (b) Bond lengths (Å) and angles (°) for Ho-MOF-NDC-2 System.

Atom	sof	Atom	sof	Atom
O21	0.484(7)	O22	0.484(7)	C21
C22	0.484(7)	C23	0.484(7)	H23
C24	0.484(7)	C25	0.484(7)	H25
C26	0.484(7)	H26	0.484(7)	
O21A	0.516(7)	O22A	0.516(7)	C21A
C22A	0.516(7)	C23A	0.516(7)	H23A
C24A	0.516(7)	C25A	0.516(7)	H25A
C26A	0.516(7)	H26A	0.516(7)	
O1A	0.490(6)	C2A	0.490(6)	H2A
N3A	0.490(6)	C4A	0.490(6)	H4A1
H4A2	0.490(6)	H4A3	0.490(6)	C5A
H5A1	0.490(6)	H5A2	0.490(6)	H5A3
O1B	0.510(6)	C2B	0.510(6)	H2B
N3B	0.510(6)	C4B	0.510(6)	H4B1
H4B2	0.510(6)	H4B3	0.510(6)	C5B
H5B1	0.510(6)	H5B2	0.510(6)	H5B3
O1C	0.501(8)	C2C	0.501(8)	H2C
N3C	0.501(8)	C4C	0.501(8)	H4C1
H4C2	0.501(8)	H4C3	0.501(8)	C5C
H5C1	0.501(8)	H5C2	0.501(8)	H5C3
O1D	1	H11D	1	H12D
C2D	0.414(13)	H2D1	0.414(13)	H2D2
C3D	0.414(13)	H3D1	0.414(13)	H3D2
H3D3	0.414(13)			

Table 10.10 (c) Site occupancy factors that deviate from unity for Ho-MOF-NDC-2 System.

10.11 Detailed Information for Ho-MOF-NDC-3 System from Single Crystal Analysis

Atom	x/a	y/b	z/c	U_{eq}
Ho1	0.0000	0.82072(3)	0.2500	0.02891(8)
Ho2	0.0000	1.0000	0.0000	0.03026(9)
O1[**]	-0.0046(8)	0.5492(10)	0.2630(7)	0.088(2)
C2[**]	-0.0063(7)	0.4323(15)	0.2215(7)	0.088(2)
N3[**]	0.0329(6)	0.4091(12)	0.1687(7)	0.130(4)
C4[**]	0.0188(7)	0.4795(17)	0.0896(7)	0.091(3)
C5[**]	0.0830(7)	0.316(2)	0.2014(12)	0.133(4)

O11	-0.04046(13)	0.7769(4)	0.03435(19)	0.0420(8)
O12	-0.06886(14)	0.7385(5)	0.14629(19)	0.0494(9)
C10	-0.07923(18)	0.7517(6)	0.0760(3)	0.0352(10)
C11	-0.14076(17)	0.7406(5)	0.0363(2)	0.0317(9)
C12	-0.18540(18)	0.7727(5)	0.0757(2)	0.0338(9)
C13	-0.24416(18)	0.7702(5)	0.0391(2)	0.0301(9)
C14	-0.29098(19)	0.8045(6)	0.0785(2)	0.0355(10)
C15	-0.34734(19)	0.7976(6)	0.0420(3)	0.0373(10)
O21	0.06816(14)	0.8137(5)	0.1765(2)	0.0530(10)
O22	0.08523(12)	0.9482(5)	0.0760(2)	0.0459(8)
C20	0.10121(17)	0.8618(6)	0.1322(2)	0.0351(10)
C21	0.16346(17)	0.8097(5)	0.1477(2)	0.0306(9)
C22	0.20173(17)	0.8628(5)	0.1025(2)	0.0308(9)
C23	0.26012(16)	0.8097(5)	0.1144(2)	0.0289(8)
C24	0.29983(18)	0.8573(5)	0.0658(3)	0.0348(9)
C25	0.35513(18)	0.7967(6)	0.0755(3)	0.0382(10)
O31	0.46076(14)	0.6291(5)	0.0880(2)	0.0558(10)
O32	0.44939(16)	0.5379(5)	0.2009(2)	0.0596(10)
C30	0.43185(19)	0.6135(6)	0.1427(3)	0.0417(11)
C31	0.37304(18)	0.6892(5)	0.1349(3)	0.0355(10)
C32	0.33634(17)	0.6443(6)	0.1837(3)	0.0349(9)
C33	0.27816(17)	0.7026(5)	0.1743(2)	0.0306(9)
C34	0.23822(19)	0.6512(6)	0.2212(3)	0.0391(10)
C35	0.18175(19)	0.7032(6)	0.2076(3)	0.0387(11)

---

[*] U_{eq} is defined as one third of the trace of the orthogonalized U_{ij} tensor.   [**] Occupation factor for O1 – C5 = 50%

Table 10.11 (a) Atomic coordinates and equivalent[*] isotropic atomic displacement parameters (Å^2) for Ho-MOF-NDC-3 System.

Ho1-O21#1	2.216(3)	Ho1-O21	2.216(3)	Ho1-O32#2	2.290(4)
Ho1-O32#3	2.290(4)	Ho1-O1	2.323(9)	Ho1-O1#1	2.323(9)
Ho1-O12	2.358(3)	Ho1-O12#1	2.358(3)	Ho2-O31#2	2.226(3)
Ho2-O31#4	2.227(3)	Ho2-O11	2.246(3)	Ho2-O11#5	2.246(3)
Ho2-O22#5	2.269(3)	Ho2-O22	2.269(3)	O1-C2	1.236(9)
C2-N3	1.427(10)	N3-C5	1.456(10)	N3-C4	1.518(10)
O11-C10	1.276(5)	O12-C10	1.244(5)	C10-C11	1.502(6)
C11-C12	1.373(6)	C11-C15#6	1.417(6)	C12-C13	1.425(6)
C13-C14	1.420(6)	C13-C13#6	1.421(8)	C14-C15	1.376(6)
C15-C11#6	1.417(6)	O21-C20	1.257(5)	O22-C20	1.251(6)
C20-C21	1.504(5)	C21-C22	1.370(6)	C21-C35	1.414(6)
C22-C23	1.421(5)	C23-C33	1.416(6)	C23-C24	1.425(6)
C24-C25	1.376(6)	C25-C31	1.410(7)	O31-C30	1.276(6)
O31-Ho2#7	2.227(3)	O32-C30	1.234(6)	O32-Ho1#7	2.290(4)
C30-C31	1.504(6)	C31-C32	1.368(6)	C32-C33	1.432(5)
C33-C34	1.415(6)	C34-C35	1.376(6)		
O21#1-Ho1-O21	176.9(2)	O21#1-Ho1-O32#2	82.64(15)	O21-Ho1-O32#2	99.88(15)
O21#1-Ho1-O32#3	99.88(15)	O21-Ho1-O32#3	82.64(15)	O32#2-Ho1-O32#3	72.6(2)
O21#1-Ho1-O1	82.3(4)	O21-Ho1-O1	94.7(4)	O32#2-Ho1-O1	144.0(5)
O32#3-Ho1-O1	142.3(4)	O21#1-Ho1-O1#1	94.7(4)	O21-Ho1-O1#1	82.3(4)
O32#2-Ho1-O1#1	142.3(4)	O32#3-Ho1-O1#1	144.0(5)	O1-Ho1-O1#1	13.4(6)
O21#1-Ho1-O12	89.43(13)	O21-Ho1-O12	89.66(13)	O32#2-Ho1-O12	72.02(15)
O32#3-Ho1-O12	141.84(15)	O1-Ho1-O12	75.3(4)	O1#1-Ho1-O12	70.4(4)
O21#1-Ho1-O12#1	89.66(13)	O21-Ho1-O12#1	89.43(13)	O32#2-Ho1-O12#1	141.84(15)
O32#3-Ho1-O12#1	72.02(15)	O1-Ho1-O12#1	70.4(4)	O1#1-Ho1-O12#1	75.3(4)
O12-Ho1-O12#1	145.5(2)	O31#2-Ho2-O31#4	180.0	O31#2-Ho2-O11	89.21(14)
O31#4-Ho2-O11	90.79(14)	O31#2-Ho2-O11#5	90.79(14)	O31#4-Ho2-O11#5	89.21(14)
O11-Ho2-O11#5	180.0	O31#2-Ho2-O22#5	84.56(13)	O31#4-Ho2-O22#5	95.45(13)
O11-Ho2-O22#5	87.64(12)	O11#5-Ho2-O22#5	92.37(12)	O31#2-Ho2-O22	95.44(13)
O31#4-Ho2-O22	84.55(13)	O11-Ho2-O22	92.36(12)	O11#5-Ho2-O22	87.63(12)
O22#5-Ho2-O22	180.0	C2-O1-Ho1	137.4(10)	O1-C2-N3	122.9(13)
C2-N3-C5	111.7(12)	C2-N3-C4	119.3(11)	C5-N3-C4	129.1(15)
C10-O11-Ho2	131.9(3)	C10-O12-Ho1	139.8(3)	O12-C10-O11	123.9(4)
O12-C10-C11	119.3(4)	O11-C10-C11	116.8(4)	C12-C11-C15#6	120.1(4)
C12-C11-C10	119.6(4)	C15#6-C11-C10	120.2(4)	C11-C12-C13	121.2(4)
C14-C13-C13#6	119.4(5)	C14-C13-C12	122.2(4)	C13#6-C13-C12	118.4(5)
C15-C14-C13	120.8(4)	-C15-C11#6	120.1(4)	C20-O21-Ho1	158.8(4)
C20-O22-Ho2	135.7(3)	O22-C20-O21	124.0(4)	O22-C20-C21	118.6(4)
O21-C20-C21	117.4(4)	C22-C21-C35	120.5(4)	C22-C21-C20	119.8(4)
C35-C21-C20	119.8(4)	C21-C22-C23	120.5(4)	C33-C23-C22	118.8(4)
C33-C23-C24	119.8(4)	C22-C23-C24	121.4(4)	C25-C24-C23	120.3(4)
C24-C25-C31	119.9(4)	C30-O31-Ho2#7	144.3(4)	C30-O32-Ho1#7	145.5(3)
O32-C30-O31	123.3(4)	O32-C30-C31	118.6(4)	O31-C30-C31	118.1(5)
C32-C31-C25	121.0(4)	C32-C31-C30	118.5(4)	C25-C31-C30	120.4(4)
C31-C32-C33	120.5(4)	C34-C33-C23	119.8(4)	C34-C33-C32	121.8(4)
C23-C33-C32	118.3(4)	C35-C34-C33	120.0(4)	C34-C35-C21	120.4(4)

Symmetry transformation codes:#1 -x,y,-z+1/2   #2 x-1/2,y+1/2,z   #3 -x+1/2,y+1/2,-z+1/2   #4 -x+1/2,-y+3/2,-z   #5 -x,-y+2,-z
#6 -x-1/2,-y+3/2,-z   #7 x+1/2,y-1/2,z

Table 10.11 (b) Bond lengths (Å) and angles (°) for Ho-MOF-NDC-3 System.

10.12 Detailed Information for Co-MOF-BTB-plate System from Single Crystal Analysis

273

Atom	x/a	y/b	z/c	U_{eq}
Co1	0.84035(3)	0.60605(3)	0.23046(2)	0.03167(14)
Co2	0.96524(4)	0.49781(3)	0.16916(2)	0.03948(16)
Co3	0.97483(4)	0.51312(4)	0.28923(2)	0.04625(18)
O1	0.90990(18)	0.51063(16)	0.23092(11)	0.0421(8)
O2	0.7575(2)	0.6924(3)	0.23201(16)	0.0806(13)
O3	1.0614(2)	0.50996(18)	0.22138(15)	0.0606(10)
O11	0.79240(19)	0.5607(2)	0.29290(11)	0.0506(9)
O12	0.8871(2)	0.5098(2)	0.33650(12)	0.0555(9)
C10	0.8206(3)	0.5316(3)	0.33113(16)	0.0413(11)
C11	0.7708(3)	0.5239(2)	0.37374(16)	0.0381(10)
C12	0.7908(3)	0.4762(3)	0.41208(18)	0.0499(13)
C13	0.7440(3)	0.4676(3)	0.4520(2)	0.0592(15)
C14	0.6778(3)	0.5108(3)	0.45483(18)	0.0500(13)
C15	0.6608(3)	0.5586(3)	0.41769(18)	0.0520(14)
C16	0.7066(3)	0.5647(3)	0.37640(17)	0.0450(12)
O21	0.5278(9)	0.0736(6)	0.6206(6)	0.079(3)
O22	0.4774(11)	0.1272(9)	0.6844(5)	0.060(2)
C20	0.5079(7)	0.1327(7)	0.6453(5)	0.051(2)
C21	0.5242(5)	0.2107(6)	0.6228(4)	0.0564(19)
C22	0.5128(8)	0.2737(7)	0.6511(5)	0.062(2)
C23	0.5272(8)	0.3434(7)	0.6309(6)	0.056(2)
C24	0.5526(4)	0.3522(6)	0.5841(6)	0.0589(19)
C25	0.5636(8)	0.2861(7)	0.5562(5)	0.055(3)
C26	0.5492(8)	0.2144(7)	0.5755(5)	0.059(3)
O21A	0.5034(7)	0.0731(5)	0.6028(5)	0.079(3)
O22A	0.4684(9)	0.1225(7)	0.6723(4)	0.060(2)
C20A	0.4931(6)	0.1303(6)	0.6316(4)	0.051(2)
C21A	0.5133(4)	0.2087(5)	0.6113(4)	0.0564(19)
C22A	0.5221(7)	0.2674(6)	0.6437(4)	0.062(2)
C23A	0.5400(7)	0.3375(6)	0.6253(5)	0.056(2)
C24A	0.5496(4)	0.3503(6)	0.5762(5)	0.0589(19)
C25A	0.5402(7)	0.2885(6)	0.5442(5)	0.055(3)
C26A	0.5217(7)	0.2166(6)	0.5616(4)	0.059(3)

O31	0.3875(2)	0.83678(18)	0.67268(13)	0.0547(9)
O32	0.4887(2)	0.8969(2)	0.64537(16)	0.0683(12)
C30	0.4474(3)	0.8395(3)	0.65019(18)	0.0423(11)
C31	0.4736(3)	0.7692(2)	0.62597(16)	0.0415(11)
C32	0.5404(3)	0.7675(3)	0.60073(19)	0.0516(13)
C33	0.5657(3)	0.7018(3)	0.57928(19)	0.0532(13)
C34	0.5247(3)	0.6343(2)	0.58263(18)	0.0495(13)
C35	0.4590(3)	0.6366(2)	0.60693(18)	0.0496(13)
C36	0.4328(3)	0.7033(3)	0.62832(19)	0.0488(13)
C41	0.6300(3)	0.5027(3)	0.49899(18)	0.0575(15)
C42	0.6160(3)	0.4336(3)	0.52040(19)	0.0597(16)
C43	0.5693(3)	0.4265(3)	0.56004(19)	0.0564(15)
C44	0.5401(3)	0.4921(3)	0.5802(2)	0.0601(16)
C45	0.5535(3)	0.5642(3)	0.55981(19)	0.0540(14)
C46	0.5978(3)	0.5681(3)	0.51806(18)	0.0555(15)
O51	0.8627(2)	0.4902(3)	0.13172(15)	0.0793(13)
O52	0.7715(2)	0.5440(2)	0.17911(12)	0.0550(9)
C50	0.7949(3)	0.5128(3)	0.1411(2)	0.0542(13)
C51	0.7392(4)	0.5004(3)	0.1005(2)	0.0607(15)
C52	0.6718(3)	0.5417(3)	0.0976(2)	0.0593(14)
C53	0.6272(3)	0.5358(4)	0.0553(2)	0.0650(16)
C54	0.6463(3)	0.4887(3)	0.0172(2)	0.0567(14)
C55	0.7113(4)	0.4454(3)	0.0222(2)	0.078(2)
C56	0.7602(4)	0.4525(3)	0.0617(2)	0.0702(17)
O61	0.5099(2)	0.8830(2)	-0.19465(16)	0.0686(11)
O62	0.4066(2)	0.8278(2)	-0.22361(15)	0.0684(12)
C60	0.4652(3)	0.8292(3)	-0.19844(19)	0.0490(11)
C61	0.4888(3)	0.7567(3)	-0.17286(18)	0.0416(11)
C62	0.4444(3)	0.6926(3)	-0.1777(2)	0.0534(14)
C63	0.4637(3)	0.6261(3)	-0.15391(19)	0.0537(14)
C64	0.5271(3)	0.6231(3)	-0.12466(19)	0.0476(12)
C65	0.5725(3)	0.6874(3)	-0.1219(2)	0.0542(14)
C66	0.5533(3)	0.7537(3)	-0.1443(2)	0.0634(15)
O71	0.6070(3)	0.1156(3)	-0.23914(18)	0.0646(14)
O72	0.5197(3)	0.0780(3)	-0.1866(2)	0.0769(18)
C70	0.5633(3)	0.1252(3)	-0.2036(2)	0.0583(18)

C71	0.56383(19)	0.2014(3)	-0.1788(2)	0.0499(16)
C72	0.5415(3)	0.2059(4)	-0.1318(3)	0.062(2)
C73	0.5407(3)	0.2768(4)	-0.1072(3)	0.0624(19)
C74	0.5627(3)	0.3417(3)	-0.1301(3)	0.0572(15)
C75	0.5852(3)	0.3360(4)	-0.1782(2)	0.0548(17)
C76	0.5866(3)	0.2660(4)	-0.2033(3)	0.0601(18)
O71A	0.5466(11)	0.0634(9)	-0.1565(7)	0.067(5)
O72A	0.4727(9)	0.1181(10)	-0.2129(6)	0.061(5)
C70A	0.5151(7)	0.1196(8)	-0.1768(5)	0.050(5)
C71A	0.5285(7)	0.1977(7)	-0.1565(4)	0.043(5)
C72A	0.5827(9)	0.2068(8)	-0.1219(5)	0.043(5)
C73A	0.5969(9)	0.2798(9)	-0.1018(5)	0.037(4)
C74A	0.5547(8)	0.3384(7)	-0.1186(5)	0.0572(15)
C75A	0.4993(9)	0.3308(8)	-0.1537(6)	0.052(5)
C76A	0.4853(9)	0.2579(8)	-0.1737(6)	0.053(5)
C81	0.6053(3)	0.4865(3)	-0.02981(19)	0.0534(14)
C82	0.5786(3)	0.5511(3)	-0.05324(19)	0.0507(13)
C83	0.5503(3)	0.5515(3)	-0.09950(18)	0.0466(12)
C84	0.5432(3)	0.4817(2)	-0.12342(19)	0.0475(12)
C85	0.5632(3)	0.4163(3)	-0.1017(2)	0.0607(15)
C86	0.5943(3)	0.4168(3)	-0.0543(2)	0.0591(15)

_____

[*] U_{eq} is defined as one third of the trace of the orthogonalized U_{ij} tensor.

Table 10.12 (a) Atomic coordinates and equivalent[*] isotropic atomic displacement parameters ($Å^2$) for Co-MOF-BTB-plate System.

_____

Atom	sof	Atom	sof	Atom	sof
O21 - C26	0.462(16)	O21A - C26A	0.538(16)		
O72 - C76	0.801(4)	O71A - C76A	0.199(4)		

_____

Table 10.12 (b) Site occupancy factors that deviate from unity for Co-MOF-BTB-plate System.

Co1-O31#1	2.069(3)	Co1-O62#2	2.073(3)	Co1-O11	2.086(3)
Co1-O1	2.093(3)	Co1-O2	2.124(4)	Co1-O52	2.151(4)
Co2-O1	1.987(3)	Co2-O32#1	2.017(3)	Co2-O51	2.085(4)
Co2-O21#3	2.158(12)	Co2-O3	2.225(4)	Co3-O72#4	1.911(5)
Co3-O1	1.957(3)	Co3-O61#2	1.985(4)	Co3-O12	2.049(3)
Co3-O3	2.439(4)	O11-C10	1.263(6)	O12-C10	1.255(6)
C10-C11	1.486(6)	C11-C16	1.355(6)	C11-C12	1.389(6)
C12-C13	1.396(7)	C12-H12	0.9400	C13-C14	1.409(7)
C13-H13	0.9400	C14-C15	1.353(7)	C14-C41	1.499(6)
C15-C16	1.411(6)	C15-H15	0.9400	C16-H16	0.9400
O21-C20	1.298(8)	O21-Co2#5	2.158(12)	O22-C20	1.214(8)
O22-Co2#5	2.257(16)	C20-C21	1.539(8)	C20-Co2#5	2.518(11)
C21-C22	1.374(9)	C21-C26	1.380(9)	C22-C23	1.376(8)
C22-H22	0.9400	C23-C24	1.378(8)	C23-H23	0.9400
C24-C25	1.409(9)	C24-C43	1.502(12)	C25-C26	1.398(8)
C25-H25	0.9400	C26-H26	0.9400	O31-C30	1.243(6)
O31-Co1#6	2.069(3)	O32-C30	1.263(6)	O32-Co2#6	2.017(3)
C30-C31	1.487(6)	C31-C36	1.375(6)	C31-C32	1.388(7)
C32-C33	1.379(7)	C32-H32	0.9400	C33-C34	1.402(7)
C33-H33	0.9400	C34-C35	1.358(7)	C34-C45	1.485(6)
C35-C36	1.400(6)	C35-H35	0.9400	C36-H36	0.9400
C41-C42	1.380(6)	C41-C46	1.397(6)	C42-C43	1.386(7)
C42-H42	0.9400	C43-C44	1.388(6)	C44-C45	1.412(6)
C44-H44	0.9400	C45-C46	1.404(6)	C46-H46	0.9400
O51-C50	1.303(7)	O52-C50	1.255(6)	C50-C51	1.495(8)
C51-C52	1.407(8)	C51-C56	1.415(8)	C52-C53	1.398(7)
C52-H52	0.9400	C53-C54	1.383(8)	C53-H53	0.9400
C54-C55	1.395(8)	C54-C81	1.469(7)	C55-C56	1.385(8)
C55-H55	0.9400	C56-H56	0.9400	O61-C60	1.244(6)
O61-Co3#7	1.985(4)	O62-C60	1.242(6)	O62-Co1#7	2.073(3)
C60-C61	1.515(6)	C61-C66	1.380(7)	C61-C62	1.387(7)
C62-C63	1.383(6)	C62-H62	0.9400	C63-C64	1.376(7)
C63-H63	0.9400	C64-C65	1.395(7)	C64-C83	1.496(6)
C65-C66	1.365(7)	C65-H65	0.9400	C66-H66	0.9400
O71-C70	1.269(8)	O72-C70	1.238(8)	O72-Co3#8	1.911(5)
C70-C71	1.507(8)	C71-C72	1.356(9)	C71-C76	1.388(9)
C72-C73	1.423(9)	C72-H72	0.9400	C73-C74	1.369(9)
C73-H73	0.9400	C74-C75	1.388(9)	C74-C85	1.531(8)
C75-C76	1.415(9)	C75-H75	0.9400	C76-H76	0.9400
C81-C82	1.390(6)	C81-C86	1.414(7)	C82-C83	1.356(7)
C82-H82	0.9400	C83-C84	1.401(6)	C84-C85	1.346(7)
C84-H84	0.9400	C85-C86	1.403(7)	C86-H86	0.9400
O31#1-Co1-O62#2	87.39(17)	O31#1-Co1-O11	173.23(14)	O62#2-Co1-O11	87.47(16)
O31#1-Co1-O1	98.57(12)	O62#2-Co1-O1	96.84(14)	O11-Co1-O1	86.42(12)
O31#1-Co1-O2	87.52(16)	O62#2-Co1-O2	88.39(17)	O11-Co1-O2	87.94(16)
O1-Co1-O2	172.12(16)	O31#1-Co1-O52	89.03(14)	O62#2-Co1-O52	175.91(15)
O11-Co1-O52	95.94(14)	O1-Co1-O52	85.67(14)	O2-Co1-O52	89.46(17)
O1-Co2-O32#1	106.21(14)	O1-Co2-O51	88.98(16)	O32#1-Co2-O51	94.90(18)
O1-Co2-O21#3	149.5(4)	O32#1-Co2-O21#3	103.1(3)	O51-Co2-O21#3	96.7(5)
O1-Co2-O3	80.22(15)	O32#1-Co2-O3	87.53(15)	O51-Co2-O3	169.17(16)
O21#3-Co2-O3	93.0(5)	O72#4-Co3-O1	120.2(2)	O72#4-Co3-O61#2	124.9(2)
O1-Co3-O61#2	112.45(15)	O72#4-Co3-O12	94.4(2)	O1-Co3-O12	93.93(14)
O61#2-Co3-O12	97.30(16)	O72#4-Co3-O3	88.74(19)	O1-Co3-O3	75.54(12)
O61#2-Co3-O3	89.40(15)	O12-Co3-O3	169.12(14)	Co3-O1-Co2	113.73(16)
Co3-O1-Co1	109.20(14)	Co2-O1-Co1	112.95(14)	Co2-O3-Co3	90.07(14)
C10-O11-Co1	132.3(3)	C10-O12-Co3	130.4(3)	O12-C10-O11	125.8(4)
O12-C10-C11	117.2(4)	O11-C10-C11	117.1(4)	C16-C11-C12	119.2(4)
C16-C11-C10	120.7(4)	C12-C11-C10	120.1(4)	C11-C12-C13	120.6(5)
C11-C12-H12	119.7	C13-C12-H12	119.7	C12-C13-C14	119.9(5)
C12-C13-H13	120.1	C14-C13-H13	120.1	C15-C14-C13	118.2(4)
C15-C14-C41	123.0(5)	C13-C14-C41	118.8(5)	C14-C15-C16	121.7(5)
C14-C15-H15	119.1	C16-C15-H15	119.1	C11-C16-C15	120.3(5)
C11-C16-H16	119.9	C15-C16-H16	119.9	C20-O21-Co2#5	90.0(7)
C20-O22-Co2#5	87.6(6)	O22-C20-O21	121.8(7)	O22-C20-C21	121.2(7)
O21-C20-C21	117.1(7)	O22-C20-Co2#5	63.6(6)	O21-C20-Co2#5	59.0(6)

277

C11-C16-H16	119.9	C15-C16-H16	119.9	C20-O21-Co2#5	90.0(7)
C20-O22-Co2#5	87.6(6)	O22-C20-O21	121.8(7)	O22-C20-C21	121.2(7)
O21-C20-C21	117.1(7)	O22-C20-Co2#5	63.6(6)	O21-C20-Co2#5	59.0(6)
C21-C20-Co2#5	169.6(5)	C22-C21-C26	123.0(6)	C22-C21-C20	117.9(6)
C26-C21-C20	119.1(7)	C21-C22-C23	117.9(7)	C21-C22-H22	121.1
C23-C22-H22	121.1	C22-C23-C24	122.8(7)	C22-C23-H23	118.6
C24-C23-H23	118.6	C23-C24-C25	117.6(6)	C23-C24-C43	125.3(10)
C25-C24-C43	117.2(10)	C26-C25-C24	121.1(7)	C26-C25-H25	119.4
C24-C25-H25	119.4	C21-C26-C25	117.6(7)	C21-C26-H26	121.2
C25-C26-H26	121.2	C30-O31-Co1#6	136.4(3)	C30-O32-Co2#6	125.6(3)
O31-C30-O32	126.2(4)	O31-C30-C31	118.0(4)	O32-C30-C31	115.8(4)
C36-C31-C32	117.6(4)	C36-C31-C30	121.0(4)	C32-C31-C30	121.4(4)
C33-C32-C31	121.4(5)	C33-C32-H32	119.3	C31-C32-H32	119.3
C32-C33-C34	120.8(5)	C32-C33-H33	119.6	C34-C33-H33	119.6
C35-C34-C33	117.5(4)	C35-C34-C45	122.6(5)	C33-C34-C45	119.9(4)
C34-C35-C36	121.8(4)	C34-C35-H35	119.1	C36-C35-H35	119.1
C31-C36-C35	120.9(4)	C31-C36-H36	119.6	C35-C36-H36	119.6
C42-C41-C46	119.6(4)	C42-C41-C14	122.6(4)	C46-C41-C14	117.8(4)
C41-C42-C43	121.9(4)	C41-C42-H42	119.0	C43-C42-H42	119.0
C42-C43-C44	118.1(4)	C42-C43-C24	123.3(7)	C44-C43-C24	118.5(7)
C43-C44-C45	121.9(4)	C43-C44-H44	119.0	C45-C44-H44	119.0
C46-C45-C44	117.9(4)	C46-C45-C34	120.4(4)	C44-C45-C34	121.6(4)
C41-C46-C45	120.3(4)	C41-C46-H46	119.8	C45-C46-H46	119.8
C50-O51-Co2	133.7(4)	C50-O52-Co1	124.9(3)	O52-C50-O51	128.4(5)
O52-C50-C51	117.1(5)	O51-C50-C51	114.5(5)	C52-C51-C56	120.3(5)
C52-C51-C50	121.5(5)	C56-C51-C50	117.8(6)	C53-C52-C51	118.7(5)
C53-C52-H52	120.6	C51-C52-H52	120.6	C54-C53-C52	121.9(6)
C54-C53-H53	119.0	C52-C53-H53	119.0	C53-C54-C55	118.1(5)
C53-C54-C81	123.6(5)	C55-C54-C81	118.1(5)	C56-C55-C54	122.6(6)
C56-C55-H55	118.7	C54-C55-H55	118.7	C55-C56-C51	118.1(6)
C55-C56-H56	120.9	C51-C56-H56	120.9	C60-O61-Co3#7	119.3(3)
C60-O62-Co1#7	142.3(3)	O62-C60-O61	126.3(5)	O62-C60-C61	117.6(4)
O61-C60-C61	115.8(5)	C66-C61-C62	119.4(4)	C66-C61-C60	121.0(5)
C62-C61-C60	119.5(4)	C63-C62-C61	120.8(5)	C63-C62-H62	119.6
C61-C62-H62	119.6	C64-C63-C62	120.1(5)	C64-C63-H63	119.9
C62-C63-H63	119.9	C63-C64-C65	118.1(4)	C63-C64-C83	121.2(4)
C65-C64-C83	120.5(4)	C66-C65-C64	122.2(5)	C66-C65-H65	118.9
C64-C65-H65	118.9	C65-C66-C61	119.2(5)	C65-C66-H66	120.4
C61-C66-H66	120.4	C70-O72-Co3#8	134.4(5)	O72-C70-O71	126.7(6)
O72-C70-C71	115.5(5)	O71-C70-C71	117.8(5)	C72-C71-C76	120.2(6)
C72-C71-C70	118.8(6)	C76-C71-C70	121.0(6)	C71-C72-C73	120.5(7)
C71-C72-H72	119.8	C73-C72-H72	119.8	C74-C73-C72	120.9(7)
C74-C73-H73	119.5	C72-C73-H73	119.5	C73-C74-C75	117.7(6)
C73-C74-C85	119.1(6)	C75-C74-C85	123.2(6)	C74-C75-C76	122.1(6)
C74-C75-H75	118.9	C76-C75-H75	118.9	C71-C76-C75	118.5(6)
C71-C76-H76	120.8	C75-C76-H76	120.8	C82-C81-C86	116.9(4)
C82-C81-C54	122.9(4)	C86-C81-C54	120.1(4)	C83-C82-C81	123.7(5)
C83-C82-H82	118.1	C81-C82-H82	118.1	C82-C83-C84	117.5(4)
C82-C83-C64	122.0(4)	C84-C83-C64	120.5(4)	C85-C84-C83	121.8(5)
C85-C84-H84	119.1	C83-C84-H84	119.1	C84-C85-C86	120.1(5)
C84-C85-C74	121.0(5)	C86-C85-C74	118.4(4)	C85-C86-C81	119.6(4)
C85-C86-H86	120.2	C81-C86-H86	120.2		

Symmetry transformation codes:#1 x+1/2,-y+3/2,z-1/2   #2 x+1/2,-y+3/2,z+1/2   #3 x+1/2,-y+1/2,z-1/2   #4 x+1/2,-y+1/2,z+1/2   #5 x-1/2,-y+1/2,z+1/2   #6 x-1/2,-y+3/2,z+1/2   #7 x-1/2,-y+3/2,z-1/2   #8 x-1/2,-y+1/2,z-1/2

Table 10.12 (c) Bond lengths (Å) and angles (°) for Co-MOF-BTB-plate System.

10.13 Detailed Information for Eu-MOF-BTB System from Single Crystal Analysis

Atom	x/a	y/b	z/c	U_{eq}
Eu1	0.3333	0.344385(4)	0.1667	0.01955(3)
O1W	0.3333	0.42965(9)	0.1667	0.0656(10)
O2	0.38672(6)	0.30262(6)	0.21966(12)	0.0274(3)
O3	0.31917(6)	0.27583(6)	0.33623(11)	0.0267(3)
C1	0.35467(8)	0.26877(8)	0.28709(17)	0.0250(4)
C2	0.35445(9)	0.21691(8)	0.30290(17)	0.0248(4)
C3	0.31439(9)	0.17523(9)	0.36286(19)	0.0293(4)
C4	0.31204(9)	0.12572(9)	0.3703(2)	0.0297(4)
C5	0.35053(8)	0.11724(8)	0.31739(19)	0.0265(4)
C6	0.39099(9)	0.15973(9)	0.2569(2)	0.0309(5)
C7	0.39256(9)	0.20870(9)	0.2498(2)	0.0299(4)
C8	0.39751(10)	0.06418(10)	0.3333	0.0282(6)
C9	0.34908(8)	0.06450(8)	0.32522(19)	0.0262(4)
C10	0.30101(8)	0.01613(8)	0.32561(19)	0.0275(4)
C11	0.30025(10)	-0.03308(10)	0.3333	0.0253(6)
C12	0.24770(10)	-0.08563(10)	0.3333	0.0261(6)
C13	0.20362(9)	-0.09140(9)	0.2735(2)	0.0321(5)
C14	0.15576(9)	-0.14040(9)	0.2723(2)	0.0320(5)
C15	0.15015(10)	-0.18318(10)	0.3333	0.0252(6)
C16	0.09722(10)	-0.23612(10)	0.3333	0.0272(6)
O4	0.06932(7)	-0.24912(7)	0.24776(14)	0.0367(4)

[*] U_{eq} is defined as one third of the trace of the orthogonalized U_{ij} tensor.

Table 10.13 (a) Atomic coordinates and equivalent[*] isotropic atomic displacement parameters (Å^2) for Eu-MOF-BTB System.

Eu1-O4#1	2.3570(16)	Eu1-O4#2	2.3570(16)	Eu1-O3#3	2.3893(14)
Eu1-O3#4	2.3894(14)	Eu1-O1W	2.438(3)	Eu1-O2	2.4500(13)
Eu1-O2#5	2.4500(13)	Eu1-O3#5	2.7493(14)	Eu1-O3	2.7494(14)
O2-C1	1.256(3)	O3-C1	1.281(3)	O3-Eu1#6	2.3894(14)
C1-C2	1.492(3)	C2-C3	1.382(3)	C2-C7	1.387(3)
C3-C4	1.386(3)	C4-C5	1.400(3)	C5-C6	1.401(3)
C5-C9	1.491(3)	C6-C7	1.381(3)	C8-C9	1.393(2)
C8-C9#7	1.393(2)	C9-C10	1.379(3)	C10-C11	1.400(2)
C11-C10#7	1.400(2)	C11-C12	1.502(4)	C12-C13	1.396(3)
C12-C13#7	1.396(3)	C13-C14	1.385(3)	C14-C15	1.374(3)
C15-C14#7	1.374(3)	C15-C16	1.513(4)	C16-O4	1.259(2)
C16-O4#7	1.259(2)	O4-Eu1#8	2.3571(16)		
O4#1-Eu1-O4#2	157.39(9)	O4#1-Eu1-O3#3	84.34(6)	O4#2-Eu1-O3#3	89.00(6)
O4#1-Eu1-O3#4	89.00(6)	O4#2-Eu1-O3#4	84.33(6)	O3#3-Eu1-O3#4	145.51(7)
O4#1-Eu1-O1W	78.69(5)	O4#2-Eu1-O1W	78.69(5)	O3#3-Eu1-O1W	72.75(4)
O3#4-Eu1-O1W	72.76(4)	O4#1-Eu1-O2	121.42(6)	O4#2-Eu1-O2	77.99(6)
O3#3-Eu1-O2	134.69(5)	O3#4-Eu1-O2	76.72(5)	O1W-Eu1-O2	143.02(4)
O4#1-Eu1-O2#5	77.99(6)	O4#2-Eu1-O2#5	121.43(5)	O3#3-Eu1-O2#5	76.73(5)
O3#4-Eu1-O2#5	134.69(5)	O1W-Eu1-O2#5	143.02(4)	O2-Eu1-O2#5	73.96(8)
O4#1-Eu1-O3#5	123.99(6)	O4#2-Eu1-O3#5	72.04(5)	O3#3-Eu1-O3#5	66.89(5)
O3#4-Eu1-O3#5	140.48(2)	O1W-Eu1-O3#5	129.73(3)	O2-Eu1-O3#5	67.80(5)
O2#5-Eu1-O3#5	49.95(5)	O4#1-Eu1-O3	72.04(5)	O4#2-Eu1-O3	123.99(6)
O3#3-Eu1-O3	140.48(2)	O3#4-Eu1-O3	66.90(5)	O1W-Eu1-O3	129.73(3)
O2-Eu1-O3	49.95(5)	O2#5-Eu1-O3	67.80(5)	O3#5-Eu1-O3	100.53(6)
C1-O2-Eu1	99.15(12)	C1-O3-Eu1#6	132.29(13)	C1-O3-Eu1	84.77(11)
Eu1#6-O3-Eu1	106.96(5)	O2-C1-O3	121.34(18)	O2-C1-C2	119.39(19)
O3-C1-C2	119.02(19)	C3-C2-C7	119.18(19)	C3-C2-C1	121.07(19)
C7-C2-C1	119.57(19)	C2-C3-C4	120.8(2)	C3-C4-C5	120.3(2)
C4-C5-C6	118.47(19)	C4-C5-C9	121.22(19)	C6-C5-C9	120.31(19)
C7-C6-C5	120.4(2)	C6-C7-C2	120.8(2)	C9-C8-C9#7	120.8(3)
C10-C9-C8	119.3(2)	C10-C9-C5	121.63(19)	C8-C9-C5	119.10(19)
C9-C10-C11	121.0(2)	C10-C11-C10#7	118.6(3)	C10-C11-C12	120.69(13)
C10#7-C11-C12	120.69(13)	C13-C12-C13#7	118.6(3)	C13-C12-C11	120.70(14)
C13#7-C12-C11	120.69(14)	C14-C13-C12	120.2(2)	C15-C14-C13	120.7(2)
C14-C15-C14#7	119.6(3)	C14-C15-C16	120.22(14)	C14#7-C15-C16	120.22(14)
O4-C16-O4#7	124.7(3)	O4-C16-C15	117.67(14)	O4#7-C16-C15	117.67(14)
C16-O4-Eu1#8	132.46(16)				

Symmetry transformation codes:#1 -y,x-y,z   #2 y+2/3,x+1/3,-z+1/3   #3 -x+y+1/3,-x+2/3,z-1/3   #4 x-y+1/3,-y+2/3,-z+2/3   #5 -x+2/3,-x+y+1/3,-z+1/3   #6 -y+2/3,x-y+1/3,z+1/3   #7 y+1/3,x-1/3,-z+2/3   #8 -x+y,-x,z

Table 10.13 (b) Bond lengths (Å) and angles (°) for Eu-MOF-BTB System.

10.14 Detailed Information for Ho-MOF-BTB System from Single Crystal Analysis

Atom	x/a	y/b	z/c	U_{eq}
Ho1	0.42488(2)	0.340227(14)	-0.043457(11)	0.02023(6)
O1	0.6830(4)	0.3658(3)	-0.0106(3)	0.0422(8)
O2	0.2173(4)	0.2353(2)	-0.0257(2)	0.0356(7)
C1	0.6732(4)	0.6283(3)	0.5416(2)	0.0214(8)
C2	0.7603(4)	0.5753(3)	0.5871(2)	0.0230(8)
C3	0.8092(4)	0.6143(3)	0.6819(2)	0.0225(8)
C4	0.7696(5)	0.7071(3)	0.7300(2)	0.0253(8)
C5	0.6825(5)	0.7620(3)	0.6866(2)	0.0239(8)
C6	0.6342(4)	0.7206(3)	0.5921(2)	0.0235(8)
C11	0.6211(4)	0.5858(3)	0.4407(2)	0.0210(8)
C12	0.5816(5)	0.6498(3)	0.3887(3)	0.0278(9)
C13	0.5373(5)	0.6113(3)	0.2940(3)	0.0275(9)
C14	0.5290(4)	0.5085(3)	0.2505(2)	0.0210(8)
C15	0.5654(4)	0.4438(3)	0.3017(2)	0.0230(8)
C16	0.6120(4)	0.4822(3)	0.3960(2)	0.0242(8)
C17	0.4868(4)	0.4654(3)	0.1485(2)	0.0222(8)
O11	0.4929(3)	0.5219(2)	0.09651(17)	0.0278(6)
O12	0.4474(3)	0.3720(2)	0.11588(18)	0.0312(7)
C21	0.9030(4)	0.5574(3)	0.7294(2)	0.0221(8)
C22	0.9997(5)	0.4954(3)	0.6840(3)	0.0269(9)
C23	1.0873(4)	0.4432(3)	0.7286(3)	0.0252(8)
C24	1.0833(4)	0.4547(3)	0.8215(2)	0.0212(8)
C25	0.9890(4)	0.5170(3)	0.8681(3)	0.0246(8)
C26	0.8979(4)	0.5666(3)	0.8225(3)	0.0245(8)
C27	1.1850(4)	0.4021(3)	0.8696(2)	0.0210(8)
O21	1.2424(3)	0.3282(2)	0.82504(18)	0.0262(6)
O22	1.2166(3)	0.4356(2)	0.95756(17)	0.0233(6)
C31	0.6423(5)	0.8621(3)	0.7386(3)	0.0245(8)
C32	0.6282(5)	0.8863(3)	0.8324(3)	0.0318(10)
C33	0.5901(5)	0.9797(3)	0.8787(3)	0.0334(10)
C34	0.5636(5)	1.0517(3)	0.8336(3)	0.0249(8)

C35	0.5786(5)	1.0287(3)	0.7406(3)	0.0296(9)
C36	0.6182(5)	0.9357(3)	0.6944(3)	0.0303(9)
C37	0.5164(4)	1.1520(3)	0.8814(3)	0.0252(8)
O31	0.5035(4)	1.1761(2)	0.96533(19)	0.0319(7)
O32	0.4883(4)	1.2122(2)	0.83422(19)	0.0352(7)
O1A	0.088(6)	0.746(3)	0.1019(5)	0.058(3)
C1A	0.0707(11)	0.7994(7)	0.1783(5)	0.059(3)
N1A	0.135(2)	0.7926(14)	0.2562(5)	0.0612(19)
C2A	0.2344(11)	0.7215(8)	0.2638(7)	0.062(3)
C3A	0.1110(18)	0.8636(12)	0.3415(6)	0.094(5)
O1B	0.103(7)	0.733(4)	0.0845(5)	0.058(3)
C1B	0.1492(12)	0.7361(8)	0.1636(6)	0.052(3)
N1B	0.124(3)	0.8052(14)	0.2372(5)	0.0612(19)
C2B	0.0392(15)	0.8857(9)	0.2352(9)	0.091(5)
C3B	0.167(2)	0.7934(14)	0.3267(7)	0.117(6)
O1C	0.8396(9)	-0.0337(5)	0.0793(10)	0.096(4)
C1C	0.7937(15)	0.0400(6)	0.1296(10)	0.075(3)
N1C	0.8148(15)	0.1329(5)	0.1252(9)	0.0533(19)
C2C	0.749(3)	0.2156(8)	0.1776(15)	0.107(6)
C3C	0.8980(18)	0.1536(10)	0.0568(10)	0.093(5)
O1D	0.804(2)	-0.0348(9)	0.155(2)	0.124(9)
C1D	0.778(3)	0.0539(11)	0.1778(18)	0.075(3)
N1D	0.823(3)	0.1219(11)	0.1396(16)	0.0533(19)
C2D	0.776(4)	0.2199(16)	0.157(3)	0.110(11)
C3D	0.912(3)	0.093(3)	0.0662(18)	0.121(10)
O1E	0.239(5)	0.685(3)	0.517(5)	0.121(17)
C1E	0.231(3)	0.777(2)	0.540(5)	0.104(15)
N1E	0.1153(6)	0.8194(4)	0.5660(5)	0.0842(18)
C2E	0.014(7)	0.780(4)	0.614(5)	0.15(2)
C3E	0.096(7)	0.919(3)	0.557(5)	0.109(18)
O1F	0.127(3)	0.6524(8)	0.541(2)	0.120(10)
C1F	0.1855(18)	0.7396(11)	0.558(4)	0.137(13)
N1F	0.1153(6)	0.8194(4)	0.5660(5)	0.0842(18)
C2F	-0.0387(11)	0.8148(19)	0.544(3)	0.119(13)
C3F	0.198(2)	0.9178(11)	0.583(3)	0.112(12)
O1G	0.3370(8)	0.8136(10)	0.5191(7)	0.147(6)

C1G	0.2456(10)	0.8598(7)	0.5609(9)	0.094(4)
N1G	0.1153(6)	0.8194(4)	0.5660(5)	0.0842(18)
C2G	0.0702(16)	0.7135(7)	0.5401(13)	0.121(6)
C3G	0.0063(15)	0.8847(11)	0.5990(17)	0.171(9)
O1W	0.2650(7)	0.1423(5)	0.6755(4)	0.113(2)
O2W	0.452(2)	0.0844(7)	0.5337(5)	0.132(5)
O3W	0.332(12)	0.080(5)	0.525(4)	0.132(5)

[*] U_{eq} is defined as one third of the trace of the orthogonalized U_{ij} tensor.

Table 10.14 (a) Atomic coordinates and equivalent[*] isotropic atomic displacement parameters ($Å^2$) for Ho-MOF-BTB System.

Atom	sof	Atom	sof	Atom	sof
O1A - C3A	0.526(8)	O1B - C3B	0.474(8)		
O1C - C3C	0.643(16)	O1D - C3D	0.357(16)		
O1E - C3E	0.116(4)	O1F - C3F	0.236(10)	O1G - C3G	0.647(10)
O2W	0.86(3)	O3W	0.14(3)		

Table 10.14 (b) Site occupancy factors that deviate from unity for Ho-MOF-BTB System.

Ho1-O12	2.334(3)	Ho1-O32#1	2.342(3)	Ho1-O1	2.361(3)
Ho1-O11#2	2.381(3)	Ho1-O2	2.399(3)	Ho1-O22#3	2.419(3)
Ho1-O21#3	2.440(3)	Ho1-O31#1	2.474(3)	Ho1-O11	2.767(3)
O1-H11	0.829(10)	O1-H12	0.828(10)	O2-H21	0.826(10)
O2-H22	0.827(10)	C1-C6	1.387(5)	C1-C2	1.392(5)
C1-C11	1.496(5)	C2-C3	1.404(5)	C3-C4	1.384(5)
C3-C21	1.484(5)	C4-C5	1.392(5)	C5-C6	1.402(5)
C5-C31	1.484(5)	C11-C16	1.390(5)	C11-C12	1.395(5)
C12-C13	1.395(5)	C13-C14	1.378(6)	C14-C15	1.387(5)
C14-C17	1.497(5)	C15-C16	1.392(5)	C17-O12	1.250(5)
C17-O11	1.269(5)	O11-Ho1#2	2.381(3)	C21-C22	1.390(5)
C21-C26	1.400(5)	C22-C23	1.379(5)	C23-C24	1.391(5)
C24-C25	1.384(5)	C24-C27	1.491(5)	C25-C26	1.381(5)
C27-O21	1.248(5)	C27-O22	1.283(4)	C27-Ho1#4	2.782(4)
O21-Ho1#4	2.440(3)	O22-Ho1#4	2.419(3)	C31-C36	1.394(5)
C31-C32	1.403(5)	C32-C33	1.377(6)	C33-C34	1.388(6)
C34-C35	1.393(5)	C34-C37	1.494(5)	C35-C36	1.377(6)
C37-O31	1.253(5)	C37-O32	1.275(5)	O31-Ho1#5	2.474(3)
O32-Ho1#5	2.342(3)	O1A-C1A	1.226(7)	C1A-N1A	1.307(6)
N1A-C2A	1.419(7)	N1A-C3A	1.442(7)	O1C-C1C	1.225(7)
C1C-N1C	1.306(6)	N1C-C2C	1.419(7)	N1C-C3C	1.443(7)
O1E-C1E	1.226(7)	C1E-N1E	1.307(6)	N1E-C2E	1.419(7)
N1E-C3E	1.443(7)	O1W-O2W	2.893(15)		
O12-Ho1-O32#1	134.79(10)	O12-Ho1-O1	81.30(13)	O32#1-Ho1-O1	79.02(12)
O12-Ho1-O11#2	116.33(10)	O32#1-Ho1-O11#2	95.88(10)	O1-Ho1-O11#2	72.76(11)
O12-Ho1-O2	77.54(11)	O32#1-Ho1-O2	93.29(12)	O1-Ho1-O2	141.05(12)
O11#2-Ho1-O2	146.17(11)	O12-Ho1-O22#3	91.56(10)	O32#1-Ho1-O22#3	128.21(10)
O1-Ho1-O22#3	140.56(10)	O11#2-Ho1-O22#3	76.10(10)	O2-Ho1-O22#3	72.68(11)
O12-Ho1-O21#3	140.77(10)	O32#1-Ho1-O21#3	74.63(10)	O1-Ho1-O21#3	136.44(12)
O11#2-Ho1-O21#3	76.14(9)	O2-Ho1-O21#3	75.07(11)	O22#3-Ho1-O21#3	53.66(9)
O12-Ho1-O31#1	81.29(10)	O32#1-Ho1-O31#1	54.20(9)	O1-Ho1-O31#1	73.54(11)
O11#2-Ho1-O31#1	138.51(10)	O2-Ho1-O31#1	71.21(11)	O22#3-Ho1-O31#1	143.89(10)
O21#3-Ho1-O31#1	114.93(9)	O12-Ho1-O11	50.02(9)	O32#1-Ho1-O11	151.34(11)
O1-Ho1-O11	74.04(11)	O11#2-Ho1-O11	67.05(10)	O2-Ho1-O11	113.82(10)
O22#3-Ho1-O11	71.87(9)	O21#3-Ho1-O11	119.81(9)	O31#1-Ho1-O11	124.40(9)
Ho1-O1-H11	116(3)	Ho1-O1-H12	128(4)	H11-O1-H12	105.8(17)
Ho1-O2-H21	126(3)	Ho1-O2-H22	117(3)	H21-O2-H22	106.1(17)
C6-C1-C2	118.7(3)	C6-C1-C11	120.8(3)	C2-C1-C11	120.6(3)
C1-C2-C3	121.1(3)	C4-C3-C2	118.8(3)	C4-C3-C21	120.7(3)
C2-C3-C21	120.5(3)	C3-C4-C5	121.6(3)	C4-C5-C6	118.3(3)
C4-C5-C31	121.2(3)	C6-C5-C31	120.5(3)	C1-C6-C5	121.6(3)
C16-C11-C12	118.2(3)	C16-C11-C1	121.3(3)	C12-C11-C1	120.5(3)
C13-C12-C11	121.0(4)	C14-C13-C12	120.2(4)	C13-C14-C15	119.4(3)
C13-C14-C17	121.4(3)	C15-C14-C17	119.1(3)	C14-C15-C16	120.5(4)
C11-C16-C15	120.7(4)	O12-C17-O11	120.9(3)	O12-C17-C14	118.2(3)
O11-C17-C14	120.8(3)	C22-C21-C26	118.2(3)	C22-C21-C3	121.5(3)
C26-C21-C3	120.3(3)	C23-C22-C21	121.2(4)	C22-C23-C24	120.0(4)
C25-C24-C23	119.5(3)	C25-C24-C27	121.4(3)	C23-C24-C27	119.0(3)
C26-C25-C24	120.4(3)	C25-C26-C21	120.7(4)	O21-C27-O22	120.1(3)
O21-C27-C24	120.7(3)	O22-C27-C24	119.2(3)	C36-C31-C32	118.0(4)
C36-C31-C5	120.2(3)	C32-C31-C5	121.9(4)	C33-C32-C31	120.6(4)
C32-C33-C34	120.9(4)	C33-C34-C35	118.9(4)	C33-C34-C37	122.0(4)
C35-C34-C37	119.1(4)	C36-C35-C34	120.2(4)	C35-C36-C31	121.4(4)
O31-C37-O32	120.7(4)	O31-C37-C34	121.1(4)	O32-C37-C34	118.2(3)
O1A-C1A-N1A	124.9(7)	C1A-N1A-C2A	124.3(5)	C1A-N1A-C3A	119.5(5)
C2A-N1A-C3A	116.1(6)	O1C-C1C-N1C	125.0(6)	C1C-N1C-C2C	124.3(5)
C1C-N1C-C3C	119.4(5)	C2C-N1C-C3C	115.9(6)	O1E-C1E-N1E	124.7(7)
C1E-N1E-C2E	124.2(6)	C1E-N1E-C3E	119.4(6)	C2E-N1E-C3E	116.0(6)

Symmetry transformation codes:#1 x,y-1,z-1   #2 -x+1,-y+1,-z   #3 x-1,y,z-1   #4 x+1,y,z+1   #5 x,y+1,z+1

Table 10.14 (c) Bond lengths (Å) and angles (°) for Ho-MOF-BTB System.

D—H···A*	d(D—H)	d(H···A)	d(D···A)	∠(DHA)
O1—H11···O22#6	0.829(10)	1.876(15)	2.686(4)	165(5)
O1—H12···O1A#2	0.828(10)	2.14(3)	2.96(3)	168(5)
O1—H12···O1B#2	0.828(10)	1.85(4)	2.66(3)	168(5)
O2—H21···O1B#7	0.826(10)	2.29(4)	3.10(4)	171(5)
O2—H21···O1A#7	0.826(10)	2.19(4)	2.99(4)	163(5)
O2—H22···O1C#8	0.827(10)	1.86(2)	2.662(7)	161(4)
O2—H22···O1D#8	0.827(10)	2.14(4)	2.89(2)	149(5)

* D - donor atom, H - hydrogen, A - acceptor.
Symmetry transformation codes:
#1 x,y-1,z-1   #2 -x+1,-y+1,-z   #3 x-1,y,z-1   #4 x+1,y,z+1   #5 x,y+1,z+1   #6 -x+2,-y+1,-z+1   #7 -x,-y+1,-z
#8 -x+1,-y,-z

Table 10.14 (d) Hydrogen bond (Å and °) information for Ho-MOF-BTB System.

10.15 Detailed Information for Co-formate-1 System from Single Crystal Analysis

Atom	x/a	y/b	z/c	U_{eq}/Uiso
Co1	0.0000	0.0000	0.0000	0.0101(2)
O1	0.2179(3)	0.2068(3)	0.05333(10)	0.0190(5)
H1	0.0936	0.3333	0.0833	0.013
C1	0.2099(5)	0.3333	0.0833	0.0110(7)
N1[a]	0.0976(14)	0.0976(14)	0.2500	0.019(2)
H1A[a]	0.1115	0.2166	0.2500	0.022
H1B[a]	0.2166	0.1115	0.2500	0.022
C2	0.0000	0.0000	0.3052(3)	0.0331(13)
H2A[b]	-0.1280	-0.0181	0.3052	0.050
H2B[b]	0.0698	0.0760	0.3402	0.050
H2C[b]	-0.0073	-0.1234	0.3071	0.050

[*] U_{eq} is defined as one third of the trace of the orthogonalized U_{ij} tensor; [a] Occupation factor = 1/6; [b] Occupation factor = 1/3.

Table 10.15 (a) Atomic coordinates and equivalent[*] and isotropic atomic displacement parameters (Å^2) for

Co-formate-1 System.

Co1-O1#1	2.101(2)	Co1-O1#2	2.101(2)	Co1-O1#3	2.101(2)
Co1-O1#4	2.101(2)	Co1-O1#5	2.101(2)	Co1-O1	2.101(2)
O1-C1	1.258(3)	C1-O1#6	1.258(3)	N1-C2#7	1.461(8)
N1-C2	1.461(8)				
O1#1-Co1-O1#2	91.37(9)	O1#1-Co1-O1#3	88.63(9)	O1#2-Co1-O1#3	180.00(12)
O1#1-Co1-O1#4	91.37(9)	O1#2-Co1-O1#4	91.37(9)	O1#3-Co1-O1#4	88.63(9)
O1#1-Co1-O1#5	88.63(9)	O1#2-Co1-O1#5	88.63(9)	O1#3-Co1-O1#5	91.37(9)
O1#4-Co1-O1#5	180.00(13)	O1#1-Co1-O1	180.0	O1#2-Co1-O1	88.63(9)
O1#3-Co1-O1	91.37(9)	O1#4-Co1-O1	88.63(9)	O1#5-Co1-O1	91.37(9)
C1-O1-Co1	126.0(2)	O1-C1-O1#6	124.9(4)	C2#7-N1-C2	113.9(8)
Co1-O1-C1-O1#6	-177.4(2)				

Symmetry transformation codes:#1 -x,-y,-z   #2 y,-x+y,-z   #3 -y,x-y,z   #4 x-y,x,-z   #5 -x+y,-x,z   #6 x-y+1/3,-y+2/3,-z+1/6
#7 y,x,-z+1/2

Table 10.15 (b) Bond lengths (Å), valence and torsion angles (°) for Co-formate-1 System.

D—H···A*	d(D—H)	d(H···A)	d(D···A)	∠(DHA)
N1—H1A···O1#8	0.92	1.95	2.836(7)	160
N1—H1B···O1#9	0.92	1.95	2.836(7)	160

* D - donor atom, H - hydrogen, A - acceptor.   Symmetry transformation codes:#1 -x,-y,-z   #2 y,-x+y,-z   #3 -y,x-y,z   #4
x-y,x,-z   #5 -x+y,-x,z   #6 x-y+1/3,-y+2/3,-z+1/6   #7 y,x,-z+1/2   #8 -y+1/3,-x+2/3,z+1/6   #9 -x+2/3,-y+1/3,-z+1/3

Table 10.15 (c) Hydrogen bond (Å and °) information for Ci-formate-1 System.

10.16 Detailed Information for Co-formate-2 System from Single Crystal Analysis

Atom	x/a	y/b	z/c	U_{eq}
Co1	0.17657(11)	0.74839(4)	0.37706(18)	0.01035(7)
C1	0.4252(4)	0.7856(2)	0.6257(7)	0.0150(3)
O11	0.33430(17)	0.8568(3)	0.5390(3)	0.0163(5)

O12	0.51756(17)	0.8585(2)	0.7141(3)	0.0175(5)
C2	0.2073(2)	0.4802(4)	0.6375(4)	0.0153(6)
O21	0.2248(2)	0.5281(3)	0.5181(3)	0.0189(5)
O22	0.22553(17)	0.3394(3)	0.7036(3)	0.0171(5)
C3	0.1564(3)	0.9766(3)	0.6315(4)	0.0129(5)
O31	0.12444(17)	0.8423(2)	0.5485(3)	0.0155(4)
O32	0.12184(18)	1.0331(2)	0.7278(3)	0.0167(5)
N1	0.47652(18)	0.1963(3)	0.6370(3)	0.0192(4)
C11	0.3703(5)	0.2313(5)	0.4693(8)	0.0281(12)
C12	0.4807(5)	0.2619(4)	0.7985(8)	0.0218(10)

[*] U_{eq} is defined as one third of the trace of the orthogonalized U_{ij} tensor.

Table 10.16 (a) Atomic coordinates and equivalent[*] and isotropic atomic displacement parameters (Å^2) for Co-formate-2 System.

Co1-O21	2.084(2)	Co1-O22#1	2.090(2)	Co1-O32#2	2.104(2)
Co1-O11	2.112(3)	Co1-O12#3	2.121(3)	Co1-O31	2.124(2)
C1-O11	1.244(5)	C1-O12	1.266(5)	C1-H1	0.9500
O12-Co1#4	2.121(3)	C2-O21	1.250(4)	C2-O22	1.252(4)
C2-H2	0.9500	O22-Co1#5	2.090(2)	C3-O32	1.258(4)
C3-O31	1.261(3)	C3-H3	0.9500	O32-Co1#6	2.104(2)
N1-C11	1.474(7)	N1-C12	1.475(6)	N1-H1A	0.9200
N1-H1B	0.9200	C11-H11A	0.9800	C11-H11B	0.9800
C11-H11C	0.9800	C12-H12A	0.9800	C12-H12B	0.9800
C12-H12C	0.9800				
O21-Co1-O22#1	89.87(9)	O21-Co1-O32#2	177.78(15)	O22#1-Co1-O32#2	90.03(10)
O21-Co1-O11	93.71(11)	O22#1-Co1-O11	89.50(10)	O32#2-Co1-O11	88.50(9)
O21-Co1-O12#3	86.69(10)	O22#1-Co1-O12#3	90.75(10)	O32#2-Co1-O12#3	91.09(11)
O11-Co1-O12#3	179.53(11)	O21-Co1-O31	91.52(10)	O22#1-Co1-O31	178.54(13)
O32#2-Co1-O31	88.56(9)	O11-Co1-O31	90.84(10)	O12#3-Co1-O31	88.91(10)
O11-C1-O12	123.97(17)	O11-C1-H1	118.0	O12-C1-H1	118.0
C1-O11-Co1	127.2(2)	C1-O12-Co1#4	127.45(18)	O21-C2-O22	125.9(3)
O21-C2-H2	117.0	O22-C2-H2	117.0	C2-O21-Co1	127.9(2)
C2-O22-Co1#5	125.5(2)	O32-C3-O31	123.6(3)	O32-C3-H3	118.2
O31-C3-H3	118.2	C3-O31-Co1	124.4(2)	C3-O32-Co1#6	125.24(18)
C11-N1-C12	112.5(4)	C11-N1-H1A	109.1	C12-N1-H1A	109.1
C11-N1-H1B	109.1	C12-N1-H1B	109.1	H1A-N1-H1B	107.8
N1-C11-H11A	109.5	N1-C11-H11B	109.5	H11A-C11-H11B	109.5
N1-C11-H11C	109.5	H11A-C11-H11C	109.5	H11B-C11-H11C	109.5
N1-C12-H12A	109.5	N1-C12-H12B	109.5	H12A-C12-H12B	109.5
N1-C12-H12C	109.5	H12A-C12-H12C	109.5	H12B-C12-H12C	109.5

Symmetry transformation codes:#1 x,-y+1,z-1/2   #2 x,-y+2,z-1/2   #3 x-1/2,-y+3/2,z-1/2   #4 x+1/2,-y+3/2,z+1/2   #5 x,-y+1,z+1/2
#6 x,-y+2,z+1/2

Table 10.16 (b) Bond lengths (Å) and angles (°) for Co-formate-2 System.

D—H···A*	d(D—H)	d(H···A)	d(D···A)	∠(DHA)
C1—H1···O32#7	0.95	2.68	3.196(4)	115
C1—H1···O21	0.95	2.74	3.253(5)	115
C2—H2···O31	0.95	2.54	3.131(4)	121
C2—H2···O21#5	0.95	2.73	3.188(4)	111
C3—H3···O22#8	0.95	2.54	3.085(4)	117
C3—H3···O11	0.95	2.67	3.173(4)	113
N1—H1A···O31#7	0.92	1.94	2.844(3)	166
N1—H1B···O12#9	0.92	1.92	2.831(3)	171

* D - donor atom, H - hydrogen, A - acceptor.
Symmetry transformation codes:#1 x,-y+1,z-1/2   #2 x,-y+2,z-1/2   #3 x-1/2,-y+3/2,z-1/2   #4 x+1/2,-y+3/2,z+1/2   #5
x,-y+1,z+1/2   #6 x,-y+2,z+1/2   #7 x+1/2,y-1/2,z   #8 x,y+1,z   #9 x,y-1,z

Table 10.16 (c) Hydrogen bond (Å and °) information for Co-formate-2 System.

10.17 Detailed Information for Mn-formate System from Single Crystal Analysis

Atom	x/a	y/b	z/c	U_{eq}
Mn1	0.0000	1.0000	0.0000	0.01351(9)
O1	0.22245(10)	1.01342(10)	0.05460(3)	0.02492(16)
C1	0.21656(16)	0.88322(16)	0.0833	0.0201(2)
H1	0.097(3)	0.763(3)	0.0833	0.055(7)
C2	0.6667	0.3333	0.02961(10)	0.0424(5)
H2	0.647(12)	0.267(7)	-0.0015(18)	0.053(16)
H3	0.669(4)	0.214(4)	0.0289(10)	0.055(7)
N2	0.6667	0.2448(4)	0.0833	0.0258(7)
H4	0.779(7)	0.227(7)	0.075(2)	0.059(14)

[*] U_{eq} is defined as one third of the trace of the orthogonalized U_{ij} tensor.

Table 10.17 (a) Atomic coordinates and equivalent[*] isotropic atomic displacement parameters ($Å^2$) for Mn-formate System.

Mn1-O1#1	2.1878(7)	Mn1-O1	2.1878(7)	Mn1-O1#2	2.1878(7)
Mn1-O1#3	2.1878(7)	Mn1-O1#4	2.1878(7)	Mn1-O1#5	2.1878(7)
O1-C1	1.2467(9)	C1-O1#6	1.2467(9)	C1-H1	1.00(2)
C2-N2	1.428(3)	C2-N2#7	1.428(3)	C2-H2	0.86(4)
C2-H3	1.01(3)	N2-H4	1.04(5)		
O1#1-Mn1-O1	89.06(3)	O1#1-Mn1-O1#2	180.00(4)	O1-Mn1-O1#2	90.94(3)
O1#1-Mn1-O1#3	90.94(3)	O1-Mn1-O1#3	180.0	O1#2-Mn1-O1#3	89.06(3)
O1#1-Mn1-O1#4	89.06(3)	O1-Mn1-O1#4	90.94(3)	O1#2-Mn1-O1#4	90.94(3)
O1#3-Mn1-O1#4	89.06(3)	O1#1-Mn1-O1#5	90.94(3)	O1-Mn1-O1#5	89.06(3)
O1#2-Mn1-O1#5	89.06(3)	O1#3-Mn1-O1#5	90.94(3)	O1#4-Mn1-O1#5	180.00(3)
C1-O1-Mn1	126.14(7)	O1-C1-O1#6	125.87(13)	O1-C1-H1	117.06(6)
O1#6-C1-H1	117.06(6)	N2-C2-H2	115(3)	N2#7-C2-H3	105.2(15)
N2#8-C2-H3	106.3(14)	C2#9-N2-C2	117.8(3)	C2#9-N2-H4	117(3)
C2-N2-H4	99(3)				
O1#1-Mn1-O1-C1	-61.09(4)	O1#2-Mn1-O1-C1	118.91(4)	O1#3-Mn1-O1-C1	78.86(15)
O1#4-Mn1-O1-C1	27.96(7)	O1#5-Mn1-O1-C1	-152.04(7)	Mn1-O1-C1-O1#6	176.25(7)

Symmetry transformation codes: #1 y-1,-x+y,-z   #2 -y+1,x-y+2,z   #3 -x,-y+2,-z   #4 -x+y-1,-x+1,z   #5 x-y+1,x+1,-z   #6 y-2/3,x+2/3,-z+1/6 #7 -y+1,x-y,z   #8 -x+y+1,-x+1,z   #9 y+1/3,x-1/3,-z+1/6

Table 10.17 (b) Bond lengths (Å) and angles (°) for Mn-formate System.

D—H···A*	d(D—H)	d(H···A)	d(D···A)	∠(DHA)
N2—H4···O1#10	1.04(5)	1.87(5)	2.902(2)	174(4)
N2—H4···O1#11	1.04(5)	2.59(5)	3.2735(7)	123(3)

* D - donor atom, H - hydrogen, A - acceptor.
Symmetry transformation codes: #10 -y+2,x-y+1,z   #11 -x+4/3,-x+y-1/3,-z+1/6

Table 10.17 (c) Hydrogen bond (Å and °) information for Mn-formate System.

10.18 Detailed Information for Tb-tetraformate System from Single Crystal Analysis

Atom	x/a	y/b	z/c	U_{eq}*/U_{iso}**
Tb1	0.755688(6)	0.605460(3)	0.50035(8)	0.00634(2)
C1	0.75968(16)	0.62073(10)	0.9920(8)	0.0132(3)
O11	0.7782(2)	0.65384(13)	0.8319(3)	0.0167(3)

O12	0.74617(16)	0.65061(14)	1.1609(3)	0.0153(4)
C2	0.4828(2)	0.50454(12)	0.7573(4)	0.0128(4)
O21	0.52827(15)	0.56323(7)	0.6847(2)	0.0136(2)
O22	0.35024(15)	0.49223(7)	0.8190(2)	0.0151(3)
C3	0.9726(2)	0.47825(10)	0.7374(3)	0.0138(3)
O31	0.84349(15)	0.50093(7)	0.6896(2)	0.0150(3)
O32	1.00326(15)	0.42885(7)	0.8602(2)	0.0146(3)
C4	0.5124(2)	0.75310(9)	0.4358(3)	0.0134(4)
O41	0.55716(13)	0.69151(6)	0.4899(3)	0.0177(2)
O42	0.39425(12)	0.78330(6)	0.5029(3)	0.0139(2)
N1	0.32630(19)	0.67636(9)	0.8153(3)	0.0174(3)
C11	0.1662(3)	0.65067(14)	0.8049(5)	0.0332(5)
C12	0.3795(3)	0.68545(13)	1.0218(4)	0.0316(5)
H1	0.7553	0.5687	0.9869	0.039(8)
H2	0.5548	0.4657	0.7668	0.035(8)
H3	1.0573	0.5010	0.6735	0.020(6)
H4	0.5707	0.7786	0.3385	0.015(6)
H1A	0.385(3)	0.6445(13)	0.777(5)	0.038(9)
H1B	0.333(4)	0.7158(12)	0.763(5)	0.042(9)
H11A	0.0975	0.6903	0.8462	0.052(6)
H11B	0.1528	0.6085	0.8936	0.052(6)
H11C	0.1422	0.6362	0.6679	0.052(6)
H12A	0.3710	0.6386	1.0924	0.050(5)
H12B	0.3165	0.7224	1.0890	0.050(5)
H12C	0.4866	0.7015	1.0215	0.050(5)

[*] U_{eq} is defined as one third of the trace of the orthogonalized U_{ij} tensor. [**] U_{iso} is shown for H atoms

Table 10.18 (a) Atomic coordinates and equivalent[*] isotropic atomic displacement parameters (Å^2) for Tb-tetraformate System.

Tb1-O41	2.3402(11)	Tb1-O22#1	2.3479(14)	Tb1-O42#2	2.3623(10)
Tb1-O32#3	2.3904(13)	Tb1-O11	2.403(2)	Tb1-O31	2.4156(14)
Tb1-O12#4	2.425(3)	Tb1-O21	2.4646(13)	C1-O11	1.243(5)
C1-O12	1.264(5)	O12-Tb1#5	2.425(3)	C2-O21	1.241(3)
C2-O22	1.251(2)	O22-Tb1#6	2.3479(14)	C3-O31	1.244(2)
C3-O32	1.250(2)	O32-Tb1#7	2.3904(13)	C4-O41	1.243(2)
C4-O42	1.254(2)	O42-Tb1#8	2.3623(10)	N1-C12	1.472(3)
N1-C11	1.477(3)	N1-H1A	0.82(2)	N1-H1B	0.80(2)
O41-Tb1-O22#1	101.58(5)	O41-Tb1-O42#2	78.73(4)	O22#1-Tb1-O42#2	149.01(7)
O41-Tb1-O32#3	144.78(6)	O22#1-Tb1-O32#3	86.83(5)	O42#2-Tb1-O32#3	77.05(5)
O41-Tb1-O11	80.94(8)	O22#1-Tb1-O11	142.32(7)	O42#2-Tb1-O11	68.65(7)
O32#3-Tb1-O11	112.86(6)	O41-Tb1-O31	141.28(7)	O22#1-Tb1-O31	78.44(5)
O42#2-Tb1-O31	120.71(6)	O32#3-Tb1-O31	73.78(5)	O11-Tb1-O31	77.07(7)
O41-Tb1-O12#4	73.67(7)	O22#1-Tb1-O12#4	75.90(7)	O42#2-Tb1-O12#4	74.52(8)
O32#3-Tb1-O12#4	75.46(5)	O11-Tb1-O12#4	138.52(5)	O31-Tb1-O12#4	140.63(7)
O41-Tb1-O21	68.08(5)	O22#1-Tb1-O21	72.88(5)	O42#2-Tb1-O21	132.67(5)
O32#3-Tb1-O21	145.74(4)	O11-Tb1-O21	73.47(6)	O31-Tb1-O21	75.26(5)
O12#4-Tb1-O21	123.40(5)	O11-C1-O12	125.35(17)	C1-O11-Tb1	127.7(2)
C1-O12-Tb1#5	133.9(2)	O21-C2-O22	125.54(18)	C2-O21-Tb1	136.44(12)
C2-O22-Tb1#6	132.31(13)	O31-C3-O32	127.16(18)	C3-O31-Tb1	133.33(13)
C3-O32-Tb1#7	129.56(12)	O41-C4-O42	123.4(2)	C4-O41-Tb1	147.93(13)
C4-O42-Tb1#8	142.78(13)	C12-N1-C11	112.33(19)	C12-N1-H1A	100(2)
C11-N1-H1A	111(2)	C12-N1-H1B	107(2)	C11-N1-H1B	109(2)
H1A-N1-H1B	117(3)				

Symmetry transformation codes:#1 -x+1,-y+1,z-1/2   #2 x+1/2,-y+3/2,z   #3 -x+2,-y+1,z-1/2   #4 x,y,z-1   #5 x,y,z+1   #6 -x+1,-y+1,z+1/2   #7 -x+2,-y+1,z+1/2   #8 x-1/2,-y+3/2,z

Table 10.18 (b) Bond lengths (Å) and angles (°) for Tb-tetraformate System.

D—H⋯A*	d(D—H)	d(H⋯A)	d(D⋯A)	∠(DHA)
N1—H1A⋯O21	0.82(2)	2.04(2)	2.853(2)	179(3)
N1—H1A⋯O41	0.82(2)	2.59(3)	2.987(3)	111(2)
N1—H1B⋯O42	0.80(2)	2.20(3)	2.925(2)	150(3)
N1—H1B⋯O11#8	0.80(2)	2.47(3)	3.126(3)	140(3)
C1—H1⋯O31	0.95	2.47	3.071(4)	121.0
C3—H3⋯O32#3	0.95	2.52	3.054(2)	115.8

* D - donor atom, H - hydrogen, A - acceptor.
Symmetry transformation codes:#1 -x+1,-y+1,z-1/2   #2 x+1/2,-y+3/2,z   #3 -x+2,-y+1,z-1/2   #4 x,y,z-1   #5 x,y,z+1
#6 -x+1,-y+1,z+1/2   #7 -x+2,-y+1,z+1/2   #8 x-1/2,-y+3/2,z

Table 10.18 (c) Hydrogen bond (Å and °) information for Tb-tetraformate System.

Bibliography

Chapter 1

(1) Allendorf, M. D.; Bauer, C. A.; Bhakta, R. K. and Houk, R. J. T. *Chem. Soc. Rev.* **2009**, *38*, 1330.

(2) Kurmoo, M. *Chem. Soc. Rev.* **2009**, *38*, 1353.

(3) O'Keeffe, M. *Chem. Soc. Rev.* **2009**, *38*, 1215.

(4) Perry IV, J. J.; Perman, J. A. and Zaworotko, M. J. *Chem. Soc. Rev.* **2009**, *38*, 1400.

(5) Tranchemontagne, D. J.; Mendoza-Cortes, J. L.; O'Keeffe, M. and Yaghi, O. M. *Chem. Soc. Rev.* **2009**, *38*, 1257.

(6) Wang, Z. and Cohen, S. M. *Chem. Soc. Rev.* **2009**, *38*, 1315.

(7) Furukawa, H.; Ko, N.; Go, Y. B.; Aratani, N.; Choi, S. B.; Choi, E.; Yazaydin, A. Ö.; Snurr, R. Q.; O'keeffe, M.; Kim, J. and Yaghi, O. M. *Science* **2010**, 1.

(8) Alaerts, L.; Seguin, E.; Poelman, H.; Thibault-Starzyk, F.; Jacobs, P. A. and De Vos, D. E. *Chem. Eur. J.* **2006**, *12*, 7353.

(9) Czaja, A. U.; Trukhan, N. and Müller, U. *Chem. Soc. Rev.* **2009**, *38*, 1284.

(10) Dincă, M.; Dailly, A.; Liu, Y.; Brown, C. M.; Neumann, D. A. and Long, J. R. *J. Am. Chem. Soc.* **2006**, *128*, 16876.

(11) Düren, T.; Bae, Y.-S. and Snurr, R. Q. *Chem. Soc. Rev.* **2009**, *38*, 1237.

(12) Férey, G. and Serre, C. *Chem. Soc. Rev.* **2009**, *38*, 1380.

(13) Gandara, F.; Gornez-Lor, B.; Gutierrez-Puebla, E.; Iglesias, M.; Monge, M. A.; Proserpio, D. M.andSnejko, N. *Chem. Mater.* **2008**, *20*, 72.

(14) Horike, S.; Dincă, M.; Tamaki, K. and Long, J. R. *J. Am. Chem. Soc.* **2008**, *130*, 5854.

(15) Lee, J.; Farha, O. K.; Roberts, J.; Scheidt, K. A.; Nguyen, S. T. and Hupp, J. T. *Chem. Soc. Rev.* **2009**, *38*, 1450.

(16) Li, J.-R.; Kuppler, R. J. and Zhou, H.-C. *Chem. Soc. Rev.* **2009**, *38*, 1477.

(17) Ma, L.; Abney, C. and Lin, W. *Chem. Soc. Rev.* **2009**, *38*, 1248.

(18) Murray, L. J.; Dincă, M. and Long, J. R. *Chem. Soc. Rev.* **2009**, *38*, 1294.

(19) Spokoyny, A. M.; Kim, D.; Sumrein, A. and Mirkin, C. A. *Chem. Soc. Rev.* **2009**, *38*, 1218.

(20) Zacher, D.; Shekhah, O.; Woll, C. and Fischer, R. A. *Chem. Soc. Rev.* **2009**, *38*, 1418.

(21) Kaye, S. S.; Dailly, A.; Yaghi, O. M.andLong, J. R. *J. Am. Chem. Soc.* **2007**, *129*, 14176.

(22) Ma, S. Q.; Sun, D. F.; Wang, X. S. and Zhou, H. C.; *Angew. Chem. Int. Ed.* **2007**, *46*, 2458.

(23) Muller, M.; Hermes, S.; Kaehler, K.; van den Berg, M. W. E.; Muhler, M. and Fischer, R. A. *Chem. Mater.* **2008**, *20*, 4576.

(24) Rowsell, J. L. C.; Spencer, E. C.; Eckert, J.; Howard, J. A. K. and Yaghi, O. M. *Science* **2005**, *309*, 1350.

(25) Sabo, M.; Henschel, A.; Froede, H.; Klemm, E. and Kaskel, S. *J. Mater. Chem.* **2007**, *17*, 3827.

(26) Serre, C.; Millange, F.; Surblé, S. and Férey, G. *Angew. Chem. Int. Ed.* **2004**, *43*, 6286.

(27) Won, J. G.; Seo, J. S.; Kim, J. H.; Kim, H. S.; Kang, Y. S.; Kim, S. J.; Kim, Y. M. and Jegal, J. G. *Adv. Mater.* **2005**, *17*, 80.

(28) Xamena, F.; Abad, A.; Corma, A. and Garcia, H. *J. Catal.* **2007**, *250*, 294.

(29) Yoon, J. W.; Jhung, S. H.; Hwang, Y. K.; Humphrey, S. M.; Wood, P. T. and Chang, J. S. *Adv. Mater.* **2007**, *19*, 1830.

(30) Zhang, J. J.; Zhao, Y.; Gamboa, S. A.; Munoz, M. and Lachgar, A. *Eur. J. Inorg. Chem.* **2008**, 2982.

(31) Qiu, S. and Zhu, G. *Coord. Chem. Rev.* **2009**, *253*, 2891.

(32)   Barrer, R. M. *Hydrothermal chemistry of zeolites,* Academic Press, London, **1982**.

(33)   Byrappa, K. and Yoshimura, M. *Handbook of hydrothermal technology*, William andrew publishing, Norwich, New York, **2001**.

(34)   Rabenau, A. *Angew. Chem. Int. Ed.* **1985**, *24*, 1026.

(35)   Walton, R. I. *Chem. Soc. Rev.* **2002**, *31*, 230.

(36) Demazeau, G. *J. Mater. Chem.* **1999**, *9*, 15.

(37)   Parr Instrument Company, Moline, IL 61265, USA.

(38) Tranchemontagne, D. J. L.; Ni, Z.; O'Keeffe, M. and Yaghi, O. M. *Angew. Chem. Int. Ed.* **2008**, *47*, 5136.

(39) Kitagawa, S. and Kondo, M. *Bull. Chem. Soc. Jpn.* **1998**, *71*, 1739.

(40) Uemura, K.; Matsuda, R. and Kitagawa, S. *J. Solid State Chem.* **2005**, *178*, 2420.

(41) Uemura, T.; Yanai, N. and Kitagawa, S. *Chem. Soc. Rev.* **2009**, *38*, 1228.

(42) Barthelet, K.; Marrot, J.; Riou, D. and Férey G. *Angew. Chem. Int. Ed.* **2002**, *41*, 281.

(43) Millange, F.; Serre, C. and Férey, G. *Chem. Commun.* **2002**, 822.

(44) Serre, C.; Millange, F.; Thouvenot, C.; Nogues, M.; Marsolier, G.; Louer, D. and Férey, G. *J. Am. Chem. Soc.* **2002**, *124*, 13519.

(45) Surblé, S.; Serre, C.; Millange, F.; Pelle, F. and Férey, G. *Solid State Sci.* **2005**, *7*, 1074.

(46) Yaghi, O. M.; O'Keeffe, M.; Ockwig, N. W.; Chae, H. K.; Eddaoudi, M. and Kim J. *Nature* **2003**, *423*, 705.

(47) Fang, Q. R.; Zhu, G. S.; Xue, M.; Sun, J. Y.; Tian, G.; Wu, G. and Qiu, S. L. *Dalton Trans* **2004**, 2202.

(48) Morris, R. E. *Chem. Comm.* **2009**, 2990.

(49) Férey, G. *J. Solid State Chem.* **2000**, *152*, 337.

(50) Shimizu, G. K. H.; Vaidhyanathan, R. and Taylor, J. M. *Chem. Soc. Rev.* **2009**, *38*, 1430.

(51) Yaghi, O. M.; Li, H.; Davis, C.; Richardson, D. and Groy, T. L. *Acc. Chem. Res* **1998**, *31*, 474.

(52) Yaghi, O. M.; O' Keeffe, M. and Kanatzidis, M. G. *J. Solid State Chem.* **2000**, *152*, 1.

(53) Rosi, N. L.; Eddaoudi, M.; Kim, J.; O'Keeffee, M. and Yaghi, O. M. *Cryst. Eng. Comm.* **2002**, *68*, 401.

(54) Kim, J.; Chen, B.; Reineke, T.M.; Li, H.; Eddaoudi, M.; Moler, D. B.; O'Keeffe, M. and Yaghi, O. M. *J. Am. Chem. Soc.* **2001**, *123*, 8239.

(55) O'Keeffe, M.; Eddaoudi, M. ; Li, H.; Reineke, T.; and Yaghi, O. M. *J. Solid State Chem.* **2000**, *152*, 3.

(56) Rowsell, J. L. C. and Yaghi, O. M. *Microporous Mesoporous Mater.* **2004**, *73*, 3.

(57) Kitagawa, S.; Kitaura, R. and Noro, S.-i. *Angew. Chem. Int. Ed.* **2004**, *43*, 2334.

(58) Long, D.-L.; Blake, A. J.; Champness, N. R.; Wilson, C. and Schröder, M. *J. Am. Chem. Soc.* **2001,** *123,* 3401.

(59) Chen, B.; Yang, Y.; Zapata, F.; Lin, G.; Qian, G. and Lobkovsky, E. B. *Adv. Mater.* **2007**, 1693.

(60) Harbuzaru, B. V.; Corma, A.; Rey, F.; Atienzar, P.; Jorda, J. L.; Garcia, H.; Ananias, D.; Carlos, L. D.andRocha, J. *Angew. Chem. Int. Ed.* **2008**, *47*, 1080.

(61) Reineke, T. M.; Eddaoudi, M.; Keeffe, M. O. and Yaghi, O. M. *Angew. Chem. Int. Ed.* **1999**, *38*, 2590.

(62) Reineke, T. M.; Eddaoudi, M.; Fehr, M.; Kelley, D. and Yaghi, O. M. *J. Am. Chem. Soc.* **1999**, *121*, 1651.

(63) Serre, C.; Millange, F.; Thouvenot, C.; Gardant, N.; Pellé, F.; and Férey, G. *J. Mater. Chem.* **2004**, *14*, 1540.

(64) Surblé, S.; Serre, C.; Millange, F. and Férey, G. *Solid State Sci.* **2006**, *8*, 413.

(65) Guo, X.; Zhu, G.; Li, Z.; Sun, F.; Yang, Z. and Qiu, S. *Chem. Commun.* **2006**, 3172.

(66) Gustafsson, M.; Bartoszewicz, A.; Martín-Matute, B.; Sun, J.; Grins, J.; Zhao, T.; Li, Z.; Zhu, G. and Zou X. *Chem. Mater.* **2010**, *22*, 3316.

(67) Luo, J.; Xu, H.; Liu, Y.; Zhao, Y.; Daemen, L. L.; Brown, C.; Timofeeva, T. V. ; Ma, S. and Zhou, H.-C. *J. Am. Chem. Soc.* **2008**, *130*, 9626.

(68) Rosi, N. L.; Kim, J.; Eddaoudi, M.; Chen, B.; O'Keeffe, M. and Yaghi, O. M. *J. Am. Chem. Soc.* **2005**, *127*, 1504.

(69) Choi, J. R.; Tachikawa, T.; Fujitsuka, M. and Majima, T. *Langmuir* **2010**, *26*, 10437.

(70) Devic, T.; Serre, C.; Audebrand, N.; Marrot, J. and Férey, G. *J. Am. Chem. Soc.* **2005**, *127*, 12788.

(71) Chui, S. S.-Y.; Siu, A.; Feng, X.; Zhang, Z. Y.; Mak, T. C. W. and Williams, I. D. *Inorg. Chem. Commun.* **2001**, *4*, 467.

(72) de Lill, D. T.; Gunning, N. S. and Cahill, C. L. *Inorg. Chem.* **2005**, *44*, 258.

(73) Serre, C.; Pelle, F.; Gardant, N. and Férey, G. *Chem. Mater.* **2004**, *16*, 1177.

(74) Zhang, Z.-H.; Shen, Z.-L.; Okamura, T.; Zhu, H.-F.; Sun, W.-Y. and Ueyama, N. *Cryst. Growth Des.* **2005**, *5*, 1191.

(75) http://www.all-creatures.org/hope/gw/02_fossil_fuels_general.htm.

(76) Schlapbach, L. and Züttel, A. *Nature* **2001**, *414*, 353.

(77) Züttel, A. *Naturwissenschaften* **2004**.

(78) DOE Office of Energy Efficiency and Renewable Energy Hydrogen, Fuel Cells & Infrastructure Technologies Program Multi-Year Research, Development and Demonstration Plan, available at: http://www.eere.energy.gov/ hydrogenandfuelcells/mypp.

(79) Rosi, N. L.; Eckert, J.; Eddaoudi, M.; Vodak, D.T.; Kim, J.; O'Keeffe, M. and Yaghi, O. M. *Science* **2003**, *300*, 1127.

(80) Yildirim, T. and Hartman, M. R. *Phys. Rev. Lett.* **2005**, *95*.

(81) Spencer, E. C.; Howard, J. A. K.; McIntyre, G. J.; Rowsell, J. L. C. and Yaghi, O. M. *Chem. Comm.* **2006**, *3*, 278.

(82) Collins, D. J. and Zhou, H.C. *J. Mater. Chem.* **2007**, *17*, 3154.

(83) Hirscher, M. and Panella, B. *Scr. Mater.* **2007**, *56*, 809.

(84) Isaeva, V. I. and Kustov, L. M. *Russ. J. Gen. Chem.* **2007**, *77*, 721.

(85) Lin, X.; Jia, J. H.; Hubberstey, P.; Schröder, M. and Champness, N. R. *Cryst. Eng. Comm.* **2007**, *9*, 438.

(86) Brown, C. M.; Liu, Y. and Neumann, D. A. *Pramana-Journal of Physics* **2008**, *71*, 755.

(87) Dincă, M. and Long, J. R. *Angew. Chem. Int. Ed.* **2008**, *47*, 6766.

(88) Liu, Y.; Kabbour, H.; Brown, C. M.; Neumann, D. A. And Ahn, C. C. *Langmuir* **2008**, *24*, 4772.

(89) Han, S. S.; Mendoza-Cortes, J. L. and Goddard Iii, W. A. *Chem. Soc. Rev.* **2009**, *38*, 1460.

(90) Moellmer, J.; Celer, E. B.; Luebke, R.; Cairns, A. J.; Staudt, R.; Eddaoudi, M. and Thommes, M. *Microporous Mesoporous Mater.* **2010**, *129*, 345.

(91) Mulfort, K. L. and Hupp, J. T. *Inorg. Chem.* **2008**, *47*, 7936.

(92) Yang, S.; Lin, X.; Blake, A. J.; Thomas, K. M.; Hubberstey, P.; Champness, N. R. and Schröder, M. *Chem. Commun.* **2008**, 6108.

(93) Wang, Q. and Johnson, J. K. *J. Chem. Phys.* **1999**, *110* 577.

(94) Dincă, M.; Dailly, A.; Tsay, C. and Long, J. R. *Inorg. Chem.* **2008**, *47*, 11.

(95) Jung, D. H.; Kim, D.; Lee, T. B.; Choi, S. B.; Yoon, J. H.; Kim, J.; Choi, K. and Choi, S. H. *J. Phys. Chem. B* **2006**, *110*, 22987.

(96) Ma, S. Q.; Sun, D. F.; Ambrogio, M.; Fillinger, J. A.; Parkin, S. and Zhou, H. C. *J. Am. Chem. Soc.* **2007**, *129*, 1858.

(97) Rowsell, J. L. C. and Yaghi, O. M. *Angew. Chem. Int. Ed.* **2005**, *44*, 4670.

(98) Chun, H.; Dubtsev, D. N.; Kim, H. and Kim, K. *Chem. Eur. J.* **2005**, *11*, 3521.

(99) Kesanli, B.; Cui, Y.; Smith, M. R.; Bittner, E. W.; Bockrath, B. C. and Lin, W. *Angew. Chem. Int. Ed.* **2005**, *44*, 72.

(100) Rzepka, M. and Lamp, P. and de la Casa-Lillo, M. A. *J. Phys. Chem. B* **1998**, *102*, 10894.

(101) Kuppler, R. J.; Timmons, D. J.; Fang, Q. R.; Li, J. R.; Makal, T. A.; Young, M. D.; Yuan, D. Q.; Zhao, D.; Zhuang, W. J. and Zhou, H. C. *Coord. Chem. Rev.* **2009**, *253*, 3042.

(102) Wu, H.; Zhou, W.andYildirim, T. *J. Phys. Chem. C* **2009**, *113*, 3029.

(103) Wu, H.; Zhou, W. and Yildirim, T. *J. Am. Chem. Soc.* **2009**, *131*, 4995.

(104) Zhou, W.; Wu, H.; Hartman, M. R. and Yildirim, T. *J. Phys. Chem. C* **2007**, *111*, 16131.

(105) Zhou, W.; Wu, H. and Yildirim, T. *J. Am. Chem. Soc.* **2008**, *130*, 15268.

(106) Gogotsi, Y.; Dash, R. K.; Yushin, G.; Yildirim, T.; Laudisio, G. and Fischer, J. E. *J. Am. Chem. Soc.* **2005**, *127*, 16006.

(107) Yang, Z. X.; Xia, Y. D. and Mokaya, R. *J. Am. Chem. Soc.* **2007**, *129*, 1673.

(108) Yushin, G.; Dash, R.; Jagiello, J.; Fischer, J. E. and Gogotsi, Y. *Adv. Funct. Mater.* **2006**, *16*, 2288.

(109) Binnemans, K. *Chem. Rev.* **2009**, *109*, 4283.

(110) Cotton, S. *Lanthanide and actinide chemistry* 2 Rev ed, John Wiley and Sons, Inc., England, **2006**.

(111) Carnall, W. T.; Fields, P. R. and Rajnak, K. *J. Chem. Phys.* **1968**, *49*, 4424.

(112) Stein, G. and Wurzberg, E. *J. Chem. Phys.* **1975**, *62*, 208.

(113) Bunzli, J. C. G. and Choppin, G. R. *Lanthanide Probes in Life, Chemical and Earth Sciences: Theory and Practice*, Elsevier Science, Netherlands, **1989**.

(114) Bunzli, J.-C. G. and Piguet, C. *Chem. Soc. Rev.* **2005**, *34*, 1048.

(115) Maas, H.; Currao, A. and Calzaferri, G. *Angew. Chem. Int. Ed.* **2002**, *41*, 2495.

Chapter 2

(1) Bravais, A. M. A. *Journal de l'Ecole polytechnique, Paris* **1850**.

(2) Reidel, D. *International tables for crystallography, Vol. A, Space group symmetry* **1983**

(3) Blakemore, J. S. *Solid State Physics* 2 ed., Cambridge: Cambridge University Press, **1969**.

(4) Rudden, M. N. and Wilson, J. *Elements of Solid State Physics* John Wiley and Sons Inc., **1993**.

(5) Suryanayana, C. and M. Grant *Norton X-ray Diffraction Plenum Press,* **1998**.

(6) Young, R. A. *The Rietveld Method. IUCr Monographs on Crystallography Oxford* 1 ed, vol. 5, 298, Oxford Science Publications, **1993**.

(7) *http://pubs.usgs.gov/of/2001/of01-041/htmldocs/xrpd.htm*.

(8) *http://www.nmai.si.edu/subpage.cfm?subpage=collections&second=conserv&third=pest_id*.

(9) West, A. R. *Basic Solid State Chemistry. 1997, Chichester: J. Wiley and Sons.*

(10) *http://www.esrf.eu/AboutUs/GuidedTour*.

(11) *Figure courtesy of Dr. Efrain Rodriguez at the NIST*.

(12) H. M. Rietveld *J. Appl. Cryst.* **1969**, 65.

(13) Larson, A. C. and Von Dreele, R. B. *GSAS, 1990, Los Alamos National Laboratory: Los Alamos, California.*

(14) Oszlányi, G. and Sütő, A. *Acta Cryst.* **2008**, *A*, 123.

(15) Oszlányi, G. and Sütő, A. *Acta Cryst.* **2005**, *A*, 147.

(16) Oszlányi, G. and Sütő, A. *Acta Cryst.* **2004**, *A*, 134.

(17) Dumas, C. and van der Lee, A. *Acta Cryst.* **2008**, *D*, 864.

(18) Wu, J. S.; Leinenweber, K.; Spence J. C. H. and O'keeffe, M. *Nat. Mater.* **2006**, *5*, 647.

(19) Zhou, Z. and Harris, K. D. M. *J. Phys. Chem. A* **2008**, *112*, 4863.

(20) Palatinus, L. *Acta Cryst.* **2004**, *A*, 604.

(21) Coelho, A. A. *Acta Cryst.* **2007**, *A*, 400.

(22) Palatinus, L. and Chapuis, G. *J. Appl. Crystallogr.* **2007**, 786.

(23) Yashima, M. and Tsunekawa, S. *Acta Cryst.* **2006**, *B*, 161.

(24) Yamamoto, K.; Takahashi, Y.; Ohshima, K.; Okamura, F. P. and Yukino, K. *Acta Cryst.* **1996**, *A*, 606.

(25) Takata, M. and Sakata, M. *Acta Cryst.* **1996**, *A*, 287.

(26) Takata, M. *Acta Cryst.* **2008**, *A*, 232.

(27) Takata, M.; Umeda, B.; Nishibori, E.; Sakata, M.; Saito, Y.; Ohno, M. and Shinohara, H. *Nature* **1995**, 46.

(28) Sakata, M.; Mori, R.; Kumazawza, S.; Takata, M. and Toraya, H. *J. Appl. Cryst.* **1990**, 526.

(29) Dinnebier, R. E.; Vensky, S.; Jansen, M. and Hanson, J. C. *Chem. Eur. J.* **2005**, 1119.

(30) de Vries, R. Y.; Briels, W. J. and Feil, D. *Phys. Rev. Lett.* **1996**, 1719.

(31) Le Bail, A.; Duroy, H. and Fourquet, J. L. *Mater. Res. Bull.* **1988**, *23*, 447.

(32) Samy, A.; Dinnebier, R. E.; van Smaalenb, S. and Jansen, M. *Acta Cryst.* **2010**, *B*, 184.

(33) Blundell, S. J. *Magnetism in condensed matter. Oxford master series in condensed matter physics.* Oxford University Press, **2001**.

(34) Cox, P. A. *The Electronic Structure and Chemistry of Solids* 1 ed., 259, Oxford Science Publications, Oxford University Press, **1993**.

(35) Harrison, W. A. *Electronic structure and the properties of solids* 1 ed., 586, New York, Dover Publications Inc., **1989**.

(36)   Raman, C. V. and Krishan, K. S. *Nature* **1928**, *121*, 501.

(37)   Turrell, G. and Corset, J. *Raman Microscopy: Developments and Applications*, eds., Elsevier Academic Press, **1996**.

(38)   Ferraro, J. R.; Nakamoto, K. and Brown, C. W. *Introductory Raman Spectroscopy*, Academic Press, **2003**.

(39)   McCreery, R. L. *Raman Spectroscopy for Chemical Analysis,* Wiley Interscience, **2000**.

(40)   Lewis, I. R. and Edwards, H. G. M. *Handbook of Raman Spectroscopy*, eds. Marcel Dekker, **2001**.

(41) Rouquerol, F.; Rouquerol, J. and Sing, K. *Adsorption by Powders and Porous Solids*, Academic Press, San Diego, London, Boston, New York, Sidney, Tokyo, Toronto,**1999**.

(42) Reccommendations, IUPAC *Pure Appl. Chem.* **1985**, *57*, 603.

(43) Langmuir, I. *J. Am. Chem. Soc.* **1916**, *22*, 2221.

(44) Brunauer, S.; Emmett, P. H. and Teller, E. *J. Am. Chem. Soc.* **1938**, *60*, 309.

(45) González, M. T.; Sepúlveda-Escribano, A.; Molina-Sabio, M. and Rodríguez-Reinoso, F. *Langmuir* **1995**, *11*, 2151.

(46) Myers, A. L. and Monson, P. A. *Langmuir* **2002**, *18*, 10261.

Chapter 3

(1) http://www.esrf.eu/UsersAndScience/Experiments/CRG/BM01/bm01-a.

(2) http://www.ncnr.nist.gov/instruments/bt1/bt1_plan.html.

(3) http://www.ncnr.nist.gov/instruments/bt1/bt1_spec.html.

(4) http://www.ncnr.nist.gov/instruments/bt1/bt1_for_xtal.html.

Chapter 4

(1) A. L. Spek, *"PLATON/SQUEEZE - An Effective Tool for Taking the Contribution of Disordered Solvent into Account in Crystal Structure Refinement."* Bijvoet Center

for Biomolecular Research, Utrecht University, Padualaan 8, 3584 CH Utrecht, Netherlands.

(2) van der Sluis, P. and Spek, A. L. *Acta Cryst.* **1990**, *A*, 194.

Chapter 5

(1) Guo, X.; Zhu, G.; Li, Z.; Sun, F.; Yang, Z. and Qiu, S. *Chem. Commun.* **2006**, 3172.

(2) Gustafsson, M.; Bartoszewicz, A.; Martín-Matute, B.; Sun, J.; Grins, J.; Zhao, T.; Li, Z.; Zhu, G. and Zou X. *Chem. Mater.* **2010**, *22*, 3316.

(3) Luo, J.; Xu, H.; Liu, Y.; Zhao, Y.; Daemen, L. L.; Brown, C.; Timofeeva, T. V. ; Ma, S. and Zhou, H.-C. *J. Am. Chem. Soc.* **2008**, *130*, 9626.

(4) Rosi, N. L.; Kim, J.; Eddaoudi, M.; Chen, B.; O'Keeffe, M. and Yaghi, O. M. *J. Am. Chem. Soc.* **2005**, *2005*, 1504.

(5) Chen, B.; Yang, Y.; Zapata, F.; Lin, G.; Qian, G. and Lobkovsky, E. B. *Adv. Mater.* **2007**, 1693.

(6) Kitagawa, S. and Kondo, M. *Bull. Chem. Soc. Jpn.* **1998**, *71*, 1739.

(7) Serre, C.; Millange, F.; Thouvenot, C.; Gardant, N.; Pellé, F.; and Férey, G. *J. Mater. Chem.* **2004**, *14*, 1540.

Chapter 6

(1) Liu, Y.; Kabbour, H.; Brown, C. M.; Neumann, D. A.andAhn, C. C. *Langmuir* **2008**, *24*, 4772.

(2) Luo, J.; Xu, H.; Liu, Y.; Zhao, Y.; Daemen, L. L.; Brown, C.; Timofeeva, T. V.; Ma, S. and Zhou, H.-C. *J. Am. Chem. Soc.* **2008**, *130*, 9626.

(3) Kaye, S. S. and Long, J. R. *J. Am. Chem. Soc.* **2005**, *127*, 6506.

(4) Wood, C. D.; Tan, B.; Trewin, A.; Niu, H.; Bradshaw, D.; Rosseinsky, M. J.; Khimyak, Y. Z.; Campbell, N. L.; Kirk, R.; Stöckel, E. and Cooper, A. I. *Chem. Mater.* **2007**, *19*, 2034.

(5) Kowalczyk, P.; Gauden, P. A.; Terzyk, A. P. and Bhatia, S. K. *Langmuir* **2007**, *23*, 3666.

(6) Navarro, J. A. R.; Barea, E.; Rodrguez-Diguez, A.; Salas, J. M.; Ania, C. O.; Parra, J. B.; Masciocchi, N.; Galli, S. and Sironi, A. *J. Am. Chem. Soc.* **2008**, *130*, 3978.

(7) Zhao, X.; Xiao, B.; Fletcher, A. J.; Thomas, K. M.; Bradshaw, D. and Rosseinsky, M. J. *Science* **2004**, *306*, 1012.

(8) Guo, X.; Zhu, G.; Li, Z.; Sun, F.; Yang, Z. and Qiu, S. *Chem. Commun.* **2006**, 3172.

(9) Wu, H.; Zhou, W. and Yildirim, T. *J. Am. Chem. Soc.* **2009**, *131*, 4995.

(10) Vidali, G.; Ihm, G.; Kim, H-Y. and Cole, M. W. *Surf. Sci. Rep.* **1991**, *12*, 133.

Chapter 7

(1) Reineke, T. M.; Eddaoudi, M.; O'Keeffe, M. and Yaghi, O. M. *Angew. Chem. Int. Ed.* **1999**, *38*, 2590.

Chapter 8

(1) Wang, X.-Y.; Gan, L.; Zhang, S.-W. and Gao, S. *Inorg. Chem.* **2004**, *43*, 4615.
(2) Coronado, E. and Dunbar, K. R. *Inorg. Chem.* **2009**, *48*, 3293.
(3) Rovira, C. and Veciana, J. *Cryst. Eng. Commun.* **2009**, *11*, 2031.
(4) Kurmoo, M. *Chem. Soc. Rev.* **2009**, *38*, 1353.
(5) Maspoch, D.; Ruiz-Molina, D. and Veciana, J. *Chem. Soc. Rev.* **2007**, *36*, 770.
(6) Wang, X.-Y.; Wang, Z. M. and Gao, S. *Chem. Commun.* **2008**, 281.
(7) Coronado, E. and Day, P. *Chem. Rev.* **2004**, *104*, 5419.
(8) Coronado, E.; Galan-Máscarós, J. R.; Gómez-García, C. J. and Laukhin, V. *Nature* **2000**, *408*, 447.
(9) Sato, O. *Acc. Chem. Res.* **2003**, *36*, 692.
(10) Evans, J. S. O.; Bénard, S.; Yu, P. and Clément, R. *Chem. Mater.* **2001**, *13*, 3813.
(11) Sato, O.; Tao, J. and Zhang, Y. Z. *Angew. Chem. Int. Ed.* **2007**, *46*, 2152.
(12) Cheng, X.-N.; Zhang, W.-X.; Lin, Y.-Y.; Zheng, Y.-Z. and Chen, X.-M. *Adv. Mater.* **2007**, *19*, 1494.
(13) Kaye, S. S.; Choi, H. J. and Long, J. R. *J. Am. Chem. Soc.* **2008**, *130*, 16921.
(14) Kurmoo, M.; Kumagai, H.; Chapmanc, K. W. and Kepert, C. J. *Chem. Commun.* **2005**, 3012.
(15) Ohkoshi, S.-I.; Arai, K.-I.; Sato, Y. and Hashimoto, K. *Nat. Mater.* **2004**, *3*, 857.
(16) Maspoch, D.; Ruiz-Molina, D.; Wurst, K.; Domingo, N.; Cavallini, M.; Biscarini, F.; Tejada, J.; Rovira, C. and Veciana, J. *Nat. Mater.* **2003**, *2*, 190.
(17) Maspoch, D.; Domingo, N.; Ruiz-Molina, D.; Wurst, K.; Tejada, J.; Rovira, C. and Veciana, J. *C. R. Chimie* **2005**, *8*, 1213.
(18) Maspoch, D.; Ruiz-Molina, D. and Veciana, J. *J. Mater. Chem.* **2004**, 2713.
(19) Ohkoshi, S.-I.; Tokoro, H.; Matsuda, T.; Takahashi, H.; Irie, H. and Hashimoto, K. *Angew. Chem. Int. Ed.* **2007**, *46*, 3238.
(20) Bai, Y. L.; Tao, J.; Wernsdorfer, W.; Sato, O.; Huang, R. B. and Zheng, L. S. *J. Am. Chem. Soc.* **2006**, *128*, 16428.
(21) Burrows, A. D.; Cassar, K.; Friend, R. M. W.; Mahon, M. F.; Rigby, S. P. and Warren, J. E. *Cryst. Eng. Comm.* **2005**, *7*, 548.
(22) Chen, W.; Wang, J.; Chen, C.; Yue, Q.; Yuan, H.; Chen, J. and Wang, S. *Inorg. Chem.* **2003**, *42*, 944.
(23) He, J. H.; Yu, J. H.; Zhang, Y. T.; Pan, Q. H. and Xu, R. R. *Inorg. Chem.* **2005**, *44*, 9279.
(24) Juillard, J. *Pure Appl. Chem.* **1977**, *49*, 885.
(25) Xie, L; Liu, S.; Gao, B.; Zhang, C.; Sun, C.; Li, D. and Su, Z. *Chem. Commun.* **2005**, 2402.
(26) Wang, Z.; Zhang, B.; Otsuka, T.; Inoue, K.; Kobayashi, H. and Kurmoo, M. *Dalton Trans.* **2004**, 2209.
(27) Jain, P.; Dalal, N. S.; Toby, B. H.; Kroto, H. W. and Cheetham, A. K. *J. Am. Chem. Soc.* **2008**, *130*, 10450.
(28) Hu, K. L.; Kurmoo, M.; Wang, Z. M. and Gao, S. *Chem. Eur. J.* **2009**, *15*, 12050.
(29) Jain, P.; Ramachandran, V.; Clark, R. J.; Zhou, H. D.; Toby, B. H.; Dalal, N. S.; Kroto, H. W. and Cheetham, A. K. *J. Am. Chem. Soc.* **2009**, *131*, 13625.

(30) Colacio, E.; Ghaze, M.; Kivekäs, R. and Moreno, J. M. *Inorg. Chem.* **2000**, *39,* 2882.

(31) Pérez, C. R.; Sanchiz, J.; Molina, M. H.; Lloret, F. and Julve, M. *Inorg. Chem.* **2000**, *39,* 1363.

(32) Yolanda, R. M.; Catalina, R. P.; Joaquín, S.; Francesc, L. and Miguel, J. *Inorg. Chim. Acta* **2001**, *318,* 159.

(33) Batten, S. R. and Robson, R. *Angew. Chem. Int. Ed.* **1998**, *37,* 1460.

(34) *Magnetic Properties of Transition Metal Compounds*; Carlin, R. L. and Van-Duyneveldt, A. J., Ed.; Springer-Verlag: New York, 1977.

(35) Swüste, C. H. W.; Botterman, A. C.; Millenaar, J. and De Jonge, W. J. M. *J. Chem. Phys.* **1977**, 5021.

(36) Srinivasan, G. and Seehra, M. S. *Phys. Rev. B* **1983**, *28,* 1.

(37) Richardson, F. S. *Chem. Rev.* **1982**, *82,* 541.